On ultra-wideband over fiber transmission systems employing semiconductor optical amplifiers

Haidar Taki

▶ **To cite this version:**

Haidar Taki. On ultra-wideband over fiber transmission systems employing semiconductor optical amplifiers. Other. Université de Bretagne occidentale - Brest, 2017. English. NNT : 2017BRES0071 . tel-01968031

HAL Id: tel-01968031
https://theses.hal.science/tel-01968031

Submitted on 2 Jan 2019

HAL is a multi-disciplinary open access archive for the deposit and dissemination of scientific research documents, whether they are published or not. The documents may come from teaching and research institutions in France or abroad, or from public or private research centers.

L'archive ouverte pluridisciplinaire **HAL**, est destinée au dépôt et à la diffusion de documents scientifiques de niveau recherche, publiés ou non, émanant des établissements d'enseignement et de recherche français ou étrangers, des laboratoires publics ou privés.

THÈSE / UNIVERSITÉ DE BRETAGNE OCCIDENTALE
sous le sceau de l'Université Bretagne Loire

pour obtenir le titre de
DOCTEUR DE L'UNIVERSITÉ DE BRETAGNE OCCIDENTALE
Mention : Optoélectronique - Hyperfréquences
École Doctorale MATHSTIC

présentée par

Haidar TAKI

Préparée au Laboratoire Lab-STICC UMR CNRS 6285
École Nationale d'Ingénieurs de Brest (ENIB)

-

On Ultra-Wideband over Fiber Transmission Systems Employing Semiconductor Optical Amplifiers

Thèse soutenue le 25 septembre 2017
devant le jury composé de :

Bernard UGUEN
Professeur des Universités, Université de Rennes 1 / Rapporteur

Christelle AUPETIT-BERTHELEMOT
Professeur des Universités, Université de Limoges / Rapporteur

Emanuel RADOI
Professeur des Universités, UBO / Examinateur

Pascal CHARGE
Professeur des Universités, Polytech Nantes / Examinateur

Stéphane AZOU
Professeur des Universités, ENI de Brest / Directeur de thèse

Ammar SHARAIHA
Professeur des Universités, ENI de Brest / Encadrant

Ali ALAEDDINE
Professeur, Lebanese University, Beirut / Directeur de thèse

Ali HAMIE
Professeur, Lebanese University, Beirut / Encadrant

Thank you my Two Beloved Grandmothers for your Great Encouragement and Support since I was a child, I Dedicate this Doctoral Thesis to both of you

Contents

1 An Introduction to Impulse Radio Ultra WideBand 19
1.1 Modern Communication Technologies 19
1.2 Ultra WideBand Definition and Regulations 20
1.3 UWB Advantages 21
1.4 UWB Applications 23
1.5 UWB Technologies 23
1.6 IR-UWB Pulse Waveforms and Modulation Types 24
1.7 UWB Challenges 28
1.8 UWB Wireless Channel Model 28
1.9 Impulse Radio over fiber 28
1.10 Contributions of this Dissertation 29

2 UWB over Fiber Communications: Literature Review and Introduction to our System 36
2.1 Optical Fiber Communications: Advantages, Methodologies, and Challenges 36
2.2 UWB Pulse Generation Techniques 39
2.3 Radio Over Fiber Transceiver Based on Mach-Zehnder Modulator 44
2.3.1 Mach-Zehnder Modulator: Principle of Operation and Transfer Function 45
2.3.2 On Optimizing the Operating Conditions of MZM 46
2.4 Introducing the Semiconductor Optical Amplifier in our Radio Over Fiber Transmission System 49
2.4.1 SOA Fundamentals 49
2.4.2 SOA Nonlinearities 51
2.4.3 SOA Interesting Features and Applications 52
2.4.4 SOA Physical Model 53
2.4.5 Adopting SOA in our UWB over fiber system 56
2.5 Summary 56

3 Pre-distortion Schemes for Mitigating Nonlinear Effects in SOA-Based IR-UWB over Fiber Systems 64
3.1 Introduction 64
3.2 Impact of SOA on propagated pulses 65
3.3 SOA Nonlinearities Mitigation via Electrical Pulses Pre-distortion 68
3.3.1 Case of 5-th derivative Gaussian pulse 69
3.3.2 Higher order of Gaussian derivative 70
3.3.3 Abraha's Combination of Gaussian Doublets 72

3.3.4 Introducing a new waveform based on a combination of Gaussian pulses . . . 75
3.3.5 Pre-distortion with different biasing currents . . . 76
3.3.6 Robustness against uncertainty for single waveforms and combinations 78
3.4 Case of a modulated impulse radio signal propagating over optical fiber link 79
3.5 Summary . . . 81

4 Analog Chirping Techniques for coping with SOA Impairments in the proposed IR-UWB over fiber system 87
4.1 Introduction . . . 87
4.2 Impact of SOA ASE noise and nonlinearities on IR-UWB pulse shapes . . 88
4.3 Noise Reduction Technique based on Up and Down Chirping via Group Delay Phasers . . . 89
4.4 Embedding Chirping Schemes in SOA-based IR-UWB over fiber systems . 92
4.4.1 Reducing the ASE noise impact via chirping . . . 93
4.4.2 SOA linearization via chirping . . . 94
4.4.3 Bias current influence . . . 96
4.4.4 Time waveforms and corresponding spectra of pulses with and without chirping . . . 96
4.5 Benefits of the chirping schemes for a modulated Impulse Radio propagating over an optical fiber . . . 99
4.6 Summary . . . 102

5 Improving the Power Efficiency of the UWB over Fiber System via Pulse Shape Randomization 106
5.1 Introduction . . . 106
5.2 Discrete Spectral Lines in Impulse Radio Systems . . . 107
5.3 Existing Randomization Techniques . . . 108
5.3.1 Time Hopping . . . 108
5.3.2 Direct Sequence . . . 109
5.4 Proposed Multi-Waveform OOK/PPM Modulation Formats . . . 109
5.5 Carrier-Based versus Carrierless Shape Randomization Techniques . . . 112
5.5.1 Carrier-Based Randomization . . . 112
5.5.2 Carrierless Randomization . . . 115
5.6 Applying the Randomization Scheme Considering our IR-UWB over Fiber System . . . 117
5.7 Summary . . . 121

6 Different Modulation Options for SOA-based UWB over Fiber Systems: An Experimental Study 124
6.1 Experimental Setup of Our SOA-based UWB over Fiber System . . . 124
6.2 Investigation of Chaotic Transmitted Reference Schemes . . . 126
6.2.1 Transmitted Reference Schemes . . . 126
6.2.2 Chaotic-Based Modulation Patterns . . . 127
6.2.3 DCSK and I-DCSK Chaotic Schemes . . . 127
6.2.4 Performance Evaluation of the Chaotic Schemes in Comparison to other non-coherent modulation formats . . . 129
6.3 Examining the Performance of Chirping with the Proposed Transmission System . . . 135

6.4 Summary 138

7 Conclusion and Perspectives **141**
7.1 Conclusion 141
7.2 Perspectives 143

Appendices **145**

A Interior Point Algorithm: A Brief Overview **146**

B SOA Model **148**

C Optilux Fiber Model based on Split-Step Fourier Algorithm **149**

D Spectra of MWOOK and MWPPM: Mathematical Development **150**

List of Figures

1.1 Cisco Forecasts 49 Exabytes per Month of Mobile Data Traffic by 2021 [3]. 19
1.2 Global Mobile Devices and Connections by 2G, 3G, and 4G+, (percentages refer to device and connections share), and LPWA (Low Power Wide Area) [3]. 20
1.3 Mobility and speed of UWB in correspondence with other existing communication technologies [4]. 20
1.4 The free space emission limit regulated by the Federal Communication Commission, the Ultra WideBand frequency range goes from 3.1 GHz to 10.6 GHz. 21
1.5 UWB intended bands specified in different regions [23]. 22
1.6 Schematic diagram for the carrier-based UWB transceiver. 23
1.7 The spectrum of single carrier (left), multi-carrier (middle), and impulse radio (right) UWB respectively. 23
1.8 Schematic diagram for the Impulse Radio UWB transceiver. 24
1.9 Normalized time waveforms of Rectangular, Laplacian, Cubic, and Gaussian pulses (left), besides to their corresponding power spectral densities (dBm/MHz) (right). *Basic* denotes the fundamental Gaussian, *Mono* corresponds to the first order derivative, and *Doub* presents the second order derivative. 24
1.10 Time waveforms of OOK (above) and PAM (below) modulation formats for a sequence of 8 bits, '1 1 0 1 0 0 1 0 '. 25
1.11 Time waveforms PPM modulation format for a sequence of 8 bits, '1 1 0 1 0 0 1 0 '. 26
1.12 Time waveforms of PSM modulation format for a sequence of 8 bits, '1 1 0 1 0 0 1 0 '. 26
1.13 Time waveform of Transmitted Reference modulation format for a sequence of 8 bits, '1 1 0 1 0 0 1 0 '. 27
1.14 A schematic diagram for a radio over fiber access network [67]. 29

2.1 A simple schematic diagram for the optical communication system. 36
2.2 Different branches and public areas supported by the optical access networks [6]. 37
2.3 Attenuation in a single mode fiber versus wavelength [8]. 38
2.4 Time waveforms (a) and corresponding spectra (b) of Gaussian Monocycle at several distances of optical link, besides to the time and frequency properties versus distance (c) [5]. 38
2.5 Two main types of pulse generation prior to over fiber propagation. 39
2.6 A simplified schematic diagram of the UWB pulse generator proposed in [62]. 42
2.7 The schematic diagram of the optical pulse generator proposed in [75]. . . 43

2.8 The schematic diagram of the optical pulse generator proposed in [5]. . . . 43
2.9 The block diagram of the optical pulse generator for the Gaussian monocycle proposed in [50] 44
2.10 The operation principle of the optical pulse generator for the Gaussian monocycle proposed in [50] 44
2.11 Block diagram of the impulse radio over fiber system adopted in this study. 45
2.12 A simple schematic diagram for the MZM structure. 45
2.13 MZM power ratio versus input voltage. 46
2.14 The power efficiency of 2 Gbps OOK based on the 5th derivative Gaussian, versus pulse shaping factor and DC biasing voltage (in optical back-to-back case), where $V_{pp} = 0.4\ V\pi$. 47
2.15 Time waveforms and power spectral densities of 5th-derivative Gaussian pulse for several V_{pp} values. 47
2.16 Power efficiency versus fiber length and V_{pp} for 2 Gbps OOK based on 5th-derivative Gaussian pulse. 48
2.17 Power efficiency versus fiber length for 2 Gbps OOK based on the 5th-derivative Gaussian, in the case of using fixed or optimal V_{pp}. 48
2.18 Simple schematic diagram for SOA structure. 50
2.19 The gain versus input optical power for several values of biasing current. . 50
2.20 System and functional applications for SOA [77]. 53
2.21 A schematic diagram describing the ADS model for SOA, and co-simulation with MATLAB. 53
2.22 One calculus section $[M_\ell]$ in the SOA, the signal and ASE intensity share the carrier density [85, 86]. 54
2.23 Block diagram of the impulse radio over fiber system with Matlab/ADS co-simulation. 56

3.1 Power Spectral Density of 5^{th} Gaussian in electrical domain and at SOA output (adopted and non-adopted to FCC mask). 65
3.2 PSR_{2GHz} of 5^{th} Gaussian versus SOA input power and peak-to-peak voltage, where no fiber is considered. 65
3.3 Average Slope Time Ratio of 5^{th} Gaussian versus SOA input power and peak-to-peak voltage, where no fiber is considered. 66
3.4 Power Efficiency of 5^{th} Gaussian versus SOA input power for several peak-to-peak voltages, where no fiber is considered. 67
3.5 The reverse of power efficiency corresponding to Abraha's Combination obtained at SOA output, as function of the values of input parameters. . . 69
3.6 Block diagram for the optimization process used for designing pre-distorted electrical waveforms. 70
3.7 Functional diagram for the optimization process based on interior point algorithm. 70
3.8 Original (Org) and pre-distorted (PD) 5^{th} Gaussian, in electrical domain (Elec) and after SOA (Opt). 71
3.9 Original (Org) and pre-distorted (PD) 6^{th} Gaussian, in electrical domain (Elec) and after SOA (Opt). 72
3.10 Abrahas proposed pulse based on a combination of Gaussian Doublets. . . 73
3.11 Original (Org) and pre-distorted (PD) C_{Doub}, in electrical domain (Elec) and after SOA (Opt). 73

3.12 Our proposed combination C_G based on the pulses g_i, in time (left) and frequency (right) domain. 74
3.13 Time waveforms and corresponding spectra of fundamental Gaussian, Doublet, 5-th Gaussian, Abraha's combination, and our novel pulse based on Gaussians. 74
3.14 Original (Org) and pre-distorted (PD) C_G, in electrical domain (Elec) and after SOA (Opt). 75
3.15 Power Efficiency of original and pre-distorted pulses directly after SOA (at 40 km) for several biasing currents; C_D, Doublets-based Abraha's combination, G_5, 5^{th} Gaussian, G_6, 6^{th} Gaussian, C_G, our proposed combination based on Gaussians. 76
3.16 Robustness against uncertainty for the 5^{th} and 6^{th} Gaussian pulses, besides to Abraha's combination of Doublets. 77
3.17 Robustness against uncertainty for our proposed pulse based on Gaussians. 77
3.18 Power Efficiency versus fiber length for 1.5 Gbps OOK based on the utilized pulses, P-SOA=0 dBm, $I_{bias} = 250$ mA, $V_{pp} = 0.5V\pi$, where SOA is placed at 40 km. 78
3.19 Irregular PSD of 1.5 Gbps OOK based on original (left) and pre-distorted (right) $C_G(t)$ after SOA (at 40km), where P-SOA=0 dBm, $I_{bias} = 250$ mA, $V_{pp} = 0.5V\pi$. 79
3.20 Regular PSD of 0.75 Gbps PPM based on original (left) and pre-distorted (right) $C_G(t)$ after SOA (at 40km), where P-SOA=0 dBm, $I_{bias} = 250$ mA, $V_{pp} = 0.5V\pi$. 80
3.21 Power Efficiency versus fiber length for 0.75 Gbps PPM based on utilized pulses, P-SOA=0 dBm, $I_{bias} = 250$ mA, $V_{pp} = 0.5V\pi$, where SOA is placed at 40 km. 80

4.1 Power Spectral Density of 5^{th} Gaussian in electrical domain and after SOA (while operating in the linear or saturation region). 88
4.2 The general principle of a wireless transmission system utilizing up and down chirping. 89
4.3 Time waveforms of 5th up-chirped Gaussian with a 1 ns duration (left), besides to the de-chirped in comparison with the original having 0.5 ns duration (right). 89
4.4 The Wigner Ville Distribution of $5th$ original Gaussian (left) besides to the up-chirped pulse (right) in electrical domain, where the chirping slope is 0.0472 ns/GHz. 90
4.5 Bit error rate versus Eb/N_0 for normal and chirped (with a slope of 0.0472 ns/GHz) transmissions over AWGN channel, considering OOK and PPM modulations. 91
4.6 Bit error rate in an AWGN channel versus maximum data rate could be achieved (associated with a specific chirping slope) for OOK and PPM modulations. 92
4.7 Up and down chirping applied before and after the optical system respectively, which includes the MZM, fiber, SOA in-line amplifier, and photodetector. 92

4.8 Time waveforms of the noisy 5th Gaussian obtained at SOA output, with (right) and without (left) chirping, P-SOA= -20 dBm, $V_{pp} = 0.1V\pi$, $I_{bias} =$ 250 mA. 93
4.9 Bit error rate versus SOA input power for several data rates of normal and chirped transmissions, considering OOK and PPM, $V_{pp} = 0.1V\pi$ and $I_{bias} = 250$ mA. 93
4.10 Average cross correlation between electrical and optical (after photo-detector) waveforms, versus SOA input power for several combinations of sinusoids, $Vpp = 0.5V\pi$, I_{bias} =250 mA. 94
4.11 Cross Correlation between electrical and optical waveforms versus chirping slope, for the 5th Gaussian pulse and Abraha's combination, where $Vpp = 0.5V\pi$, I_{bias} =250mA, P-SOA=0 dBm. 94
4.12 The input-to-output mapping for Abraha's combination after being passed through SOA, without (left) and with (right) chirping, where P-SOA=0 dBm, $I_{bias} = 250$ mA, $V_{pp} = 0.5V\pi$. 95
4.13 Power Efficiency of original and chirped pulses directly after SOA (at 40 km) for several biasing currents, where $Vpp = 0.5\,V\pi$ and P-SOA= 0 dBm. 96
4.14 Original (Org) 5th Gaussian in electrical domain (Elec) and at SOA output (Opt), besides to the chirped (0.0472 ns/GHz) pulse after SOA. 97
4.15 Original (Org) Abraha's combination in electrical domain (Elec) and at SOA output (Opt), besides to the chirped (0.0472 ns/GHz) pulse after SOA. 98
4.16 Power spectral density of the original, up chirped, and de-chirped 5^{th} Gaussian in electrical domain, where the chirping slope is 0.0472 ns/GHz. . . . 98
4.17 Power Efficiency versus fiber length for 1 Gbps OOK based on the utilized pulses, P-SOA=0 dBm, $I_{bias} = 250$ mA, $V_{pp} = 0.5V\pi$, where SOA is placed at 40 km. 99
4.18 Abraha's combination at 100 km (60 km after SOA) with (right) and without (left) chirping, where P-SOA=0 dBm, $I_{bias} = 250$ mA, $V_{pp} = 0.5V\pi$. . . 99
4.19 PSD of 1 Gbps OOK based on original (left) and chirped (right) Abraha's combination after SOA (at 40km), where P-SOA=0 dBm, $I_{bias} = 250$ mA, $V_{pp} = 0.5V\pi$. 100
4.20 PSD of 0.5 Gbps PPM based on original (left) and chirped (right) Abraha's combination after SOA (at 40km), where P-SOA=0 dBm, $I_{bias} = 250$ mA, $V_{pp} = 0.5V\pi$. 101
4.21 Power Efficiency versus fiber length for 0.5 Gbps PPM based on the utilized pulses, P-SOA=0 dBm, $I_{bias} = 250$ mA, $V_{pp} = 0.5V\pi$, where SOA is placed at 40 km. 101

5.1 The power spectral density for 0.5 Gbps (left) and 2 Gbps (right) OOK signal based on the 5^{th} derivative Gaussian pulse. 107
5.2 Time Representation for 1 symbol extracted from a TH-PPM signal, consisting of 5 frames/symbol, and 5 chips/frame, the TH code is [2 5 3 1 4] and T_c=1 ns, where the basic transmitted pulse is the Gaussian Monocycle. 108
5.3 Time Representation for 2 symbols extracted from a DS-PAM signal, consisting of 5 frames/symbol, the DS code is [1 -1 1 1 -1] and T_f=1 ns, where the basic transmitted pulse is the Gaussian Doublet. 109

5.4 A simple description for Multi-Waveform PPM transmission, where each frame consists of 2 time slots. 110
5.5 The Peak-to-Average Spectral Ratio versus number of pulses used for OOK randomization, at different data rates. 112
5.6 The Peak-to-Average Spectral Ratio versus number of pulses used for PPM randomization, at different data rates. 112
5.7 Power Spectral Densities of 2Gbps standard OOK (left) and multi-waveform OOK based on 4 pulses (right). 113
5.8 Power Spectral Densities of 1 Gbps classical PPM (left) and MWPPM based on 4 pulses (right). 114
5.9 Power Efficiency versus the number of pulses used for 2 Gbps MWOOK and 1 Gbps MWPPM. 114
5.10 Average Power versus the number of pulses used for 2 Gbps MWOOK and 1 Gbps MWPPM. 115
5.11 The 5-th optimal Gaussian used for OOK-PPM, besides to 4-th/5-th pulses utilized with MWOOK-MWPPM. 115
5.12 The power spectral densities of 5-th optimal Gaussian used for standard OOK-PPM, besides to that of 4-th and 5-th pulses utilized with MWOOK-MWPPM. 116
5.13 Peak-to-Average Spectral Ratio versus data rate for OOK-MWOOK based on 4^{th} and 5^{th} derivatives of Gaussian. 117
5.14 Peak-to-Average Spectral Ratio versus data rate for PPM-MWPPM based on 4^{th} and 5^{th} derivatives of Gaussian. 117
5.15 Power Efficiency versus Fiber Length, where MZM is injected by 15 dBm Laser Power. 118
5.16 Power Efficiency Improvement (or Gain) versus Fiber Length for different input optical powers to MZM. 118
5.17 Power Spectral Densities for 2 Gbps OOK-MWOOK based on 4^{th}-5^{th} derivatives of Gaussian Pulses at SOA output, where I_{bias}=100 mA. 119
5.18 Power Spectral Densities for 1 Gbps PPM-MWPPM based on 4^{th}-5^{th} derivatives of Gaussian Pulses at SOA output, where I_{bias}=100 mA. 119
5.19 Power Efficiency versus Fiber Length, using SOA placed at 40 km, and biased with 150 mA at 15 dBm. 120
5.20 Power Efficiency Improvement (Gain) versus Fiber Length in case of utilizing SOA at 40 km for several biasing currents, with a laser power of 15 dBm. 120

6.1 A schematic diagram for the experimental setup, (Amp: Amplifier, MZM: Mach-Zehnder Modulator, SMF: Single Mode Fiber, SOA: Semi-conductor Optical Amplifier, Att: Attenuator, PC: Polarization Controller, PD: Photo-detector). 125
6.2 A real photo for the experimental equipments. 125
6.3 The auto-correlation function of the chaotic sequence (a) with the corresponding probability density function (b). 127
6.4 The logistic map function and iterations for r=4 (a), besides to the time trajectories versus number of chips (b), where r is a parameter which influences the sequence dynamics. 128
6.5 Block diagram of the DCSK transmission system 128

6.6 Block diagram of the I-DCSK transmission system 129
6.7 Time jittering to frame size ratio versus the frame index in the received signal, and corresponding probability distribution. 129
6.8 Time waveform and corresponding spectrum of the electrical Gaussian monocycle utilized with OOK and PPM, where $\sigma = 70$ ps. 130
6.9 Received PPM symbol just after SOA (at 40 km), where the laser output power is 7 dBm and I_{bias}= 200 mA. 130
6.10 Time waveforms and corresponding power spectral density of 2-DCSK operating at 0.25 Gbps, where the laser output power is 7 dBm, I_{bias}= 200 mA, and SOA is placed at 40 km (the time waveform is a truncation of only 10 symbols). 131
6.11 Time waveforms and corresponding power spectral density of 4-I-DCSK operating at 0.25 Gbps, where the laser output power is 7 dBm, I_{bias}= 200 mA, and SOA is placed at 40 km (the time waveform is a truncation of only 10 symbols). 131
6.12 Time waveforms and corresponding power spectral density of OOK operating at 0.5 Gbps, where the laser output power is 7 dBm, I_{bias}= 200 mA, and SOA is placed at 40 km (the time waveform is a truncation of only 10 symbols). 132
6.13 Time waveforms and corresponding power spectral density of PPM operating at 0.25 Gbps, where the laser output power is 7 dBm, I_{bias}= 200 mA, and SOA is placed at 40 km (the time waveform is a truncation of only 10 symbols). 132
6.14 Bit error rate versus received optical power (just before SOA) for DCSK, I-DCSK, OOK, and PPM modulation schemes, where I_{bias}= 200 mA and SOA is placed at 40 km. 133
6.15 Reference and data waveforms of the received DCSK (up) and I-DCSK (down) signals corresponding to one symbol, where the laser output power is 7 dBm, I_{bias}= 200 mA, and SOA is placed at 40 km. 133
6.16 The probability density function of the 2-DCSK (up) and 4-I-DCSK (down) cross correlation measured just before decision, for electrical back-to-back (left) and after photo-detector (right), where the laser output power is 4 dBm, I_{bias}= 200 mA, and SOA is placed at 40 km. 134
6.17 Time waveforms of the original (left) and up-chirped (right) combination of modulated Gaussians in electrical domain, where σ =180 ns, f_1= 0.4 GHz, f_2 = 0.8 GHz, and the slope is 10 ns/GHz. 135
6.18 The time waveforms of the received pulse with and without chirping (at a slope of 10 ns/GHz) besides to the original pulse in electrical domain, where the laser output power is 2 dBm and I_{bias}= 200 mA. 136
6.19 Cross correlation to energy ratio versus laser output power for I_{bias}= 100 mA and I_{bias}= 200 mA, the chirping slope is 10 ns/GHz and SOA is placed at 40 km. 137
6.20 Bit error rate versus received optical power (just before SOA) for chirped and non-chirped OOK and PPM modulation schemes, where I_{bias}= 200 mA and SOA is placed at 40 km. 137
6.21 Received OOK just after SOA (at 40 km) in the case of no chirping (up) and chirping (down) with a slope of 10 ns/GHz, where the laser output power is 3 dBm and I_{bias}= 200 mA. 138

A.1 General scheme of an interior point method 147
A.2 Interior point optimization path. 147

B.1 Values of the parameters for SOA model [4]. 148

List of Tables

1.1 A summary of the main characteristics of UWB in comparison with other wireless technologies [24]. 22

3.1 Parameters (σ_1, σ_2, σ_3, a_2/a_1, a_3/a_1) of electrical generated pulses, and the spectral characteristics (f_{peak}, B_{10}, BL_{34}) of corresponding waveforms at SOA output (placed at 40 km). Besides to the power efficiencies (%) in electrical domain and after SOA, with P-SOA= 0 dBm, $I_{bias} = 250\ mA$, and $V_{pp} = 0.5\ V_\pi$. 71

4.1 The set of chirping slopes considered in the study, and the corresponding time shift, besides to the pulse duration and resultant data rate (R) for OOK or PPM. 91

4.2 Pulse Shaping Factors of electrical generated waveforms, and spectral characteristics (f_{peak}, B_3, B_{10}, BL_{34}) of corresponding pulses at SOA output (placed at 40 km). Besides to the power efficiencies (%) in electrical domain and after SOA, with P-SOA= 0 dBm, $I_{bias} = 250\ mA$, and $V_{pp} = 0.5\ V_\pi$. 97

Abbreviations

Amplified Spontaneous Emission (ASE)
Amplitude Shift Keying (ASK)
Arbitrary Waveform Generator (AWG)
Asymmetric Mach-Zehnder Interferometer (AMZI)
Average Slope Time Ratio (ASTR)
Balanced Photo-Detector (BPD)
Binary Phase Shift Keying (BPSK)
Binary/Quadrature Phase Shift Keying (BPSK/QPSK)
Bit Error Rate (BER)
Central Unit (CU)
Coded OFDM (COFDM)
Complementary Code Keying (CCK)
Complementary Metal Oxide Semiconductor (CMOS)
Cross Correlation to Energy Ratio (XCTER)
Cross Phase Modulation (XPM)
Delay Line (DL)
Differential Chaos Shift Keying (DCSK)
Direct Sequence (DS)
Direct Sequence Spread Spectrum (DSSS)
Discrete to Continuous Spectral Ratio (DCSR)
Distributed Feedback Laser (DFB)
Electrical Spectrum Analyzer (ESA)
Electro-Optic Modulator (EOM)
Erbium Doped Fiber Amplifier (EDFA)
Extinction Ratio (ER)
Federal Communication Commission (FCC)
Fiber Bragg Grating (FBG)
Fiber-to-the-Home (FTTH)
Forward Error Correction (FEC)
Frequency Hopping Spread Spectrum (FHSS)
Gaussian Frequency Shift Keying (GFSK)
Global System for Mobile (GSM)
Improved DCSK (I-DCSK)
Impulse Radio (IR)
Laser Diode (LD)
Mach-Zehnder Interferometer (MZI)
Mach-Zehnder Modulator (MZM)
M-ary Quadrature Amplitude Modulation (M-QAM)
Mode-Locked Fiber Laser (MLFL)
Multiband OFDM (MB-OFDM)
Multi-Waveform On Off Keying (MWOOK)
Multi-Waveform Pulse Position Modulation (MWPPM)
Offset-QPSK (O-QPSK)
On Off Keying (OOK)
Optical Band Pass Filter (OBPF)
Optical Coupler (OC)

Optical Modulation Analyzer (OMA)
Optical Sampling Oscillator (OSO)
Optical Signal to Noise Ratio (OSNR)
Optical Spectrum Analyzer (OSA)
Optical Variable Delay Line (OVDL)
Orthogonal Frequency Division Multiplexing (OFDM)
Peak-to-Average Spectral Ratio (PASR)
Personal Area Network (PAN)
Polarization Beam Splitter (PBS)
Polarization Controller (PC)
Polarization Maintaining Fiber (PMF)
Polarization Modulator (PolM)
Power Spectral Density (PSD)
Pulse Amplitude Modulation (PAM)
Pulse Position Modulation (PPM)
Pulse Shape Modulation (PSM)
Radio Frequency (RF)
Radio over Fiber (RoF)
Remote Antenna Units (RAUs)
Self Phase Modulation (SPM)
Semiconductor Optical Amplifier (SOA)
Single Mode Fiber (SMF)
Time Hopping (TH)
Transmitted Reference (TR)
Transverse-Electric (TE)
Transverse-Magnetic (TM)
Tunable Laser Diode (TLD)
Ultra WideBand (UWB)
Variable Attenuator (ATT)
Wireless Local Area Network (WLAN)

Introduction

The growing demand for high speed and low power transmission systems nowadays, increases the attention towards ultra wideband (UWB) radio technology, which is a promising solution for new generations of short-range broadband wireless communications. UWB was regularly born in 2002, when the Federal Communication Commission (FCC) approved its free space propagation within a 7.5 GHz band and -41.3 dBm/MHz maximum emitted power. UWB over fiber has been an attractive topic to investigate for many researchers, as by exploiting the benefits of optical link a high quality of transmission could be achieved at long distances. The Impulse Radio (IR) UWB, which is a cost effective approach offering a low order of generation complexity, is the central topic of investigation in this dissertation. The target is to enhance the IR-UWB over fiber system performance considering different alternatives, where the proposed transceiver is based on a low cost Semiconductor Optical Amplifier (SOA). The latter has been adopted with the view to get a reach extension within the optical access network. Long optical link transmission requires operating in the SOA saturated regime so as to get a high amplifier gain. That translates into strong nonlinearities acting on propagated waveforms, which lead to spectral distortions and a consequent degradation in the power efficiency. These nonlinearities have been mitigated via analog pre-distortion schemes, based on the derivatives of a Gaussian pulse and their combinations. By tuning the input pulses parameters via global optimization, we change the dynamics of output waveforms and correct SOA impact. In this way, high power efficiencies have been consistently achieved for a strongly saturated input power. The feasibility of this approach has been examined considering On Off Keying (OOK) and Pulse Position Modulation (PPM) formats, pre-distortion has shown a great potential for long spans in the optical link. In addition to nonlinearity, another challenge is the Amplified Spontaneous Emission (ASE) noise inherent to SOA, which may degrade the bit error rate performance of the over fiber system. A phaser-based processing technique has been employed to simultaneously linearize SOA characteristics and attenuate the ASE impact. Symmetrical up and down chirping in electrical domain and after SOA has proved to be effective in enhancing the transmission performance. Based on the fact that a lower order of four wave mixing and cross gain modulation is obtained against signals with less frequency diversity, we reduced SOA nonlinear effects via analog chirping schemes and increased the correlation of the output pulses with original ones. Utilizing Gaussian pulse derivatives and combinations, a substantial improvement has been carried out for low and high input powers entering the amplifier. A very good error performance and power efficiency have been obtained with OOK and PPM, while propagating over a large extension of single mode fiber. The power efficiency of the UWB signal is highly influenced by the modulation pattern, and it is well known that pulse repetition associated with impulse radio transmission may result in discrete lines added to the overall spectrum, hence violating the maximum power limit imposed by the regulatory bodies. Thus, besides to pre-distortion and chirping techniques, an advanced type of modulation has been investigated as a complementary approach, so as to suppress these spectral spikes and enhance the power efficiency. The key concept is randomizing the shape of transmitted pulses; to do so, each data symbol is represented by multi-waveforms satisfying orthogonality. We have mathematically derived the closed-form expressions of the power spectral densities corresponding to the modified OOK and PPM formats. The potential of the proposed scheme, which can be either employed for impulse radio or carrier-based systems, has been studied in electrical domain and by con-

sidering the UWB over optical fiber application. Utilizing Gaussian pulse derivatives, our approach proves to be effective for PPM and OOK with an advantage in terms of power efficiency at short distances, with a link extension by adopting the SOA in-line amplifier. Finally, the performance of differential chaos shift keying (DCSK) modulation has been examined for the first time by taking into account the optical link effects. The encouraging advantages of DCSK, which is a type of transmitted reference scheme, are the good error performance besides to the ease of practical design implementation. Experimental results illustrate the effectiveness of DCSK in comparison with other non-coherent modulation schemes, a lower probability of error was obtained at receiver side without adding more complexity to the conventional system.

Chapter 1 states a general overview about impulse radio ultra wideband transmission, and advanced technologies in wireless telecommunications. The ultra wideband technology is defined, with some focusing on its regulations, advantages, and applications. Impulse radio approach is also introduced, besides to its conventional pulse types and modulation formats. Finally a concise presentation for the original contributions of this thesis is made. Chapter 2 explores the UWB over fiber technology, and summarizes the research progress in optical pulse generation techniques. Our basic over fiber system relying on Mach-Zehnder Modulator is introduced, which has been also integrated with the Semiconductor Optical Amplifier placed for in-line amplification purpose. Analog predistortion schemes are investigated in chapter 3, with the aim to mitigate Semiconductor Optical Amplifier nonlinearities. We show that impulse radio power efficiency could be enhanced based on several pre-distortion concepts. In chapter 4, we propose a novel configuration based on up and down phasers placed before and after the optical system respectively. The target is to reduce inherent nonlinearities as well the Amplified Spontaneous Emission noise. Interesting results are obtained in terms of power efficiency and bit error rate performance. In chapter 5, we address the problem of discrete spectral spikes resulting from On Off Keying or Pulse Position Modulation characteristics, and propose a new modulation scheme randomizing the pulse shape. The performance gain is illustrated in electrical domain first, and then by considering the over fiber system with and without in-line amplification. The main goal of chapter 6 is to present an experimental demonstration for some of the investigated schemes. Differential Chaos Shift Keying has been adopted with the over fiber system. The potential of chirping technique has been experimentally validated and interesting results have been achieved. In the final chapter, we conclude our work and highlight on the main outcomes of this thesis, besides, several investigations are suggested for optical ultra wideband future research.

Chapter 1

An Introduction to Impulse Radio Ultra WideBand

1.1 Modern Communication Technologies

Communication systems have been a key branch in humans daily life, thanks to the globally distributed networks, information and ideas can be easily shared from any two corners in our planet. A rapid exchange of speech, image, music, or computer data, is provided by the emerging broadcasting technologies. The raising demand of high quality data transfer necessitates a periodic advancement in the communication strategies and topologies. The existing wireless systems nowadays are mainly the metropolitan area networks, personal area networks, and local area networks [1,2]. Figure 1.1 illustrates the growing mobile data traffic from 2016 to 2021 carried out from Cisco recent studies [3], it is expected that the data usage amount will reach 49 exabytes per month by 2021. Figure 1.2 shows the number of devices or connections versus years for 2G, 3G, 4G+ (corresponding to 4G combined with 5G small share connections), and Low Power Wide Area (LPWA) technologies. A higher generation network connectivity has to be developed each time period in order to fit the public demand. In 2021, it is predicted that 53% of the global communication devices will be integrable with 4G technology. 5G will emerge in 2020, where the expected number of connections is 2.3 million that will exhibit a sharp increase by 2021 [3]. A complementary approach to these technologies is Ultra WideBand

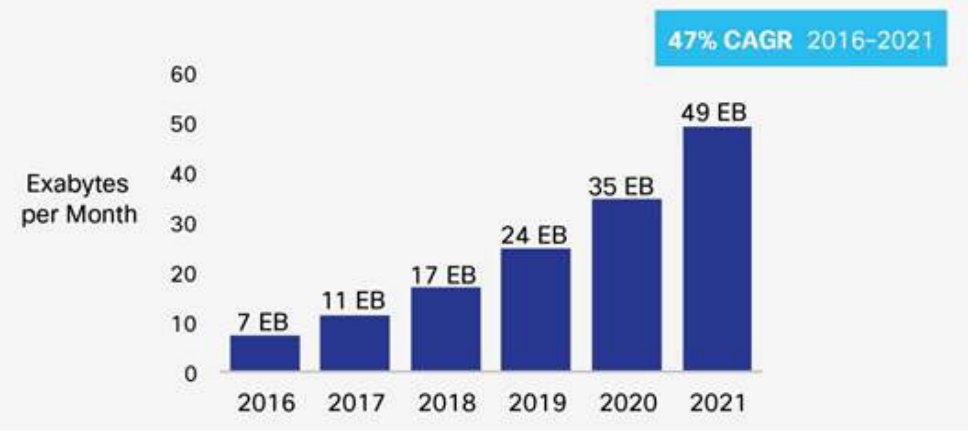

Figure 1.1: Cisco Forecasts 49 Exabytes per Month of Mobile Data Traffic by 2021 [3].

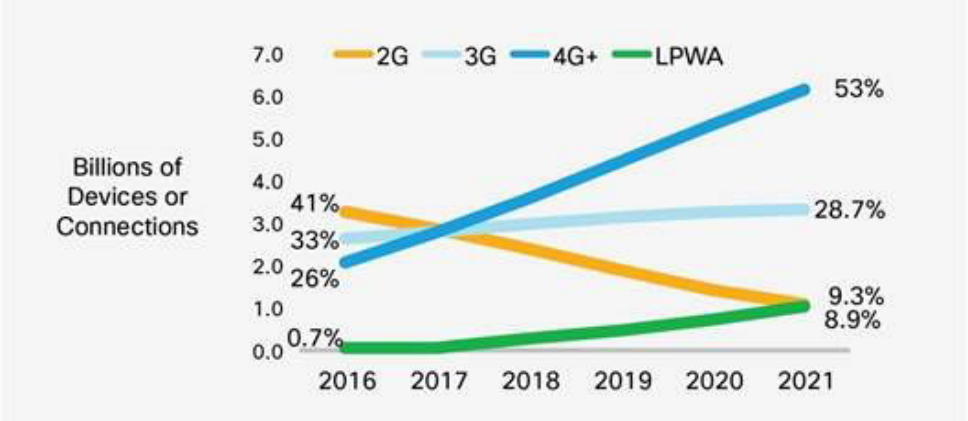

Figure 1.2: Global Mobile Devices and Connections by 2G, 3G, and 4G+, (percentages refer to device and connections share), and LPWA (Low Power Wide Area) [3].

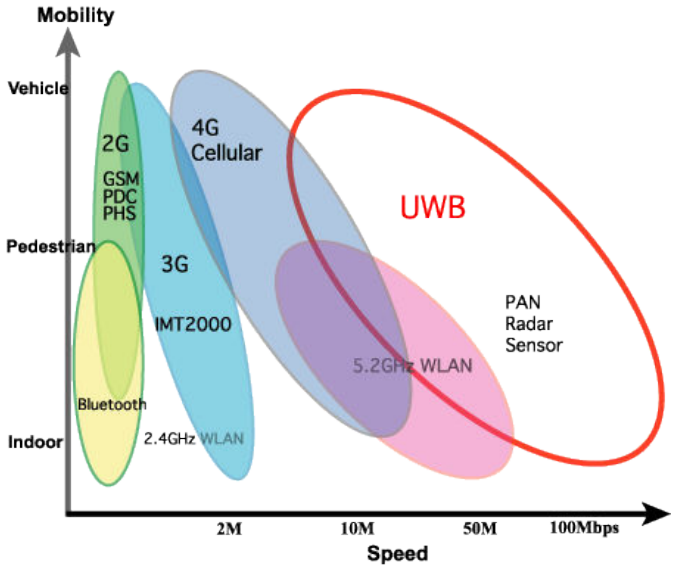

Figure 1.3: Mobility and speed of UWB in correspondence with other existing communication technologies [4].

(UWB), as illustrated in fig. 1.3 [4], which is suitable for high speed transmission scenarios within a short range coverage areas [5,6]. UWB is based on transmitting signals with an extremely large bandwidth and small radiated power [7,8]. Significant efforts have been applied by recent researchers to commercialize UWB and overcome its challenges [9–20]. In the next sections, we introduce UWB in terms of definition and regulations, with some focusing on the advantages, applications, and technologies.

1.2 Ultra WideBand Definition and Regulations

Based on the definition of the Federal Communication Commission (FCC) in United States [5,6,21], the term ultra wideband corresponds to any signal having a 10 dB bandwidth $B_{10} > 500$ MHz or a fractional bandwidth $B_f > 0.2$.

$$B_f = \frac{B_{10}}{f_c} \tag{1.1}$$

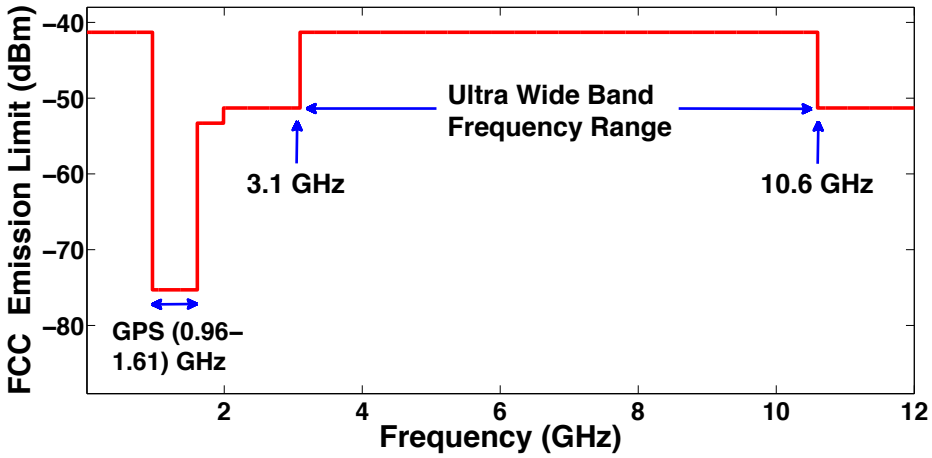

Figure 1.4: The free space emission limit regulated by the Federal Communication Commission, the Ultra WideBand frequency range goes from 3.1 GHz to 10.6 GHz.

with

$$f_c = \frac{f_H + f_L}{2} \tag{1.2}$$

where f_L and f_H correspond to the lower and upper limits of the 10 dB bandwidth respectively. In 2002, FCC allowed UWB devices to operate within a particular spectral mask in order to avoid dangerous interference with other narrow band communication systems [22]. According to this regulation the transmitted power spectral density of UWB has to stay below the limit of -41.3 dBm/MHz in the frequency range of [3.1,10.6] GHz. Figure 1.4 describes the standard mask in the United States of America, the emission limit corresponds to the noise level of electronic devices, so UWB signals act as a harmless noise with respect to other communication bodies. Figure 1.5 states the intended bands for UWB propagation in different regions [23], we can notice that the maximum band is licensed by USA regulations, this leads to a higher data rate of transmission and better signal-to-noise ratio. Table 1.1 summarizes the main characteristics and aspects of UWB in comparison with other communication technologies, the wideband property allows spread spectrum techniques to be applied, also different modulation options could be adopted [24].

1.3 UWB Advantages

Equation (1.3) expresses Shannon's capacity of transmission $C_{bits/second}$ versus the bandwidth B and SNR in Additive White Gaussian Noise channels. It could be pointed out that, due to the large bandwidth (7.5 GHz), UWB signals can reach a very high transmission rate at low probability of error. Ultra short time pulses also have a great potential in localization and tracking, high accuracy can be achieved while estimating the distance between transmitter and receiver, thanks to the low time scaling. Moreover, the wideband characteristic provides the capability to resolve multipath components, and reconstruct the transmitted signal via coherent rake receiver. Hence, UWB has a kind of robustness against fading effects in dispersive channels. In addition, as the UWB has a very low emission power and high bandwidth, it is a noise like signal, that adds more difficulty for

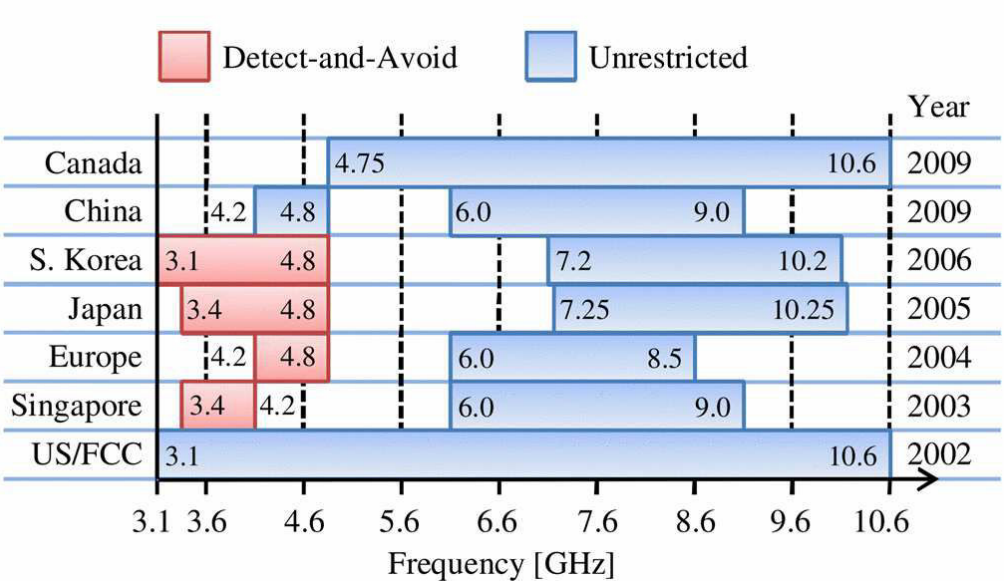

Figure 1.5: UWB intended bands specified in different regions [23].

Standard	Bluetooth	UWB	ZigBee	Wi-Fi
IEEE specification	802.15.1	802.15.3a	802.15.4	802.11a/b/g
Frequency band	2.4 GHz	3.1-10.6 GHz	868/915 MHz 2.4 GHz	2.4 GHz; 5 GHz
Nominal range	10 m	10 m	10 - 100 m	100 m
Nominal TX power	0 - 10 dBm	-41.3 dBm/MHz	(-25) - 0 dBm	15 - 20 dBm
Number of RF channels	79	(1-15)	1/10; 16	14 (2.4 GHz)
Channel bandwidth	1 MHz	500 MHz - 7.5 GHz	0.3/0.6 MHz ; 2 MHz	22 MHz
Modulation type	GFSK	BPSK, PAM, PSM, PPM, OOK	BPSK (+ ASK), O-QPSK	BPSK, QPSK , COFDM, CCK, M-QAM
Spreading	FHSS	DS-UWB, MB-OFDM	DSSS	DSSS, CCK, OFDM

Table 1.1: A summary of the main characteristics of UWB in comparison with other wireless technologies [24].

irregular bodies to steal information from the communication system [5–7, 21].

$$C_{bits/second} = B \times \log_2 \left(1 + SNR\right) \tag{1.3}$$

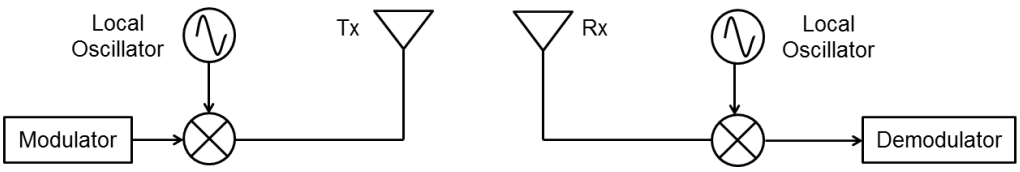

Figure 1.6: Schematic diagram for the carrier-based UWB transceiver.

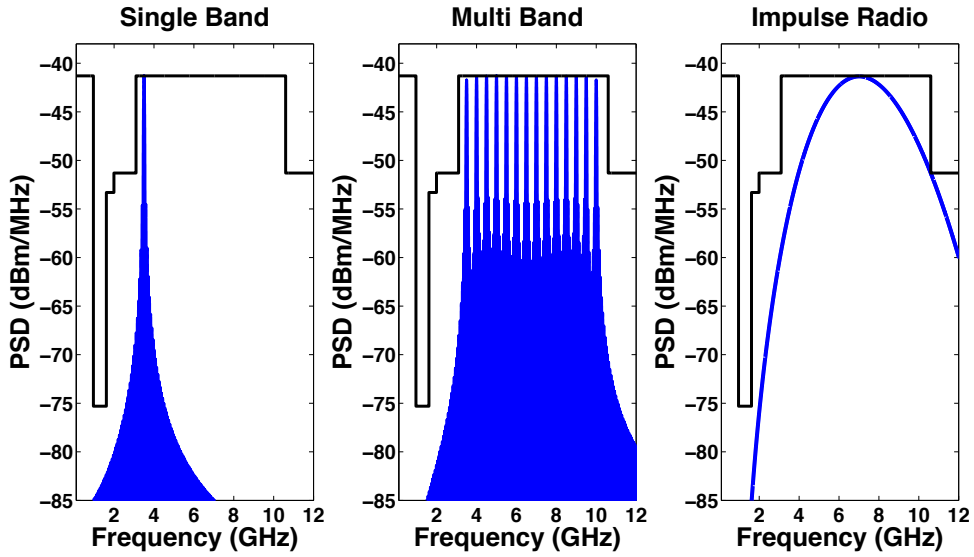

Figure 1.7: The spectrum of single carrier (left), multi-carrier (middle), and impulse radio (right) UWB respectively.

1.4 UWB Applications

Thanks to its attractive features, UWB is a good candidate for various applications in civilian, military, and commercial fields. Examples include local and wide area networks, sensor networks, emergency communications, personal area networks, and multimedia-rich communications. Besides to the radar, as a centimeter resolution can be obtained due to the fine positioning characteristics. In addition to other applications like remote sensing, home automation, wireless streaming video distribution, medical imaging, home security, automotive industry, tracking, and electronic applications [5–7, 21, 25].

1.5 UWB Technologies

The UWB generated signals can be classified into two main types, the carrier-based scheme, and impulse radio technique [5]:

Carrier-Based Schemes

This approach consists in multiplying the generated signal by a sinusoid for shifting the spectrum towards the frequency band of interest, as depicted in fig. 1.6. It could be a single carrier or multi-carrier technique, as shown in fig. 1.7. The advantage with this type of transmission is the flexibility in controlling the central frequency with respect to

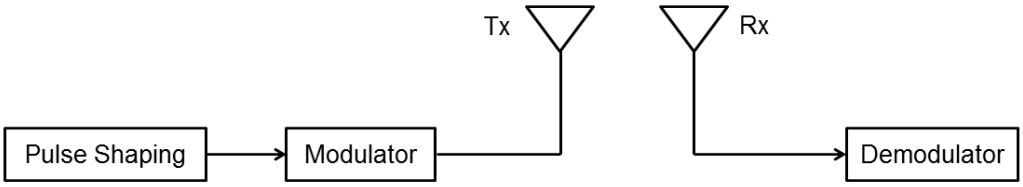

Figure 1.8: Schematic diagram for the Impulse Radio UWB transceiver.

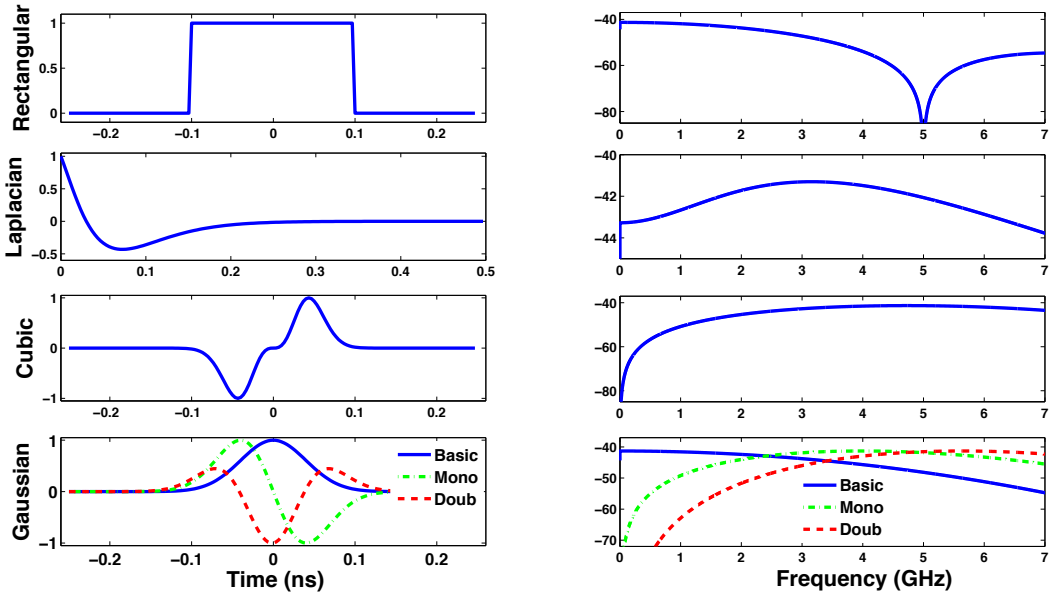

Figure 1.9: Normalized time waveforms of Rectangular, Laplacian, Cubic, and Gaussian pulses (left), besides to their corresponding power spectral densities (dBm/MHz) (right). *Basic* denotes the fundamental Gaussian, *Mono* corresponds to the first order derivative, and *Doub* presents the second order derivative.

FCC mask, but at the price of a higher order of complexity as local oscillators have to be adopted [26, 27].

Impulse Radio Technique

This technique relies on pulses with ultra short duration and low duty cycle which directly occupies the high frequency band. As described in fig. 1.8, the modulated signal is transmitted without being multiplied by a carrier, this baseband approach is cost effective and simple. Figure 1.7 (right) plots the spectrum of an impulse radio waveform, the peak frequency is close to the center of FCC mask, without shifting the spectrum by the use of a local oscillator [28–31]. The main contributions of our investigations will be focused on impulse radio.

1.6 IR-UWB Pulse Waveforms and Modulation Types

Several pulse waveforms can be adopted in impulse radio, mainly the Rectangular, Sinc, Hermite, Laplacian, Cubic, and Gaussian pulses [5, 32–37]. Figure 1.9 describes the time

waveforms (left) besides to corresponding spectra (right) of the Rectangular, Laplacian, Cubic, fundamental Gaussian, first Gaussian derivative, and second Gaussian derivative. In fact, Gaussian pulses will be the candidates in our work due to their good compliance with FCC mask [37], besides to the possibility to be generated via basic electronic circuits [33]. Equation (1.4) expresses the formula of the fundamental Gaussian, where σ is the pulse shaping factor.

$$g(t) = exp\Big(-\frac{t^2}{2\sigma^2}\Big) \tag{1.4}$$

The pulses spectral characteristic with respect to FCC mask will be evaluated using the criterion of power efficiency:

$$\eta = \frac{\int_{3.1\,GHz}^{10.6\,GHz} S_p(f)\,df}{\int_{3.1\,GHz}^{10.6\,GHz} S_{FCC}\,df} \times 100\% \tag{1.5}$$

where $S_p(f)$ denotes the power spectral density for a pulse $p(t)$ [38].

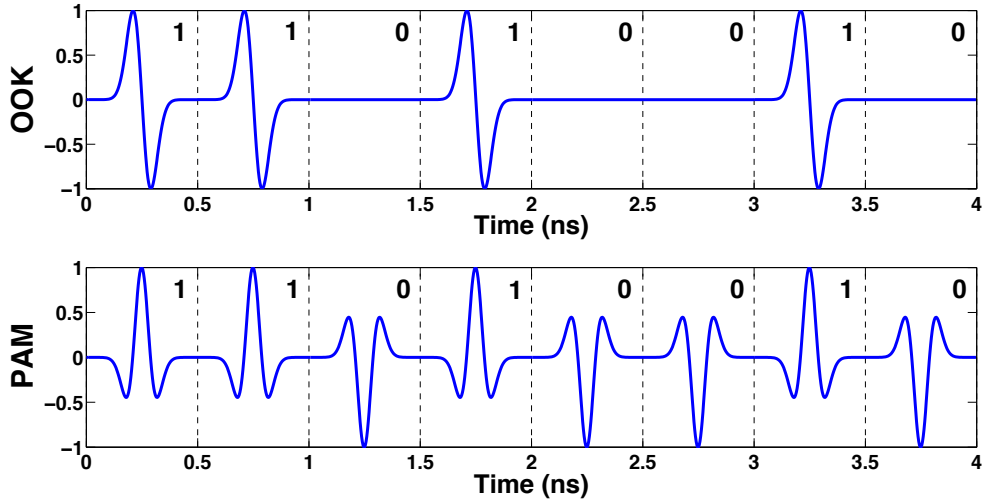

Figure 1.10: Time waveforms of OOK (above) and PAM (below) modulation formats for a sequence of 8 bits, '1 1 0 1 0 0 1 0 '.

Regarding the modulation schemes applied with IR-UWB, numerous modulation options exist, mainly Pulse Amplitude Modulation (PAM), Pulse Position Modulation (PPM), On Off Keying (OOK), Pulse Shape Modulation (PSM), Binary Phase Shift Keying (BPSK), in addition to Transmitted Reference (TR) schemes [5, 7, 39–44]. Equation (1.6) defines a PAM modulated signal $\big(s_{PAM}(t)\big)$, where a_k is the amplitude associated with the k^{th} symbol having a time duration T_s. OOK and BPSK belong to the PAM family, where $a_k \in \{0, 1\}$ or $a_k \in \{-1, 1\}$ respectively. Equations (1.7) and (1.8) describe the expressions of PPM and PSM modulations respectively, where $a_k \in \{0, 1\}$ and δ is the modulation index. Figures 1.10 to 1.12 show the time waveforms of different modulation options corresponding to 8 bits data sequence. The formula of the transmitted reference signal is expressed in eq. (1.9), where the time waveform is described in fig. 1.13. As noticed, for each symbol a reference pulse is transmitted before the data one, enabling a channel state information [45]. The modulated pulse is delayed by T_d, where $T_d \geq T_p$ (T_p is the pulse duration). Detecting the transmitted symbols is based on cross correlation performed

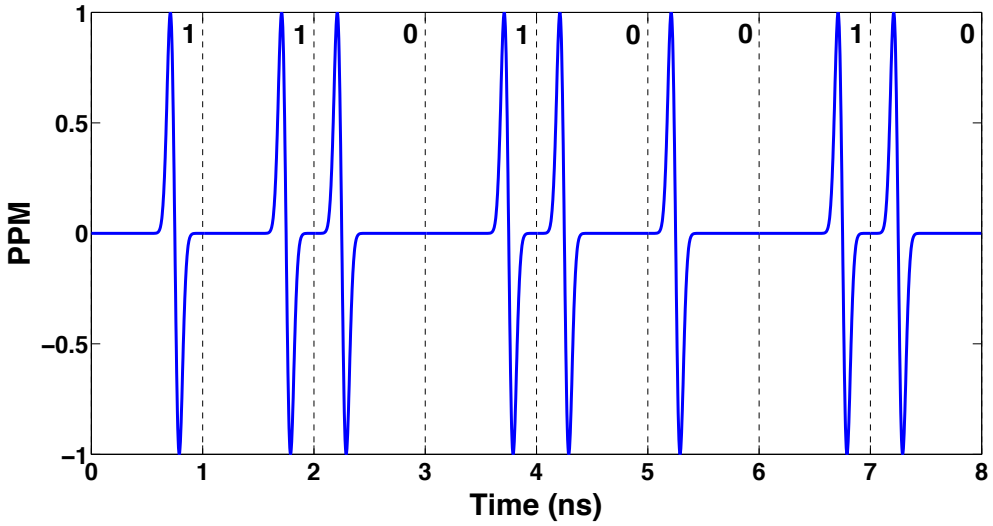

Figure 1.11: Time waveforms PPM modulation format for a sequence of 8 bits, '1 1 0 1 0 0 1 0 '.

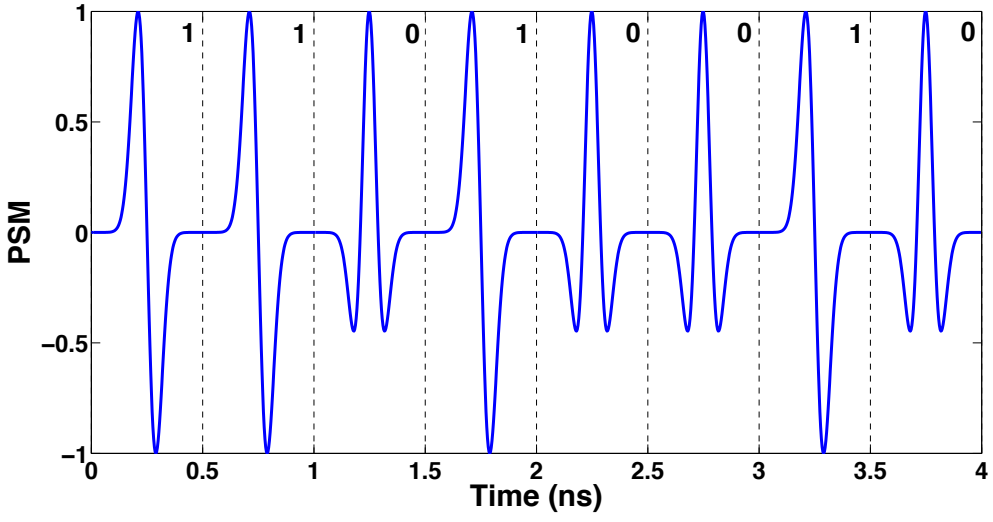

Figure 1.12: Time waveforms of PSM modulation format for a sequence of 8 bits, '1 1 0 1 0 0 1 0 '.

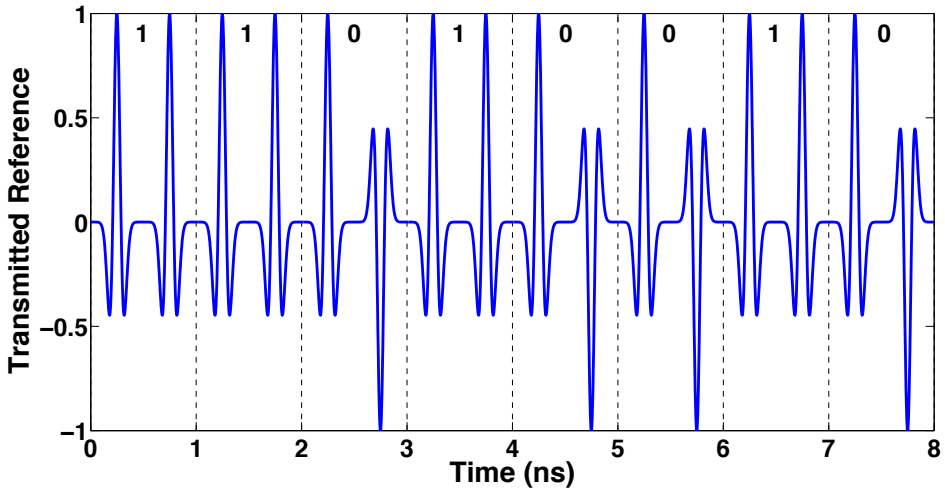

Figure 1.13: Time waveform of Transmitted Reference modulation format for a sequence of 8 bits, '1 1 0 1 0 0 1 0 '.

between the two received pulses in each frame.

$$s_{PAM}(t) = \sum_k a_k p(t - kT_s) \tag{1.6}$$

$$s_{PPM}(t) = \sum_k p(t - kT_s - a_k\delta) \tag{1.7}$$

$$s_{PSM}(t) = \sum_k p_k(t - kT_s) \tag{1.8}$$

$$s_{TR}(t) = \sum_k p(t - kT_s) + a_k p(t - kT_s - T_d) \tag{1.9}$$

Non-coherent energy detection approaches mainly deal with OOK and orthogonal PPM, which have been adopted in this thesis due to their simplicity; in addition to the Differential Chaos Shift Keying (DCSK) schemes which belong to TR family [46].

Transmitting impulse radio pulse train results in discrete spectral spikes due to time periodicity. These comb lines may violate FCC mask, hence, applying spectrum smoothing techniques is important so as to attenuate the intensity of the discrete lines. Direct Sequence (DS) and Time Hopping (TH) smoothing schemes are mainly adopted in the literature, which randomize the amplitude or time position of transmitted waveforms respectively [47–50]. As will be discussed in the sequel, the time dynamics of any modulation pattern determines the corresponding spectral behavior. Our key objective is to get an efficient spectrum under FCC mask, the transmission efficiency of a modulated UWB signal will be evaluated based on the criterion:

$$\eta_M = \frac{P_{\mathcal{F}}}{max(\overline{P_{\mathcal{F}}})} \tag{1.10}$$

where $P_{\mathcal{F}}$ stands for the power collected over a frequency band of interest $\mathcal{F}$ (typically the [3.1-10.6] GHz band) for the electrical signal at antenna input, and $max(\overline{P_{\mathcal{F}}})$ denoting the total power evaluated over the same band for an OOK or PPM modulated signal based

on the *sinc* pulse, which is optimal in the sense that it corresponds to a 100% spectrum use (full coverage of the spectral mask). η_M is different than η, as the latter represents the efficiency for a single waveform and not for a stream of modulated pulses.

1.7 UWB Challenges

Going towards high frequency is challenging from the practical side [51–55], as it is not easy to fabricate electronic circuits and equipments capable to operate at high frequency band [56–59], also designing antennas becomes more sophisticated and expensive [60–62]. Moreover, the emission constraints associated to UWB free-space propagation [22] add a trade off between the data rate and transmission distance. So, highly efficient UWB are required in order to get a reach extension with an acceptable level of bit error rate. In this thesis, we propose several methodologies for enhancing the UWB transmission system performance, main approaches are based on controlling the generated pulse dynamics and modulation characteristics as will be shown in the sequel.

1.8 UWB Wireless Channel Model

Channel modeling activities started after the approval of the Federal Communication Commission for UWB wireless propagation [63, 64]. The IEEE 802.15.4a channel model covers indoor residential, indoor office, industrial, besides to open outdoor environments, considering both line of sight and non line of sight scenarios [65]. Attenuation and delay dispersion are the two main aspects that have to be taken into account in any model [66]. There are some classical parameters used to evaluate a channel, like the average path loss, power delay profile, fading statistics, root mean square delay spread, number of multi-path components occupying a specific percentage of the received energy [65]. The target of channel modeling approaches is to be as realistic as possible, more accurate model requires a greater number of observations and measurements, so as to get a broad data base of numerical values corresponding to impulse response realizations [65].

1.9 Impulse Radio over fiber

The radio over fiber concept is a pertinent solution for distributing data signals over land networks integrated with the wireless channel [67]. As stated in fig. 1.14, the central unit of a base station provides several remote antennas via embedded fiber links, so as to cover all branches in the public area [67–70]. With UWB, due to power limitation against free-space operation, only a few meters could be covered in wireless channels. UWB over fiber has received a great deal of attention from numerous research centers, thanks to the attractive features of the optical fiber, high transmission speed could be achieved with a very good bit error rate performance [70–72]. The main interest in this thesis is the impulse radio concept, with stream of pulses being distributed over the fiber prior to wireless propagation [73]; these signals can be electrically or optically generated [74] as will be shown in the next chapter, which summarizes different solutions for impulse radio over fiber generation and transmission techniques.

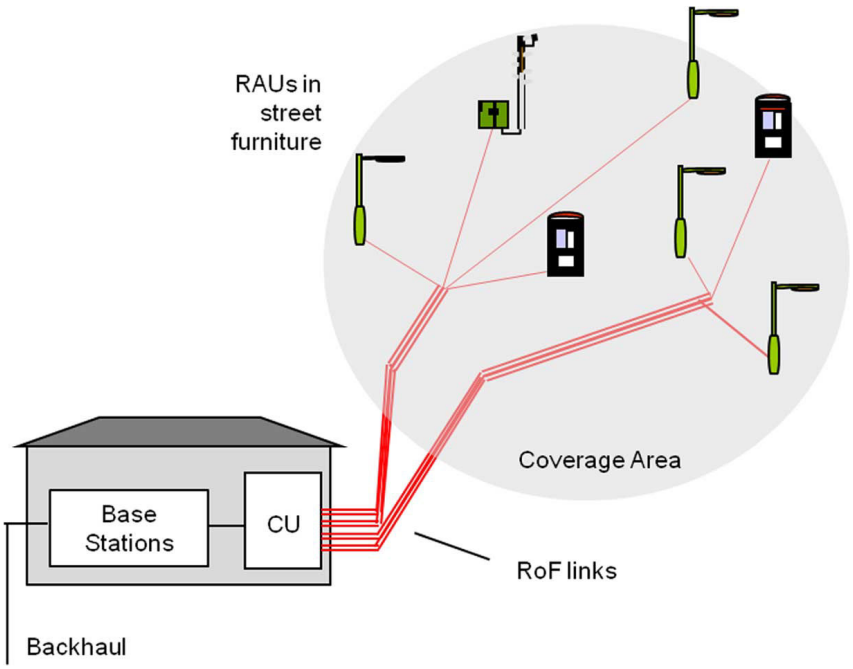

Figure 1.14: A schematic diagram for a radio over fiber access network [67].

1.10 Contributions of this Dissertation

In this thesis, six main contributions are investigated:

(1) Analog pre-distortion techniques have been applied to face the nonlinear effects inherent to optical amplification;

(2) A novel power efficient waveform has been designed based on a linear combination of fundamental Gaussian pulses;

(3) Phaser-based processing schemes are proposed for jointly reducing the optical system noise and nonlinearities;

(4) Pulse shape randomization is investigated to improve the power efficiency of modulated impulse radio signals;

(5) Differential chaos shift keying scheme is applied for the first time with the over fiber transmission system;

(6) An experimental demonstration for ultra wideband over fiber is performed;

Bibliography

[1] M. Jacobsson, I. Niemegeers, and S. H. d. Groot, Pesonal Networks: Wireless Networking for Personal Devices. Jhon Wiley & Sons, Ltd, 2010.

[2] A. Ng'oma, H. Yang, and J. George, "Integrated fiber-wireless networks: What, Why and How," in AFRICON, pp. 1–6, Sept. 2011.

[3] Cisco Visual Networking Index: Global Mobile Data Traffic Forecast Update, 2016–2021, White Paper, Feb 2017.

[4] Report of IECP Forum of Glocom by Prof. Ryuji Kohno, Yokohama National Univ., Ultra Wide Band Technology, 2003.

[5] Di Benedetto, M. G. (Ed.). (2006). UWB communication systems: a comprehensive overview (Vol. 5). Hindawi Publishing Corporation.

[6] I. Oppermann, M. Hämäläinen, J. Iinatti, UWB: Theory and Applications, John Wiley & Sons, 2005.

[7] M. Ghavami, L. Michael, R. Kohno, Ultra Wideband Signals and Systems in Communication Engineering, John Wiley & Sons, 2007.

[8] G.R. Aiello, G.D. Rogerson, Ultra-wideband wireless systems, IEEE Microwave Mag. 4 (2) (2003) 36–47.

[9] Nguyen, C., & Miao, M. (2017). UWB Impulse Transmitter Design. In Design of CMOS RFIC Ultra-Wideband Impulse Transmitters and Receivers (pp. 25-55). Springer International Publishing.

[10] Goyal, V., & Dhaliwal, B. S. (2017). Performance Improvement of Ultra Wideband Multiple Access Modulation System using a new Optimal Pulse Shape. Advanced Electromagnetics, 6(1), 20-28.

[11] Harrison, S. T., & Driessen, P. F. (2017). Robust TC-OLA Reception With Frequency Domain Equalization for Ultrawideband (UWB) Applications. IEEE Communications Letters, 21(3), 656-659.

[12] Niemela, V., Haapola, J., Hamalainen, M., & Iinatti, J. (2017). An Ultra Wideband Survey: Global Regulations and Impulse Radio Research Based on Standards. IEEE Communications Surveys & Tutorials.

[13] Vendik, I., Rusakov, A., Kanjanasit, K., Hong, J., & Filonov, D. (2017). Ultra-Wideband (UWB) Planar Antenna with Single-, Dual-, and Triple-Band Notched Characteristic Based on Electric Ring Resonator. IEEE Antennas and Wireless Propagation Letters.

[14] Lu, J., Wang, J., & Gu, H. (2016). Design of compact balanced ultra-wideband bandpass filter with half mode dumbbell DGS. Electronics Letters, 52(9), 731-732.

[15] Chen, D., Wang, R., Xiang, P., Pu, T., Fang, T., Li, Y., ... & Huang, J. (2016). Ultra-wideband signal generator based on cross gain modulation effect in a distributed feedback laser. Optics & Laser Technology, 84, 64-71.

[16] Xiong, H. (2017). An Efficient Narrowband Interference Suppression Approach in Ultra-Wideband Receiver. IEEE Sensors Journal, 17(9), 2741-2748.

[17] Hussain, M. G., Shishter, Y. M., & Al-Gharabally, M. H. (2016, May). Ultraw-ideband impulse communications using M-ary digital modulation schemes. In Microwave, Radar and Wireless Communications (MIKON), 2016 21st International Conference on (pp. 1-4). IEEE.

[18] Darvazehban, A., Manoochehri, O., Salari, M. A., Dehkhoda, P., & Tavakoli, A. (2017). Ultra-Wideband Scanning Antenna Array With Rotman Lens. IEEE Transactions on Microwave Theory and Techniques.

[19] Choi, J. W., Nam, S. S., & Cho, S. H. (2016). Multi-Human Detection Algorithm based on an Impulse Radio Ultra-Wideband Radar System. IEEE Access, 4, 10300-10309.

[20] Aggrawal, H., Puhl, R., Studer, C., & Babakhani, A. (2017). Ultra-Wideband Joint Spatial Coding for Secure Communication and High-Resolution Imaging. IEEE Transactions on Microwave Theory and Techniques.

[21] Porcino, D., & Hirt, W. (2003). Ultra-wideband radio technology: potential and challenges ahead. IEEE communications magazine, 41(7), 66-74.

[22] FCC Report and Order, In the Matter of Revision of Part 15 of the Commission's Rules Regarding Ultra-Wideband Transmission Systems, FCC 02–48 (2002).

[23] Fernandes, J. R., & Wentzloff, D. (2010, May). Recent advances in IR-UWB transceivers: An overview. In Circuits and Systems (ISCAS), Proceedings of 2010 IEEE International Symposium on (pp. 3284-3287). IEEE.

[24] Lee, J. S., Su, Y. W., & Shen, C. C. (2007, November). A comparative study of wireless protocols: Bluetooth, UWB, ZigBee, and Wi-Fi. In Industrial Electronics Society, 2007. IECON 2007. 33rd Annual Conference of the IEEE (pp. 46-51). Ieee.

[25] Fontana, R. J. (2004). Recent system applications of short-pulse ultra-wideband (UWB) technology. IEEE Transactions on microwave theory and techniques, 52(9), 2087-2104.

[26] Yang, L., & Giannakis, G. B. (2003). Digital-carrier multi-band user codes for baseband UWB multiple access. Journal of Communications and Networks, 5(4), 374-385.

[27] Batra, A., Balakrishnan, J., Aiello, G. R., Foerster, J. R., & Dabak, A. (2004). Design of a multiband OFDM system for realistic UWB channel environments. IEEE Transactions on Microwave theory and techniques, 52(9), 2123-2138.

[28] M.Z. Win, R.A. Scholtz, Impulse radio: How it works, IEEE Commun.Lett.2(2) (1998)36–38.

[29] J.R.Fernandes, D.Wentzloff, Recent advances in IR-UWB transceivers: an overview, in: Proceedings of 2010 IEEE International Symposium In Circuits and Systems(ISCAS),2010,pp.3284–3287.

[30] Win, M. Z., & Scholtz, R. A. (2000). Ultra-wide bandwidth time-hopping spread-spectrum impulse radio for wireless multiple-access communications. IEEE Transactions on communications, 48(4), 679-689.

[31] Parr, B., Cho, B., Wallace, K., & Ding, Z. (2003). A novel ultra-wideband pulse design algorithm. IEEE Communications Letters, 7(5), 219-221.

[32] Dilmaghani, R. S., Ghavami, M., Allen, B., & Aghvami, H. (2003, September). Novel UWB pulse shaping using prolate spheroidal wave functions. In Personal, Indoor and Mobile Radio Communications, 2003. PIMRC 2003. 14th IEEE Proceedings on (Vol. 1, pp. 602-606). IEEE.

[33] Kim, H., & Joo, Y. (2005, June). Fifth-derivative Gaussian pulse generator for UWB system. In Radio Frequency integrated Circuits (RFIC) Symposium, 2005. Digest of Papers. 2005 IEEE (pp. 671-674). IEEE.

[34] Hu, B., & Beaulieu, N. C. (2005). Pulse shapes for ultrawideband communication systems. IEEE Transactions on wireless communications, 4(4), 1789-1797.

[35] Chen, X., & Kiaei, S. (2002). Monocycle shapes for ultra wideband system. In Circuits and Systems, 2002. ISCAS 2002. IEEE International Symposium on (Vol. 1, pp. I-I). IEEE.

[36] Kim, Y., Jang, B., Shin, C., & Womack, B. F. (2005). Orthonormal pulses for high data rate communications in indoor UWB systems. IEEE Communications Letters, 9(5), 405-407.

[37] Sheng, H., Orlik, P., Haimovich, A. M., Cimini, L. J., & Zhang, J. (2003, May). On the spectral and power requirements for ultra-wideband transmission. In Communications, 2003. ICC'03. IEEE International Conference on (Vol. 1, pp. 738-742). IEEE.

[38] S.T. Abraha, C. Okonkwo, P. A. Gamage, E. Tangdiongga, and T. Koonen, "Routing of power efficient IR-UWB wireless and wired services for in-building network applications," *J. Lightw. Technol.*, 30(11), pp. 1651-1663, 2012.

[39] Choi, J. D., & Stark, W. E. (2002). Performance of ultra-wideband communications with suboptimal receivers in multipath channels. IEEE Journal on selected areas in communications, 20(9), 1754-1766.

[40] Siwiak, K. (2004). Ultra Wideband Radio. John Wiley & Sons, Inc..

[41] Hu, B., & Beaulieu, N. C. (2004). Accurate evaluation of multiple-access performance in TH-PPM and TH-BPSK UWB systems. IEEE Transactions on communications, 52(10), 1758-1766.

[42] Ghavami, M., Michael, L. B., Haruyama, S., & Kohno, R. (2002). A novel UWB pulse shape modulation system. Wireless Personal Communications, 23(1), 105-120.

[43] Usuda, K., Zhang, H., & Nakagawa, M. (2004, November). M-ary pulse shape modulation for PSWF-based UWB systems in multipath fading environment. In Global Telecommunications Conference, 2004. GLOBECOM'04. IEEE (Vol. 6, pp. 3498-3504). IEEE.

[44] Liu, H. (2003). Error performance of a pulse amplitude and position modulated ultra-wideband system over lognormal fading channels. IEEE Communications Letters, 7(11), 531-533.

[45] Quek, T. Q., & Win, M. Z. (2005). Analysis of UWB transmitted-reference communication systems in dense multipath channels. IEEE Journal on Selected Areas in Communications, 23(9), 1863-1874.

[46] Fang, Y., Han, G., Chen, P., Lau, F. C., Chen, G., & Wang, L. (2016). A survey on DCSK-based communication systems and their application to UWB scenarios. IEEE Communications Surveys & Tutorials, 18(3), 1804-1837.

[47] G. M. Maggio, N. Rulkov, and L. Reggiani, "Pseudo-chaotic time hopping for UWB impulse radio," *IEEE Trans. Circ. and Syst. I*, 48(12), pp. 1424-1435, 2001.

[48] H. Zhang and T. A. Gulliver, "Biorthogonal pulse position modulation for time-hopping multiple access UWB communications," *IEEE Trans. Wireless Commun.*, 4(3), pp. 1154-1162, 2005.

[49] J. Romme and L. Piazzo, "On the power spectral density of time-hopping impulse radio," *Ultra Wideband Systems and Technologies-IEEE*, pp. 241-244, 2002.

[50] A. Pearce, H. Nie, and Z. Chen, "Spectral spike reduction for ultra-wideband impulse radio system," *Microwave Symposium Digest, IEEE MTT-S International*, pp. 1-3, 2012.

[51] Lampe, L., & Witrisal, K. (2010, May). Challenges and recent advances in IR-UWB system design. In Circuits and Systems (ISCAS), Proceedings of 2010 IEEE International Symposium on (pp. 3288-3291). IEEE.

[52] Scholtz, R. A., Weaver, R., Homier, E., Lee, J. A. L. J., Hilmes, P. A. H. P., Taha, A., & Wilson, R. A. W. R. (2000). UWB radio deployment challenges. In Personal, Indoor and Mobile Radio Communications, 2000. PIMRC 2000. The 11th IEEE International Symposium on (Vol. 1, pp. 620-625). IEEE.

[53] Roy, S., Foerster, J. R., Somayazulu, V. S., & Leeper, D. G. (2004). Ultrawideband radio design: The promise of high-speed, short-range wireless connectivity. Proceedings of the IEEE, 92(2), 295-311.

[54] Cavallari, R., Martelli, F., Rosini, R., Buratti, C., & Verdone, R. (2014). A survey on wireless body area networks: Technologies and design challenges. IEEE Communications Surveys & Tutorials, 16(3), 1635-1657.

[55] Patel, M., & Wang, J. (2010). Applications, challenges, and prospective in emerging body area networking technologies. IEEE Wireless communications, 17(1).

[56] Aiello, G. R. (2003, June). Challenges for ultra-wideband (UWB) CMOS integration. In Radio Frequency Integrated Circuits (RFIC) Symposium, 2003 IEEE (pp. 497-500). IEEE.

[57] Diao, S., Zheng, Y., & Heng, C. H. (2009). A CMOS ultra low-power and highly efficient UWB-IR transmitter for WPAN applications. IEEE Transactions on Circuits and Systems II: Express Briefs, 56(3), 200-204.

[58] Gharpurey, R. (2005). A broadband low-noise front-end amplifier for ultra wideband in 0.13-/spl mu/m CMOS. IEEE Journal of Solid-State Circuits, 40(9), 1983-1986.

[59] Saari, V., Kaltiokallio, M., Lindfors, S., Ryynanen, J., & Halonen, K. A. (2009). A 240-MHz low-pass filter with variable gain in 65-nm CMOS for a UWB radio receiver. IEEE Transactions on Circuits and Systems I: Regular Papers, 56(7), 1488-1499.

[60] Chen, Z. N., Wu, X. H., Li, H. F., Yang, N., & Chia, M. Y. W. (2004). Considerations for source pulses and antennas in UWB radio systems. IEEE Transactions on Antennas and Propagation, 52(7), 1739-1748.

[61] Wang, S. B., Niknejad, A. M., & Brodersen, R. W. (2006). Circuit modeling methodology for UWB omnidirectional small antennas. IEEE Journal on Selected Areas in Communications, 24(4), 871-877.

[62] Lizzi, L., Viani, F., Azaro, R., & Massa, A. (2008). Design of a miniaturized planar antenna for FCC UWB communication systems. Microwave and Optical Technology Letters, 50(7), 1975-1978.

[63] Molisch, A. F., Foerster, J. R., & Pendergrass, M. (2003). Channel models for ultrawideband personal area networks. IEEE wireless communications, 10(6), 14-21.

[64] Molisch, A. F. (2005). Ultrawideband propagation channels-theory, measurement, and modeling. IEEE transactions on vehicular technology, 54(5), 1528-1545.

[65] Molisch, A. F., Balakrishnan, K., Chong, C. C., Emami, S., Fort, A., Karedal, J., ... & Siwiak, K. (2004). IEEE 802.15. 4a channel model-final report. IEEE P802, 15(04), 0662.

[66] Molisch, A. F., Cassioli, D., Chong, C. C., Emami, S., Fort, A., Kannan, B., ... & Win, M. Z. (2006). A comprehensive standardized model for ultrawideband propagation channels. IEEE Transactions on Antennas and Propagation, 54(11), 3151-3166.

[67] Wake, D., Nkansah, A., & Gomes, N. J. (2010). Radio over fiber link design for next generation wireless systems. Journal of Lightwave Technology, 28(16), 2456-2464.

[68] Cooper, A. J. (1990). 'Fibre/radio'for the provision of cordless/mobile telephony services in the access network. Electronics Letters, 26(24), 2054-2056.

[69] Wake, D., Webster, M., Wimpenny, G., Beacham, K., & Crawford, L. (2004, October). Radio over fiber for mobile communications. In Microwave Photonics, 2004. MWP'04. 2004 IEEE International Topical Meeting on (pp. 157-160). IEEE.

[70] Ramaswami, R., Sivarajan, K., & Sasaki, G. (2009). Optical networks: a practical perspective. Morgan Kaufmann.

[71] Pan, S., & Yao, J. (2010). UWB-over-fiber communications: modulation and transmission. Journal of Lightwave Technology, 28(16), 2445-2455.

[72] Pan, S., & Yao, J. (2010). Performance evaluation of UWB signal transmission over optical fiber. IEEE Journal on selected areas in communications, 28(6).

[73] Taki, H., Azou, S., Hamie, A., Al Housseini, A., Alaeddine, A., & Sharaiha, A. (2017). On phaser-based processing of impulse radio UWB over fiber systems employing SOA. Optical Fiber Technology, 36, 33-40.

[74] Yao, J., Zeng, F., & Wang, Q. (2007). Photonic generation of ultrawideband signals. Journal of Lightwave Technology, 25(11), 3219-3235.

Chapter 2

UWB over Fiber Communications: Literature Review and Introduction to our System

In the previous chapter, we have defined the UWB technology in terms of regulation and system approach; a new concept is introduced here, the radio over fiber transmission, which is an interesting topic that has been investigated in the past decade. In the next sections, we talk briefly about the integrated fiber-to-wireless communications, besides to the types of pulse generation associated with the optical transmission. Then, we present the radio over fiber system based on Mach-Zehnder Modulator (MZM) considered in this study, with some focusing on its function and how the operating conditions could be optimized. Finally, we introduce the usage of Semiconductor Optical Amplifier (SOA) as an in-line amplifier, with the view to achieve a reach extension at limited cost and complexity. A description about the SOA function and physical characteristics is presented in the last section.

2.1 Optical Fiber Communications: Advantages, Methodologies, and Challenges

As discussed in the previous chapter, the UWB wireless service area is limited to a few meters due to the power constraints of the regularity bodies. Therefore, establishing a wired-to-wireless integrated network is a key step to extend the coverage zone to a number of kilometers [1]. The electric cable is not a promising solution for UWB transmission, due

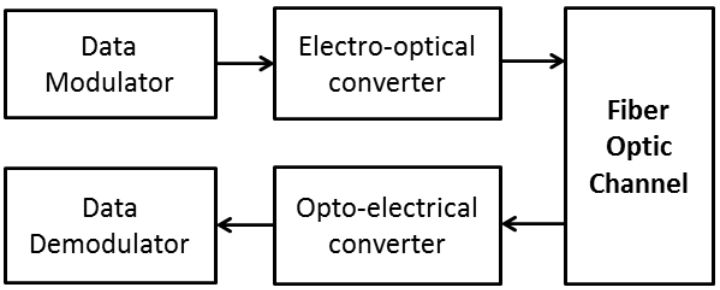

Figure 2.1: A simple schematic diagram for the optical communication system.

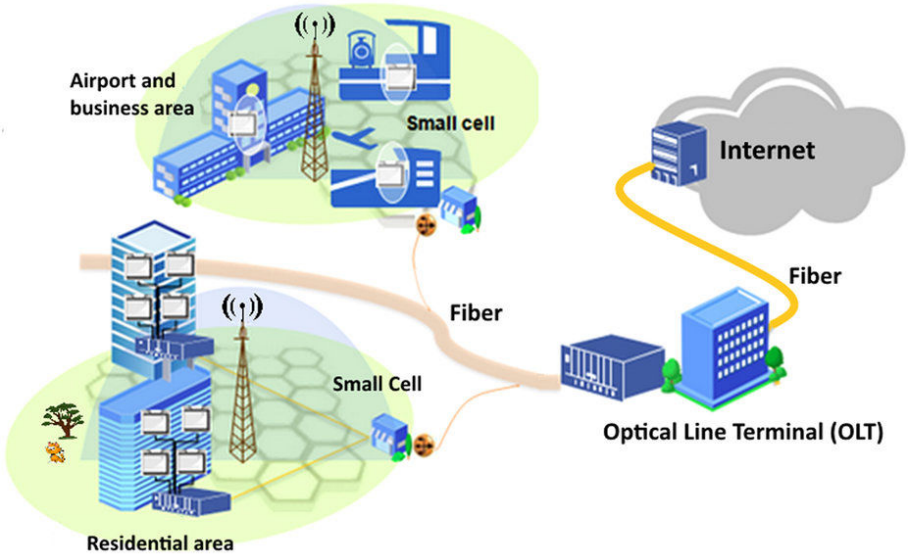

Figure 2.2: Different branches and public areas supported by the optical access networks [6].

to its band limitation and high attenuation associated with the copper characteristics [2]. The most pertinent approach is to exploit the beneficial properties of the optical link so as to get a better quality of service; over fiber transmission has drawn a great interest for researchers in the field of broadband communications [3–5]. The over fiber transmission system is described in fig. 2.1; the original data is carried by an optical beam, which propagates over the fiber to reach the receiver, where a direct detection is performed to extract the electrical waveforms before demodulation. As stated in fig. 2.2, data signals can be distributed by the optical access network over several links to supply different branches; airports, business areas, residential areas, and small cells, all can make use of the Internet service; where routing management is performed via an optical switching center [6].

The outstanding features of the fiber optic channel are the large bandwidth (which theoretically goes to 20 THz), the immunity to electromagnetic interference, low propagation loss, besides to the small physical dimensions and flexibility in twisting without causing a damage [3]. It is a dielectric waveguide capable to transport the light from one node to another, consisting of a central core through which the electromagnetic beam propagates, surrounded by a cladding layer and a thick external plastic jacket for protection [7]. The attenuation in the fiber is a function of the central wavelength [8] as shown in fig. 2.3; in our work we operate around 1.5 µm, which is associated with an attenuation of approximately 0.2 dB/km. Another challenge related to over fiber propagation is the chromatic dispersion, which introduces a frequency dependent phase shift, and consequently distorts the shape of the transmitted waveform [5]. Figure 2.4 shows the time waveforms and corresponding spectra of the Gaussian Monocycle observed at several SMF distances up to 40 km; we can see a decrease in the 10 dB bandwidth and central frequency as moving along the fiber, that is due to the time chirping caused by dispersion, which also depends on the optical power applied at fiber input [5]. Equation (2.1) describes the impact of single mode fiber on an optical baseband pulse $E(z,t)$ traveling along a distance z, where β_2 is the coefficient of group-velocity [9]. The solution of this partial differential equation, which is obtained by the Fourier transform, is expressed in eq. (2.2), where ω

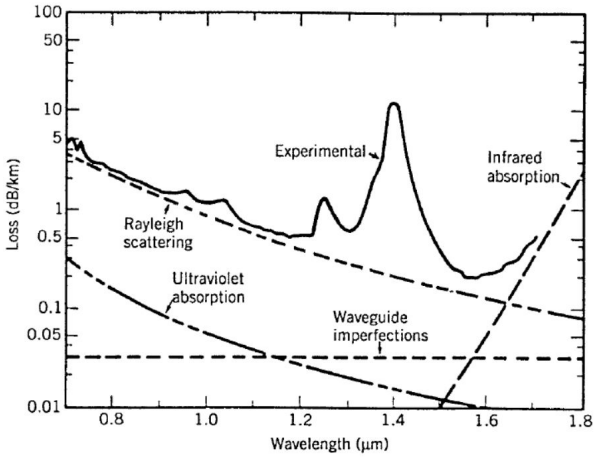

Figure 2.3: Attenuation in a single mode fiber versus wavelength [8].

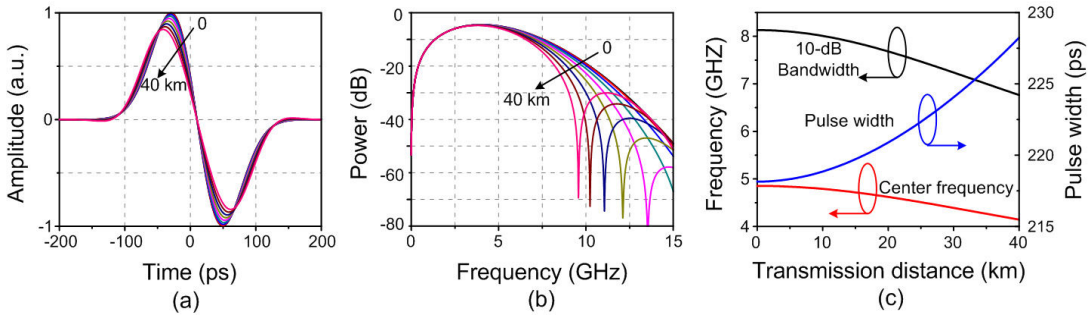

Figure 2.4: Time waveforms (a) and corresponding spectra (b) of Gaussian Monocycle at several distances of optical link, besides to the time and frequency properties versus distance (c) [5].

is the angular frequency. So due to chromatic dispersion, the fiber acts as an all-pass filter with a transfer function expressed in eq. (2.3), where D is the dispersion coefficient with a typical value of 17 ps/(km.nm), λ is the wavelength, and c is the free-space light propagation velocity.

$$j\frac{\partial E(z,t)}{\partial z} = \frac{\beta_2}{2}\frac{\partial^2 E(z,t)}{\partial t^2} \tag{2.1}$$

$$\hat{E}(z,\omega) = \hat{E}(0,\omega)\exp\left(\frac{j}{2}\beta_2\omega^2 z\right) \tag{2.2}$$

$$H(z,w) = \exp\left(\frac{j}{2}\beta_2 w^2 z\right) = \exp\left(\frac{-jD\lambda^2}{4\pi c}w^2 z\right) \tag{2.3}$$

Chromatic dispersion could be reduced by several digital or analog schemes; placing a compensating fiber can totally cancel the dispersion impact but at the expense of increased cost and complexity. At the transmitter side, pulse generation techniques have to be applied before entering the fiber, as will be discussed in the next section. Reconverting the optical field into an electrical voltage signal at receiver side is performed via square-law direct detection, several types of photo-detectors are commercially available, such as PN-junction diode (PIN) or Avalanche Photodiode (APD) [10–12]. Photo-detectors could be also integrated with a pre (optical) or post (electrical) amplifier so as to push up the signal power before demodulation [4, 13].

2.2 UWB Pulse Generation Techniques

In order to transmit a signal over fiber one of the two techniques has to be applied, either electrical-to-optical conversion for the designed waveforms or direct generation of the target UWB pulse in optical domain. Figure 2.5 shows the simple block diagram describing the two methods. Intensity modulation requires an electrical generation of UWB signals prior to optical carrier modulation; digital or analog techniques could be applied to design ultra short pulses which can modulate the optical field produced by a laser source [14–30]. On the optical domain side, various methods exist for generating microwave signals by optical means [31–47]; the attractive feature with such approaches is the absence of electrical part in the transmitter system architecture, besides to the high immunity against electromagnetic interference [32].

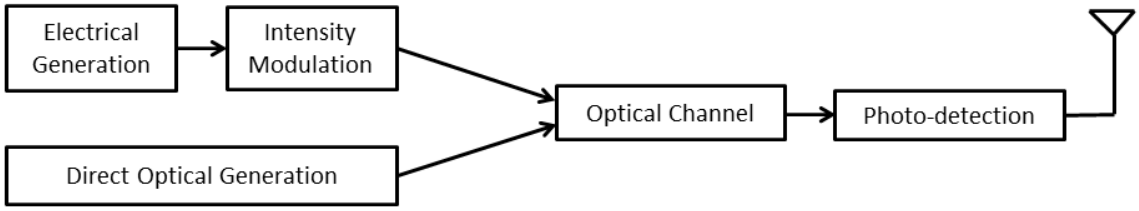

Figure 2.5: Two main types of pulse generation prior to over fiber propagation.

Tables 2.1 and 2.2 summarize the most popular scenarios investigated in literature, including electro-optic conversion and direct optical pulse generation. In [48, 49], UWB pulses are generated based on optical suppressed carrier modulation; while in [16, 25, 50–53] and [36, 39, 50, 54–56], several waveforms are designed by exploiting the physical characteristics of MZM or SOA respectively. In [5, 27, 38], Gaussian Monocycles and Doublets are produced via phase or polarization modulation followed by frequency discrimination. Getting benefit from the relaxation oscillations of a laser could be a good way to generate high order UWB signals, as demonstrated in [21, 57, 58]. Gain switching and external modulation was also investigated [26, 59], besides to optical pulse shaping and frequency-to-time mapping [60–62]. The reflective SOA has been an attractive tool for several designers, who succeeded in shaping different impulse radio waveforms by exploiting the dynamics of this optical component [63–66]. Many publications deal with external modulation [17, 20, 67–71], and in some studies it is proposed to generate UWB signals by taking advantage of a laser or fiber nonlinearity [72–74]. From a broad literature review, we propose a short summary of a few techniques with distinct key concepts in the following paragraphs. Our selection relies on various criteria including originality of the proposed results, effectiveness from a practical point of view and implementation using classical components.

In [62], the authors experimentally demonstrate a prototype for generating UWB signals by all optical means. As illustrated in fig. 2.6, the passive mode-locked fiber laser (MLFL) generates ultra short pulses which can be spectrally shaped via flattening filter; then the optical signal propagates in a dispersive medium, particularly it is a 5.46 km piece of single mode fiber, which can perform a frequency-to-time mapping. The lower and upper bands of the spectrum are cut by the two cascaded chirped gratings tunable filters.

Ref	Key Principle	Main Components	Output Waveform	Additional Information
[48, 49]	Optical suppressed carrier modulation	[48] RF source, external cavity laser, 2 MZMs, 3 FBGs, 2 EDFAs	No classical waveform	2.5 Gbps of Amplitude Shift Keying, 40 GHz carrier frequency, 44 km of optical link
		[49] RF source, 2 MZMs, OBPF		25 GHz millimeter wave, B10= 5.5 GHz ; 156.25 Mbps of RZ
[16, 25, 50, 51, 52, 53]	Exploiting MZM Characteristics	[16] MZM	Doublet	0.5 Gbps of Bi-phase Modulation. Pulse Width, 270 ps, B10= 8 GHz, fc=4 GHz
		[25] 2 MZMs, OVDL	Doublet, Monocycle, Triplet	Positive Monocycle, fc=4.3 GHz , B10= 7.1 GHz, Bf=1.65 Negative Monocycle, fc=4.3 GHz , B10= 8.1 GHz, Bf=1.88
		[50] Biasing voltage controller, MZM, SOA	Monocycle	Positive Monocycle, fc =5 GHz, B10=8.7 GHz Negative Monocycle, fc =4.3 GHz, B10=10.6 GHz
		[51] RF source, phase shifter, 3 MZMs	Gaussians, Trapezoidal, Triangular, Sawtooth, Sinc	Period of basic Gaus, 30 ps, Monocycle, 9.18 ps, Doublet, 8 ps ; Trapezoidal, 25 ps, Triangular, 33 ps, Sawtooth, 47 ps ; 1 Gbps
		[52] 2 MZMs, 2 OVDL	Doublet, Monocycle	Doublet, 290 ps, Bf= 1.323, Negative Monocycle, 230 ps, Bf= 1.255, Positive Monocycle, 240 ps, Bf= 1.26
		[53] 2 RF drivers, dual MZM	Monocycle	Transmitting 5 Gbps by a simultaneous modulation of: phase, amplitude, and position
[36, 39, 50, 54, 55, 56]	Exploiting SOA Characteristics	[36] Normal & tunable LDs, MZM, SOA, 2 OBPF	[36,39,50, 54,56] Monocycles & semi-monocycles	Positive Monocycle, Bf=1.25 ; Negative Monocycle, Bf=1.75
		[39] 2 tunable LDs, MZM, SOA, 2 FBGs		Monocycle period, 48 ps, fc=5 GHz, B10=9.4 GHz, Bf=1.88 ; Data rate 0.84 Gbps
		[50] Biasing voltage controller, MZM, SOA		Positive Monocycle, fc =5 GHz, B10=8.7 GHz Negative Monocycle, fc =4.3 GHz, B10=10.6 GHz
		[54] Normal & tunable LDs, MZM, SOA	[55] Monocycles, Doublets, & high order Gaussians	B10=8.75 GHz, fc=5 GHz, Bf=1.75, Data rate achieved: 1.25 Gbps
		[55] 4 LDs, 2 SOAs, EOM, 4 OVDLs, 2 de-multiplexers		A bit rate of 0.2 Gbps, with a duty cycle of 1/64
		[56] EOM, 2 SOAs, optical processing unit		Repetition rate: 12.5 GHz Duty cycle, 1/64 ; Maximum free spectral range: 16.7 GHz
[27, 38, 5]	Phase/Polarization modulation, frequency discrimination	[27] 2 Arbitrary wave plates, FBG, polarization modulator	Monocycles & Doublets	Monocycle, Bf=1.5, B10=9.3 GHz ; Doublet, Bf= 1.6, B10=10.5 GHz
		[38] Tunable LD, phase modulator, FBG		Monocycle, B10=7.94 GHz, fc=3.45 GHz; Doublet, B10=8.8 GHz, fc=7.14 GHz
		[5] polarization maintaining fiber, polarization modulator and controllers		Monocycle, B3=6.8 GHz, B10=12.4 GHz, (no Doublets)
[21, 57, 58]	Exploiting the relaxation oscillations of a laser	[21] Normal laser, MZM, DFB	No classical waveform	781.25 Mbps of BPSK ; 30 km of SMF
		[57] Direct modulation laser, optical filter, DFB, MZM	Pulses close to high order Gaussian	First method: fc=5.7 GHz, B10=4.5 GHz, Bf=0.78 ; Second method: fc=6.3 GHz, B10=3.8 GHz, Bf=0.61 ; Data rate: 781 Mbps
		[58] MZM, DFB, optical filters, directly modulated laser	High order Gaussian	fc=6.3 GHz, B10=3.8 GHz, Bf= 0.61 ; Data rate: 781.25 Mbps ; 30 km of SMF

Table 2.1: A summary for the most popular optical generation techniques described in literature.

[26, 59]	Gain switching & External Modulation	[26] Gain switched laser, external modulators, SMF, DFBs, delay line	Doublet	1.625 Gbps PPM, over several distances of optical link reaching 37 km
		[59] Gain switched laser, external modulator, SMF or FBG, filter, delay line	Novel pulse	15-25 km distances are considered in the SMF ; 3.5 m of free-space propagation
[60, 61, 62]	Optical pulse shaping & frequency-to-time mapping	[60] Mode locked fiber laser, FBG, optical modulator, flattening filter, SMF, delay line	Novel UWB pulse	Power efficiency, 63.6%, Gain > 11.6 & 5.9 dB over the monocycle & doublet ; Antenna & amplifier effects are considered
		[61] Mode locked fiber laser, tunable optical filter, SMF, FBG	Monocycle & Doublet	Monocycle period, 185 ps, fc=6 GHz, B10=9 GHz, Bf=1.5 Doublet period, 45 ps, B10=9.5 GHz
		[62] Mode locked fiber laser, delay line, flattening filter, SMF, 2 optical filters, FBG	Monocycle & Doublet, novel pulse	Monocycle σ=62.4 ps, violates FCC by 25 dB ; Doublet, σ=66.3 ps, violates FCC by 15 dB, Novel pulse, match FCC
[63, 64, 65, 66]	Exploiting the Reflective SOA characteristics	[63] Tunable laser, MZM, delay line, 2 reflective SOAs, polarization beam splitter	Monocycle, Doublet, Triplet, Quadruplet	Monocycle, period, 45 ps, fc= 3.3 GHz, B10= 5.8 GHz, Bf= 1.76 ; Doublet period, 60 ps, fc= 5.7 GHz, B10= 8.1 GHz, Bf=1.4
		[64] Tunable laser source, MZM, reflective SOA	Gaussian pulses	First pulse: 60 ps, fc=3.9GHz, B10=9.66 GHz, Bf=1.81 Second pulse: 62 ps, fc= 3.9 GHz, B10=8.48 GHz, Bf=1.79
		[65] Tunable laser, MZM, 2 reflective SOAs	Monocycle, Doublet, Triplet	Monocycle: 114 ps, fc= 3.1 GHz, B10=5.2 GHz ; Doublet: 78 ps, fc=3.8 GHz, B10=5.3 GHz ; Triplet: 54 ps, fc=4.5 GHz, B10=11 GHz
		[66] Tunable laser, MZM, reflective SOA	No classical pulse	Bf > 0.89 ; A signal of 1.56 Gbps RZ over 20 km SMF
[17, 20, 67, 68, 69, 70, 71]	External Modulation	[17] Variable Fiber Delay Line, Phase Modulator & Shifter	Monocycle, Doublet	Monocycle period, 69 ps, B10=7.33 GHz ; Doublet period, 53 ps, B10=5.4 GHz
		[20] 3 tunable LDs, intensity modulator, highly nonlinear fiber, delay line	Monocycle, Doublet, Novel Pulse	Monocycle period, 0.4 ns ; Doublet period, 0.4 ns ; FCC- compliant pulse period, 0.5 ns, & η= 50.59 %
		[67] 2 tunable LDs, phase modulator, programmable optical filter, SMF	Monocycle, Doublet	Mono, fc=4.5 GHz, B10= 8.2 GHz, Bf=1.82 ; Doub, fc =5.2 GHz, B10=6.8 GHz ; 0.39 Gbps
		[68] 2 tunable LDs, 2 phase modulators, MZI, optical delay line, highly nonlinear fiber, optical filter	Doublet, Triplet	fc= 5.1 GHz, Bf= 1 ; Data rate: 731.25 Mbps Duty cycle: 1/16
		[69] 2 phase modulators, frequency discriminator	Monocycle, Doublet, & others	The best pulse, (5 combined monocycles): fc=6.6 GHz, B10 =7.2 GHz, Bf=1.09, η=47.4%
		[70] Electro-absorption modulator-integrated DFB, isolator	Doublet	fc=6.8 GHz, B10=7.8 GHz, Bf= 1.15 ; Data rate: 1.25 Gbps 50 km SMF is considered
		[71] Polarization modulator & controllers, MZM, FBG, & polarizers	Doublet	Simultaneous up & down streams of 1.25 Gbps over 25 km SMF
[72 73, 74]	Exploiting laser or fiber nonlinearity	[72] External cavity laser, MZM, DFB	5^{th} Gaus like -pulse	3.125 Gbps OOK over 25 km SMF; 2.9 meters propagation distance considered
		[73] LD, isolator, electro-absorption modulator	Chaotic signal	Data rate, 300 Mbps. Pulses period, 3 ns, Fractional bandwidths: 1.81, 1.43, & 2.14
		[74] Highly nonlinear fiber, modulator, differential detector, delay line, filter	Doublet	Output pulse period: 33 ps or 100 ps (depending on the band pass filter) ; fc=25 GHz, Bf=1.2 ; Pulse repetition rate, 1.25 GHz

Table 2.2: A summary for the most popular optical generation techniques described in literature.

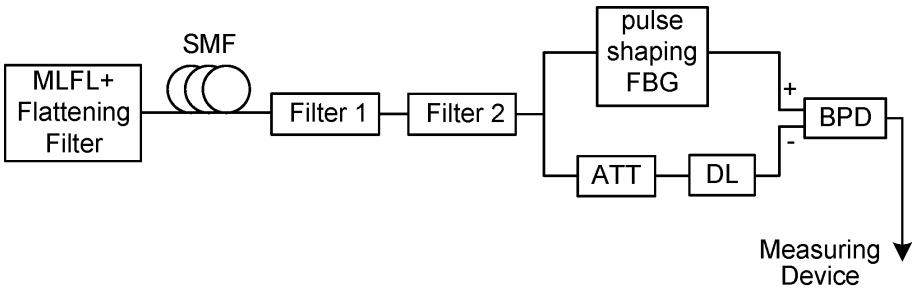

Figure 2.6: A simplified schematic diagram of the UWB pulse generator proposed in [62].

The optical pulse is then divided into two arms; in the first, a fiber Bragg grating (FBG) with a complex apodization profile imprints the optimized pulse shape on the spectrum of the source, and the gratings are written by ultra violet scanning; in the second arm, an optical delay line (DL) and a variable attenuator (ATT) are placed for balancing the amplitude and the time shift between the two arms. Finally, an optical intensity-to-voltage conversion occurs in the balanced photo-detector (BPD) to produce the target waveform. The output pulse is designed by systematically calibrating the central wavelengths of the filters, semi-Gaussian monocycles and doublets have been generated, besides to a power efficient FCC-compliant waveform obtained at a relatively higher order of complexity. This setup has a kind of robustness against environmental changes, as the fiber components are less sensitive to such perturbations.

In [75], a new technique has been proposed to generate polarity-switchable UWB Gaussian pulses in optical domain. As stated in fig. 2.7, the laser diode (LD) produces an electromagnetic wave in order to be phase modulated, where the latter is injected with an electrical Gaussian pulse. The modulated optical signal at PM output enters the Asymmetric Mach-Zehnder Interferometer (AMZI), which is formed by cascading two polarization maintaining fibers (PMF) with their fast axes $\pi/4$ radians aligned, and followed by a polarization beam splitter (PBS). A polarization controller (PC) is placed at the PMF input for adjusting the polarization direction of the incident wave to get an angle of 0 or $\pi/4$ radians to one principle axis of the PMF, which can also add a static phase shift between the two orthogonal polarization components along the directions of the fast and slow axes of the PMF. For generating a Gaussian monocycle, a first order differentiation has to be performed by the AMZI, that can be established by aligning the polarization direction of the phase-modulated signal with one principle axis of the first PMF. The beam is equally distributed along the two principle axes at the second PMF, with a time delay and phase differences introduced by the PMF birefringence and the PC respectively. Therefore, the induced current at the photo-detector (PD) output becomes approximately proportional to the first order difference of the input Gaussian. When a Gaussian doublet is targeted, a second order differentiation is required, that is done by aligning the polarization direction of the light wave to make a deviation of $\pi/4$ radians with the principle axes of the first PMF. The output electrical current becomes proportional with the second order difference of the input Gaussian. Monocycles and Doublets have been practically generated, with fractional bandwidths of 1.77 and 1.4 respectively. The benefits of the proposed configuration are the low cost and small size, besides to the operation stability with UWB communications.

Pan has experimentally demonstrated the concept of optical pulse generation based on

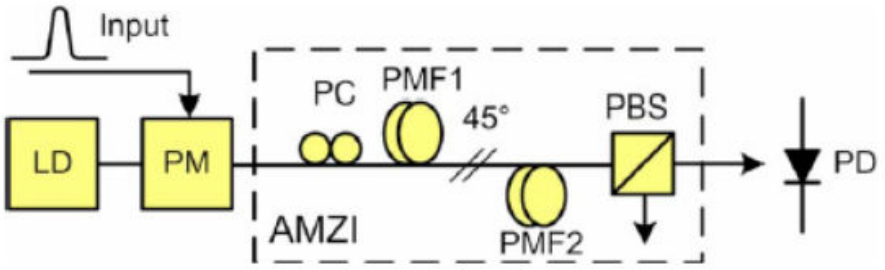

Figure 2.7: The schematic diagram of the optical pulse generator proposed in [75].

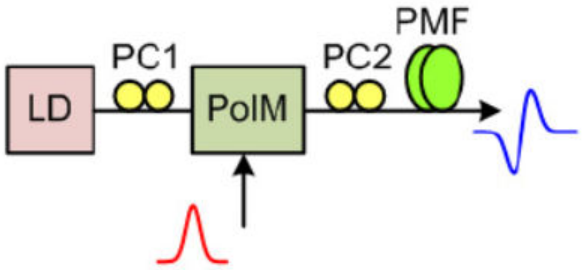

Figure 2.8: The schematic diagram of the optical pulse generator proposed in [5].

adopting two-tap photonic microwave delay-line filter with opposite polarization as a differential system [5]. The schematic diagram is shown in fig. 2.8; the configuration relies on a laser diode followed by two polarization controllers (PC1 and PC2) with a polarization modulator (PolM) in between, and a section of polarization maintaining fiber is placed just before the photo-detector. Non-coherent detection has been employed in order to protect the generated signal against optical interference. The input Gaussian pulse is injected to the PolM, which can support both TE and TM modes but with opposite phase modulation indices. When a linearly polarized incident light is oriented at an angle of $\pi/4$ radians to one principal axis of the PolM, complementary phase modulated signals are generated along the two principal axes. The optical field then enters the PMF after being passed by the polarization controller, the latter is used to align the principal axes of the PolM to make a $\pi/4$ radians deviation with the PMF principal axes. Detecting the resultant field by square-law produces a current which is proportional to the first order difference of the input Gaussian, so the output waveform becomes a Gaussian monocycle. The advantage of this configuration is the low order of complexity, besides to the fact that the generated pulse is chirp free, since the horizontal and vertical components of the optical field have a fixed phase.

Yu has proposed and experimentally demonstrated a novel generation scheme for Gaussian monocycles reported in [50]. As described in fig. 2.9, the setup consists of a tunable laser diode (TLD) source followed by a MZM and SOA, where the BIAS is a voltage source that controls the operating point of MZM, and the BPG is a bit pattern generator which produces the return-to-zero electrical signal. The lightwave radiated from the TLD is launched into the MZM to be intensity modulated before entering SOA, while the latter operates in the saturated gain region. The optical coupler (OC) then divides the propagated field by 10:90 power ratio, 90% goes to the optical sampling oscilloscope (OSO) for time display and the remaining is injected to the photo-detector, to be converted into a voltage signal before entering the electrical spectrum analyzer (ESA). The concept of

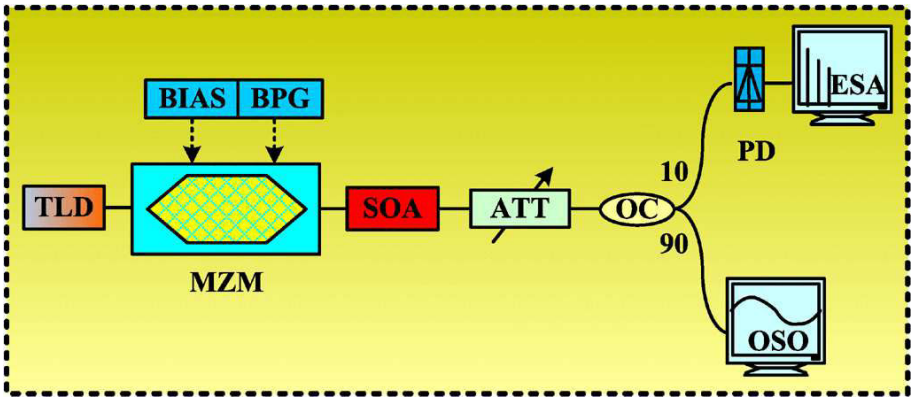

Figure 2.9: The block diagram of the optical pulse generator for the Gaussian monocycle proposed in [50]

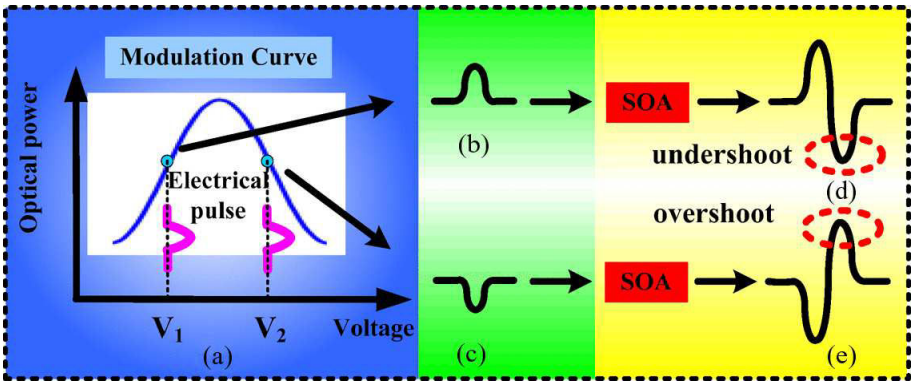

Figure 2.10: The operation principle of the optical pulse generator for the Gaussian monocycle proposed in [50]

generation is explained in fig. 2.10, when applying V_1 at the bias, MZM operates in the positive slope interval of the modulation curve, and the output pulse is in-phase with the electrical one, and after being amplified by SOA the carrier density stays at a higher level. When the positive Gaussian enters the SOA, the optical signal is boosted and a direct decrease occurs in the carrier density, that leads to a smaller gain and an undershoot in the waveform just after the positive pulse. The carrier density then returns back into the initial level and the optical pedestal at other time is uniformly amplified. A positive Gaussian monocycle is generated by this process; and on the contrary, when the biasing voltage is V_2, a negative monocycle is obtained due to the negative slope of MZM at this point. So in this work, not only a Gaussian monocycle is designed, but also there is a flexibility to transmit a bipolar modulated signal based on triggering the MZM biasing voltage at limited order of complexity.

2.3 Radio Over Fiber Transceiver Based on Mach-Zehnder Modulator

In this work, our candidate for intensity modulation is the Lithium Niobate single arm MZM; which has an interesting performance characteristics in comparison with other electro-optical converters, mainly the low optical loss, high power handling capability, broad optical bandwidth, and robustness against fluctuations in temperature [30]. Fig-

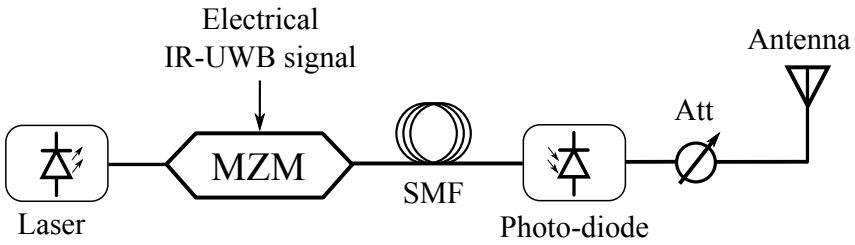

Figure 2.11: Block diagram of the impulse radio over fiber system adopted in this study.

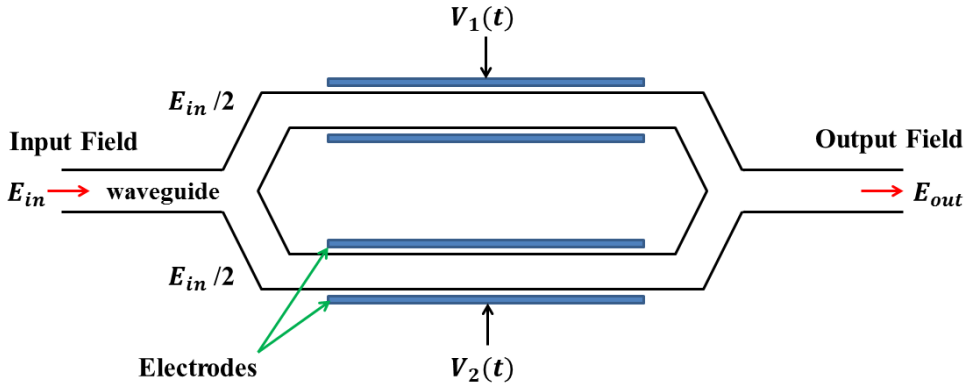

Figure 2.12: A simple schematic diagram for the MZM structure.

ure 2.11 presents our basic optical system, the transmitter relies on MZM with a half-wave voltage $V\pi$= 6 V, biased at V_{DC}= $1.5V\pi$ by the electrical UWB signal with a continuous wave light applied at its input (laser diode signal). The channel is made of a Single Mode Fiber (SMF). At the receiver side (just before wireless transmission), a photo-detector converts the optical power into an electrical voltage signal, the latter being attenuated before entering the antenna so as to meet FCC mask. The thermal and shot noises of the photo-detector have not been taken into account, as both are negligible with respect to the signal power at our operating conditions. In this thesis, we mainly focus on the optical part of the system, hence, the received signal is analyzed directly after the photo-detector, while ignoring antenna effects.

2.3.1 Mach-Zehnder Modulator: Principle of Operation and Transfer Function

The MZM operation principle is described in fig. 2.12, the input optical field is equally distributed over the two arms, where each is surrounded by two electrodes. A voltage dependent time delay is applied by the electrical signals ($V_1(t)$ and/or $V_2(t)$) for both propagating fields. Thanks to this interferometric structure, the phase difference is converted into an intensity when both fields are combined, and a data signal can modulate the input optical power [76]. As a single-arm configuration is adopted in the sequel, $V_1(t)$ is the unique input voltage ($V_2(t) = 0$). Figure 2.13 shows the MZM transfer function versus input voltage V_{in} (which is here $V_1(t)$), where V_{in} includes V_{DC} and $v(t)$ as described in eq. (2.4), and $v(t)$ could be expressed in terms of the peak-to-peak voltage (V_{pp}) and the normalized UWB signal $S_N(t)$ as shown in eq. (2.5). In addition of the basic MZM, a quadrature modulator can be formed utilizing two parallel and independently driven

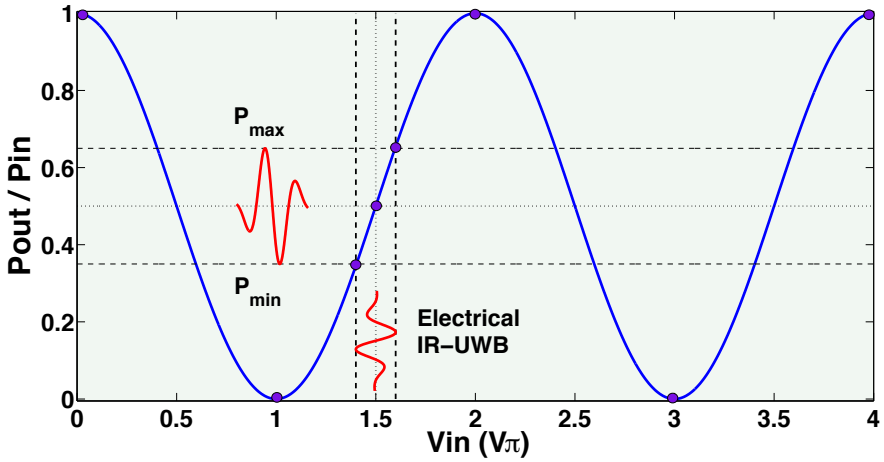

Figure 2.13: MZM power ratio versus input voltage.

MZMs, with a static phase shift of $\pi/2$ in between. The resultant synthesized signal is a complex one which is suitable for IQ modulation patterns like QAM [76].

$$P_{out}(t) = P_{in}\, cos^2\Big(\frac{\pi}{2V\pi}\big(V_{DC} + v(t)\big)\Big) \tag{2.4}$$

$$v(t) = V_{pp} \times S_N(t) \tag{2.5}$$

The oscillating term in the MZM transfer function adds nonlinear effects to the output optical pulses. After the photo-detector, the DC component is removed from the received electrical signals prior to electromagnetic propagation, making thus a compromise between the average power and linearity as will be shown in the sequel.

2.3.2 On Optimizing the Operating Conditions of MZM

Increasing the peak-to-peak voltage adds strong nonlinearities to the input UWB pulse, but raising at the same time the extinction ratio (ER) P_{max}/P_{min} and average output power. Larger ER translates into better bit error rate performance, as an energy detector-based non-coherent receiver is targeted. The average power at the fiber input directly influences the optical transmission reach that can be achieved. RoF networks with wide covering necessitates a large enough available power at the transmitter side, which corresponds to a large V_{pp}. On the other hand, free space transmission involves a strict power limitation imposed by the regulatory bodies (FCC mask), and MZM linearity becomes important to meet such constraint, which can be achieved by operating at small V_{pp}. Therefore, an optimization of MZM operating conditions has to be done for satisfying both constraints.

In fig. 2.14, we consider the power efficiency η_M of a modulated signal (1.10) to evaluate the MZM characteristics for a relatively wide range of DC biasing voltage, where $V_{pp} = 0.4$ $V\pi$. The modulation scheme is OOK operating at 2 Gbps and based on the 5th Gaussian (5th order derivative of the fundamental Gaussian expressed in (1.4)), while considering a broad range of pulse shaping factor. Regarding the latter, the best operating point lies at 51 ps for which the spectrum peak is located at the midpoint of the UWB frequency interval, with a non-symmetrical response due to FCC mask shape. About the biasing

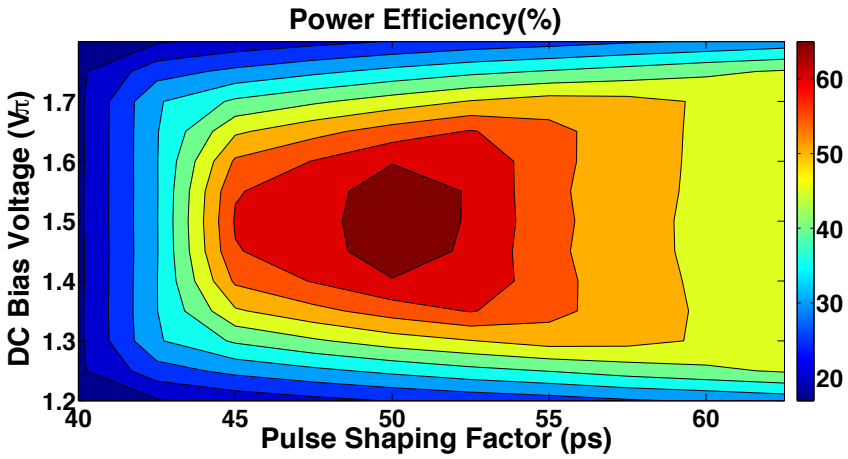

Figure 2.14: The power efficiency of 2 Gbps OOK based on the 5th derivative Gaussian, versus pulse shaping factor and DC biasing voltage (in optical back-to-back case), where $V_{pp} = 0.4\ V\pi$.

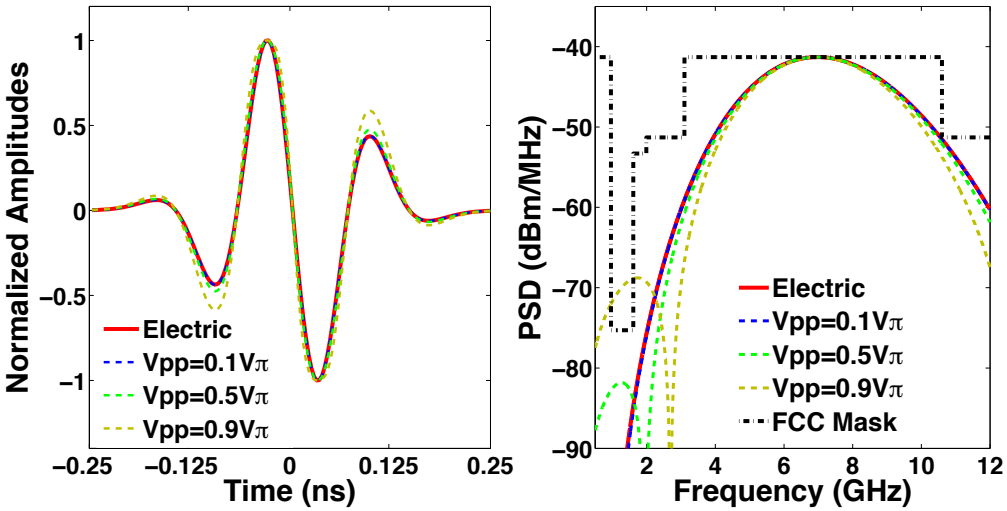

Figure 2.15: Time waveforms and power spectral densities of 5th-derivative Gaussian pulse for several V_{pp} values.

voltage impact, the optimum efficiency is associated with the most linear region at V_{DC}= $1.5V\pi$, moving away from this point yields to a spectral distortion caused by the sharp curve of power ratio, the contour plot vertical symmetry is due to the cosine parity for MZM.

Figure 2.15 shows the influence of V_{pp} in time and frequency domain for 5th-derivative Gaussian pulse. As V_{pp} increases more time spread is obtained, specially at positive and negative peaks, leading to low frequency components which violate FCC mask in the most restricted region [0.96-1.61] GHz corresponding to GPS band. This dangerous interference obliges the transmitter to attenuate the UWB signal so as to respect FCC limit, and consequently a low power efficiency is obtained.
At short distances, where the optical power is relatively high, applying large V_{pp} leads to a strong spectral violation of FCC mask; hence, there is no benefit from the high electrical power available as it is impossible to transmit a signal with a non-regular spectrum. At

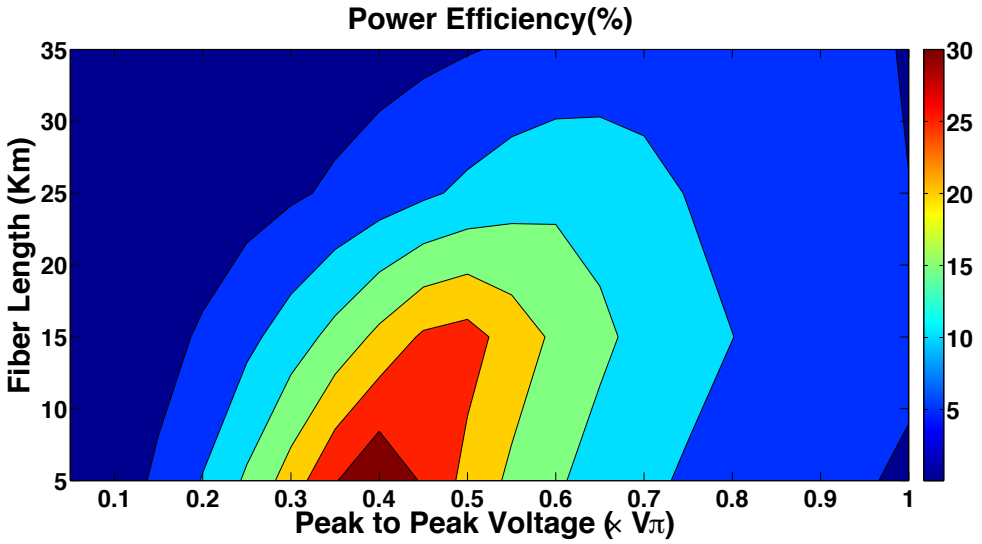

Figure 2.16: Power efficiency versus fiber length and V_{pp} for 2 Gbps OOK based on 5th-derivative Gaussian pulse.

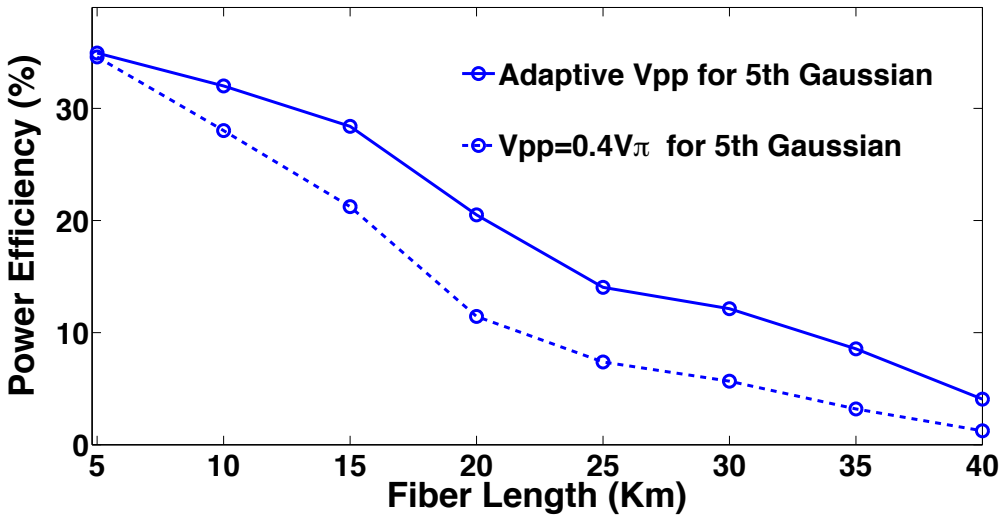

Figure 2.17: Power efficiency versus fiber length for 2 Gbps OOK based on the 5th-derivative Gaussian, in the case of using fixed or optimal V_{pp}.

long distances, a decrease in the spectrum level occurs due to optical attenuation of the fiber. Therefore, linearity is no longer important, as operating far below FCC mask raises the priority towards high average power instead of perfect spectral shape, thus an increase in the V_{pp} is necessary to get a better performance. So the trade-off between linearity and output power depends on the fiber length that have to be considered; the corresponding optimal V_{pp} at MZM input is investigated in the sequel.

The power efficiency of 2 Gbps OOK based on the 5th-derivative Gaussian is plotted in fig. 2.16 for a wide range of V_{pp} and fiber length. The optimum performance is obtained in the interval $[0.3V\pi,\ 0.5V\pi]$ at low distances, where no significant effects of dispersion/attenuation occur. As noticed, the contour plot is not symmetrical around the vertical line, so the axis of symmetry has a right deviation from the vertical direction, due to optical power degradation through fiber which necessitates a compensation by increasing V_{pp}. The power efficiency has been studied versus single mode fiber length in fig. 2.17 for 2 Gbps OOK based on 5th-derivative Gaussian pulse. Following the traditional approach, having as the only interest the linearity, we could fix the peak-to-peak voltage at $V_{pp} = 0.4\ V\pi$, which maximizes the efficiency at low fiber distances. But it is clear that keeping this particular value for operating over larger distances is no longer the best choice. Therefore, better performance does not necessarily mean high linearity for external modulation.

2.4 Introducing the Semiconductor Optical Amplifier in our Radio Over Fiber Transmission System

The semiconductor optical amplifier illustrated in fig. 2.18 is an electro-optic device which acts to amplify an input light signal under specific operating conditions [77–79]. The amplification process occurs in the active layer, and the power gain is due to the external electric current I_{bias} injected to SOA via the electrode. The propagated signal is confined to the active region via an internal waveguide, and weak confinement leads to an optical loss due to the leakage of some signal parts into the surrounding cladding. An amplified spontaneous emission (ASE) noise is added to the propagated signal, which is produced during amplification [77].

2.4.1 SOA Fundamentals

SOA can be characterized by several parameters, mainly the gain, gain saturation, optical bandwidth, noise figure, and the polarization sensitivity [77].

SOA Gain and Saturation

The optical gain of the SOA is defined as the output to input power ratio P_{out}/P_{in}. It depends on the operating wavelength, biasing current, and input power, the fabrication material of the active region has also an influence on the gain dynamics. The single pass optical gain is defined as [77]:

$$G = e^{gL} = e^{\left(\Gamma g_m(\lambda,N) - \alpha_{int}\right)L} \tag{2.6}$$

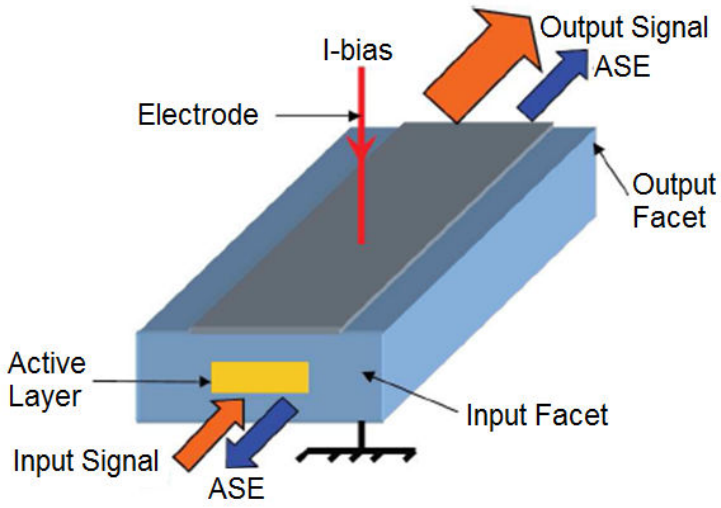

Figure 2.18: Simple schematic diagram for SOA structure.

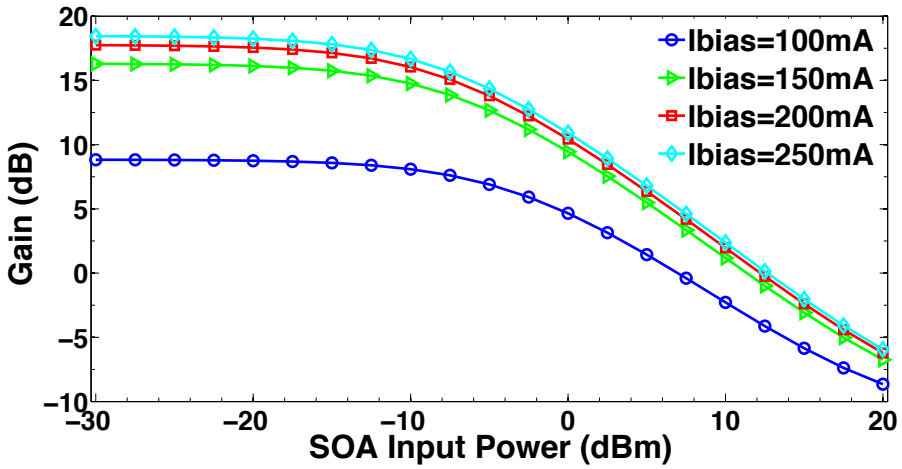

Figure 2.19: The gain versus input optical power for several values of biasing current.

where g is the net gain, L is the SOA length, Γ is the optical confinement factor, $g_m(\lambda, N)$ denotes the material gain, λ is the wavelength, N is the carrier density, and α_{int} is the internal loss coefficient. The SOA gain is plotted in fig. 2.19 versus input power for several biasing currents. As noticed, the gain has a nonlinear function with respect to the biasing current. A gain saturation is obtained at high power, when the carrier density in the active region become drained causing for a gain degradation. Saturation occurs when the gain becomes 3 dB below its maximum value obtained in the linear region (at low input powers), the corresponding output power is called the saturated power, which is inversely proportional with the optical confinement factor [77]. When SOA is used as an amplifier, better performance is obtained in the linear gain region, so a higher saturation point is targeted; but in case of using SOA for intensity modulation, a lower carrier life time is required so as to increase the modulation bandwidth and improve the transmission capacity, that requires an operation in the strong gain saturation [80, 81].

Optical Bandwidth

The optical gain bandwidth is defined as the wavelength range where the gain is not below 3 dB of its maximum (occurring at the central wavelength). The gain bandwidth depends on the SOA structure, materials, and operational parameters, it has an inverse relation with the cavity length and optical confinement factor [77]. Higher optical bandwidth makes the amplifier more pertinent for adoption in communication systems, as less distortions are resulted with broadband amplified signals.

Noise Figure

The noise figure N_f is defined as the input-to-output signal-to-noise ratio, where in addition to the shot and thermal noises induced by the photo-detector, two types of noises are inherent to SOA amplification. The signal-spontaneous beat noise and spontaneous-spontaneous beat noise are due to the presence of ASE, where their average powers $\sigma^2_{sig-ase}$ and $\sigma^2_{ase-ase}$ are expressed in eq. (2.7) and eq. (2.8) respectively [6, 77].

$$\sigma^2_{sig-ase} = 4qR_{A/W}GP_{in}(G-1)n_{sp}B_e \tag{2.7}$$

$$\sigma^2_{ase-ase} = 4q^2(G-1)^2n^2_{sp}B_eB_{opt} \tag{2.8}$$

Where q is the electron charge, $R_{A/W}$ is the responsivity, G is the gain, P_{in} denotes the input power, n_{sp} is the spontaneous-emission factor, B_e is the electrical bandwidth, and B_{opt} is the optical bandwidth [6, 77]. When a high power optical signal is injected, the signal-spontaneous beat noise is the dominant, whereas the spontaneous-spontaneous beat noise significantly arises at low powers. The noise figure in the SOA depends on the wavelength, input optical power, and biasing current, it is expressed as:

$$N_f = \frac{2P_{ASE}}{hfGB_{opt}} + \frac{1}{G} \tag{2.9}$$

where P_{ASE} is the average power for ASE noise, h is the Planck's constant, and f is the frequency of the input signal [82].

Polarization Sensitivity

Due to the geometrical shape of the SOA active region, the gain depends on the polarization state of the input beam, since the confinement factor and effective mode index differ between the transverse-electric (TE) and transverse-magnetic (TM) modes; which is a drawback in some applications, as a non-constant output power can be obtained due to any change in the polarization. Tensile strain makes the TM material gain higher than that of TE. It is therefore possible to balance the influence of TE and TM confinement factors leading to polarization independence.

2.4.2 SOA Nonlinearities

Regarding the SOA impact against propagated signal dynamics, several types of nonlinear effects are inherent to the amplification process, mainly the self gain modulation, cross gain modulation, self phase modulation, cross phase modulation, and four wave mixing. These nonlinearities are due to the variations in the carrier density induced by SOA [77]. All affect on the output signal quality, higher degree of distortion appears at large input powers and biasing currents, linearization techniques being important so as to overcome these effects and enhance the performance.

Self gain modulation

When operating in the SOA saturated region, the variation in the optical power associated with the input signal causes for changes the optical gain, this phenomenon is called self-gain modulation (SGM) [77].

Cross-gain modulation

The cross gain modulation (XGM) is a nonlinear optical effect where the intensity of one signal wavelength can affect the gain of another signal wavelength due to the change in the carrier density that influences all input signals to the SOA. The variation in the carrier density lead to pattern effects and inter-channel crosstalk. The XGM effect could be useful in several application as for example for wavelength conversion [77].

Self phase modulation

The refractive index and material gain of SOA depend on the carrier density, so the phase and gain of the optical field are coupled via gain saturation. The carrier density changes due to the wave propagation through SOA active area, which lead to a change in the effective index and consequently in the propagation coefficient, this phenomenon is called self phase modulation (SPM). It could be pertinent to exploit the benefits of SPM, by using it as a dispersion compensator placed before or after the optical link [77].

Cross phase modulation

For a multi-wavelengths input signal, besides to SPM, a cross phase modulation (XPM) occurs between different signal wavelengths. The intensity of a specific wavelength signal can affect the refractive index of a different wavelength signal, that is due to the change in the carrier density. Thanks to this effect, a wavelength converter could be also established via an interferometric structure of SOAs, where the phase change is converted into an intensity modulation [77].

Four wave mixing

When two optical fields are injected into SOA, having same polarization but different frequencies (f_1 & f_2), a coherent nonlinear process occurs, where the amplifier gain is modulated at the beat frequency ($f_2 - f_1$) and a new field is produced. Such a four wave mixing effect could be used for wavelength conversion, dispersion compensation, and optical de-multiplexing [77].

2.4.3 SOA Interesting Features and Applications

Semiconductor optical amplifiers have several attractive features, such as, low power dissipation, capable for usage in photonic integrated circuits, low cost, large scale monolithic integration capability, besides to the full coverage of the entire fiber transmission window. Regarding SOA system applications, the amplifier could be adopted as a booster to push up the transmitted power, as an in-line amplifier to compensate the optical losses in long-haul links, or as a pre-amplifier to increase the receiver sensitivity [77, 83]. Figure 2.20 describes the system and functional applications for SOA, examples include wavelength

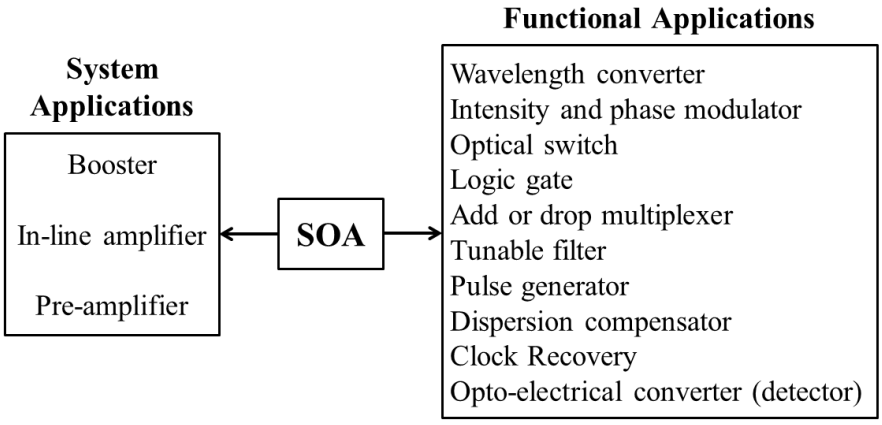

Figure 2.20: System and functional applications for SOA [77].

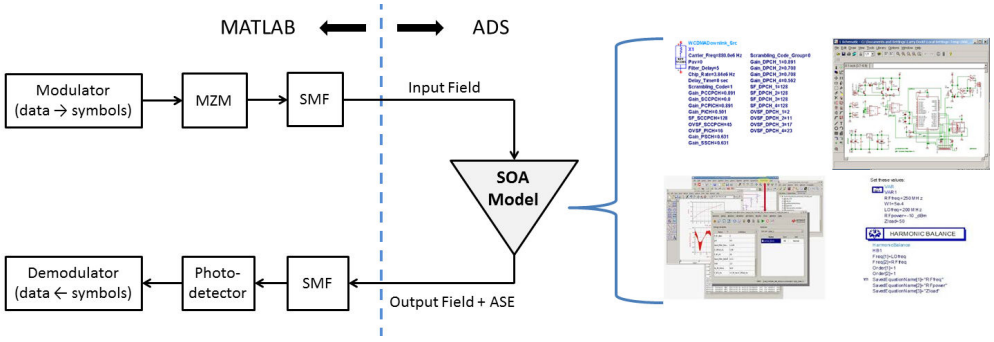

Figure 2.21: A schematic diagram describing the ADS model for SOA, and co-simulation with MATLAB.

conversion, switching, optical amplification, intensity modulation, pulse generation and shaping, logic gating, and other signal processing functions [77].

2.4.4 SOA Physical Model

SOA has been modeled by ADS [84], which is a rich software having a broad library and contains a lot of functional blocks, it is capable to simulate several types of analog and digital setups. ADS allows static, dynamic, transient, and harmonic balance simulations, so it is an effective tool for nonlinear modeling. Figure 2.21 describes the Matlab-ADS co-simulation; the modulated optical signal is imported into ADS where the SOA function is performed, the output field and ASE intensity are then re-loaded in MATLAB.

The designed SOA model is based on dividing the active region into S calculation sections, in order to get a more accurate calculation of the carrier density; since the latter is assumed to be constant along the section length (each section is considered as a semi-linear medium) [85, 86]. Figure 2.22 describes the input and output fields for a ℓth section in the SOA having a carrier density N_ℓ, $F_{in}^{\pm}(t)$ and $F_{out}^{\pm}(t)$ are the input and output fields, where the + (or −) sign corresponds to the propagation in the direction of (or opposite to) the device length. In the positive sense, which is considered from the left to the right, the input (or output) of the ℓth section is the output (or input) of the [ℓ-1]th (or [ℓ+1]th) section, and the opposite is true for the negative sense. In addition to the signal field,

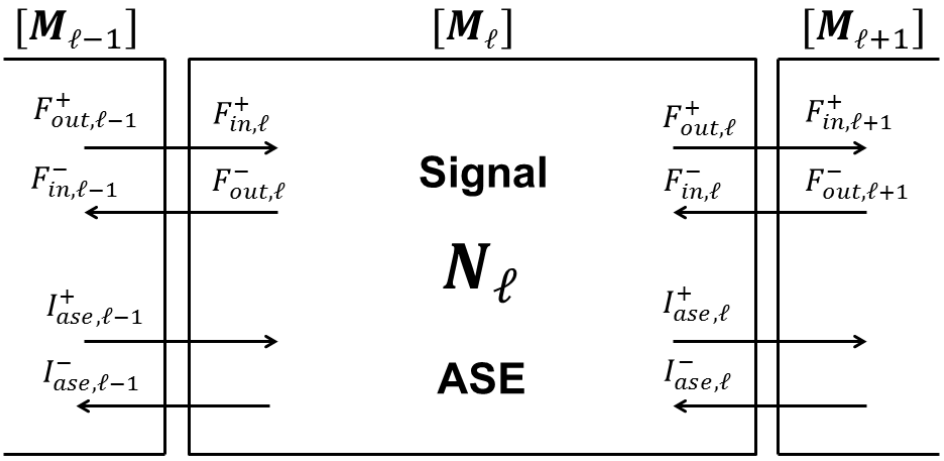

Figure 2.22: One calculus section $[M_\ell]$ in the SOA, the signal and ASE intensity share the carrier density [85,86].

there is also the ASE intensity ($I^{\pm}_{ase,\ell}$ and $I^{\pm}_{ase,\ell-1}$) which has been also considered in the model.

$$\begin{bmatrix} F^{+}_{in}(t) \\ F^{-}_{out}(t) \end{bmatrix} = \begin{bmatrix} e^{+\,i\,k(\omega_i - i\frac{d}{dt})\,L_s} & 0 \\ 0 & e^{-\,i\,k(\omega_i - i\frac{d}{dt})\,L_s} \end{bmatrix} \times \begin{bmatrix} F^{+}_{out}(t) \\ F^{-}_{in}(t) \end{bmatrix} \tag{2.10}$$

Equation (2.10) describes the time domain transfer matrix model, where k is the wavevector, ω_i is the carrier angular frequency, and L_s is the device length [85,86]. By considering the Taylor expansion of the wavevector, taking into account the time delay and spectral dispersion, the solution of the propagation equation becomes:

$$F^{\pm}_{out}(t) = \left[e^{-i\,k^{(0)}_{N,\omega_i}\,L_s}\right]\left[e^{-\,k^{(1)}_{N,\omega_i}\,L_s\,\frac{d}{dt}}\right]\left[e^{i\,k^{(2)}_{N,\omega_i}\,\frac{L_s}{2}\,\frac{d^2}{dt^2}}\right]\left(F^{\pm}_{in}(t)\right) \tag{2.11}$$

where

$$k^{(m)}_{N,\omega_i} = \left.\frac{d^m k(N,\omega)}{d\omega^m}\right|_{\omega_i} \tag{2.12}$$

The different orders of k vector derivatives give the following relations:

$$k^{(0)}_{N,\omega_i} = k(N,\omega_i) = \frac{\omega_i}{c}\,n_{eq}(N,\omega_i) + \frac{i}{2}\,g_n(N,\omega_i) \tag{2.13}$$

$$k^{(1)}_{N,\omega_i} = \frac{n_g(N,\omega_i)}{c} + \frac{i}{2}\left.\frac{\partial g_n(N,\omega)}{\partial\omega}\right|_{\omega_i} \tag{2.14}$$

$$k^{(2)}_{N,\omega_i} = \frac{1}{c}\left.\frac{\partial n_g(N,\omega)}{\partial\omega}\right|_{\omega_i} + \frac{i}{2}\left.\frac{\partial^2 g_n(N,\omega)}{\partial\omega^2}\right|_{\omega_i} \tag{2.15}$$

where

$$n_g(N,\omega) = n_{eq}(N,\omega_i) + \omega\,\frac{\partial n_{eq}(N,\omega)}{\partial\omega} \tag{2.16}$$

g_n and n_{eq} are the net gain and refractive index respectively expressed in [86]. For the whole active layer consisting of S cascaded sections $[M_j]$, eq. (2.10) could be generalized to obtain:

$$\begin{bmatrix} F^{+}_{in}(t) \\ F^{-}_{out}(t) \end{bmatrix} = [M_1][M_2].....[M_{S-1}][M_S] = \begin{bmatrix} F^{+}_{out}(t) \\ F^{-}_{in}(t) \end{bmatrix} \tag{2.17}$$

The electrical injected current, stimulated and unstimulated recombinations, besides to the spontaneous emission recombination, all are considered in computing the carrier density [85, 86]. The specifications of the SOA are mentioned in Appendix B. The carrier density evolution in each calculus section is given by the following rate equation:

$$\frac{dN_\ell}{dt} = \frac{I_{el,\ell}}{q_e\, L_s\, \omega d} - R_{sig} - R_{ase} - R_{nsti} \tag{2.18}$$

with

$I_{el,\ell}$	electrical current flowing in the ℓth section;
$L_s\, \omega d$	active zone numerical section volume;
q_e	elementary electrical charge;
R_{sig}	recombination rate due to the amplification of the signals;
R_{ase}	recombination rate due to the amplification of amplified spontaneous emission;
R_{nsti}	nonstimulated recombination rate.

Where the stimulated recombination rates are considered to be proportional to light intensity. For M_{sig} signals propagating in the ℓth section, the recombination rate is given by:

$$R_{sig} = \sum_{i=1}^{M_{sig}} R_{sig}(N_\ell, \omega_i) \tag{2.19}$$

$$R_{sig}(N_\ell, \omega_i) = \frac{g_m(N_\ell, \omega_i)}{\hbar\, \omega_i}$$

$$\times \frac{1}{L_s} \int_0^{L_s} \left(\left| e^{-ik(N_\ell,\, \omega_i - i\frac{d}{dt})z}\; F^+_{in,\ell,i}(t) \right|^2 + \left| e^{-ik(N_\ell,\, \omega_i - i\frac{d}{dt})z}\; F^-_{in,\ell,i}(t) \right|^2 \right) dz \tag{2.20}$$

where

$$k\Big(N_\ell,\, \omega_i - i\frac{d}{dt}\Big) = \sum_{m=0}^{\infty} \frac{d^m\big(k(N_\ell, \omega)\big)}{d\omega^m}\bigg|_{\omega_i} \left(\Big(- i\frac{d}{dt}\Big)^m / m! \right) \tag{2.21}$$

The non-stimulated recombination rate is given by:

$$R_{nsti} = A_{nr} N_\ell + B_{ns} N_\ell^2 + C_{Au} N_\ell^3 \tag{2.22}$$

where A_{nr} is the nonradiative recombination coefficient on traps and impurity centers, B_{ns} is the spontaneous recombination coefficient, and C_{Au} is the Auger recombination coefficient [85, 86].

The propagation equations of the ASE intensity in the ℓth calculation section are:

$$I^+_{ase,\ell} = e^{g_m(N_\ell, \lambda_{ase})L_s}\; I^+_{ase,\ell-1} + I_{sp}(N_\ell, \lambda_{ase}) \tag{2.23}$$

$$I^-_{ase,\ell-1} = e^{g_m(N_\ell, \lambda_{ase})L_s}\; I^-_{ase,\ell} + I_{sp}(N_\ell, \lambda_{ase}) \tag{2.24}$$

where $I_{sp}(N_\ell, \lambda_{ase})$ is the spontaneous emission generated in the ℓth section, expressed in [85].

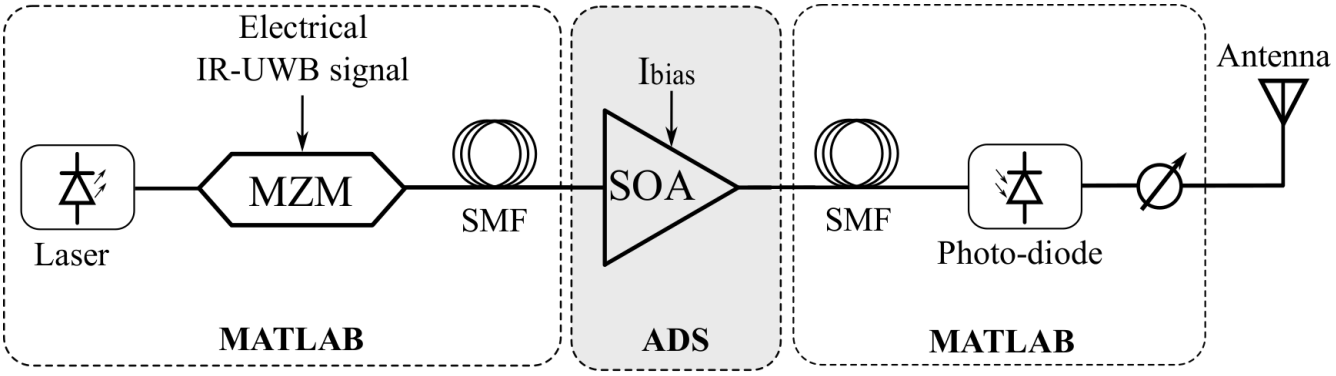

Figure 2.23: Block diagram of the impulse radio over fiber system with Matlab/ADS co-simulation.

2.4.5 Adopting SOA in our UWB over fiber system

As will be illustrated in the sequel, an optical amplification for the impulse radio signals is required to get a reach extension. Various types of amplifiers have been proposed in literature [87], but to the best of our knowledge, the use of SOA for in-line and pre amplification of UWB optical signals has not been investigated until now. We consider the SOA as an attractive solution for such low cost and low complexity systems. Figure 2.23 describes the new integrated system for in-line amplification scenario, where pre-amplification can be obtained by simply removing the second piece of the SMF. The same ADS software-based model as in [84] is adopted for the SOA, as it has proved to be highly accurate and in very good agreement with experimental data. The potential of SOA in enhancing the transmission system performance is illustrated in the next chapters, and an experimental demonstration for the case of pre-amplification is covered in the last chapter.

2.5 Summary

In this chapter, we talked briefly about the radio over fiber communications and its interesting features, then an overview for the UWB pulse generation techniques was done. Our basic impulse radio optical transmission system is then introduced, and we show how the operating conditions of MZM could be optimized. Afterward, we considered the SOA amplifier for reach extension purpose, a short description about this component was done, including the amplification concept, SOA main characteristics, and nonlinear effects. The latter degrade the system performance, hence, a special effort is applied to overcome these nonlinearities; that is the core of the next chapter, we propose analog pre-distortion schemes as a pertinent solution for mitigating SOA nonlinear effects.

Bibliography

[1] Gambiroza, V., Sadeghi, B., & Knightly, E. W. (2004, September). End-to-end performance and fairness in multihop wireless backhaul networks. In Proceedings of the 10th annual international conference on Mobile computing and networking (pp. 287-301). ACM.

[2] Shelby, R. A., Smith, D. R., & Schultz, S. (2001). Experimental verification of a negative index of refraction. science, 292(5514), 77-79.

[3] Ramaswami, R., Sivarajan, K., & Sasaki, G. (2009). Optical networks: a practical perspective. Morgan Kaufmann.

[4] Pan, S., & Yao, J. (2010). UWB-over-fiber communications: modulation and transmission. Journal of Lightwave Technology, 28(16), 2445-2455.

[5] Pan, S., & Yao, J. (2010). Performance evaluation of UWB signal transmission over optical fiber. IEEE Journal on selected areas in communications, 28(6).

[6] https://encrypted-tbn0.gstatic.com/images?q=tbn:ANd9GcS8WotN_W3hSmtUHEuODJ-dDSSP2ipPY8LsTinJ-S0LanAWFK7q

[7] Knight, J. C., Birks, T. A., Russell, P. S. J., & Atkin, D. M. (1996). All-silica single-mode optical fiber with photonic crystal cladding. Optics letters, 21(19), 1547-1549.

[8] G. P. Agrawal, Fiber-Optic Communication Systems, 3 ed. John Wiley & Sons, Inc., New York, 2002.

[9] G. P. Agrawal, Nonlinear Fiber Optics. San Diego, CA: Academic, 2001.

[10] Namekata, N., Adachi, S., & Inoue, S. (2010). Ultra-low-noise sinusoidally gated avalanche photodiode for high-speed single-photon detection at telecommunication wavelengths. IEEE Photonics Technology Letters, 22(8), 529-531.

[11] Kang, Y., Liu, H. D., Morse, M., Paniccia, M. J., Zadka, M., Litski, S., ... & Zaoui, W. S. (2009). Monolithic germanium/silicon avalanche photodiodes with 340 GHz gain–bandwidth product. Nature photonics, 3(1), 59-63.

[12] Su, S., Cheng, B., Xue, C., Wang, W., Cao, Q., Xue, H., ... & Wang, Q. (2011). GeSn pin photodetector for all telecommunication bands detection. Optics express, 19(7), 6400-6405.

[13] Caillaud, C., Chanclou, P., Blache, F., Angelini, P., Duval, B., Charbonnier, P., ... & Achouche, M. (2015). Integrated SOA-PIN detector for high-speed short reach applications. Journal of Lightwave Technology, 33(8), 1596-1601.

[14] Hunsperger, R. G. (1991). Applications of Integrated Optics and Current Trends. In Integrated Optics: Theory and Technology (pp. 300-321). Springer Berlin Heidelberg.

[15] Yu, J., Jia, Z., Yi, L., Su, Y., Chang, G. K., & Wang, T. (2006). Optical millimeter-wave generation or up-conversion using external modulators. IEEE Photonics Technology Letters, 18(1), 265-267.

[16] Wang, Q., & Yao, J. (2006). UWB doublet generation using nonlinearly-biased electro-optic intensity modulator. Electronics Letters, 42(22), 1304-1305.

[17] Li, J., Xu, K., Fu, S., Wu, J., Lin, J., Tang, M., & Shum, P. (2007). Ultra-wideband pulse generation with flexible pulse shape and polarity control using a Sagnac-interferometer-based intensity modulator. Optics express, 15(26), 18156-18161.

[18] Capmany, J., & Novak, D. (2007). Microwave photonics combines two worlds. Nature photonics, 1(6), 319-330.

[19] Wang, Q., & Yao, J. (2007). An electrically switchable optical ultrawideband pulse generator. Journal of Lightwave Technology, 25(11), 3626-3633.

[20] Zhou, E., Xu, X., Lui, K. S., & Wong, K. K. Y. (2010). A power-efficient ultra-wideband pulse generator based on multiple PM-IM conversions. IEEE Photonics Technology Letters, 22(14), 1063-1065.

[21] Yu, X., Gibbon, T. B., & Monroy, I. T. (2009). Experimental demonstration of all-optical 781.25-Mb/s binary phase-coded UWB signal generation and transmission. IEEE Photonics Technology Letters, 21(17), 1235-1237.

[22] Chi, H., Zou, X., & Yao, J. (2009). Analytical models for phase-modulation-based microwave photonic systems with phase modulation to intensity modulation conversion using a dispersive device. Journal of lightwave technology, 27(5), 511-521.

[23] Li, W., & Yao, J. (2012). A wideband frequency tunable optoelectronic oscillator incorporating a tunable microwave photonic filter based on phase-modulation to intensity-modulation conversion using a phase-shifted fiber Bragg grating. IEEE Transactions on Microwave Theory and Techniques, 60(6), 1735-1742.

[24] Capmany, J., Mora, J., Gasulla, I., Sancho, J., Lloret, J., & Sales, S. (2013). Microwave photonic signal processing. Journal of Lightwave Technology, 31(4), 571-586.

[25] Yu, Y., Dong, J., Li, X., & Zhang, X. (2011). Ultra-wideband generation based on cascaded Mach–Zehnder modulators. IEEE Photonics Technology Letters, 23(23), 1754-1756.

[26] Shams, H., Kaszubowska-Anandarajah, A., Perry, P., Anandarajah, P., & Barry, L. P. (2010). Electro-optical generation and distribution of ultrawideband signals based on the gain switching technique. Journal of Optical Communications and Networking, 2(3), 122-130.

[27] Wang, Q., & Yao, J. (2007). An electrically switchable optical ultrawideband pulse generator. Journal of Lightwave Technology, 25(11), 3626-3633.

[28] N. Dagli, "Wide-bandwidth lasers and modulators for RF photonics," IEEE Trans. Microw. Theory Techn., vol. 47, pp. 1151–1171, 1999.

[29] E. L. Wooten, K. M. Kissa, A. Yi-Yan, E. J. Murphy, D. A. Lafaw, P., F. Hallemeier, D. Maack, D. V. Attanasio, D. J. Fritz, G. J. McBrien, and D. E. Bossi, "A review of lithium niobate modulators for fiber-optic communications systems," IEEE J. Select. Topics Quantum Electron., vol. 6, pp. 69–82, 2000.

[30] Li, G. L., & Yu, P. K. L. (2003). Optical intensity modulators for digital and analog applications. Journal of Lightwave Technology, 21(9), 2010-2030.

[31] J. Yao, F. Zeng, and Q. Wang, "Photonic generation of ultra-wideband signals," J. Lightw. Technol., vol. 43, pp. 3219–3235, Nov. 2007.

[32] J. Yao, "Photonics for ultrawideband communications," IEEE Microw. Mag., vol. 10, pp. 82–95, June 2009.

[33] Yao, J. (2009). Photonics for ultrawideband communications. IEEE Microwave Magazine, 10(4).

[34] Chen, X., & Kiaei, S. (2002). Monocycle shapes for ultra wideband system. In Circuits and Systems, 2002. ISCAS 2002. IEEE International Symposium on (Vol. 1, pp. I-I). IEEE.

[35] Zeng, F., & Yao, J. (2006). Ultrawideband impulse radio signal generation using a high-speed electrooptic phase modulator and a fiber-Bragg-grating-based frequency discriminator. IEEE photonics technology letters, 18(19), 2062-2064.

[36] Dong, J., Zhang, X., Xu, J., Huang, D., Fu, S., & Shum, P. (2007). Ultrawideband monocycle generation using cross-phase modulation in a semiconductor optical amplifier. Optics Letters, 32(10), 1223-1225.

[37] Bolea, M., Mora, J., Ortega, B., & Capmany, J. (2009). Optical UWB pulse generator using an N tap microwave photonic filter and phase inversion adaptable to different pulse modulation formats. Optics express, 17(7), 5023-5032.

[38] Zeng, F., & Yao, J. (2006). Ultrawideband impulse radio signal generation using a high-speed electrooptic phase modulator and a fiber-Bragg-grating-based frequency discriminator. IEEE photonics technology letters, 18(19), 2062-2064.

[39] Wang, Q., Zeng, F., Blais, S., & Yao, J. (2006). Optical ultrawideband monocycle pulse generation based on cross-gain modulation in a semiconductor optical amplifier. Optics letters, 31(21), 3083-3085.

[40] Abtahi, M., Magné, J., Mirshafiei, M., Rusch, L. A., & LaRochelle, S. (2008). Generation of power-efficient FCC-compliant UWB waveforms using FBGs: Analysis and experiment. Journal of Lightwave Technology, 26(5), 628-635.

[41] Khan, M. H., Shen, H., Xuan, Y., Zhao, L., Xiao, S., Leaird, D. E., ... & Qi, M. (2010). Ultrabroad-bandwidth arbitrary radiofrequency waveform generation with a silicon photonic chip-based spectral shaper. Nature Photonics, 4(2), 117-122.

[42] Zeng, F., & Yao, J. (2006). An approach to ultrawideband pulse generation and distribution over optical fiber. IEEE Photonics Technology Letters, 18(7), 823-825.

[43] Wang, C., Zeng, F., & Yao, J. (2007). All-fiber ultrawideband pulse generation based on spectral shaping and dispersion-induced frequency-to-time conversion. IEEE Photonics Technology Letters, 19(3), 137-139.

[44] Yao, J., Zeng, F., & Wang, Q. (2007). Photonic generation of ultrawideband signals. Journal of Lightwave Technology, 25(11), 3219-3235.

[45] Soltanian, M. R. K., Amiri, I. S., Alavi, S. E., & Ahmad, H. (2015). All optical ultrawideband signal generation and transmission using mode-locked laser incorporated with add-drop microring resonator. Laser Physics Letters, 12(6), 065105.

[46] Li, W., Wang, W. T., Sun, W. H., Wang, L. X., & Zhu, N. H. (2014). Photonic generation of background-free millimeter-wave ultra-wideband pulses based on a single dual-drive Mach–Zehnder modulator. Optics letters, 39(5), 1201-1203.

[47] J. Chou, Y. Han, and B. Jalali. Adaptive RF-photonic arbitrary waveform generator. IEEE Photonics Technology Letters, 15(4):581–583, 2003.

[48] Wiberg, A., Perez-Millan, P., Andres, M. V., Andrekson, P. A., & Hedekvist, P. O. (2005). Fiber-optic 40-GHz mm-wave link with 2.5-Gb/s data transmission. IEEE Photonics Technology Letters, 17(9), 1938-1940.

[49] Zhang, F., & Pan, S. (2013). Background-free millimeter-wave ultra-wideband signal generation based on a dual-parallel Mach-Zehnder modulator. Optics express, 21(22), 27017-27022.

[50] Yu, Y., Dong, J., Li, X., & Zhang, X. (2012). UWB monocycle generation and bi-phase modulation based on Mach–Zehnder modulator and semiconductor optical amplifier. IEEE Photonics Journal, 4(2), 327-339.

[51] Yan, J., Xia, Z., Zhang, S., Bai, M., & Zheng, Z. (2015). A flexible waveforms generator based on a single dual-parallel Mach–Zehnder modulator. Optics Communications, 334, 31-34.

[52] You, H., Pei, L., Ning, T., Li, J., Gao, S., Wen, X., & Chen, H. (2013). A photonic ultra-wideband pulse generator by employing two paralleled Mach–Zehnder modulators. Optik-International Journal for Light and Electron Optics, 124(22), 5829-5832.

[53] Cao, P., Hu, X., Wu, J., Zhang, L., Jiang, X., & Su, Y. (2014). Photonic generation of 3-D UWB signal using a dual-drive Mach-Zehnder modulator. IEEE Photonics Technology Letters, 26(14), 1434-1437.

[54] Dong, J., Zhang, X., Xu, J., & Huang, D. (2008). Filter-free ultrawideband generation based on semiconductor optical amplifier nonlinearities. Optics communications, 281(4), 808-813.

[55] Moreno, V., Rius, M., Mora, J., Muriel, M. A., & Capmany, J. (2013). Integrable high order UWB pulse photonic generator based on cross phase modulation in a SOA-MZI. Optics express, 21(19), 22911-22917.

[56] Moreno, V., Rius, M., Mora, J., Muriel, M. A., & Capmany, J. (2014). UWB monocycle generator based on the non-linear effects of an SOA-integrated structure. IEEE Photonics Technology Letters, 26(7), 690-693.

[57] Yu, X., Gibbon, T. B., Pawlik, M., Blaaberg, S., & Monroy, I. T. (2009). A photonic ultra-wideband pulse generator based on relaxation oscillations of a semiconductor laser. Optics express, 17(12), 9680-9687.

[58] Yu, X., Gibbon, T. B., Rodes, R., Pham, T. T., & Monroy, I. T. (2013). System wide implementation of photonically generated impulse radio ultra-wideband for gigabit fiber-wireless access. Journal of lightwave technology, 31(2), 264-275.

[59] Mirshafiei, M., Ghazisaeidi, A., Lemus, D., LaRochelle, S., & Rusch, L. A. (2012). Upconversion of gain-switched laser pulses for optical generation of UWB signals. Journal of Lightwave Technology, 30(2), 207-214.

[60] Abtahi, M., Mirshafiei, M., LaRochelle, S., & Rusch, L. A. (2008). All-optical 500-Mb/s UWB transceiver: An experimental demonstration. Journal of Lightwave Technology, 26(15), 2795-2802.

[61] Wang, C., Zeng, F., & Yao, J. (2007). All-fiber ultrawideband pulse generation based on spectral shaping and dispersion-induced frequency-to-time conversion. IEEE Photonics Technology Letters, 19(3), 137-139.

[62] Abtahi, M., Mirshafiei, M., Magné, J., Rusch, L. A., & LaRochelle, S. (2008). Ultrawideband waveform generator based on optical pulse-shaping and FBG tuning. IEEE Photonics Technology Letters, 20(2), 135-137.

[63] Feng, H., Fok, M. P., Xiao, S., Ge, J., Zhou, Q., Locke, M., ... & Hu, W. (2014). A reconfigurable high-order UWB signal generation scheme using RSOA-MZI structure. IEEE Photonics Journal, 6(2), 1-7.

[64] Chen, G., & Pan, S. (2013, January). A UWB over fiber system based on frequency-dependent gain saturation in a RSOA. In Radio and Wireless Symposium (RWS), 2013 IEEE (pp. 133-135). IEEE.

[65] Feng, H., Xiao, S., Yi, L., & Hu, W. (2014). Photonic generation of reconfigurable orders ultrawideband signals by using cascaded RSOAs. IEEE Photonics Technology Letters, 26(9), 908-910.

[66] Chen, G., & Pan, S. (2012). Photonic generation of ultrawideband signals based on frequency-dependent gain saturation in a reflective semiconductor optical amplifier. Optics letters, 37(20), 4251-4253.

[67] Yang, C., Xia, L., Fu, S., & Liu, D. (2014). A UWB pulse generation based on a phase modulator and programmable filter. Optics Communications, 318, 166-170.

[68] Li, W., Wang, L. X., Hofmann, W., Zhu, N. H., & Bimberg, D. (2012). Generation of ultra-wideband triplet pulses based on four-wave mixing and phase-to-intensity modulation conversion. Optics express, 20(18), 20222-20227.

[69] Li, P., Chen, H., Chen, M., & Xie, S. (2012). Gigabit/s photonic generation, modulation, and transmission for a reconfigurable impulse radio UWB over fiber system. IEEE photonics journal, 4(3), 805-816.

[70] Chang, Y. M., Lee, J., Koh, D., Chung, H., & Lee, J. H. (2010). Ultrawideband doublet pulse generation based on a semiconductor electroabsorption modulator and its distribution over a fiber/wireless link. Journal of Optical Communications and Networking, 2(8), 600-608.

[71] Cui, W., Shao, T., & Yao, J. (2013). Wavelength reuse in a UWB over fiber system based on phase-modulation to intensity-modulation conversion and destructive interferencing. Journal of Lightwave Technology, 31(17), 2904-2912.

[72] Gibbon, T. B., Yu, X., Gamatham, R., Gonzalez, N. G., Rodes, R., Jensen, J. B., ... & Monroy, I. T. (2010). 3.125 Gb/s impulse radio ultra-wideband photonic generation and distribution over a 50 km fiber with wireless transmission. IEEE Microwave and Wireless Components Letters, 20(2), 127-129.

[73] Zheng, J. Y., Zhang, M. J., Wang, A. B., & Wang, Y. C. (2010). Photonic generation of ultrawideband pulse using semiconductor laser with optical feedback. Optics letters, 35(11), 1734-1736.

[74] Zadok, A., Wu, X., Sendowski, J., Yariv, A., & Willner, A. E. (2010). Photonic generation of ultra-wideband signals via pulse compression in a highly nonlinear fiber. IEEE Photonics Technology Letters, 22(4), 239-241.

[75] Pan, S., & Yao, J. (2009). Switchable UWB pulse generation using a phase modulator and a reconfigurable asymmetric Mach-Zehnder interferometer. Optics letters, 34(2), 160-162.

[76] Peucheret, C., & Fotonik, D. T. U. (2012). Generation and detection of optical modulation formats. Dept. of Photonics Engg, Technical University of Denmark.

[77] M.J. Connelly, Semiconductor Optical Amplifiers, Kluwer, Boston, MA, 2002.

[78] Mukai, T., Yamamoto, Y., & Kimura, T. (1982). S/N and error rate performance in AlGaAs semiconductor laser preamplifier and linear repeater systems. IEEE Transactions on Microwave Theory and Techniques, 30(10), 1548-1556.

[79] Simon, J. (1987). GaInAsP semiconductor laser amplifiers for single-mode fiber communications. Journal of lightwave technology, 5(9), 1286-1295.

[80] Wei, J. L., Hamié, A., Giddings, R. P., & Tang, J. M. (2009). Semiconductor optical amplifier-enabled intensity modulation of adaptively modulated optical OFDM signals in SMF-based IMDD systems. Journal of Lightwave Technology, 27(16), 3678-3688.

[81] Hamié, A., Hamzé, M., Taki, H., Makouk, L., Sharaiha, A., Alaeddine, A., ... & Tang, J. M. (2014). Two cascaded SOAs used as intensity modulators for adaptively modulated optical OFDM signals in optical access networks. Optics express, 22(13), 15763-15777.

[82] R. B. Picard, M. Alouini, J. Lopez, N. Vodjdani, and J-C. Simon, "Impact of the Gain Saturation Dynamics in Semiconductor Optical Amplifiers on the Characteristics of an Analog Optical Link," IEEE J. Lightw. Technol., vol. 23, no. 8, pp. 2420-2426, 2005.

[83] Spiekman, L. H., Wiesenfeld, J. M., Gnauck, A. H., Garrett, L. D., Van Den Hoven, G. N., Van Dongen, T., ... & Binsma, J. J. M. (2000). Transmission of 8 DWDM channels at 20 Gb/s over 160 km of standard fiber using a cascade of semiconductor optical amplifiers. IEEE Photonics Technology Letters, 12(6), 717-719.

[84] H. Khaleghi, P. Morel, A. Sharaiha, T. Rampone, Experimental validation of numerical simulations and performance analysis of a coherent optical-OFDM transmission system employing a semiconductor optical amplifier, J. Lightwave Technol. 31 (1) (2013) 161–170.

[85] P. Morel, "Modélisation des amplificateurs optiques à sémi-conducteurs : du composant au système," Mémoire de thèse, Laboratoire RESO ENIB/Brest,ED-SICMA, 2006.

[86] P. Morel and A. Sharaiha, "Wideband Time-Domain Transfer Matrix Model Equivalent Circuit for Short Pulse Propagation in Semiconductor Optical Amplifiers," Quantum Electronics, IEEE Journal of, vol. 45, no. 2, pp. 103-116, Feb 2009.

[87] D.R. Zimmerman, L.H. Spiekman, Amplifiers for the masses: EDFA, EDWA, and SOA amplets for metro and access networks, J. Lightwave Technol. 22 (1) (2004) 63–70.

Chapter 3

Pre-distortion Schemes for Mitigating Nonlinear Effects in SOA-Based IR-UWB over Fiber Systems

Achieving a reach extension requires operating in the SOA saturated regime, that translates into strong nonlinearities and spectral distortions, which drops the power efficiency of propagated pulses. In this chapter, after studying the SOA response versus operating conditions, we will enhance the system performance by applying simple analog pre-distortion schemes for various derivatives of the Gaussian pulse and their combination. A novel pulse shape will be also designed by linearly combining three basic Gaussian pulses, offering a very good spectral efficiency (>55%) for a high power (0 dBm) at the amplifier input. Furthermore, the potential of our technique will be examined considering a 1.5 Gbps-OOK and 0.75 Gbps-PPM modulation schemes. Pre-distortion will prove an advantage for a large extension of the optical link (150 Km), with a SOA-based amplification at 40 Km.

3.1 Introduction

As stated in the second chapter, in-line amplification is a key function for achieving a reach extension of any optical communication network. The low cost Semiconductor Optical Amplifiers [1] are good candidates in the context of Impulse Radio over fiber transmissions, the essence of IR being the simplicity with the objective of a wide use. Unfortunately, the nonlinear effects inherent to amplification may cause strong distortions in the propagating signals and a degradation in the power efficiency. The target is to get a reach extension without downgrading the wireless coverage area, which depends on the transmitted signal characteristics at antenna output, with the constraint to respect the regulation associated to UWB free space propagation. Therefore, a highly efficient transmission is required which means that the pulse shapes must be preserved along the transmission in order to collect the maximum possible power under the FCC spectral mask. Hence, overcoming SOA nonlinear distortions becomes a key objective. In the literature, numerous linearization techniques dealing with over fiber transmission have been investigated [2–4]. Here, we examine the potential of analog pre-distortion by tuning some key parameters of generated pulses, so as to get highly efficient pulse shapes at the receiver side. The best parameters of pre-distorted input pulses are extracted via global optimization based on the interior point algorithm [5]. The resultant waveforms are studied considering modulated IR signals; it is shown that a significant enhancement in

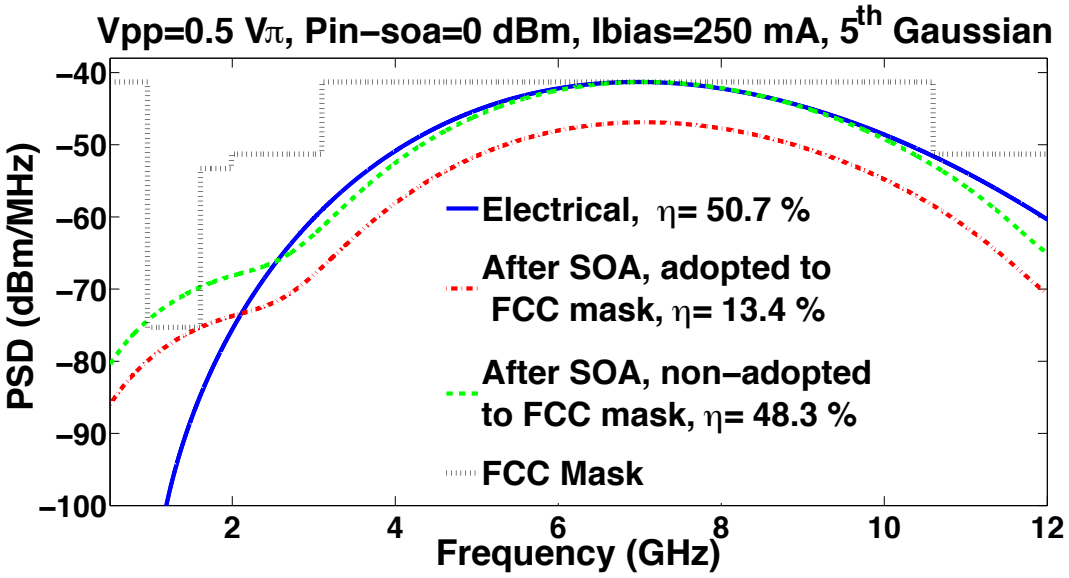

Figure 3.1: Power Spectral Density of 5^{th} Gaussian in electrical domain and at SOA output (adopted and non-adopted to FCC mask).

the efficiency can be achieved for a large optical link extension, while operating at limited cost and complexity.

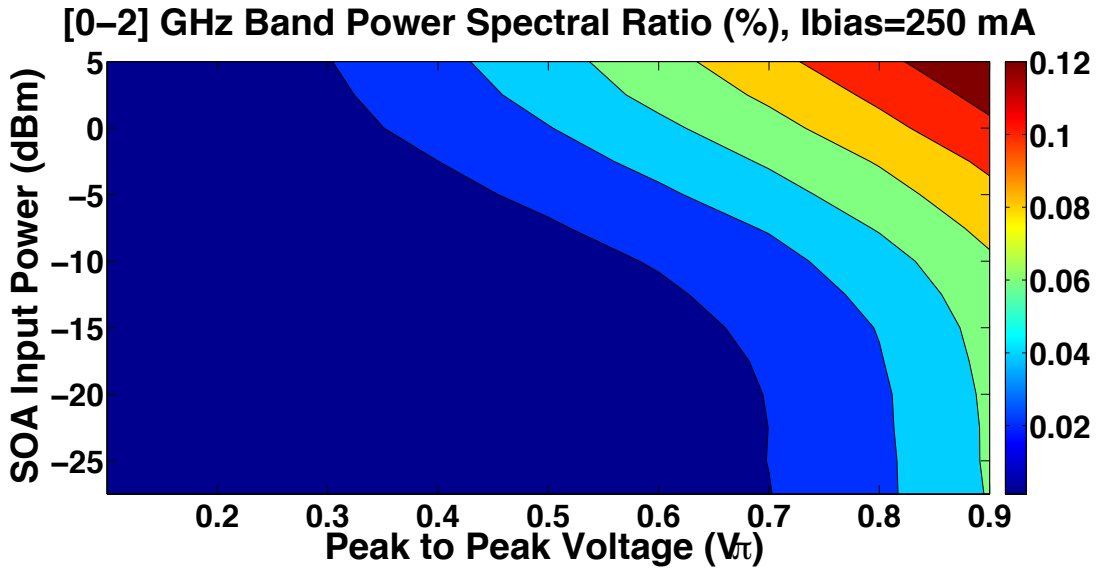

Figure 3.2: PSR_{2GHz} of 5^{th} Gaussian versus SOA input power and peak-to-peak voltage, where no fiber is considered.

3.2 Impact of SOA on propagated pulses

In our SOA-based over-fiber system, increasing the transmission distance requires operating in the saturated region of the SOA, which yields various nonlinear impairments affecting the transmitted signal. On the non-coherent receiver side, the resulting distortion will be characterized in terms of power efficiency with respect to the FCC mask

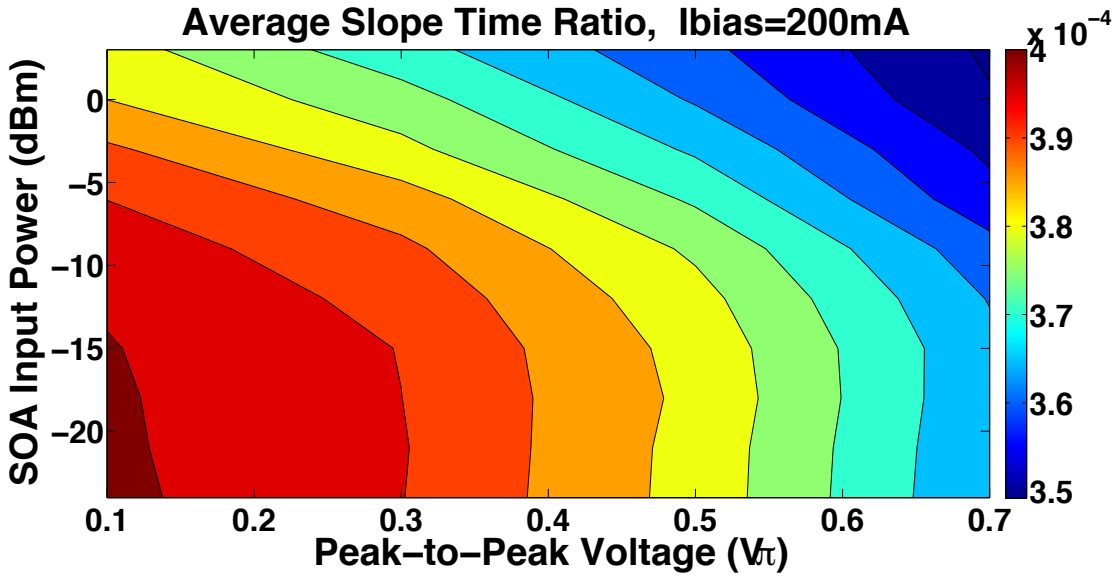

Figure 3.3: Average Slope Time Ratio of 5^{th} Gaussian versus SOA input power and peak-to-peak voltage, where no fiber is considered.

defined in the first chapter, which is computed after photo-detector while antenna effects are ignored. To have a look at SOA impact, fig. 3.1 shows the spectral response of the 5-th order derivative Gaussian pulse in electrical domain (solid-blue) and after being passed through SOA (dashed-green), without propagation in fiber. The PSD of the optical pulse violates FCC mask in the most restricted region corresponding to GPS band $[0.96 - 1.61]$ GHz, where the low power level (-75.3 dBm/MHz) is greatly challenging. So the average signal power has to be reduced so as to meet this limit, leading to a significant impact on the power efficiency (degradation $> 30\%$). Hence, spectrum enhancement requires eliminating the low frequency components induced by SOA. A simple criterion for evaluating this impact is the 2 GHz Power Spectral Ratio (PSR_{2GHz}), which corresponds to the ratio between the power collected in the [0,2] GHz band with respect to the overall PSD:

$$PSR_{2GHz} = \frac{\int_0^{2GHz} S_p(f)df}{\int_0^{\infty} S_p(f)df} \times 100\% \tag{3.1}$$

This criterion is analyzed in fig. 3.2 for the case of the 5^{th} derivative Gaussian pulse, with different peak-to-peak voltage and laser power, where $I_{bias} = 250$ mA. A quick rise of the PSR can be clearly observed, especially for $V_{pp} > 0.5\ V_{\pi}$ where strong nonlinearities act on the propagated pulse. From the time domain point of view, we define a criterion for studying the smoothness of SOA output pulses, the Average Slope Time Ratio (ASTR) expressed in eq. (3.2), where $p_n(t)$ corresponds to the normalized form of $p(t)$ ($\max\{p_n(t)\}=1$) and T is the pulse duration. The time derivative measures the slope, which is also weighted by the instantaneous power, and averaging gives an indication about the smoothness (or sharpness) of the output waveform. The result in fig. 3.3 justifies that in fig. 3.2, what could be concluded is that not all the dynamics of an optical pulse are conserved when passing by SOA, high frequency components are reduced and a less degree of sharpness is obtained. In the following, we investigate the benefits of electrical

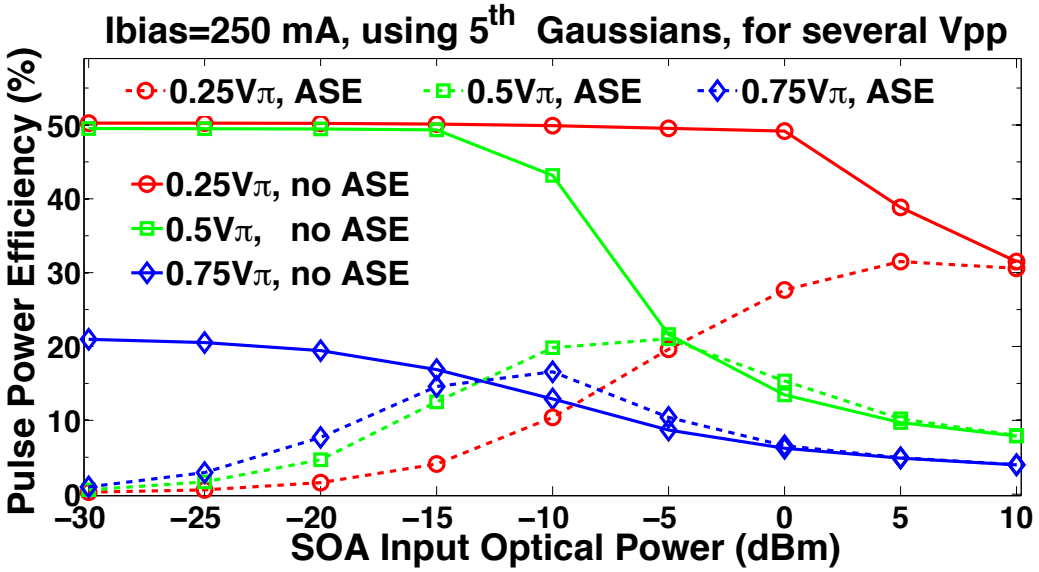

Figure 3.4: Power Efficiency of 5^{th} Gaussian versus SOA input power for several peak-to-peak voltages, where no fiber is considered.

pulse pre-compensation with the view to avoid any power efficiency degradation.

$$ASTR_{p(t)} = \frac{\int_{-T/2}^{T/2} \left| \frac{d\, p_n(t)}{dt} \times p_n^2(t) \right| dt}{T \times \int_{-T/2}^{T/2} p_n^2(t)\, dt} \tag{3.2}$$

The power efficiency of the 5^{th} order Gaussian pulse is plotted in fig. 3.4 versus SOA input power, for $I_{bias} = 250$ mA. When the Amplified Spontaneous Emission (ASE) noise is ignored, a degradation in the power efficiency is observed as we move towards higher input powers. The bad impact of SOA particularly occurs at large V_{pp} (e.g. $V_{pp} = 0.75V\pi$), where the drop in the efficiency results from the large spectral distortion. On the opposite, for $V_{pp} = 0.25V\pi$, a semi-linear gain behavior is ensured, leading to a very good spectral efficiency (approximately 50%) over a broad range of input power, reaching the saturation region (0 dBm). In the noisy case, the power efficiency is evaluated via Monte-Carlo simulations with the computation of the average overs 100 runs; as can be clearly seen, the pseudo-linear gain characteristics is no longer preserved due to the larger noise influence at lower input power. Thus, there is a compromise between linearity and optical signal to noise ratio (OSNR), which depends upon the peak-to-peak voltage. As can be seen, the ASE impact on pulse dynamics tends to be reduced for large V_{pp}; it is a positive aspect but at the cost of increased sensitivity to nonlinearities. For $V_{pp} = 0.25V\pi$, the rise in efficiency is due to the increasing OSNR, combined with limited nonlinear effects. Prior to strong saturation, a slight increase in the efficiency ($< 5\%$) is noticed for the noisy signals over normal ones, for any V_{pp}, that is due to the power added by ASE noise within the UWB mask. We can systematically verify the convergence between solid and dashed lines at very high input power, resulting from a negligible noise power. For the remaining part of this chapter, we will assume a medium value $V_{pp} = 0.5V\pi$, which is interesting in the sense that it both represents the noisy and nonlinear characteristics typically associated with SOA.

3.3 SOA Nonlinearities Mitigation via Electrical Pulses Pre-distortion

To overcome the nonlinear effects, electrical or optical linearization techniques could be applied [2–4] [6–15]. Optical schemes can operate over a wide bandwidth and some techniques are even specifically designed for SOA [16,17], but due to either high cost or bandwidth limitations associated to radio frequency control circuits, these schemes are not considered in our study. Digital electrical domain linearization methods (pre-distortion, post-distortion) are interesting for their flexibility but we see the bandwidth/sampling requirements as a drawback for a low cost IR-UWB system; so, we preferred to go towards the alternative of analog pre-distortion, consisting in designing circuits at the transmitter or/and receiver sides so as to suppress the nonlinear distortion components resulting from SOA amplification. Two approaches have been investigated in this direction, the first is based on optimizing the parameters of generated waveforms so as to maximize the power efficiency at SOA output, as will be explained in the following sections. Where the second relies on adding up and down phasers acting as pre and post distorters, as will be discussed in the next chapter.

Regarding the pulse design, the Complementary Metal–Oxide–Semiconductor (CMOS) makes a good candidate technology, as it is a simple low cost approach and capable to generate ultra short time pulses. CMOS devices consist of p-type and n-type metal oxide semiconductor field effect transistors, and associated with a high noise immunity and low static power consumption [18–21]. As reported in various studies, tunable UWB Gaussian pulse generators can be designed via CMOS technology [22–24]. So, we made the assumption of a tunable Gaussian pulse generator, such as the generated pulse $x(t, \mathbf{p})$ can be shaped with arbitrary parameters $\mathbf{p}$: shaping factor for the case of a single Gaussian pulse, or pulse shaping factors, weighting coefficients, besides to the delay for a linear combination of Gaussian pulses. Then our aim is to identify the best tuning parameters $\mathbf{p^*}$ in the sense of a maximized power efficiency at the SOA output. The amplifier transfer function is relatively complicated, as it is a combination of several nonlinear effects, thus preventing the derivation of the pre-distorted pulses in electrical domain [1]. Therefore, adopting global optimization schemes is a pertinent approach, while dealing with the SOA as a black box, and with the aim to maximize the output power efficiency regardless inherent characteristics. Our work is partially similar to that of Mirshafiei *et al.* [25], who addressed the pre-compensation against antenna effects, based on combinations of Gaussian pulses generated in the optical domain. Considering the sky cross antenna, circular monopole, besides to the monopole with two steps antenna, he has experimentally succeeded in optimizing the performance of Gaussian Monocycle, Gaussian 5-th order derivative, in addition to a novel FCC-compliant pulse. He adopted a high pass filter and got benefit from the bandpass nature of the UWB antenna so as to shape the spectrum of resultant pulses [25]. Our contribution is different in the sense that we mitigate SOA nonlinearities, which are very specific, and we consider that pulses are generated/pre-distorted in electrical domain. Numerous global optimization algorithms are investigated in the literature [26–34], but in our case optimizing the pulse spectrum is challenging due to the FCC mask hard constraints; on the other side, dealing with SOA effects is also tricky specially for large biasing currents. Hence, a relatively wide search interval has to be considered in optimization, so as to increase the probability of obtaining effective pulse

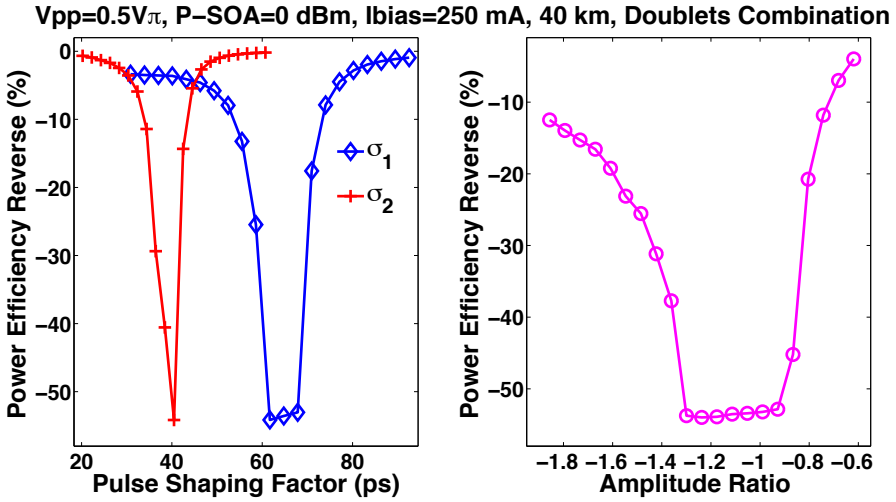

Figure 3.5: The reverse of power efficiency corresponding to Abraha's Combination obtained at SOA output, as function of the values of input parameters.

shapes. Besides, the objective function has to be taken into account while choosing the optimization scheme; in fig. 3.5 we study the power efficiency of Doublets-based Abraha's combination (that will be discussed in the sequel) at SOA output, where the input parameters are the pulse shaping factors (σ_1 and σ_2) (left) besides to the amplitude ratio between Doublets (right). The objective function is the reverse of the power efficiency, we can notice that it is convex with respect to the 3 variables, and the aim is to maximize the power efficiency (minimize its reverse). Based on that, the interior point has been chosen as the optimization scheme, since it is a nonlinear convex algorithm and associated with a large multi-dimensional search space [5] [35–41]. As illustrated in fig. 3.6 and fig. 3.7, all distinct parameters are initialized at their optimum in electrical domain, so the algorithm can start from these values to re-optimize the pulse shape obtained at the optical system output. Optimization is based on the concept that, any search path leading to a reduction in the cost function is a good direction to follow, and when no improvement appears in any direction then the current point is considered to be the optimum (for more information the algorithm is summarized in the appendix) [35]. As will be shown in the sequel, the interior point scheme is highly effective, and a significant improvement in the performance has been achieved thanks to this approach. Regarding the practical aspects, this process could be automatically implemented in a closed loop transceiver system, utilizing software-to-hardware interfaces. In our setup, SOA was placed at 40 km, the operating point corresponding to an input power P-SOA$= 0\ dBm$, which is a strong gain saturation point, while MZM is driven by $V_{pp} = 0.5V\pi$. These operating conditions are fixed for the remaining part of the chapter.

3.3.1 Case of 5-th derivative Gaussian pulse

The 5^{th} derivative Gaussian pulse is an attractive target for impulse radio system designers, due to its very good matching to FCC mask and acceptable order of generation complexity [42–46]. As expressed in eq. (3.3), the pulse shaping factor (σ) is the only variable which can be calibrated, with a simultaneous influence on the 10 dB bandwidth (B_{10}) and on the central frequency. Table 3.1 displays all the parameters of utilized pulses, besides to the power efficiencies in electrical domain and at SOA output (the spec-

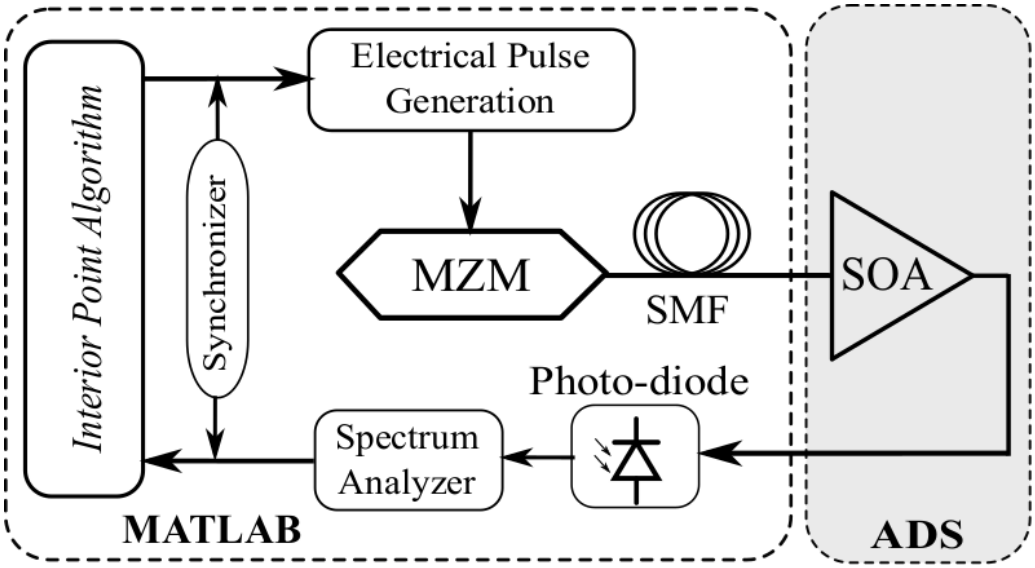

Figure 3.6: Block diagram for the optimization process used for designing pre-distorted electrical waveforms.

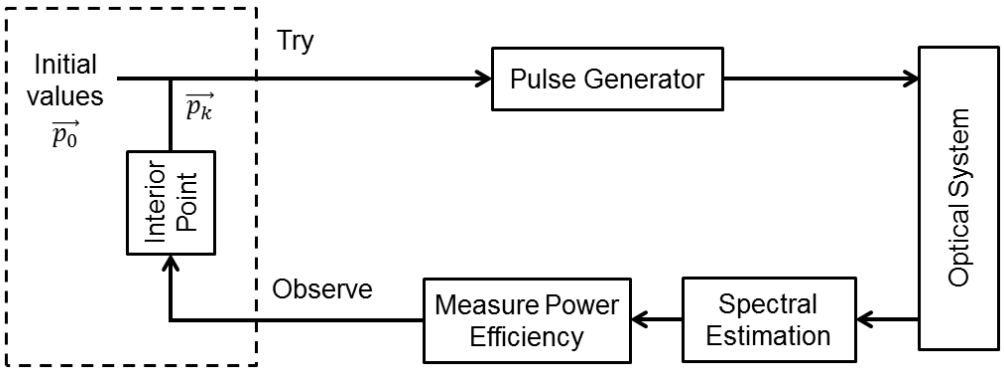

Figure 3.7: Functional diagram for the optimization process based on interior point algorithm.

tral characteristics being evaluated at this point). Figure 3.8 describes the original and pre-distorted (PD) pulses in electrical domain and at SOA output, in the case of placing the photo-detector directly after SOA, where the spectra are plotted in the noise-free case (ASE noise not considered for spectrum readability). We can clearly see in fig. 3.8 and table 3.1 that the pre-distorted pulse exhibits only a small improvement in power efficiency ($< 5\%$), due to the single degree of freedom. Therefore it is better to search for more appropriate pulse shapes to be adopted with pre-distortion.

$$x_5(t) = \frac{A}{\sqrt{2\pi}}\Big(\frac{-t^5}{\sigma^{11}} + \frac{10t^3}{\sigma^9} - \frac{15t}{\sigma^7}\Big)exp\Big(-\frac{t^2}{2\sigma^2}\Big) \tag{3.3}$$

3.3.2 Higher order of Gaussian derivative

In fact, avoiding GPS band requires shifting the spectrum towards higher frequencies. The spectral peak for any n^{th} order Gaussian pulse derivative $x_n(t)$ is $f_{peak} = \frac{\sqrt{n}}{2\pi\sigma}$, where

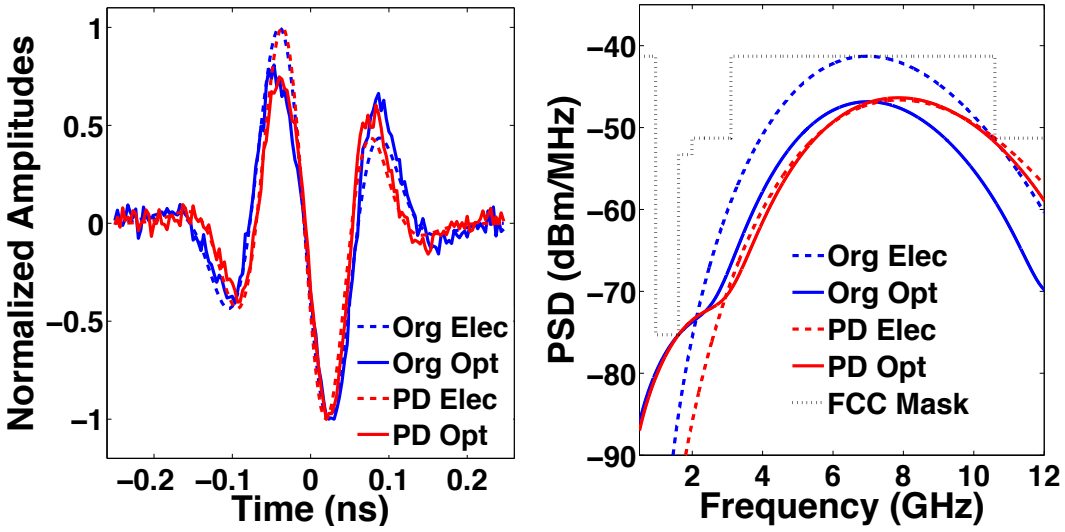

Figure 3.8: Original (Org) and pre-distorted (PD) 5^{th} Gaussian, in electrical domain (Elec) and after SOA (Opt).

Pulses	σ_1 (ps)	σ_2 (ps)	σ_3 (ps)	a_2/a_1	a_3/a_1	η(%) Elec	f_{peak} (GHz)	B_{10} (GHz)	BL_{34} (GHz)	η(%) SOA
Org 5^{th} Gaussian	51	x	x	x	x	50.7	7	6.17	6.11	13.7
Pre-distorted 5^{th} Gaussian	45.07	x	x	x	x	15.74	7.86	6.95	6.88	17.2
Org 6^{th} Gaussian	53.83	x	x	x	x	47.94	7.23	6.13	6.41	17
Pre-distorted 6^{th} Gaussian	72.45	x	x	x	x	37.28	5.5	4.85	3.92	38
Org x_{C_D}	43.02	43.02	x	-1	x	57.2	6.45	6.84	6.05	6.96
Pre-distorted x_{C_D}	61.68	40.47	x	-1.24	x	1.6	6.2	7.34	4.56	54.1
Org x_{C_G}	34.27	83.96	49.98	0.12	-0.89	56.47	6.13	6.74	3.81	7.1
Pre-distorted x_{C_G}	80.71	60.71	28.03	2.81	-3.3	1.53	6.1	7.45	4.35	56.1

Table 3.1: Parameters (σ_1, σ_2, σ_3, a_2/a_1, a_3/a_1) of electrical generated pulses, and the spectral characteristics (f_{peak}, B_{10}, BL_{34}) of corresponding waveforms at SOA output (placed at 40 km). Besides to the power efficiencies (%) in electrical domain and after SOA, with P-SOA= 0 dBm, $I_{bias} = 250\ mA$, and $V_{pp} = 0.5\ V_\pi$.

the spectrum is expressed as [47]

$$X_n(f) = A\Big(j2\pi f\Big)^n exp\Big(-\frac{(2\pi f\sigma)^2}{2}\Big) \tag{3.4}$$

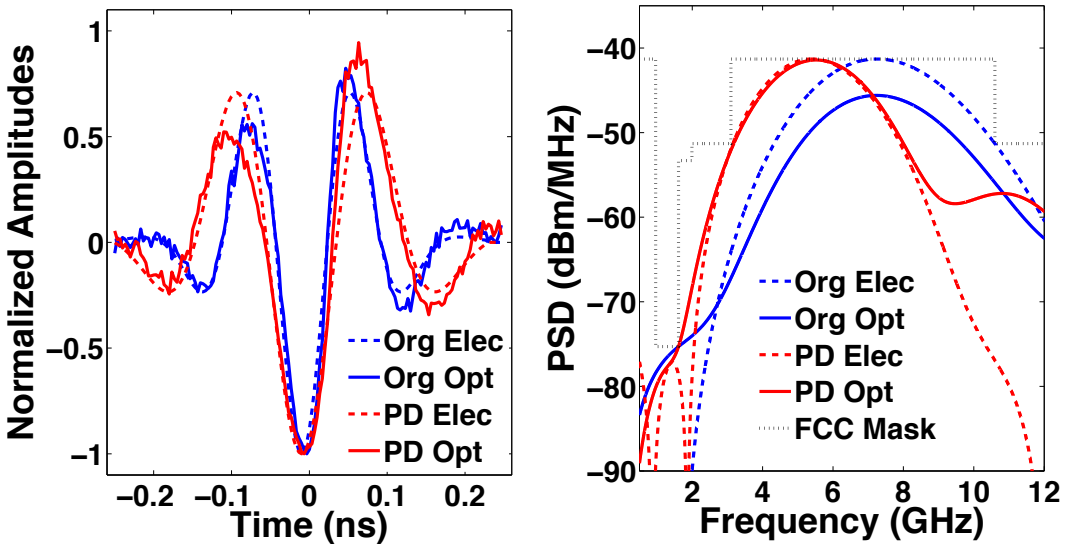

Figure 3.9: Original (Org) and pre-distorted (PD) 6^{th} Gaussian, in electrical domain (Elec) and after SOA (Opt).

To step up the power spectral density under FCC mask, we have to reduce B_{10} by utilizing higher values of σ, as shown by (3.4). Increasing σ can be compensated by augmenting n, hence making a separate control for B_{10} and f_{peak}. Adopting a higher order of derivation gains more flexibility in shaping the spectrum, as being far from the most severely power-restricted band (corresponding to GPS), and consequently it becomes much easier to design a pre-distorted waveform. The benefit of the 6-th derivative Gaussian appears in fig. 3.9, where the time domain formula is expressed in (3.5). By lowering the 10 dB bandwidth of the pre-distorted pulse spectrum, we have enabled an increase in the efficiency ($> 20\%$) without violating the regular limit, as also shown in table 3.1. With this scenario, the pre-distortion block could be implemented as a simple differentiator, which can enhance the performance at limited complexity.

$$x_6(t) = \frac{A}{\sqrt{2\pi}}\Big(-\frac{15}{\sigma^7} + \frac{45t^2}{\sigma^9} - \frac{15t^4}{\sigma^{11}} + \frac{t^6}{\sigma^{13}}\Big)exp\Big(-\frac{t^2}{2\sigma^2}\Big) \tag{3.5}$$

3.3.3 Abraha's Combination of Gaussian Doublets

A notable enhancement in the power efficiency has been achieved with single pulse pre-distortion, but the improvement is inherently limited by the small degree of freedom. Hence, a more effective approach is to apply a combination of waveforms, so as to get a superior control of the resultant pulse dynamics, as will be presented later. Several combinations have been proposed in the literature [48–50], but taking into account practical constraints, it is better to conserve simple combinations within the Gaussian family. We considered the recent work of Abraha *et al.*, who developed a FCC-compliant pulse based on a linear combination of Gaussian doublets [51]. The two basic Doublets $x_{21}(t), x_{22}(t)$ have different weighting coefficients and shaping factors:

$$C_D(t) = a_1 x_{21}(t) + a_2 x_{22}(t-\tau) \tag{3.6}$$

$$x_{2i}(t) = \frac{A}{\sqrt{2\pi\sigma_i^3}}\Big(k\frac{t^2}{\sigma_i^2} - 1\Big)exp\Big(-\frac{t^2}{2\sigma_i^2}\Big) \tag{3.7}$$

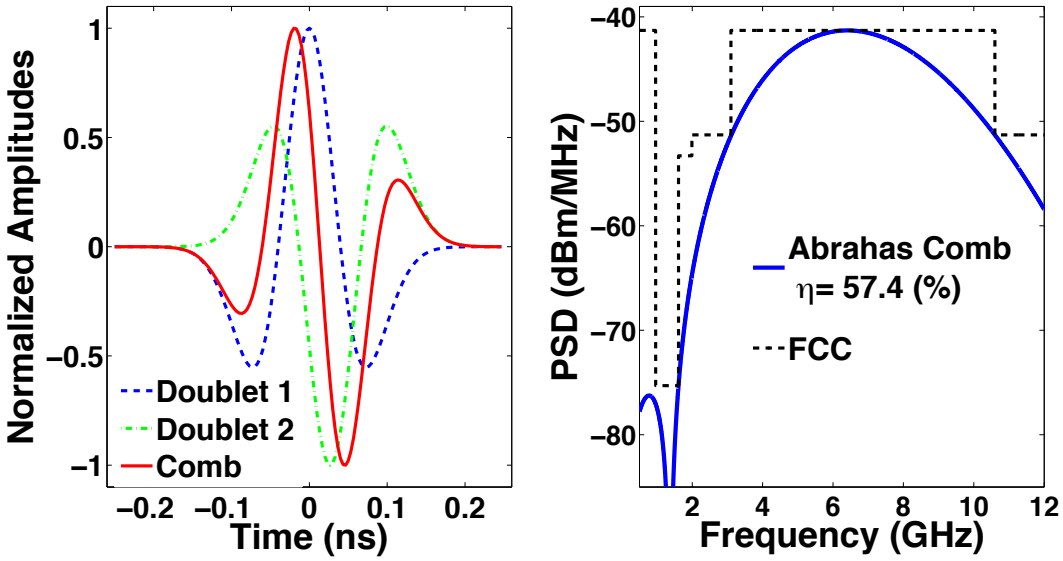

Figure 3.10: Abrahas proposed pulse based on a combination of Gaussian Doublets.

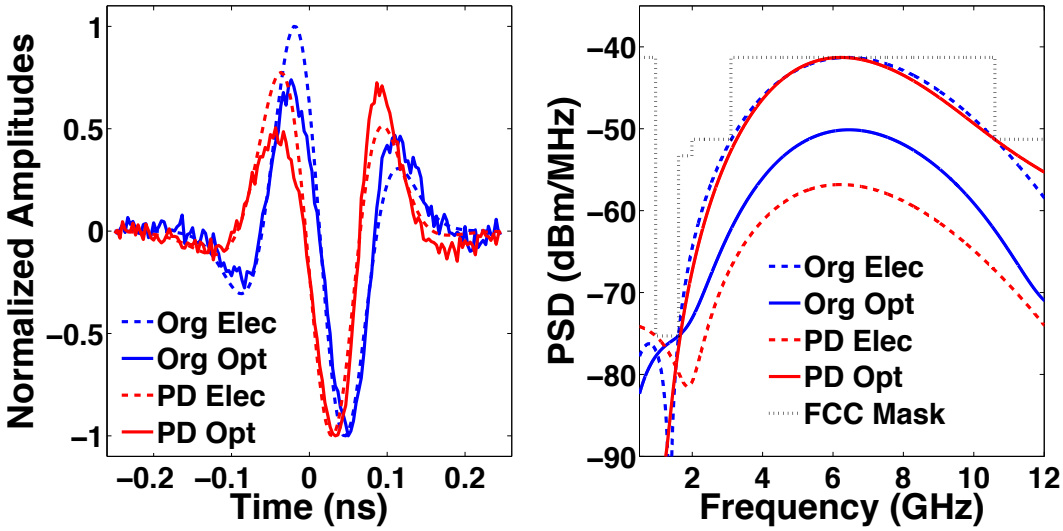

Figure 3.11: Original (Org) and pre-distorted (PD) C_{Doub}, in electrical domain (Elec) and after SOA (Opt).

where a_1 and a_2 are the weighting factors, τ is a time delay between pulses, fixed at τ=25 ps, and $k = 1.16$ is an arbitrary scaling of the modified Doublet. Figure 3.10 describes the time and frequency plots of Abraha's combination; as can be seen, the resultant spectrum highly exploits the area under FCC and a very good power efficiency is obtained. In table 3.1, BL_{34} is defined as the left -34 dB bandwidth (frequency space between f_L and f_{peak}), this criteria is useful to evaluate the spectrum in correspondence with GPS band. The term A is always set at 1, as it has no influence on dynamics for single waveforms; and in case of combinations, only the relative amplitude between elementary pulses is important, since the real intensity for signals at photo-detector output is controlled by the laser power and peak-to-peak voltage. In Abraha's work, utilized doublets are similar with opposite polarities, as a high pass filtering is performed by the spectral oscillating term resulting from time delay. We don't preserve these conditions with pre-distortion,

as the target is to mitigate SOA non-linearity by exploiting all the degrees of freedom associated to the linear combination of pulses. Therefore, different shaping factors and weighting coefficients have been considered in our work. A significant jump in the power efficiency ($> 45\%$) is illustrated in fig. 3.11 and table 3.1 for the pre-distorted combination of Doublets. The increase in the 10 dB bandwidth from 6.84 GHz to 7.34 GHz has enlarged the spectral coverage area under FCC mask, besides to the 1.5 GHz reduction in BL_{34}, which permits a step up in the PSD without exceeding GPS limit. The peak of the spectrum exactly matches FCC limit (-41.3 dBm/MHz) at $f_{peak} = 6.2\ GHz$, which is not so far from the center of the UWB mask, thanks to pre-distortion.

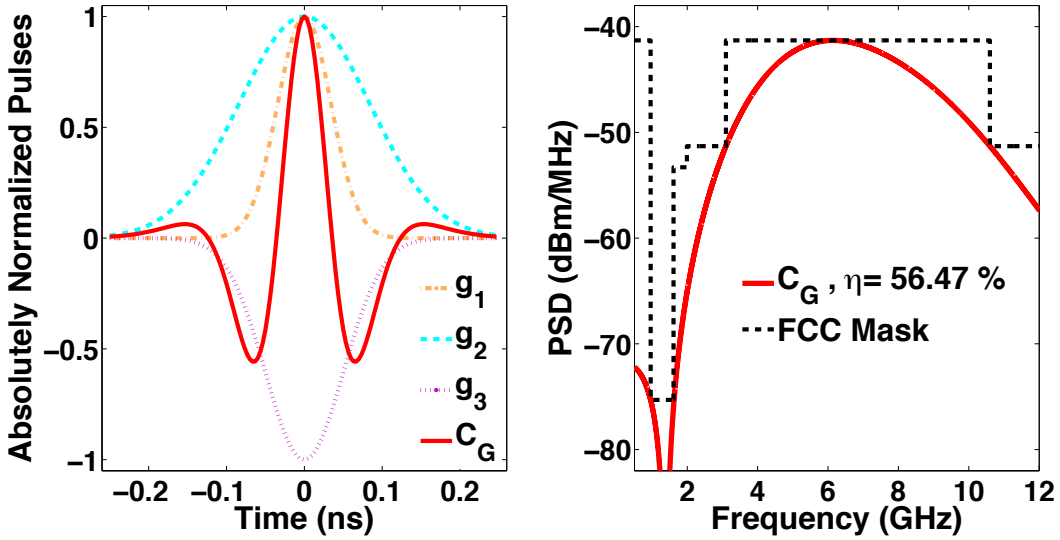

Figure 3.12: Our proposed combination C_G based on the pulses g_i, in time (left) and frequency (right) domain.

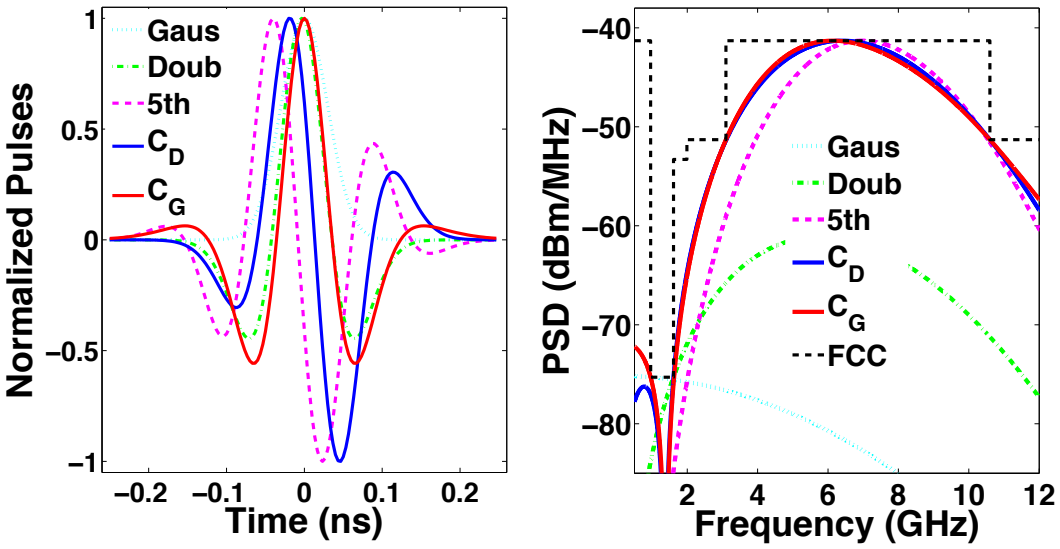

Figure 3.13: Time waveforms and corresponding spectra of fundamental Gaussian, Doublet, 5-th Gaussian, Abraha's combination, and our novel pulse based on Gaussians.

3.3.4 Introducing a new waveform based on a combination of Gaussian pulses

The performance gain obtained when increasing the number of tuning parameters has motivated us to go towards higher orders of combinations. A new pulse shape is now proposed, based on a linear combination of three fundamental Gaussian pulses:

$$C_G(t) = a_1 g_1(t) + a_2 g_2(t) + a_3 g_3(t) \tag{3.8}$$

recall

$$g_i(t) = exp\Big(-\frac{t^2}{2\sigma_i^2}\Big) \tag{3.9}$$

Such a combination enables a pre-distortion with 5 variables $(\sigma_1, \sigma_2, \sigma_3, a_2/a_1, a_3/a_1)$,

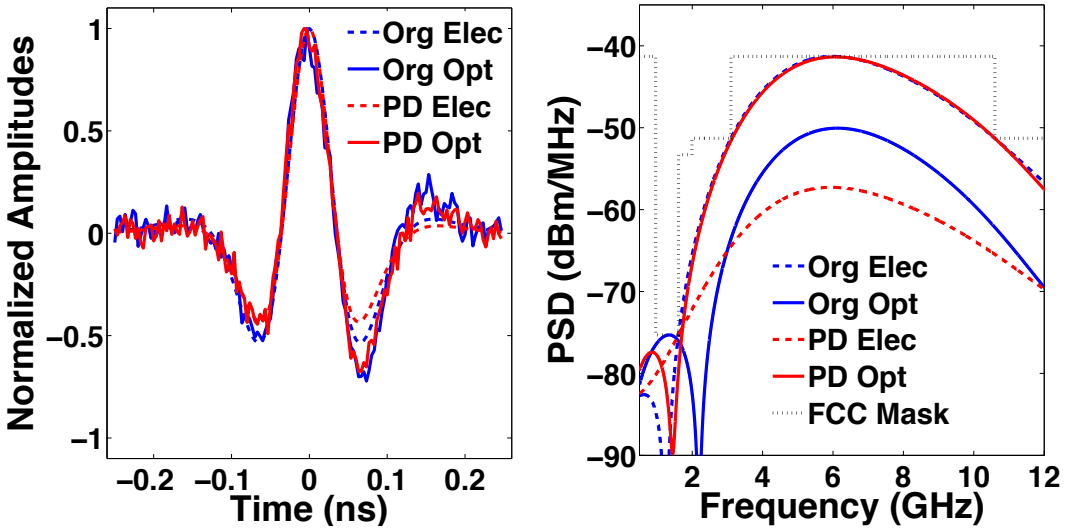

Figure 3.14: Original (Org) and pre-distorted (PD) C_G, in electrical domain (Elec) and after SOA (Opt).

which promises for a better power efficiency obtained at SOA output. The weighting coefficients have been optimized as described in table 3.1. The resultant waveform is depicted in fig. 3.12 (left); it has a negligible DC component due to the opposite polarities of Gaussian amplitudes, with an energy being concentrated at a higher frequency range due to zero crossings. The peak frequency is 6.14 GHz, where the 3 dB and 10 dB bandwidths are B_3= 4.1 GHz and B_{10}=7.5 GHz respectively, which is in very good agreement with the UWB spectral mask. As illustrated in fig. 3.12 (right), a highly efficient pulse waveform is obtained, offering a power efficiency of η=56.47%, which outperforms the 5-th derivative Gaussian pulse (50.7%) and is close to Abraha's combination of Doublets (57.2%) in electrical domain. In fig. 3.13, we can observe the fundamental Gaussian and Doublet besides to their combinations, the novel developed pulse dominates Abraha's waveform in the sense that a significant shift (> 6 GHz) in the central frequency is achieved due to this combination, as if it is a carrier-based scheme but with no local oscillator used. An important feature associated with our approach is the absence of any time differentiator nor delay line, which may reduce the system cost and complexity [42, 47, 51]. As can be seen in fig. 3.14, our combination has carried out the best power efficiency at SOA output (η = 56.1%), which performs better than Abraha's combination of Doublets

(54.1%), thanks to the larger number of tuning parameters. After SOA, the pre-distorted spectrum has a close peak frequency to the original one (6.1 GHz), but covering a larger 10 dB bandwidth (7.45 GHz). Here there is a special case, the original spectrum at SOA output hits FCC mask at low frequencies due to the presence of a significant left side lobe, the main lobe staying far from the FCC limit even at the 34 dB band. This spectral characteristic results from the combining of time spread and windowing effect, which can be efficiently overcome by designing a pre-distorted pulse (better distribution of the pulse energy inside the time window). Unfortunately, the pulse undergoes a time spread after amplification, thus the energy outside the 0.5 ns slot is no more negligible, which translates into significant sidelobes in frequency domain (*sinc* influence). The pre-distortion processing has enabled a significant change in the pulse dynamics so as to render this time windowing effect negligible. What could be concluded regarding the optimization results is that the interior point algorithm reveals to be an excellent choice, as the maximum resultant efficiencies obtained are close to that in electrical domain, which is the target limit to be achieved regardless the type of optimization algorithm.

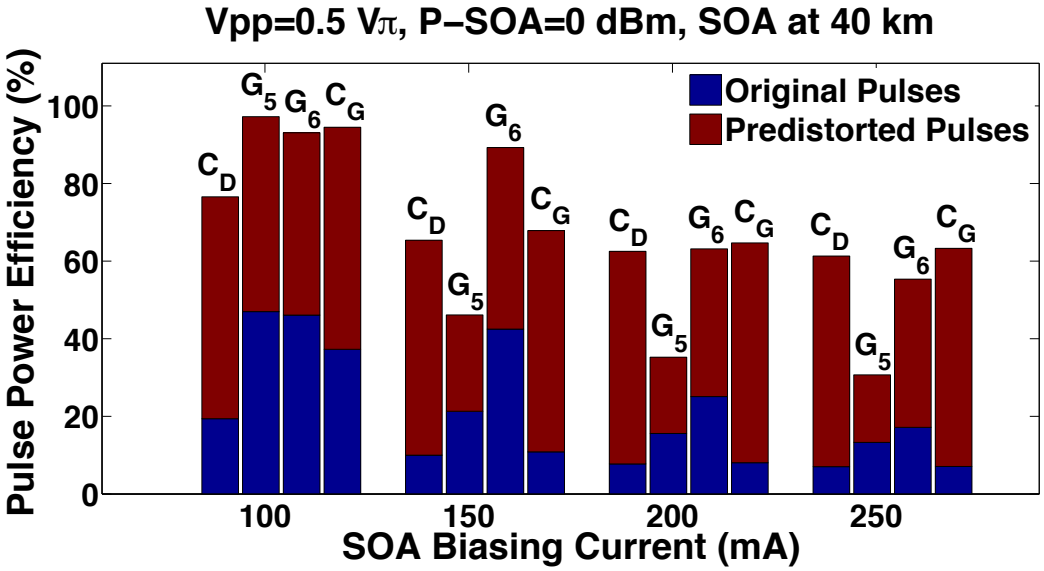

Figure 3.15: Power Efficiency of original and pre-distorted pulses directly after SOA (at 40 km) for several biasing currents; C_D, Doublets-based Abraha's combination, G_5, 5^{th} Gaussian, G_6, 6^{th} Gaussian, C_G, our proposed combination based on Gaussians.

3.3.5 Pre-distortion with different biasing currents

The carrier density in the SOA active region depends on the external injected current [1], hence, the influence of cross gain modulation, self and cross phase modulation, besides to four wave mixing, is a function of the biasing current. Therefore, the latter has to be considered while evaluating our pre-distortion scheme, as it is not the same degree of distortion which occurs at different settings. This is illustrated in fig. 3.15, where we can see that for low biasing currents (100 mA), the 5^{th} and 6^{th} Gaussian pulses exhibit a small degradation in the power efficiency; whereas a significant decrease (>30%) is noticed for the combination of Doublets. In fact, efficient pulses in electrical domain are usually more affected by the optical system nonlinearity, as their spectrum has no margin with respect to FCC mask, thus any small spectral deviation is enough to violate the regular

limit. Applying a larger biasing current increases the order of nonlinear effects, which leads to lower spectral efficiencies for all waveforms. Nevertheless, we observe that no great change appears after 200 mA, that could be justified by the optical gain saturation occurring at 0 dBm input power. The pre-distortion technique is effective with all biasing currents, but as a reach extension is targeted, the value of 250 mA has been adopted, which corresponds to the highest optical power obtained at SOA output. For such conditions, our newly designed pulse offers a neat advantage over the 5-th or 6-th derivative Gaussian waveforms, and is slightly more effective than Abraha's pre-distorted pulse.

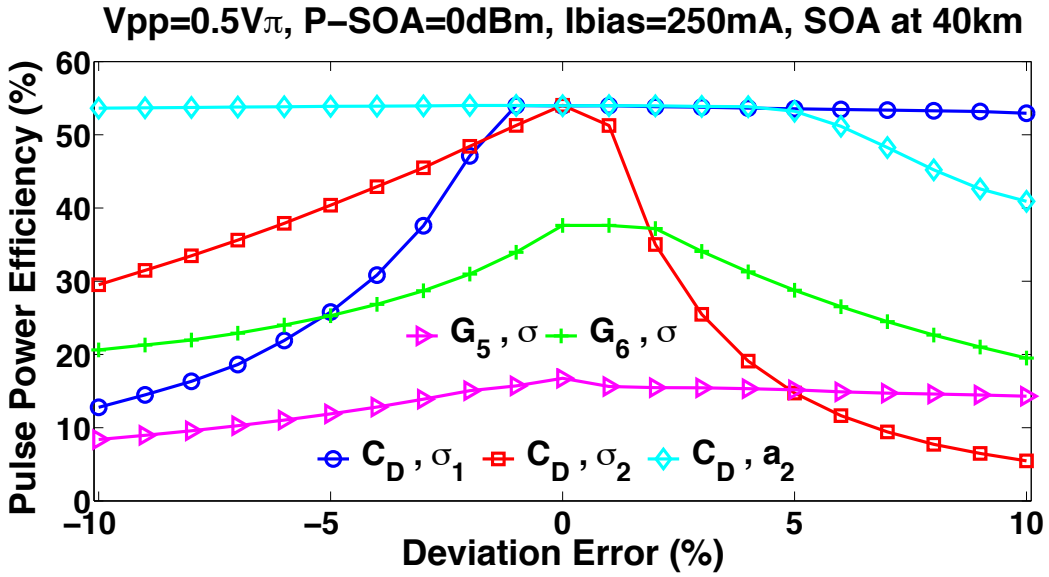

Figure 3.16: Robustness against uncertainty for the 5^{th} and 6^{th} Gaussian pulses, besides to Abraha's combination of Doublets.

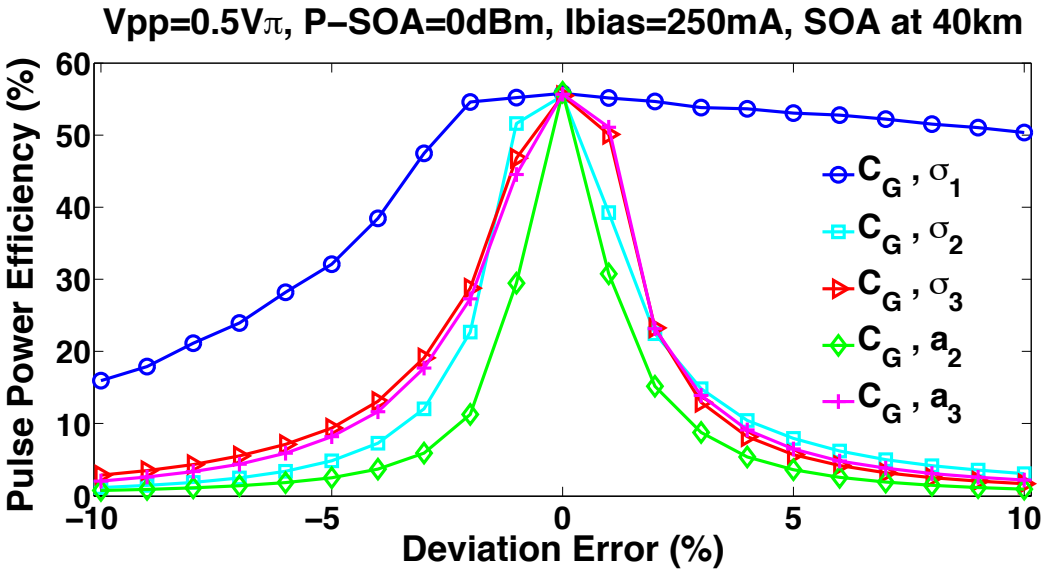

Figure 3.17: Robustness against uncertainty for our proposed pulse based on Gaussians.

3.3.6 Robustness against uncertainty for single waveforms and combinations

Robustness against uncertainties is a common target aspect for electronics and communication system designers, as it is difficult to assume perfect operating conditions, due to the environmental changes, channel effects, and practical constraints [52–60]; specially in our work, since only theoretical models have been considered for the different pulse shapes. From a practical point of view, some uncertainties are expected to occur in the CMOS circuits that could be designed to generate the various pulses. So, we study here the impact of any parametric deviation with respect to the optimum solution discussed previously. Figure 3.16 illustrates the change in the power efficiency due to parametric uncertainty for the 5-th and 6-th Gaussian pulses, together with the Doublets-based combination. G_5 and G_6 show a kind of immunity against systematical errors, as σ is the unique variable which controls the dynamics of a single pulse. The problem appears with Abraha's combination, which exhibits a relative robustness against σ_1 and a_2 deviations; unfortunately, any slight change in σ_2 is enough to drop off the spectral efficiency, specially for negative deviation errors, knowing that it is not a simultaneous change in the combination variables. We can point out that the newly designed pulse is the most sensitive against system uncertainties, as shown in fig. 3.17. In fact, it is much more influenced than other waveforms, as it relies on a larger number of pulses, and all parameters have been optimized simultaneously, so any change in one of the variables makes all the set no more optimal. Besides, fundamental Gaussian pulses have strong DC component, which can re-appear in our combination due to any loss in the basic pulses symmetry (positive/negative symmetry which cancels the DC), and consequently lead to a fast degradation in the power efficiency ($\eta < 5\%$ for a deviation error of 10%).

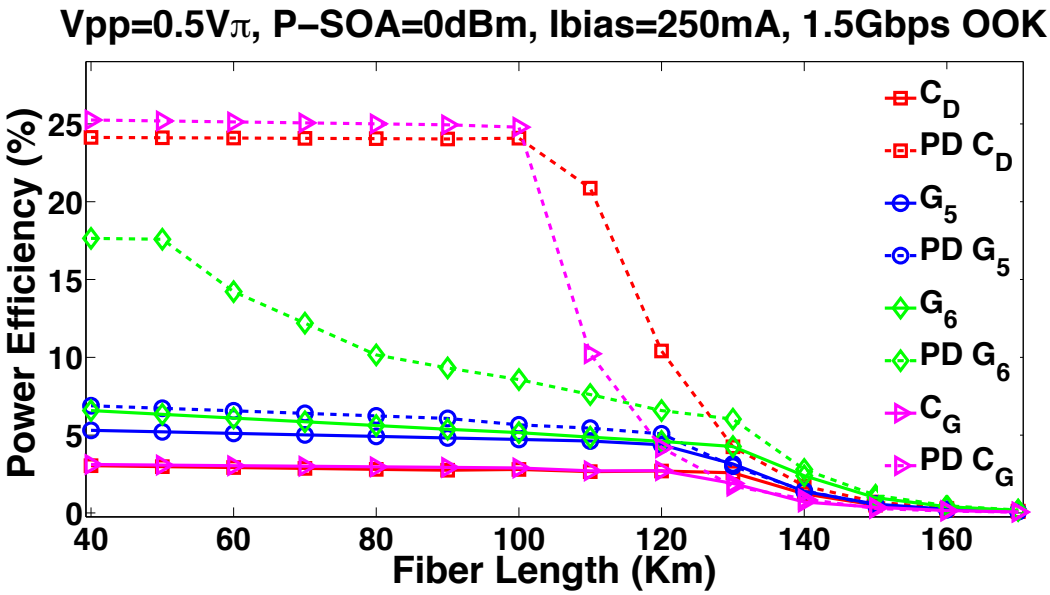

Figure 3.18: Power Efficiency versus fiber length for 1.5 Gbps OOK based on the utilized pulses, P-SOA=0 dBm, $I_{bias} = 250$ mA, $V_{pp} = 0.5V\pi$, where SOA is placed at 40 km.

3.4 Case of a modulated impulse radio signal propagating over optical fiber link

Evaluation in terms of pulse spectral response is not sufficient as a real transmission system is targeted, considering a data modulated impulse radio is a key approach so as to examine the pertinence of our pre-distortion technique. On Off Keying (OOK) and Pulse Position Modulation (PPM) schemes have been the candidates, the interest with such modulation formats being that no coherent receiver is required (demodulation process via energy detection). The effects of the optical link (attenuation and chromatic dispersion) before SOA have been taken into account, as they have an influence on the pulse dynamics entering the amplifier, depending on the covered distance, fiber input power, and peak-to-peak power swing. Therefore, the optimum parameters of pre-distorted waveforms have been extracted considering SOA located at 40 km, where the operating conditions are the same as mentioned in table 3.1. Based on the criterion of power efficiency of a modulated signal defined in the first chapter, the advantage of pre-distortion is depicted in fig. 3.18 for a 1.5 Gbps OOK. A significant improvement is gained over a large enough traveling distance (40 km to 150 km), knowing that no pre-amplifier has been placed for modulated signals before the antenna. The degradation in the curves is due to frequency shaping and deviation caused in fiber [61] (with a chromatic dispersion of 17 ps/nm/km), so the central frequency and B_{10} are no more preserved specially at large extension link. This improvement is justified by the fact that, the envelope of spectral spikes for OOK or PPM takes the shape of basic transmitted waveform, so perfect pulse shapes lead to an efficient spectrum associated with the modulated impulse radio signal. Between 40

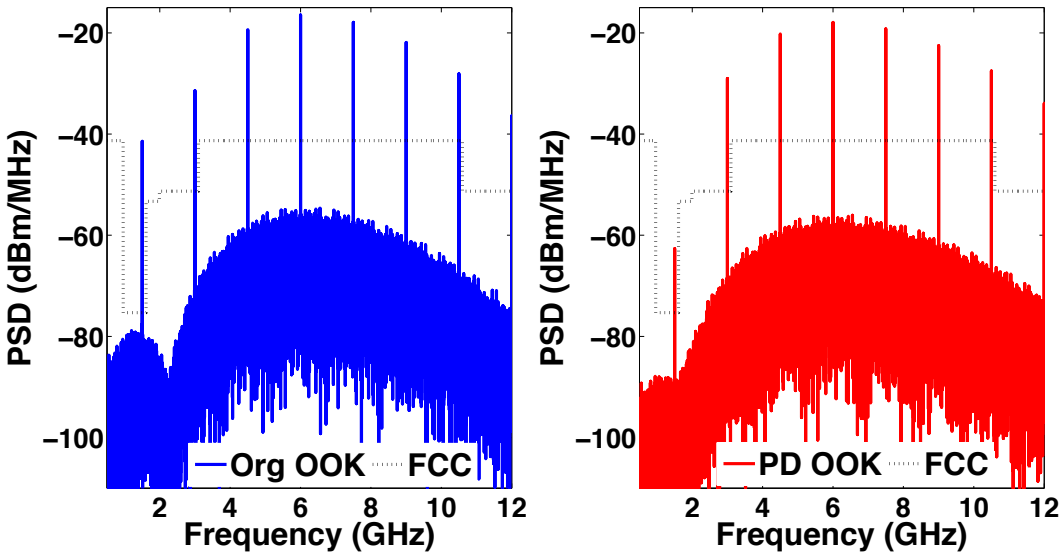

Figure 3.19: Irregular PSD of 1.5 Gbps OOK based on original (left) and pre-distorted (right) $C_G(t)$ after SOA (at 40km), where P-SOA=0 dBm, $I_{bias} = 250$ mA, $V_{pp} = 0.5V\pi$.

km and 100 km, a flat response is noticed in the curves corresponding to combinations of pulses, which results from the fact that all spectra are already above FCC level, thus the signal has to be systematically attenuated so as to respect the mask. Our waveform exhibits a faster degradation than Doublets at large distances, as it has less immunity against fiber effects. The PSD of the C_G - based OOK signal at SOA output is plotted

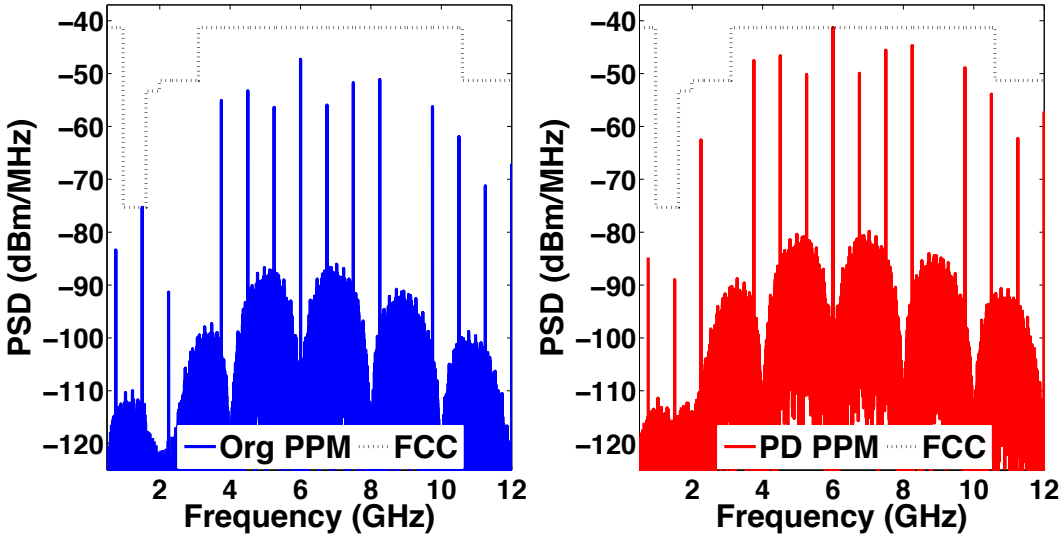

Figure 3.20: Regular PSD of 0.75 Gbps PPM based on original (left) and pre-distorted (right) $C_G(t)$ after SOA (at 40km), where P-SOA=0 dBm, $I_{bias} = 250$ mA, $V_{pp} = 0.5V\pi$.

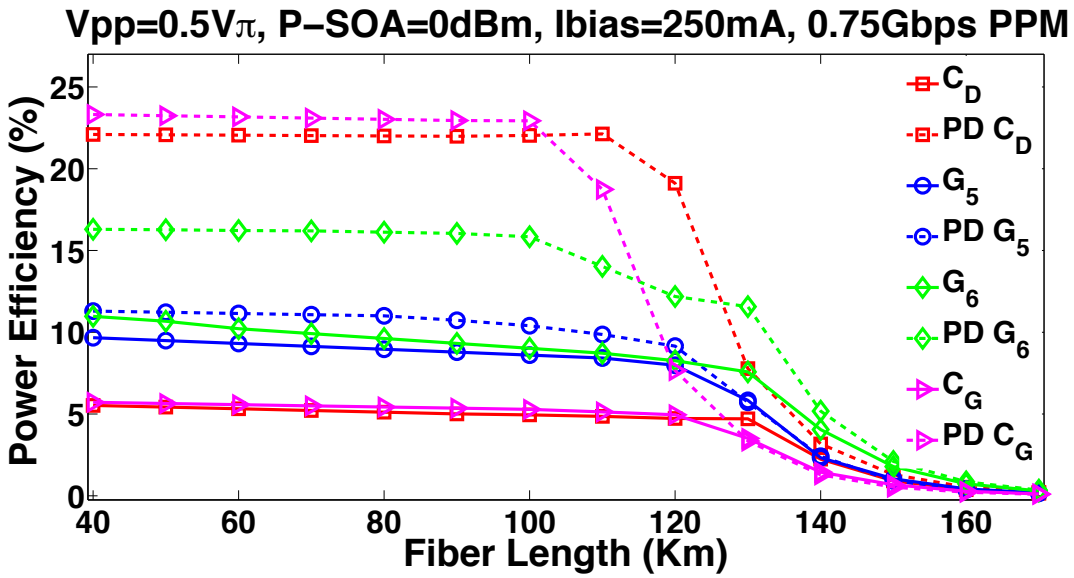

Figure 3.21: Power Efficiency versus fiber length for 0.75 Gbps PPM based on utilized pulses, P-SOA=0 dBm, $I_{bias} = 250$ mA, $V_{pp} = 0.5V\pi$, where SOA is placed at 40 km.

in fig. 3.19, with no attenuation. Apparently, the spectral shaping at low frequency band is the reason beyond efficiency enhancement, so a higher power level can be achieved by the spectra when adapted to FCC mask, as shown in fig. 3.20 for a 0.75 Gbps PPM. Figure 3.21 proves that the same conclusion could be drawn for PPM regardless the covered distance, where the PPM index exactly equals the pulse period (0.5 ns). Therefore, our pre-distortion scheme has always validated a good potential, while reaching a coverage of 150 km in the optical link, fitting the request of Fiber-to-the-Home (FTTH) networks reported in the literature [62]. The enhancement in the power efficiency may translate into a higher signal-to-noise ratio obtained at the antenna output, which promises with a lower probability of error in energy detection receivers. Regarding the practical aspects, we can understand that the performance gain comes at the price of a larger complexity;

depending on application constraints, adopting higher order of derivation with a single pulse shape could be more suitable than applying a combination of pulses, and utilizing a combination of two pulses may be much simpler than using a set of three pulses. In the next chapter, we show that a better performance can be realized when up and down chirping technique is adopted. As will be illustrated, chirping is a relatively more complicated scheme which outperforms pre-distortion in the sense that not only SOA nonlinearities could be mitigated, but also the impact of Amplified Spontaneous Emission noise can be reduced.

3.5 Summary

In this chapter, analog pre-distortion schemes have been investigated for coping with SOA nonlinearities, the target being to optimize the power efficiency of amplified pulses at SOA output. Two linear combinations of Gaussian waveforms were utilized, the first is based on Abraha's combination of Doublets, and the second has been newly designed based on fundamental Gaussians. Both have proved to be highly effective for correcting SOA impact. Using higher orders of Gaussian derivatives is an alternative solution offering a lower potential but with less complexity. Over a large extension of optical link, our pre-distortion approach has exhibited an enhancement in the power efficiency of 1.5 Gbps-OOK and 0.75 Gbps-PPM transmissions. In the next chapter, we introduce a novel technique based on chirping, which aims to linearize SOA characteristics and reduce the ASE noise simultaneously.

Bibliography

[1] M. J. Connelly, Semiconductor Optical Amplifiers. Boston, MA:Kluwer, 2002.

[2] K. Roberts, L. Chuandong, L. Strawczynski, M. O'sullivan, and I. Hardcastle, "Electronic precompensation of optical nonlinearity," *IEEE Photon. Technol. Letters*, 18(1-4), 403-405, 2006.

[3] E. Ip and J. M. Kahn, "Compensation of dispersion and nonlinear impairments using digital back propagation," *J. Lightw. Technol.*, 26(20), 3416-3425, 2008.

[4] A. J. Lowery, "Fiber nonlinearity pre-and post-compensation for long-haul optical links using OFDM," *Optics Express*, 15(20), 12965-12970, 2007.

[5] J. E. Mitchell, P. P. Pardalos, and M. G. C. Resende. Interior point methods for combinatorial optimization. In D.-Z. Du and P. Pardalos, editors, Handbook of Combinatorial Optimization , vol. 1, pp. 189-297. Kluwer Academic Publishers, 1998.

[6] Morgan, D. R., Ma, Z., Kim, J., Zierdt, M. G., & Pastalan, J. (2006). A generalized memory polynomial model for digital predistortion of RF power amplifiers. IEEE Transactions on signal processing, 54(10), 3852-3860.

[7] Muhonen, K. J., Kavehrad, M., & Krishnamoorthy, R. (2000). Look-up table techniques for adaptive digital predistortion: A development and comparison. IEEE transactions on vehicular technology, 49(5), 1995-2002.

[8] Bassam, S. A., Helaoui, M., & Ghannouchi, F. M. (2011). 2-D digital predistortion (2-D-DPD) architecture for concurrent dual-band transmitters. IEEE Transactions on Microwave Theory and Techniques, 59(10), 2547-2553.

[9] Kim, J., & Konstantinou, K. (2001). Digital predistortion of wideband signals based on power amplifier model with memory. Electronics Letters, 37(23), 1417-1418.

[10] Ding, L., Zhou, G. T., Morgan, D. R., Ma, Z., Kenney, J. S., Kim, J., & Giardina, C. R. (2004). A robust digital baseband predistorter constructed using memory polynomials. IEEE Transactions on Communications, 52(1), 159-165.

[11] Raab, F. H., Asbeck, P., Cripps, S., Kenington, P. B., Popovic, Z. B., Pothecary, N., ... & Sokal, N. O. (2002). Power amplifiers and transmitters for RF and microwave. IEEE transactions on Microwave Theory and Techniques, 50(3), 814-826.

[12] Cavers, J. K. (1990). Amplifier linearization using a digital predistorter with fast adaptation and low memory requirements. IEEE transactions on vehicular technology, 39(4), 374-382.

[13] Killey, R. I., Watts, P. M., Mikhailov, V., Glick, M., & Bayvel, P. (2005). Electronic dispersion compensation by signal predistortion using digital processing and a dual-drive Mach-Zehnder modulator. IEEE Photonics Technology Letters, 17(3), 714-716.

[14] Kenington, P. B. (2000). High linearity RF amplifier design. Artech House, Inc..

[15] Vuolevi, J. H., Rahkonen, T., & Manninen, J. P. (2001). Measurement technique for characterizing memory effects in RF power amplifiers. IEEE Transactions on Microwave Theory and Techniques, 49(8), 1383-1389.

[16] C. Tai, S.-L. Tzeng, H.-C. Chang, and W. I. Way, "Reduction of non-linear distortion in mqw semiconductor optical amplifier using light injection and its application in multichannel m-qam signal transmission systems," *IEEE Photon. Technol. Lett.* , vol. 10, pp. 609–611, Apr. 1998

[17] F. Tabatabai, H. S. Al-Raweshidy, "Feed-Forward Linearization Technique for Reducing Non-Linearity in Semiconductor Optical Amplifier," *J. Lightw. Technol.*, vol.25, No. 9, pp.2667-2674, Sep. 2007.

[18] Lee, T. H. (2003). The design of CMOS radio-frequency integrated circuits. Cambridge university press.

[19] Chen, S. W. M., & Brodersen, R. W. (2006). A 6-bit 600-MS/s 5.3-mW Asynchronous ADC in 0.13- *mu hboxm* CMOS. IEEE Journal of Solid-State Circuits, 41(12), 2669-2680.

[20] O'Donnell, I. D., & Brodersen, R. W. (2005). An ultra-wideband transceiver architecture for low power, low rate, wireless systems. IEEE Transactions on vehicular technology, 54(5), 1623-1631.

[21] Zhang, H., & Sánchez-Sinencio, E. (2011). Linearization techniques for CMOS low noise amplifiers: A tutorial. IEEE Transactions on Circuits and Systems I: Regular Papers, 58(1), 22-36.

[22] J. Han, C. Nguyen, "Ultra-wideband electronically tunable pulse generators", *IEEE Microwave and Wireless Components Letters*, vol. 14, No. 3, pp. 112 - 114, 2004.

[23] H. Kim, Y. Joo, and S. Jung, "A tunable CMOS UWB pulse generator," in Proc. IEEE International Conference on Ultra-Wideband, pp. 109–112, Waltham, MA, Sep. 24-27, 2006.

[24] R. Thai-Singama, F. Du-Burck, M. Piette, "Demonstration of a Low-Cost Ultrawideband Transmitter in the 3.1–10.6-GHz Band", *IEEE Transaction on Circuits and Systems–II: Express briefs*, vol. 59, no. 7, pp. 389–393, Jul. 2012.

[25] M. Mirshafiei, M. Abtahi, and L. A. Rusch, "Ultra-wideband pulse shaping: bypassing the inherent limitations of the Gaussian monocycle," *IET Communications*, vol. 6, no. 9, pp. 1068-1074, 2012.

[26] Liang, J. J., Qin, A. K., Suganthan, P. N., & Baskar, S. (2006). Comprehensive learning particle swarm optimizer for global optimization of multimodal functions. IEEE transactions on evolutionary computation, 10(3), 281-295.

[27] Storn, R., & Price, K. (1997). Differential evolution–a simple and efficient heuristic for global optimization over continuous spaces. Journal of global optimization, 11(4), 341-359.

[28] Karaboga, D., & Basturk, B. (2007). A powerful and efficient algorithm for numerical function optimization: artificial bee colony (ABC) algorithm. Journal of global optimization, 39(3), 459-471.

[29] Weise, T. (2009). Global optimization algorithms-theory and application. Self-published, 2.

[30] Elbeltagi, E., Hegazy, T., & Grierson, D. (2005). Comparison among five evolutionary-based optimization algorithms. Advanced engineering informatics, 19(1), 43-53.

[31] Mahdavi, M., Fesanghary, M., & Damangir, E. (2007). An improved harmony search algorithm for solving optimization problems. Applied mathematics and computation, 188(2), 1567-1579.

[32] Goffe, W. L., Ferrier, G. D., & Rogers, J. (1994). Global optimization of statistical functions with simulated annealing. Journal of econometrics, 60(1-2), 65-99.

[33] Rahnamayan, S., Tizhoosh, H. R., & Salama, M. M. (2008). Opposition-based differential evolution. IEEE Transactions on Evolutionary computation, 12(1), 64-79.

[34] Deb, K., Agrawal, S., Pratap, A., & Meyarivan, T. (2000, September). A fast elitist non-dominated sorting genetic algorithm for multi-objective optimization: NSGA-II. In International Conference on Parallel Problem Solving From Nature (pp. 849-858). Springer Berlin Heidelberg.

[35] Byrd, R. H., Hribar, M. E., & Nocedal, J. (1999). An interior point algorithm for large-scale nonlinear programming. SIAM Journal on Optimization, 9(4), 877-900.

[36] Wachter, A., & Biegler, L. T. (2006). On the implementation of an interior-point filter line-search algorithm for large-scale nonlinear programming. Mathematical programming, 106(1), 25-57.

[37] Nesterov, Y., & Nemirovskii, A. (1994). Interior-point polynomial algorithms in convex programming. Society for industrial and applied mathematics.

[38] Wright, S. J. (1997). Primal-dual interior-point methods. Society for Industrial and Applied Mathematics.

[39] Mehrotra, S. (1992). On the implementation of a primal-dual interior point method. SIAM Journal on optimization, 2(4), 575-601.

[40] Alizadeh, F. (1995). Interior point methods in semidefinite programming with applications to combinatorial optimization. SIAM journal on Optimization, 5(1), 13-51.

[41] Kim, S. J., Koh, K., Lustig, M., Boyd, S., & Gorinevsky, D. (2007). An Interior-Point Method for Large-Scale l_1-Regularized Least Squares. IEEE journal of selected topics in signal processing, 1(4), 606-617.

[42] H. Jin, L. Jiang, W. Hao, C. Sheng, H. Qijun, and Z. Yueping, "A CMOS fifth-derivative Gaussian pulse generator for UWB applications," *Journal of Semiconductors*, 35(9), 095005, 2014.

[43] Kim, H., & Joo, Y. (2005, June). Fifth-derivative Gaussian pulse generator for UWB system. In Radio Frequency integrated Circuits (RFIC) Symposium, 2005. Digest of Papers. 2005 IEEE (pp. 671-674). IEEE.

[44] Kim, H., Park, D., & Joo, Y. (2004). All-digital low-power CMOS pulse generator for UWB system. Electronics Letters, 40(24), 1534-1535.

[45] Salehi-Abari, O., & Plett, C. (2010, May). A differential 5 th derivative Gaussian pulse generator for UWB transceivers. In Circuits and Systems (ISCAS), Proceedings of 2010 IEEE International Symposium on (pp. 1089-1092). IEEE.

[46] Moreira, L. C., Silveira, D. M., van Noije, W. A., & Kofuji, S. T. (2010, March). A 5 th derivative Gaussian pulse CMOS IR-UWB generator using a Phase Detector. In German Microwave Conference, 2010 (pp. 154-157). IEEE.

[47] H. Sheng, P. Orlik, A. M. Haimovich, Jr. L. J. Cimini, and J. Zhang, "On the spectral and power requirements for ultra-wideband transmission," *In Communications, 2003. ICC'03. IEEE International Conference*, Vol. 1, pp. 738-742, 2003.

[48] M. Wang, S. Yang, & S. Wu, "A GA-based UWB pulse waveform design method. Digital Signal Processing," 18(1), 65-74, 2008.

[49] M. Matsuo, M. Kamada, & H. Habuchi, "Design of UWB pulses based on B-splines," *Circuits and Systems, ISCAS, IEEE International Symposium*, pp. 5425-5428, 2005.

[50] da Silva, J. A. N., & de Campos, M. L. (2007). Spectrally efficient UWB pulse shaping with application in orthogonal PSM. IEEE Transactions on Communications, 55(2), 313-322.

[51] S.T. Abraha, C. Okonkwo, P. A. Gamage, E. Tangdiongga, and T. Koonen, "Routing of power efficient IR-UWB wireless and wired services for in-building network applications," *J. Lightw. Technol.*, 30(11), pp. 1651-1663, 2012.

[52] Ali, S., Maciejewski, A. A., Siegel, H. J., & Kim, J. K. (2004). Measuring the robustness of a resource allocation. IEEE Transactions on Parallel and Distributed Systems, 15(7), 630-641.

[53] Kassam, S. A., & Poor, H. V. (1985). Robust techniques for signal processing: A survey. Proceedings of the IEEE, 73(3), 433-481.

[54] Zheng, G., Wong, K. K., & Ottersten, B. (2009). Robust cognitive beamforming with bounded channel uncertainties. IEEE Transactions on Signal Processing, 57(12), 4871-4881.

[55] El-Keyi, A., & Champagne, B. (2009). Collaborative uplink transmit beamforming with robustness against channel estimation errors. IEEE Transactions on Vehicular Technology, 58(1), 126-139.

[56] Rong, Y., Vorobyov, S. A., & Gershman, A. B. (2006). Robust linear receivers for multiaccess space-time block-coded MIMO systems: A probabilistically constrained approach. IEEE Journal on Selected Areas in Communications, 24(8), 1560-1570.

[57] Buchegger, S., & Le Boudec, J. Y. (2003). A robust reputation system for mobile ad-hoc networks (No. LCA-REPORT-2003-006).

[58] Biguesh, M., Shahbazpanahi, S., & Gershman, A. B. (2004). Robust downlink power control in wireless cellular systems. EURASIP Journal on Wireless Communications and Networking, 2004(2), 261-272.

[59] Quet, P. F., AtaşLar, B., Iftar, A., ÖZbay, H., Kalyanaraman, S., & Kang, T. (2002). Rate-based flow controllers for communication networks in the presence of uncertain time-varying multiple time-delays. Automatica, 38(6), 917-928.

[60] Petersen, I. R., & Savkin, A. V. (1999). Robust Kalman filtering for signals and systems with large uncertainties. Springer Science & Business Media.

[61] Pan, S., & Yao, J. (2010). Performance evaluation of UWB signal transmission over optical fiber. IEEE Journal on selected areas in communications, 28(6).

[62] R. Llorente, T. Alves, M. Morant, M. Beltran, J. Perez, A. Cartaxo, and J. Marti, "Ultra-wideband radio signals distribution in FTTH networks," *IEEE Photon. Technol. Lett.*, 20(11), pp. 945-947, 2008.

Chapter 4

Analog Chirping Techniques for coping with SOA Impairments in the proposed IR-UWB over fiber system

Pre-distortion schemes have proved to be effective in reducing SOA nonlinearity, but have no influence on the Amplified Spontaneous Emission noise intensity. In this chapter, we investigate a phaser-based processing technique so as to improve the system performance over a much broader power range. By applying symmetrical up/down analog chirping (at the transmitter and receiver, respectively), we have reduced the ASE power and nonlinearity simultaneously. Based on the 5th Gaussian pulse and Abraha's combination of doublets, a significant improvement has been achieved at low and high input powers entering the amplifier (<-15 dBm and 0 dBm), recording a very good bit error rate performance and high power efficiency. Interesting results have been obtained for 1 Gbps OOK and 0.5 Gbps PPM transmissions, while reaching a distance of 160 km in the optical fiber, thanks to the proposed scheme.

4.1 Introduction

As mentioned in the previous chapter, employing SOA in the over fiber communication system may lead to some drawbacks, mainly the Amplified Spontaneous Emission noise [1, 2] and the nonlinear effects acting on the pulse waveform [3]. Both degrade the performance of the optical system, lower power efficiencies being achieved due to distortion, besides to the increased number of errors obtained at the receiver side. In order to overcome the SOA distortions, noise reduction and linearization techniques have to be applied, without adding more complexity to the conventional system architecture. Various methodologies concerning these two topics have been investigated in literature [4–12]. The objective in the third chapter was to pre-distort against SOA nonlinear impairments by adjusting the parameters of input waveforms. This scheme was based on global optimization requiring a feedback in the electro-optical system. A special effort is applied here to examine the benefits of chirping in upgrading the overall system performance. Following the work of Nikfal *et al.* [13], who has recently succeeded in enhancing the signal-to-noise ratio of UWB systems via group delay phasers. As a first step, symmetrical up and down chirping has shown to be effective against ASE influence in our system. Then we proved that SOA nonlinear effects could be also mitigated, as frequency decomposition reduces the order of four wave mixing and cross gain modulation for propagated

signals. Up-down chirping could be considered as a pre-post distortion technique, which has improved the power efficiency of transmitted impulse radio signals, while traveling along a broad distance in the optical link.

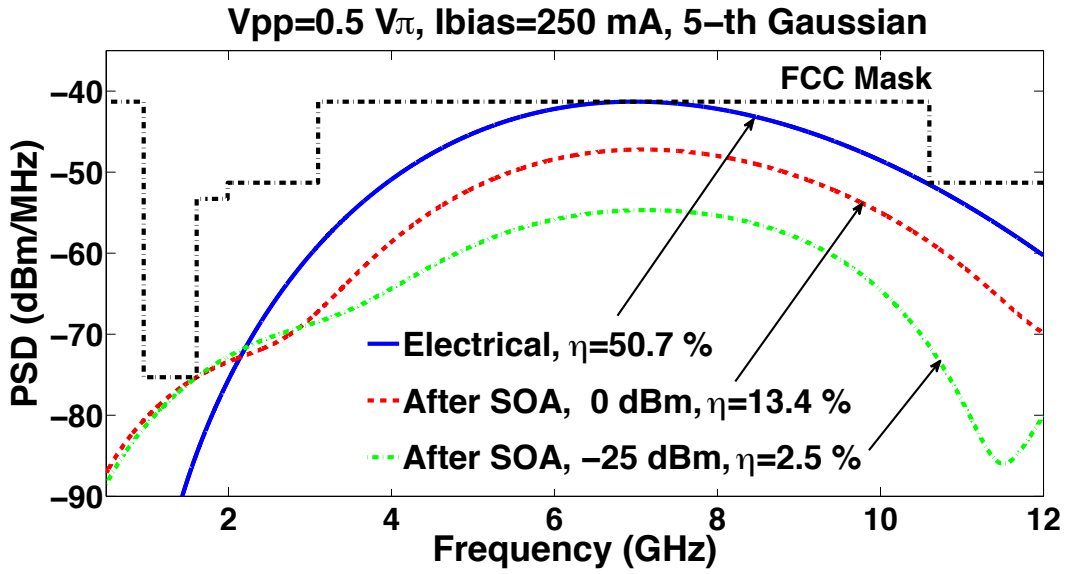

Figure 4.1: Power Spectral Density of 5^{th} Gaussian in electrical domain and after SOA (while operating in the linear or saturation region).

4.2 Impact of SOA ASE noise and nonlinearities on IR-UWB pulse shapes

The extension of the optical link depends on the applied power at fiber input, which is a function of the amplifier gain; hence, the coverage area of the optical access network is determined by the operating point of SOA. To have a look at the amplifier impact, we have studied the spectral response of the 5-th order derivative Gaussian pulse before and after being passed through SOA, where the peak-to-peak voltage has been fixed at 0.5 $V\pi$, and the biasing current was 250 mA. Figure 4.1 shows the spectrum in electrical domain (solid-blue), where the dot-dashed-green and dashed-red curves correspond to the spectra obtained at SOA output, while operating in the linear (-25 dBm input power) and saturation region (0 dBm input power), respectively. For both operating points, the spectrum of the resultant pulse (after photo-detector) violates FCC mask in the most restricted band $[0.96-1.61]$ GHz corresponding to GPS, where the low power level (-75.3 dBm/MHz) is greatly challenging. At linear gain region, the distortion in the spectrum is due to ASE characteristics, as it is a white noise having a flat spectral response. While at saturation, distortion is due to the strong nonlinear effects acting on the propagated pulse waveform. Hence, the average signal power has to be reduced so as to meet the regular limit, leading to a significant degradation in the power efficiency ($> 35\%$) at both operating points, specially for the noisy case. In the previous chapter, we have studied the power efficiency versus SOA input power while considering several peak-to-peak voltages. It has been shown that high input powers bring strong nonlinearities specially at large V_{pp}, and low powers are associated with a small signal-to-noise ratio particularly at low V_{pp}. We also indicate that the trade off between linearity and SNR is controlled by the

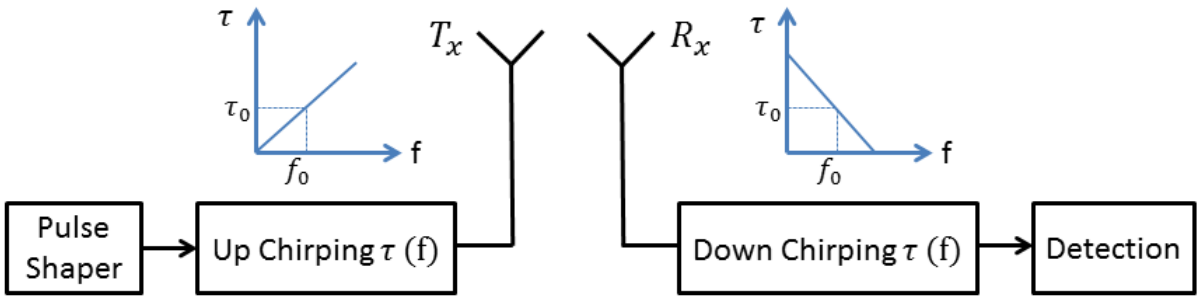

Figure 4.2: The general principle of a wireless transmission system utilizing up and down chirping.

maximum voltage swing. The latter has been fixed at V_{pp}= 0.5 $V\pi$ when studying the nonlinearity aspect in the remaining part of the chapter, as it is a medium value that well describes the SOA behavior versus operating point. Reducing the noise impact in UWB communication systems has been a common target for different designers [13–21]. The interest in Nikfal's work is that it is a relatively simple approach, which may be well suited for our SOA-based over fiber transceiver [13]. In the next section, Nikfal's configuration will be introduced with the view to be adopted in our optical system afterwards.

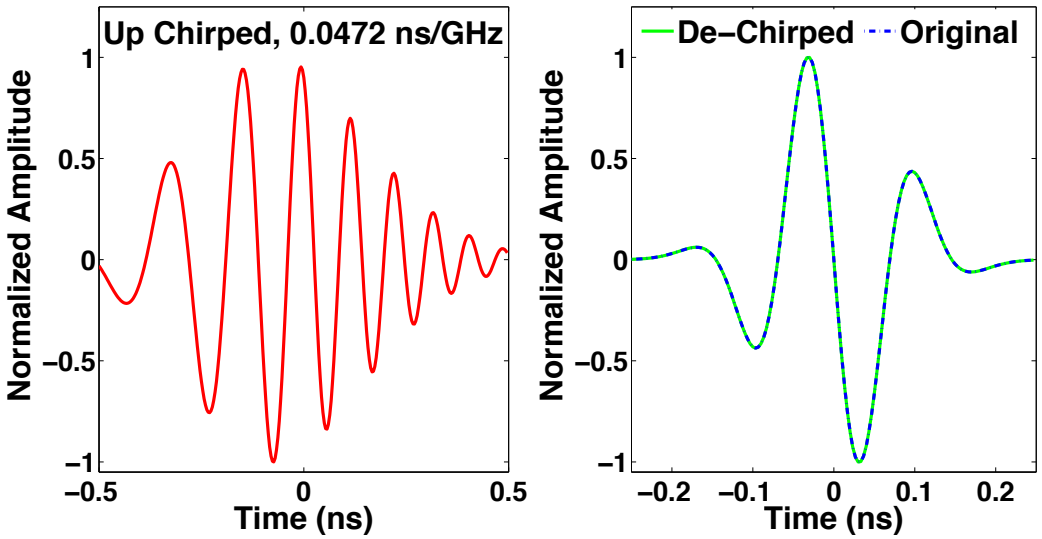

Figure 4.3: Time waveforms of 5th up-chirped Gaussian with a 1 ns duration (left), besides to the de-chirped in comparison with the original having 0.5 ns duration (right).

4.3 Noise Reduction Technique based on Up and Down Chirping via Group Delay Phasers

The system architecture investigated by Nikfal is described in fig. 4.2, which aims to enhance the signal-to-noise ratio at receiver side [13]. The key function is performed by the phaser, which has a dispersive structure with controllable group delay [22]. Such a

component operates linear up or down chirping on the input signal, thus stretching or compressing the pulse without making a change in the total energy. Therefore, if the ratio of the pulse duration before to after phaser is M, then the corresponding value for the average power is $1/M$. The transmitter operates a linear up chirping for the data pulses before entering the channel, while at receiver side, the instantaneous frequencies are equalized so as to compress the pulse to an enhanced waveform that is essentially identical to the original one (down chirping being performed with an absolutely equal slope to that of the transmitter). Several investigations originating from the chirp concept have been reported in literature, which include real-time spectrum sniffing and enhancing the resolution of analog signal-processing systems [23, 24].

In equations (4.1), (4.2), and (4.3), we describe the time and frequency domain expressions of the chirped signal, besides to the frequency dependent time delay function $\tau(f)$, where $x(t)$ is the original pulse before entering the phaser, a is the chirping slope, and b is the delay offset. In fig. 4.3 (left), we show the time waveform of an up-chirped $5th$ order Gaussian pulse, with a chirping slope of 0.0472 ns/GHz; when a down chirping is applied with opposite polarity, the resultant pulse can exactly match the original one as verified in fig. 4.3 (right).

$$y(t) = x\big(t + \tau(f)\big) \tag{4.1}$$

$$\tau(f) = af + b \tag{4.2}$$

$$\begin{aligned} Y(f) &= X(f)\, exp\big(2\pi f\, \tau(f)\, j\big) \\ &= X(f)\, exp\big(2\pi a f^2 j\big)\, exp\big(2\pi f b j\big) \end{aligned} \tag{4.3}$$

A key point to mention is that no local oscillator is required to generate the chirped

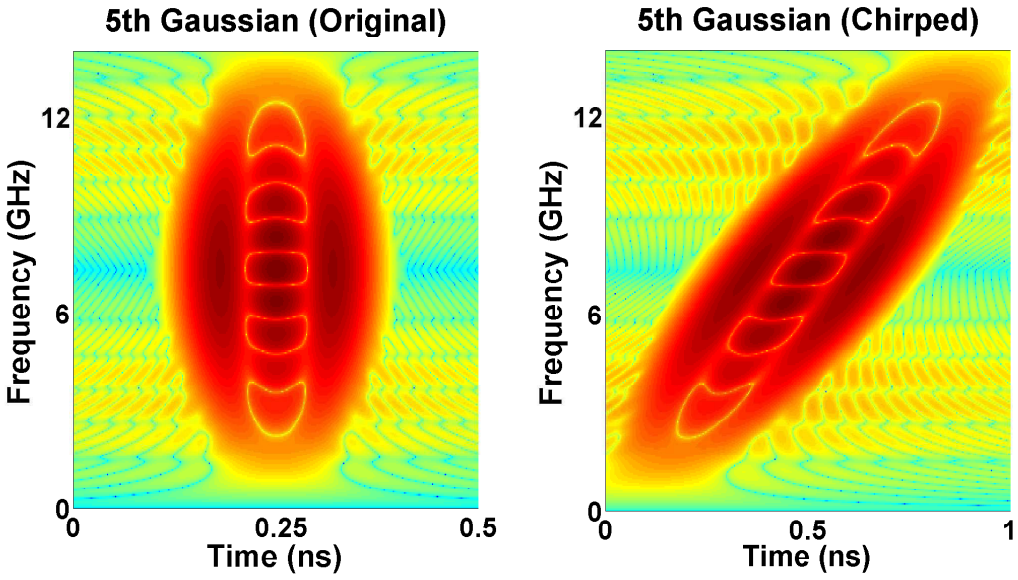

Figure 4.4: The Wigner Ville Distribution of $5th$ original Gaussian (left) besides to the up-chirped pulse (right) in electrical domain, where the chirping slope is 0.0472 ns/GHz.

pulse, it is a simple phaser [25, 26] which follows the pulse shaper. Figure 4.4 (left) states the Wigner Ville Distribution [27] of the normal pulse; as can be seen, several frequency components exist at different time instants simultaneously, specially at the center of the waveform. By up chirping we make a partial separation so that the peak

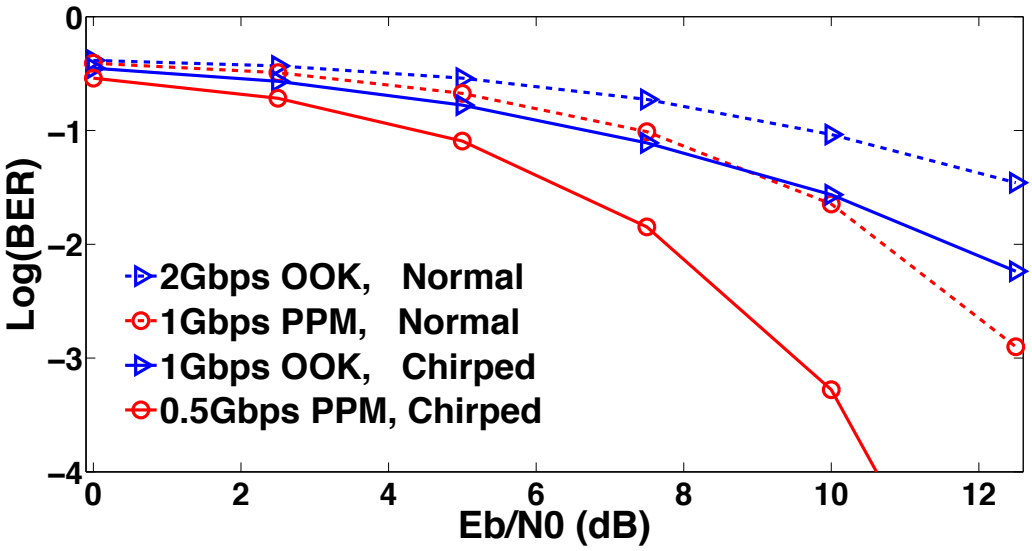

Figure 4.5: Bit error rate versus Eb/N_0 for normal and chirped (with a slope of 0.0472 ns/GHz) transmissions over AWGN channel, considering OOK and PPM modulations.

Chirping Slope (ns/GHz)	τ_{max} (ns)	T_p (ns)	R_{OOK} (Gbps)	R_{PPM} (Gbps)
0	0	0.5	2	1
0.0052	0.055	0.555	1.8	0.9
0.0118	0.125	0.625	1.6	0.8
0.0202	0.214	0.714	1.4	0.7
0.0314	0.333	0.833	1.2	0.6
0.0472	0.5	1	1	0.5

Table 4.1: The set of chirping slopes considered in the study, and the corresponding time shift, besides to the pulse duration and resultant data rate (R) for OOK or PPM.

frequency increases with time, less frequency overlap being obtained for the chirped pulse as illustrated in fig. 4.4 (right). In the case of up-chirping, we consider $b = 0$ as no need for a delay offset, whereas for down chirping, the value of b must not go under the maximum time shift applied in the negative way. Chirping affects only the phase of the spectrum without varying its magnitude (4.3), hence there is no influence on the power spectral density, which is a positive point for this approach, as no impact is observed in terms of power efficiency. Table 4.1 states different values of chirping slopes, each associated with a maximum time shift τ_{max}, computed as $\tau_{max} = a \times f_{max} = a \times 10.6$ GHz, as the energy of input pulses is negligible for frequencies above the FCC upper bound. Assuming f_{max} exists at the end of the pulse interval, the new pulse duration T_p becomes the old one (0.5 ns) added to τ_{max}. Therefore, the data rate for an On Off Keying (OOK) modulated signal having a unit processing gain is $1/T_p$, whereas for a non-coherent Pulse Position Modulation (PPM) it is $1/(2T_p)$. In [13], the authors have proved an enhancement in the SNR; unfortunately, there was no evaluation in terms of bit error rate (BER) performance. Here we evaluate the BER versus Eb/N_0 in an AWGN

channel. We can see an improvement for both OOK and PPM modulations as observed in fig. 4.5, where the chirping slope is 0.0472 ns/GHz. Lower number of errors is obtained at the cost of data rate as illustrated in fig. 4.6, where OOK operates at the maximum data rate and PPM occupies only the half. Increasing the chirping slope broadens the pulse duration, and consequently degrades the transmission speed but enhances the quality of service on the other side.

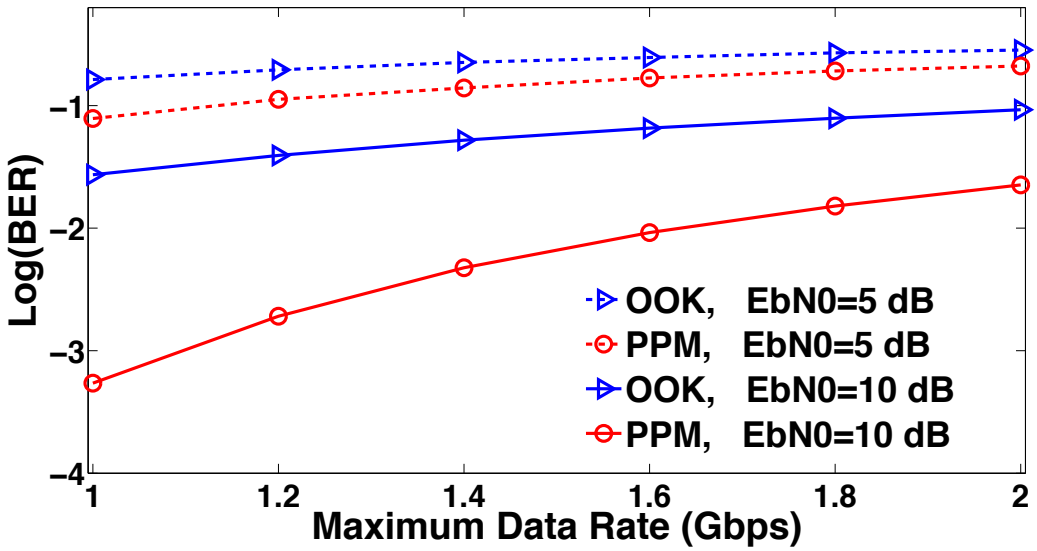

Figure 4.6: Bit error rate in an AWGN channel versus maximum data rate could be achieved (associated with a specific chirping slope) for OOK and PPM modulations.

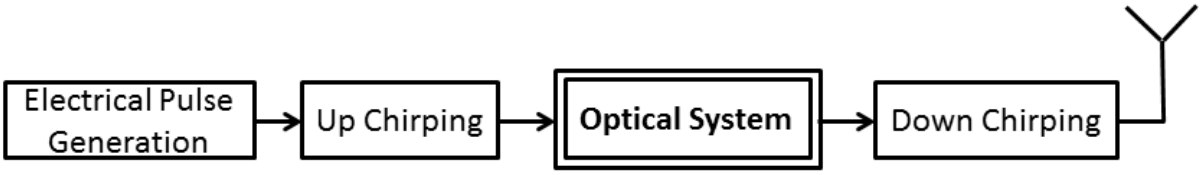

Figure 4.7: Up and down chirping applied before and after the optical system respectively, which includes the MZM, fiber, SOA in-line amplifier, and photo-detector.

4.4 Embedding Chirping Schemes in SOA-based IR-UWB over fiber systems

The great potential offered by chirping technique presented in the previous section has motivated us to apply it in our SOA-based IR-UWB over fiber system. Nikfal considered the Gaussian and Burst noises [13], here we examine up-down chirping scheme in reducing the ASE noise effects inherent to SOA, the interesting feature of this mechanism is that it is a low cost analog approach. The block diagram of the proposed system is described in fig. 4.7, with up and down chirping taking place before and after the optical system respectively. The initial target was to follow the work in [13] and investigate the same concept while considering a radio over fiber application. Then, as will be shown in the

sequel, chirping proves to be a good alternative for enhancing the power efficiency of amplified pulses by reducing the order of SOA nonlinearity. To the best of our knowledge, this has not been examined in the literature until now.

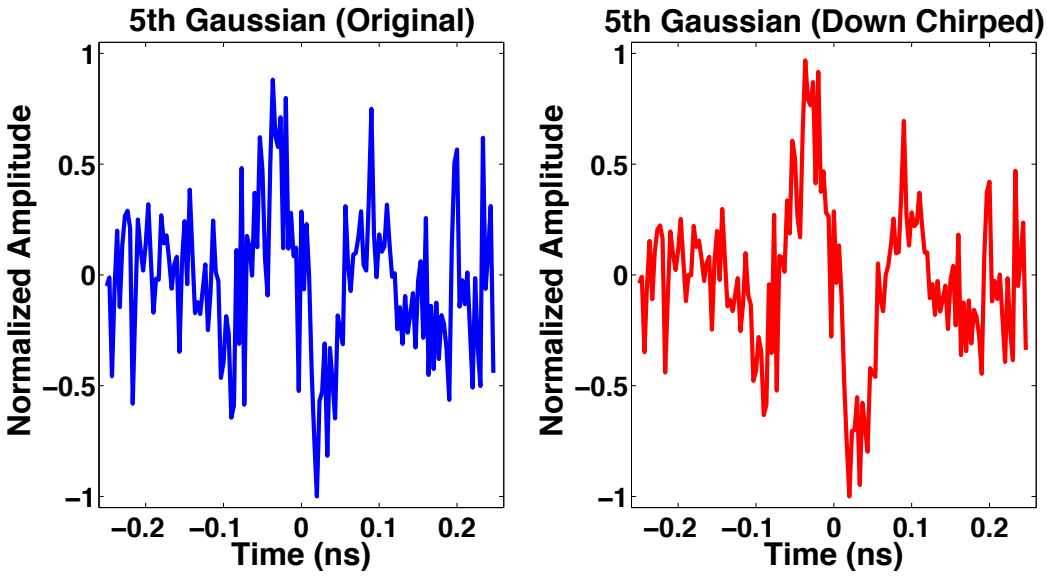

Figure 4.8: Time waveforms of the noisy 5th Gaussian obtained at SOA output, with (right) and without (left) chirping, P-SOA= -20 dBm, $V_{pp} = 0.1V\pi$, $I_{bias} = 250$ mA.

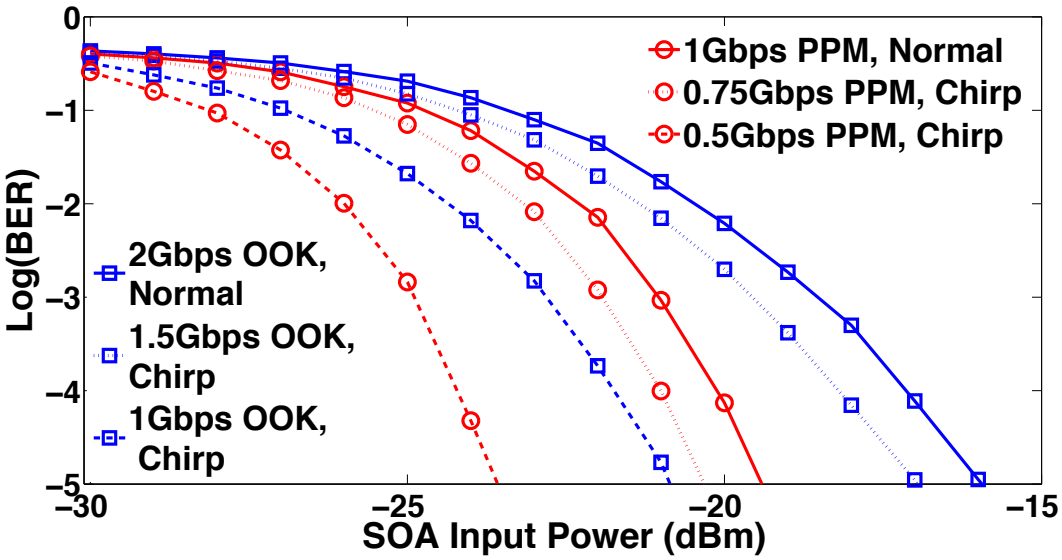

Figure 4.9: Bit error rate versus SOA input power for several data rates of normal and chirped transmissions, considering OOK and PPM, $V_{pp} = 0.1V\pi$ and $I_{bias} = 250$ mA.

4.4.1 Reducing the ASE noise impact via chirping

Figure 4.8 shows the time waveforms of the $5th$ order Gaussian pulse obtained at SOA output, with (right) and without (left) chirping, where the slope is 0.0472 ns/GHz and SOA operates in the linear region (-20 dBm input power). Thanks to chirping, we observe a notable increase in the signal-to-noise ratio even with ASE noise. Like in AWGN channel,

the reduction in the noise impact translates into a better BER performance, as illustrated in fig. 4.9 for several data rates of OOK and PPM modulation formats, where $V_{pp} = 0.1V\pi$ and $I_{bias} = 250$ mA.

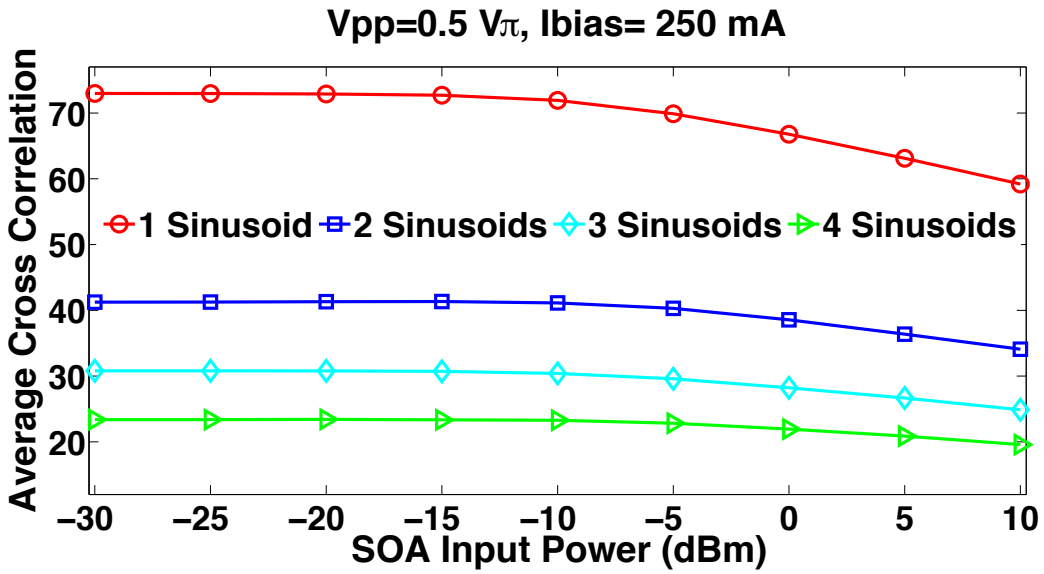

Figure 4.10: Average cross correlation between electrical and optical (after photo-detector) waveforms, versus SOA input power for several combinations of sinusoids, $Vpp = 0.5V\pi$, I_{bias} =250 mA.

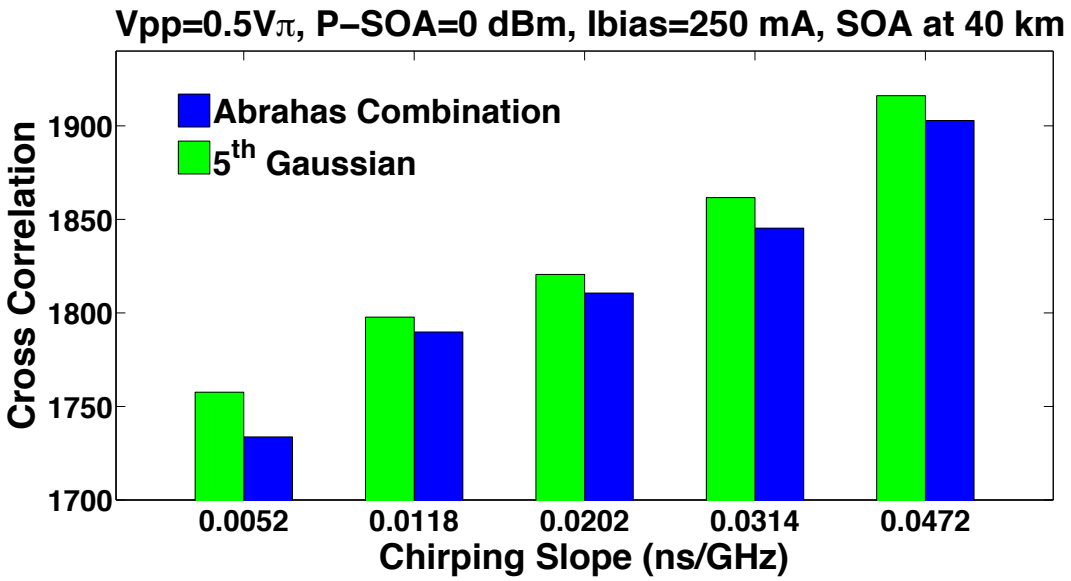

Figure 4.11: Cross Correlation between electrical and optical waveforms versus chirping slope, for the 5th Gaussian pulse and Abraha's combination, where $Vpp = 0.5V\pi$, I_{bias} =250mA, P-SOA=0 dBm.

4.4.2 SOA linearization via chirping

Besides to the improvement in system performance while operating in the SOA linear region, we can also enhance the power efficiency of pulses obtained at SOA output, by

reducing the order of nonlinearity through up and down chirping. A lower order of cross gain modulation and four-wave mixing is obtained if a single frequency is processed at a time, rather than amplifying the whole frequency components simultaneously [28]. Hence, stretching the pulse over time reduces the SOA nonlinearity, as different frequency components can pass through the amplifier at separate time instants. Based on this concept, we enter chirped signals at the SOA input in order to get less distortion, and after photo-detection the original pulse can be reconstructed via down chirping. This strategy could be classified as a new type of linearization in addition to existing pre-distortion and post-distortion schemes employed for power amplifiers [4–11]. The average cross-correlation

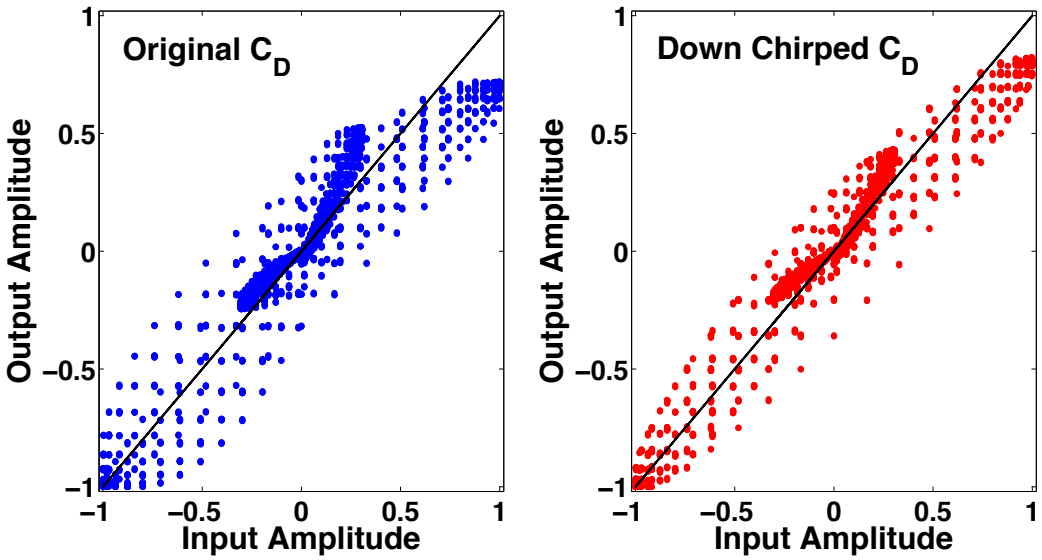

Figure 4.12: The input-to-output mapping for Abraha's combination after being passed through SOA, without (left) and with (right) chirping, where P-SOA=0 dBm, $I_{bias} = 250$ mA, $V_{pp} = 0.5V\pi$.

between pulses before and after SOA has been studied for different combinations of sinusoids, where the total set includes 4 frequencies, (f_1= 4 GHz, f_2= 6 GHz, f_3= 8 GHz, f_4= 10 GHz). Figure 4.10 reveals that a better correlation between electrical and optical (photo-detected after SOA) pulses is achieved for combinations based on a lower number of frequencies.

The 5-th derivative Gaussian pulse [29] besides to Doublets-based Abraha's combination (C_D) [30], have been the candidate waveforms in this work. That is due to their good power efficiencies and limited order of generation complexity, as mentioned in the previous chapter. To examine first the potential of chirping, several slopes have been considered for both waveforms. Figure 4.11 illustrates that a better cross correlation is being achieved at higher chirping slopes, while operating at a strong saturation point (0 dBm), promising with an enhancement in the pulse power efficiency when chirping is adopted. The dominance of the $5th$ Gaussian over C_D is due to original pulse dynamics. The highest slope (0.0472 ns/GHz) has been considered in the remaining part of the study. For a better clarification, we can see in fig. 4.12 the input-to-output amplitude mapping associated to Abraha's combination without (left) and with (right) chirping, the distribution of the points is more close to the linear response, that validates the effectiveness of our approach.

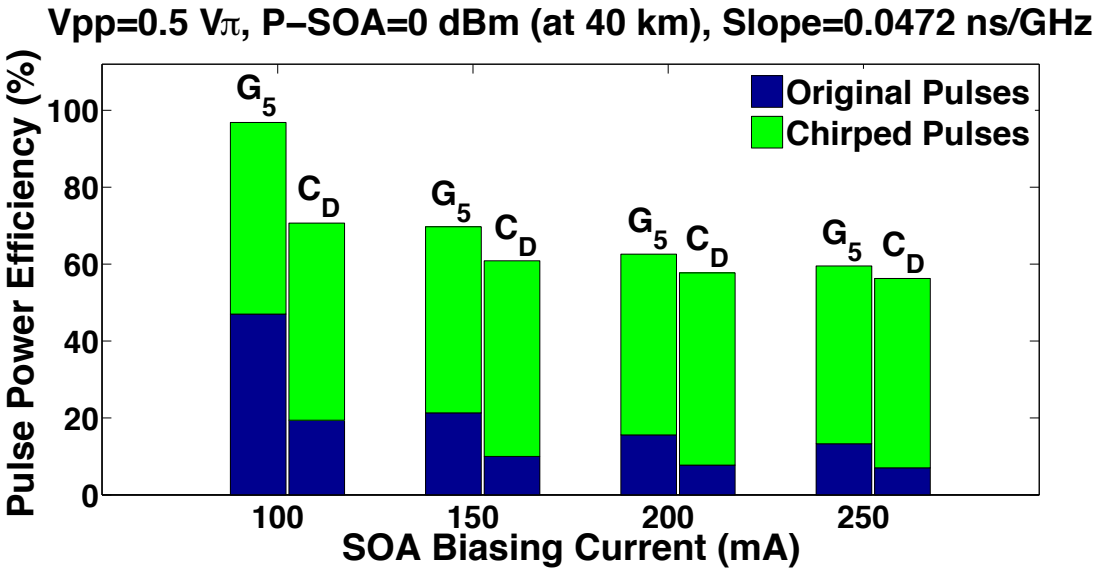

Figure 4.13: Power Efficiency of original and chirped pulses directly after SOA (at 40 km) for several biasing currents, where $Vpp = 0.5\,V\pi$ and P-SOA= 0 dBm.

4.4.3 Bias current influence

As mentioned in the third chapter, SOA nonlinearities depend on the biasing current, so the latter has to be considered while evaluating the chirping scheme performance. Figure 4.13 plots the power efficiency versus biasing current for the normal and chirped pulses, where P-SOA=0 dBm and V_{pp}=0.5 $V\pi$. Abraha's waveform is more sensitive to SOA nonlinear impairments, as the spectrum in electrical domain has a high 10 dB bandwidth, so any spectral deviation is enough to violate FCC mask, and a fast step-down in the efficiency will be obtained. For I_{bias}=100 mA, only a small decrease in the power efficiency is noticed for the 5th Gaussian with respect to the electrical domain response (table 4.2), unlike the combination of doublets where a significant degradation (close to 38 %) is observed. Operating at a larger biasing current leads to an increase in the saturation output power [28,31], which brings strong nonlinearities acting on the propagated pulses, and consequently lower power efficiencies are being obtained for both waveforms. After 200 mA, only a small change appears, as the amplifier reaches a saturated gain due to the high input power and current applied. The key point here is that we can always see an improvement for the chirped signals over original ones. The biasing current will be fixed at 250 mA for next simulations, as associated with the highest optical gain matching the request of reach extension.

4.4.4 Time waveforms and corresponding spectra of pulses with and without chirping

Figures 4.14 and 4.15 describe the time and frequency plots of candidate pulses in electrical domain and at the output of SOA (directly after photo-detector), where the spectra are plotted in the noise-free case (ASE noise not considered for spectrum readability). Resulting time distortions are characterized in terms of the power efficiency defined in the first chapter, as a non-coherent energy detection receiver is targeted. Table 4.2 states the parameters of applied waveforms, besides to the power efficiencies and spectral character-

Pulses	σ (ps)	η(%) Elec	f_{peak} (GHz)	B_3 (GHz)	B_{10} (GHz)	BL_{34} (GHz)	η(%) SOA
Original 5th Gaussian	51	50.7	7	3.43	6.17	6.11	13.7
Chirped 5th Gaussian	51	50.7	7.04	3.63	6.63	4.87	46.24
Original Abraha's Pulse	43.02	57.2	6.45	3.82	6.84	6.05	6.96
Chirped Abraha's Pulse	43.02	57.2	6.63	4.14	7.43	4.93	49.23

Table 4.2: Pulse Shaping Factors of electrical generated waveforms, and spectral characteristics (f_{peak}, B_3, B_{10}, BL_{34}) of corresponding pulses at SOA output (placed at 40 km). Besides to the power efficiencies (%) in electrical domain and after SOA, with P-SOA= 0 dBm, $I_{bias} = 250\ mA$, and $V_{pp} = 0.5\ V_{\pi}$.

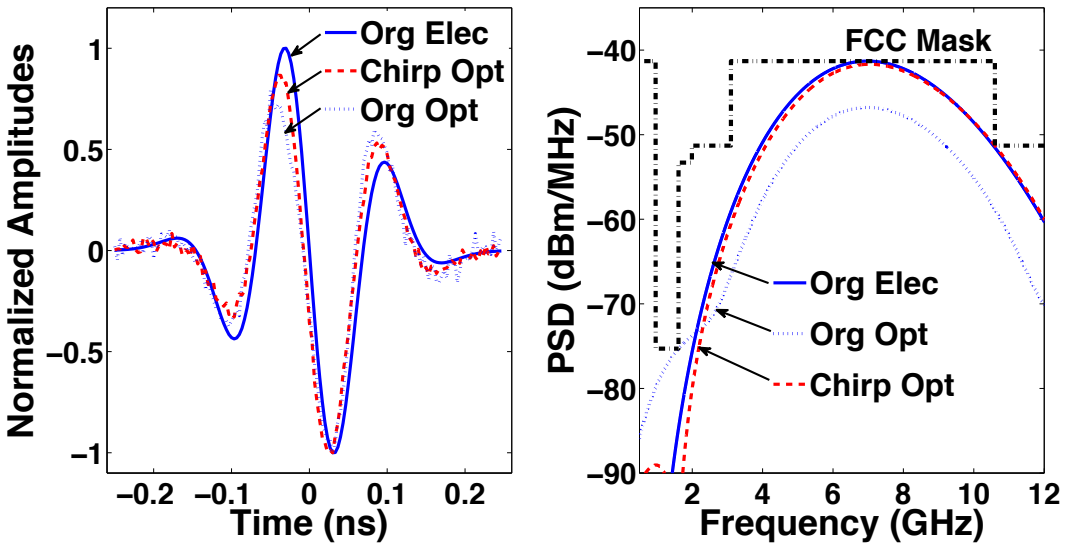

Figure 4.14: Original (Org) 5th Gaussian in electrical domain (Elec) and at SOA output (Opt), besides to the chirped (0.0472 ns/GHz) pulse after SOA.

istics evaluated at SOA output. Recall that BL_{34} is the left -34 dB bandwidth (distance between the lower frequency f_L and f_{peak}), which is useful to evaluate the spectrum in correspondence with GPS band. We can notice that the same waveforms are generated in electrical domain, and chirping has no drawback on the pulse spectral behavior, as also illustrated in fig. 4.16. A significant raise in the power efficiency is observed for both waveforms in figures 4.14 and 4.15, specially for Abraha's combination, where we have an increase in the 3 dB and 10 dB bandwidth, from 3.82 to 4.14 GHz and 6.84 to 7.43 GHz respectively, besides to the 1.12 GHz reduction in BL_{34}. Both permit for a step up in the PSD under FCC mask while covering a large spectral area without violating the regular limit, even in the most power restricted region corresponding to GPS band. The spectrum is centered at f_{peak}= 6.63 GHz, which is not so far from the middle of UWB mask (6.85 GHz). A lower power efficiency is recorded for the chirped 5th Gaussian with

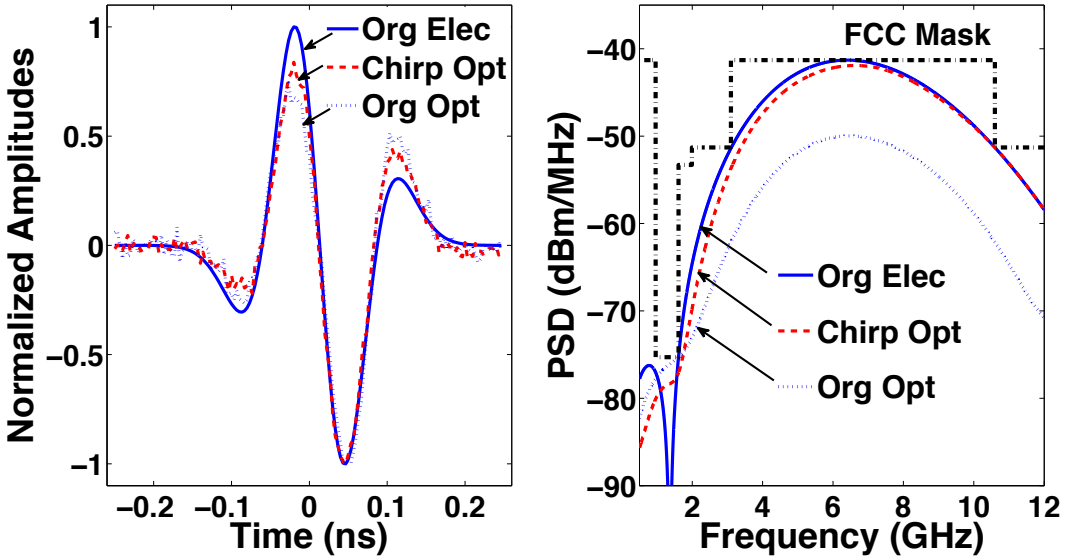

Figure 4.15: Original (Org) Abraha's combination in electrical domain (Elec) and at SOA output (Opt), besides to the chirped (0.0472 ns/GHz) pulse after SOA.

respect to Abraha's pulse after SOA, knowing that it has a higher cross correlation for the same conditions (fig. 4.11). This is due to the initial difference in the efficiency of electrical waveforms; otherwise, the optical-to-electrical ratio of the 5th Gaussian (46.24% / 50.7% = 0.91) is greater than for Abraha's combination (49.23% / 57.2% = 0.86). An important point to mention is that, not like usual linearization techniques, this approach is based on complementary pre and post-distortion being performed symmetrically on the transmitter and receiver sides. In the next section, we illustrate the potential of chirping considering a modulated signal passing over an optical fiber link.

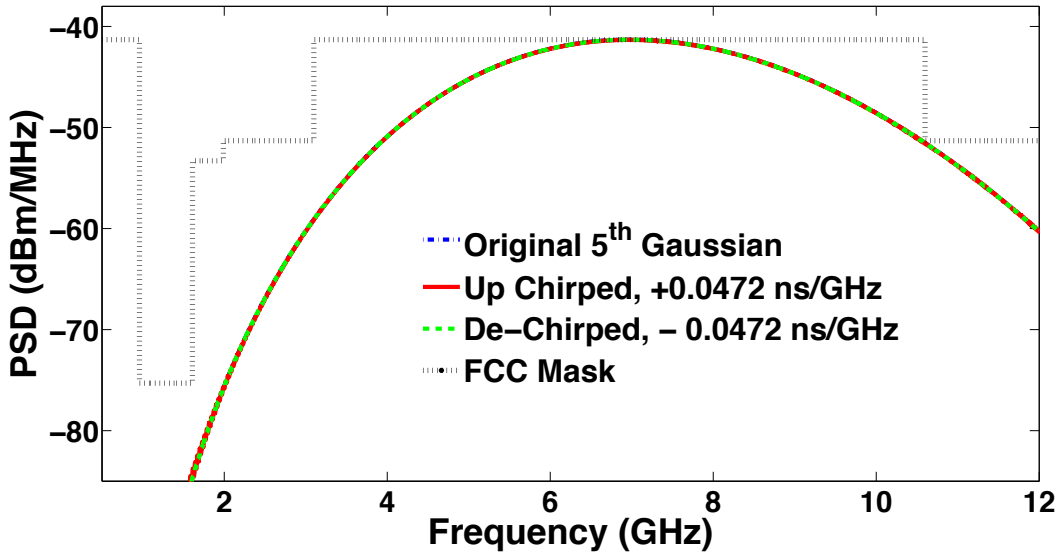

Figure 4.16: Power spectral density of the original, up chirped, and de-chirped 5^{th} Gaussian in electrical domain, where the chirping slope is 0.0472 ns/GHz.

4.5 Benefits of the chirping schemes for a modulated Impulse Radio propagating over an optical fiber

Like in previous investigations, we have to consider a modulated UWB signal passing through an optical link so as to examine the potential of chirping technique. Here, SOA operates at strong saturation (P-SOA=0 dBm) with a large biasing current (I_{bias} = 250 mA), where $V_{pp} = 0.5V\pi$ and the amplifier is placed 40 km apart from MZM. The two pieces of single mode fiber (before and after SOA) have an attenuation factor of 0.2 dB/Km and a chromatic dispersion of 17 ps/nm/km, we evaluate the performance in terms of the power efficiency for a modulated IR-UWB defined in the first chapter.

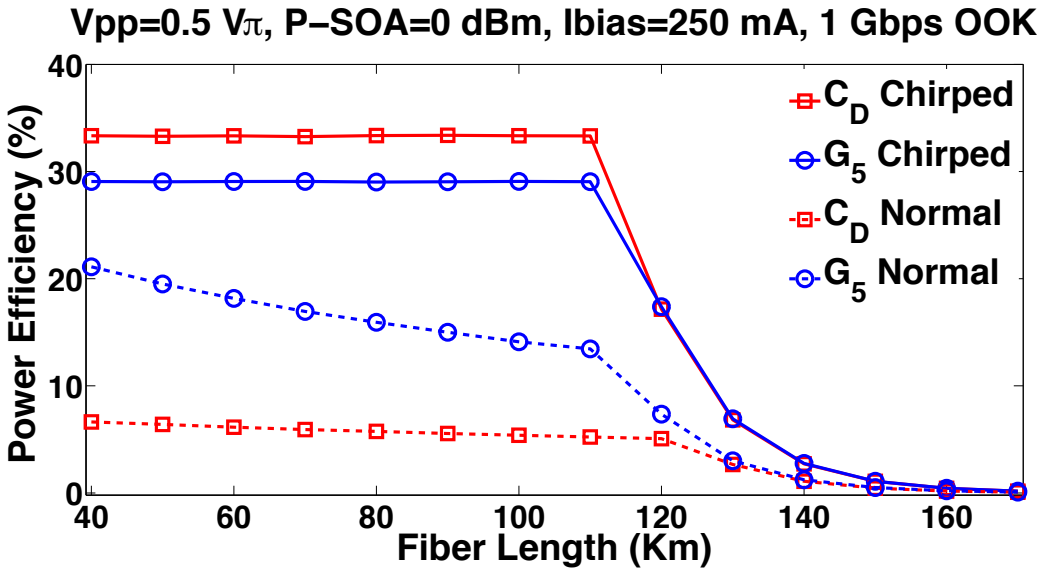

Figure 4.17: Power Efficiency versus fiber length for 1 Gbps OOK based on the utilized pulses, P-SOA=0 dBm, I_{bias} = 250 mA, $V_{pp} = 0.5V\pi$, where SOA is placed at 40 km.

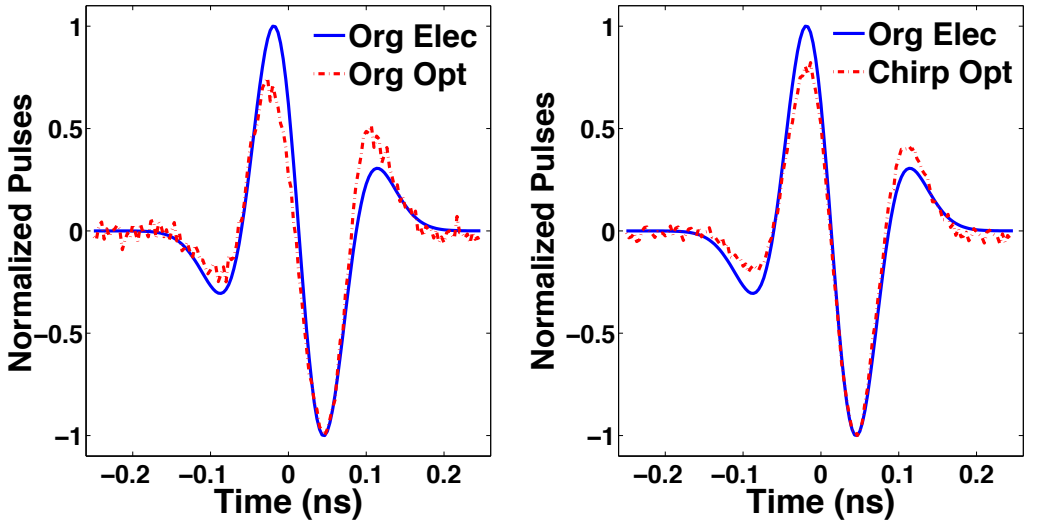

Figure 4.18: Abraha's combination at 100 km (60 km after SOA) with (right) and without (left) chirping, where P-SOA=0 dBm, I_{bias} = 250 mA, $V_{pp} = 0.5V\pi$.

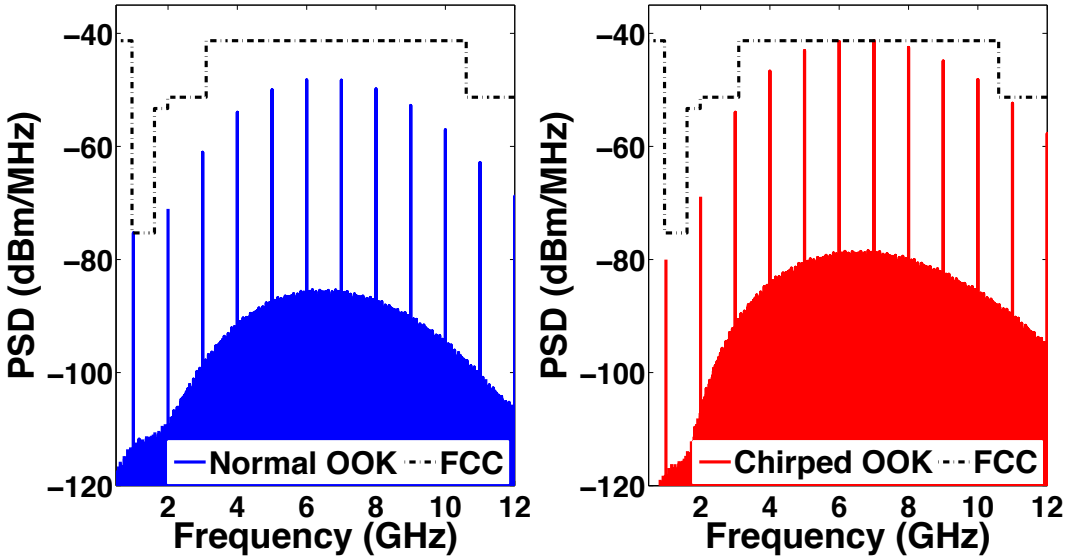

Figure 4.19: PSD of 1 Gbps OOK based on original (left) and chirped (right) Abraha's combination after SOA (at 40km), where P-SOA=0 dBm, $I_{bias} = 250$ mA, $V_{pp} = 0.5V\pi$.

In fig. 4.17 we can see the advantage of chirping technique considering a 1 Gbps OOK; for both waveforms the chirped signal outperforms the original one while traveling along a large enough distance, knowing that no pre-amplifier has been placed for modulated signals before the antenna. Recall, this improvement is justified by the fact that the envelope of spectral spikes for OOK or PPM takes the shape of basic transmitted waveform, so perfect pulse shapes lead to an efficient spectrum associated with the modulated impulse radio. Due to frequency shaping and deviation caused in fiber [32], the power efficiency decreases as the signal propagates over the optical channel, since the central frequency and B_{10} are no more preserved specially at large extension link. The flat response of the curves between 40 km and 110 km, is due to the fact that all spectra are already above FCC mask, therefore the signal has to be systematically attenuated so as to respect the standard limit. At large distances the spectrum goes under FCC mask; hence no need for up and down chirping, as nonlinearity becomes no more harmful. The time waveforms of Abraha's combination at 100 km has been plotted in fig. 4.18; as we can see, the de-chirped pulse has a better correlation with the electrical waveform than the original one. Not a high noise intensity is observed in these waveforms, as SOA operates in the saturation region. The power spectral density of the OOK signal based on C_D at SOA output is plotted in fig. 4.19. Obviously, the spectral shaping at low frequency band is the reason beyond efficiency enhancement, so a higher power level can be gained by the spectra when adapted to FCC mask, as also illustrated in fig. 4.20 for the case of 0.5 Gbps PPM. From fig. 4.21, we find out the same conclusion for PPM; hence, the proposed up-down chirping technique has proved to be effective for a coverage of 160 km, which can fit the demand of extended reach Fiber-to-the-Home (FTTH) networks [33]. Here we consider OOK and PPM formats with non-coherent energy detection; otherwise, chirping is a general approach which could be adopted with other modulation schemes. The performance gain is due to linearizing the SOA characteristics, which is theoretically not limited to any type of transmission. This approach outperforms pre-distortion from several aspects. In fact, here there is no need for a feedback in the electro-optical system to apply an optimization process, saving thus complexity and computational time. Since

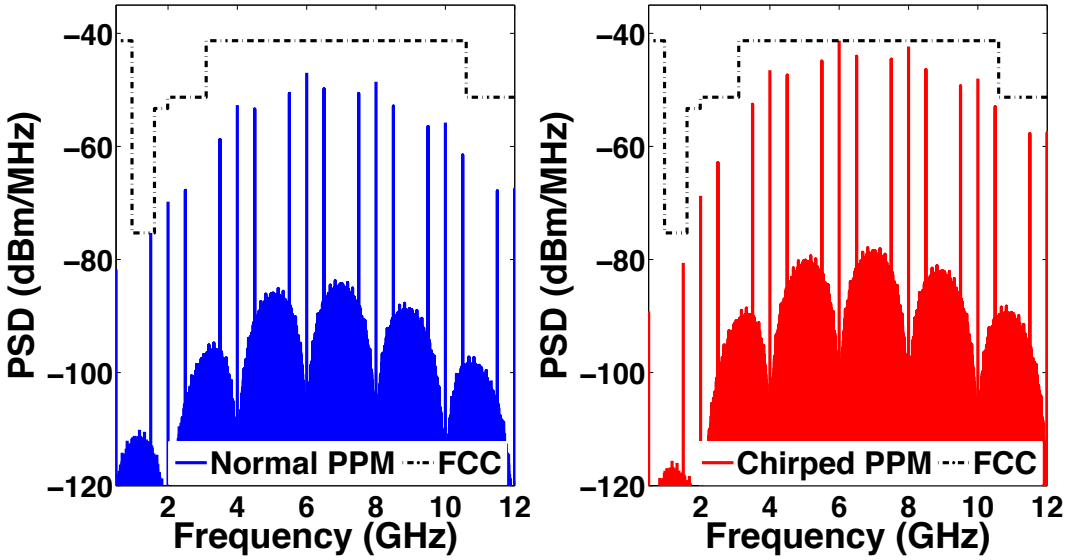

Figure 4.20: PSD of 0.5 Gbps PPM based on original (left) and chirped (right) Abraha's combination after SOA (at 40km), where P-SOA=0 dBm, $I_{bias} = 250$ mA, $V_{pp} = 0.5V\pi$.

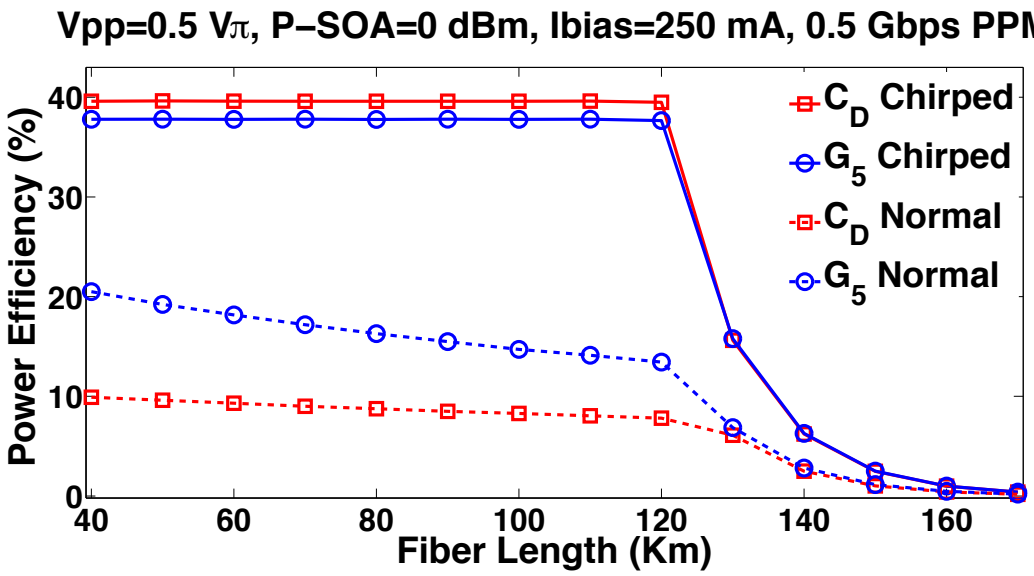

Figure 4.21: Power Efficiency versus fiber length for 0.5 Gbps PPM based on the utilized pulses, P-SOA=0 dBm, $I_{bias} = 250$ mA, $V_{pp} = 0.5V\pi$, where SOA is placed at 40 km.

with chirping, the improvement in the efficiency is relative to the slope of the phaser, accordingly it is a well known relation and not a search for the optimal settings. Besides, the new scheme performs well for both 5th Gaussian and Abrahas combination, unlike the previous approach which is more effective when adopted with combinations of waveforms. However, not the same effectiveness for chirping is expected when going towards practical implementations, since a performance degradation may occur due to the imperfections produced by commercial phasers. Besides, chirping-based transmission is sensitive to time jitter, as a perfect synchronization is required in order to reconstruct the original signal by down chirping. Also, it is difficult to make an exact symmetrical up/down chirping, some uncertainties are expected which may slightly distort the output received signals.

So till now, our approach seems to be pertinent from a theoretical point of view, while the real evaluation necessitates an experimental demonstration, that will be presented in the sequel. In this chapter, we show that pre-distortion and chirping schemes have the potential to enhance the transmission efficiency by optimizing the pulse spectrum, unfortunately, the power efficiency of the whole UWB signal is very low even for perfect pulse shapes, due to the discrete spectral spikes resulted from modulation pattern [34]. In the next chapter, a new spectrum smoothing technique is investigated as a complementary approach, which aims to reduce the intensity of these comb lines and improve the spectral efficiency of the whole transmitted UWB.

4.6 Summary

In this chapter, an analog up-down chirping technique has been applied in our SOA-based impulse radio over fiber system. The aim is to enhance the performance in terms of bit error rate and power efficiency. Utilizing phaser-based processing, we mitigated the order of SOA nonlinearity at strong saturation, besides to the ASE noise reduction at linear region. A significant increase in the pulse efficiency of the 5th Gaussian (>30%) and Abraha's combination (>40%) waveforms has been recorded. The potential of our approach has been examined considering a 1 Gbps OOK and 0.5 Gbps PPM modulation formats, a better bit error rate performance and higher power efficiencies have been achieved, while propagating over a large extension of single mode fiber. In the next chapter, we will show that besides to pre-distortion and chirping schemes, playing in the modulation pattern could be also pertinent for enhancing the transmission efficiency.

Bibliography

[1] A. D. McCoy, P. Horak, B. C., Thomsen, M. Ibsen, & D. J. Richardson, "Noise suppression of incoherent light using a gain-saturated SOA: Implications for spectrum-sliced WDM systems," *Journal of Light wave Technology*, 23(8), 2399, 2005.

[2] P. Baveja, D. N. Maywar, A. M. Kaplan, & G. P. Agrawal, "Self-phase modulation in semiconductor optical amplifiers: impact of amplified spontaneous emission," *IEEE Journal of Quantum Electronics*, 46(9), 1396-1403, 2010.

[3] H. Taki, S. Azou, A. Hamie, A. Al Housseini, A. Alaeddine and A. Sharaiha, "Simple pre-distortion schemes for improving the power efficiency of SOA-based IR-UWB over fiber systems," *Optics communications*, 382, 225-231, 2016.

[4] K. Roberts, L. Chuandong, L. Strawczynski, M. O'sullivan, and I. Hardcastle, "Electronic precompensation of optical nonlinearity," *IEEE Photon. Technol. Letters*, 18(1-4), 403-405, 2006.

[5] E. Ip and J. M. Kahn, "Compensation of dispersion and nonlinear impairments using digital back propagation," *J. Lightw. Technol.*, 26(20), 3416-3425, 2008.

[6] A. J. Lowery, "Fiber nonlinearity pre-and post-compensation for long-haul optical links using OFDM," *Optics Express*, 15(20), 12965-12970, 2007.

[7] J. Kim, & K. Konstantinou, "Digital predistortion of wideband signals based on power amplifier model with memory," *Electronics Letters*, 37(23), 1, 2001.

[8] R. Marsalek, P. Jardin, & G. Baudoin, "From post-distortion to pre-distortion for power amplifiers linearization," *IEEE Communications Letters*, 7(7), 308-310, 2003.

[9] X. Zhang, R. Zhu, D. Shen, and T Liu, "Linearization Technologies for Broadband Radio-Over-Fiber Transmission Systems," *Photonics*, vol. 1, no.4, pp. 455-472, 2014.

[10] C. Tai, S.-L. Tzeng, H.-C. Chang, and W. I. Way, "Reduction of non-linear distortion in mqw semiconductor optical amplifier using light injection and its application in multichannel m-qam signal transmission systems," *IEEE Photon. Technol. Lett.* , vol. 10, pp. 609–611, Apr. 1998

[11] F. Tabatabai, H. S. Al-Raweshidy, "Feed-Forward Linearization Technique for Reducing Non-Linearity in Semiconductor Optical Amplifier," *J. Lightw. Technol.*, vol.25, No. 9, pp.2667-2674, Sep. 2007.

[12] Ying, K., Chen, D., Pan, Z., Zhang, X., Cai, H., & Qu, R. (2016, November). Intensity noise reduction technique of fiber laser via intracavity SOA structure. In Asia Communications and Photonics Conference (pp. AS1A-4). Optical Society of America.

[13] B. Nikfal, Q. Zhang, & C. Caloz, "Enhanced-SNR impulse radio transceiver based on phasers," *IEEE Microwave and Wireless Components Letters*, 24(11), 778-780, 2014.

[14] Lin, Y. J., Hsu, S. S., Jin, J. D., & Chan, C. Y. (2007). A 3.1–10.6 GHz ultra-wideband CMOS low noise amplifier with current-reused technique. IEEE Microwave and Wireless Components Letters, 17(3), 232-234.

[15] Liao, C. F., & Liu, S. I. (2007). A broadband noise-canceling CMOS LNA for 3.1–10.6-GHz UWB receivers. IEEE Journal of Solid-State Circuits, 42(2), 329-339.

[16] Bevilacqua, A., & Niknejad, A. M. (2004). An ultrawideband CMOS low-noise amplifier for 3.1-10.6-GHz wireless receivers. IEEE Journal of solid-state circuits, 39(12), 2259-2268.

[17] Yu, Y. H., Chen, Y. J. E., & Heo, D. (2007). A 0.6-v low power uwb cmos lna. IEEE microwave and wireless components letters, 17(3), 229-231.

[18] Moez, K., & Elmasry, M. I. (2008). A low-noise CMOS distributed amplifier for ultra-wide-band applications. IEEE transactions on Circuits and systems II: Express briefs, 55(2), 126-130.

[19] Chen, K. H., & Liu, S. I. (2012). Inductorless wideband CMOS low-noise amplifiers using noise-canceling technique. IEEE Transactions on Circuits and Systems I: Regular Papers, 59(2), 305-314.

[20] Ho, S. S., & Saavedra, C. E. (2010). A CMOS broadband low-noise mixer with noise cancellation. IEEE Transactions on Microwave Theory and Techniques, 58(5), 1126-1132.

[21] Heydari, P. (2007). Design and analysis of a performance-optimized CMOS UWB distributed LNA. IEEE Journal of Solid-State Circuits, 42(9), 1892-1905.

[22] Q. Zhang, D. L. Sounas, & C. Caloz, "Synthesis of cross-coupled reduced-order dispersive delay structures (DDSs) with arbitrary group delay and controlled magnitude," *IEEE Transactions on Microwave Theory and Techniques*, 61(3), 1043-1052, 2013.

[23] B. Nikfal, B., S. Gupta, & C. Caloz, "Increased group-delay slope loop system for enhanced-resolution analog signal processing," *IEEE Transactions on Microwave Theory and Techniques*, 59(6), 1622-1628, 2011.

[24] B. Nikfal, D. Badiere, M. Repeta, B. Deforge, S. Gupta, & C. Caloz, "Distortion-less real-time spectrum sniffing based on a stepped group-delay phaser," *IEEE microwave and wireless components letters*, 22(11), 601-603, 2012.

[25] Zhang, Q., Gupta, S., & Caloz, C. (2012). Synthesis of narrowband reflection-type phasers with arbitrary prescribed group delay. IEEE Transactions on Microwave Theory and Techniques, 60(8), 2394-2402.

[26] Gupta, S., Zhang, Q., Zou, L., Jiang, L. J., & Caloz, C. (2015). Generalized coupled-line all-pass phasers. IEEE Transactions on Microwave Theory and Techniques, 63(3), 1007-1018.

[27] L. Cohen, Time-Frequency Analysis. Englewood Cliffs, NJ: Prentice-Hall, 1995.

[28] M. J. Connelly, Semiconductor Optical Amplifiers. Boston, MA:Kluwer, 2002.

[29] H. Jin, L. Jiang, W. Hao, C. Sheng, H. Qijun, and Z. Yueping, "A CMOS fifth-derivative Gaussian pulse generator for UWB applications," *Journal of Semiconductors*, 35(9), 095005, 2014.

[30] S.T. Abraha, C. Okonkwo, P. A. Gamage, E. Tangdiongga, and T. Koonen, "Routing of power efficient IR-UWB wireless and wired services for in-building network applications," *J. Lightw. Technol.*, 30(11), pp. 1651-1663, 2012.

[31] Hsu, D. Z., Lee, S. L., Gong, P. M., Lin, Y. M., Lee, S. S., & Yuang, M. C. (2004). High-efficiency wide-band SOA-based wavelength converters by using dual-pumped four-wave mixing and an assist beam. IEEE Photonics Technology Letters, 16(8), 1903-1905.

[32] Pan, S., & Yao, J. (2010). Performance evaluation of UWB signal transmission over optical fiber. IEEE Journal on selected areas in communications, 28(6).

[33] R. Llorente, T. Alves, M. Morant, M. Beltran, J. Perez, A. Cartaxo, and J. Marti, "Ultra-wideband radio signals distribution in FTTH networks," *IEEE Photon. Technol. Lett.*, 20(11), pp. 945-947, 2008.

[34] Nakache, Y. P., & Molisch, A. F. (2003, April). Spectral shape of UWB signals-influence of modulation format, multiple access scheme and pulse shape. In Vehicular Technology Conference, 2003. VTC 2003-Spring. The 57th IEEE Semiannual (Vol. 4, pp. 2510-2514). IEEE.

Chapter 5

Improving the Power Efficiency of the UWB over Fiber System via Pulse Shape Randomization

In the two previous chapters, we show that simple pre-distortion schemes besides to analog chirping techniques are capable to enhance the power efficiency of transmitted pulses. However, the modulation format can also play a significant role in determining the efficiency of the whole transmission, as mentioned in the introduction. In this chapter, a simple pulse shape randomization scheme is introduced for improving the performance of UWB communication systems using On Off Keying (OOK) or Pulse Position Modulation (PPM) formats. The advantage of the proposed scheme, which can be either employed for Impulse Radio or for carrier-based systems, is first theoretically studied based on closed-form derivations of power spectral densities. Then, we investigate an application to our IR-UWB over optical fiber system, by utilizing the 4-th and 5-th orders of Gaussian derivatives. Our approach proves to be effective for 1 Gbps-PPM and 2 Gbps-OOK transmissions, with an advantage in terms of power efficiency at short distances, which could be eventually broadened by the use of SOA in-line amplifier.

5.1 Introduction

As stated in the introduction, the power limitation of FCC against UWB operation has raised the need for highly efficient UWB transmission [1], hence pulse shaping and spectrum smoothing are mandatory to increase the transmitted power without violation of FCC regular limit [2]. Pulse shaping can improve the envelope of the overall spectrum, but has no influence on the discrete spectral peaks resulting from modulation patterns. Smoothing the spectrum of modulated signals requires a change in the statistical properties of the pulse train, time randomization being important so as to reduce the intensity of frequency comb lines. Direct sequence (DS) and Time Hopping (TH) are the mostly utilized randomization techniques, based on varying the pulse amplitude or time position respectively [3–5]. The main drawback for DS is the complexity associated with multilevel generation, and randomizing in terms of polarity [6] is not suitable for unipolar encoding like OOK or PPM. Hopping the pulse position between different chips in case of TH requires a larger symbol duration, which consequently lowers the data rate and may not be pertinent for high speed applications. In this work, a simple randomization technique is adopted for improving the system performance; it consists in changing the pulse

waveform over time while keeping the same time location and scaling factor. The energy per bit is conserved for all transmitted frames/symbols, in order to fit the requirement of non-coherent energy-detection based UWB systems [7]. The proposed Multi-Waveform OOK (MWOOK) and Multi-Waveform PPM (MWPPM) modulation schemes have been applied to the Radio over Fiber system introduced in the second chapter. Our scheme has proved a better power efficiency at short and broad distances of fiber, without and with using SOA respectively.

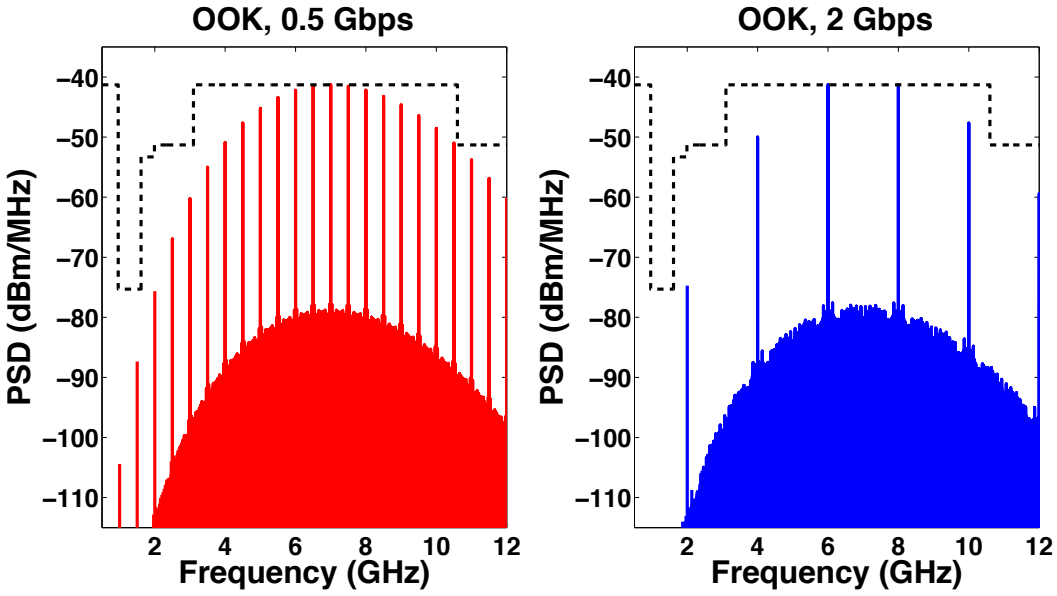

Figure 5.1: The power spectral density for 0.5 Gbps (left) and 2 Gbps (right) OOK signal based on the 5^{th} derivative Gaussian pulse.

5.2 Discrete Spectral Lines in Impulse Radio Systems

Studying the spectral behavior of the transmitted UWB signal is a key point for analyzing the interference effects against other existing wireless systems. An impulse radio signal $w(t)$ with a fixed frame T can be expressed as

$$w(t) = \sum_k a_k p(t - T_k) \tag{5.1}$$

where $T_k = kT + \varepsilon_k$ and $p(t)$ is the basic transmitted waveform, a_k and ε_k are considered as two random processes related to the original data. Equation 5.2 describes the power spectral density of $w(t)$, where $c_k(f) = a_k e^{-2\pi j f \varepsilon_k}$ [8]. A bad spectral phenomenon appears with this pattern of transmission, presented by the spectral spikes located at multiples of frame repetition frequency, these discrete lines are due to periodicity in time domain. Figure 5.1 displays the spectrum of an OOK modulated UWB operating at 0.5 Gbps (left) and 2 Gbps (right), based on the 5^{th} derivative Gaussian pulse. As shown, the distance between frequency comb lines exactly equals to the data rate, and a significant degradation in the transmitted signal power occurs due to these spectral peaks.

$$S_w(f) = \left|P(f)\right|^2 \Big[\frac{\sigma_c^2(f)}{T} + \frac{|\mu_c(f)|^2}{T^2} \sum_k \delta\big(f - \frac{k}{T}\big)\Big] \tag{5.2}$$

5.3 Existing Randomization Techniques

Smoothing the spectrum requires randomizing the transmitted signal in order to reduce periodicity in time domain. Till now, two randomization schemes have been investigated in the literature, the first is based on changing the pulse position inside the transmitted frame, called Time Hopping (TH) [3–5]. The other is Direct Sequence (DS) [6], which consists in randomizing the amplitude of the transmitted waveform without varying its time location.

5.3.1 Time Hopping

Equation 5.3 describes the time hopped UWB signal modulated by PPM, where T_s is the symbol period, T_f is the frame duration, N_s is the number of frames per symbol, T_c denotes the chip time, c_j corresponds to the j^{th} chip, δ is the modulation index of PPM, and d_k denotes the k^{th} data bit. Similarly for the case of Pulse Amplitude Modulation (PAM), the transmitted time signal is expressed in equation (5.4). Figure 5.2 shows the time waveform of a TH-PPM, with a processing gain of N_s=5, exactly equals to the number of chips, where the chip code is c=[2 5 3 1 4] and T_c=1 ns. Increasing the number of chips leads to a higher degree of randomization, which consequently improves the spectrum at the cost of data rate.

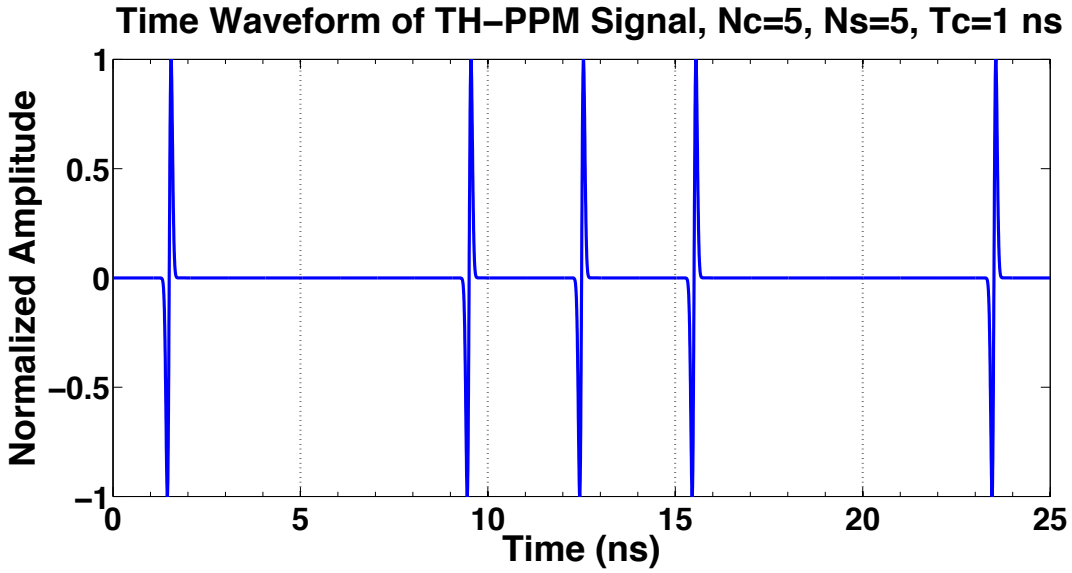

Figure 5.2: Time Representation for 1 symbol extracted from a TH-PPM signal, consisting of 5 frames/symbol, and 5 chips/frame, the TH code is [2 5 3 1 4] and T_c=1 ns, where the basic transmitted pulse is the Gaussian Monocycle.

$$s_{TH-PPM}(t) = \sum_{k} \sum_{j=0}^{N_s-1} p(t - kT_s - jT_f - c_jT_c - d_k\delta) \tag{5.3}$$

$$s_{TH-PAM}(t) = \sum_{k} \sum_{j=0}^{N_s-1} d_k p(t - kT_s - jT_f - c_jT_c) \tag{5.4}$$

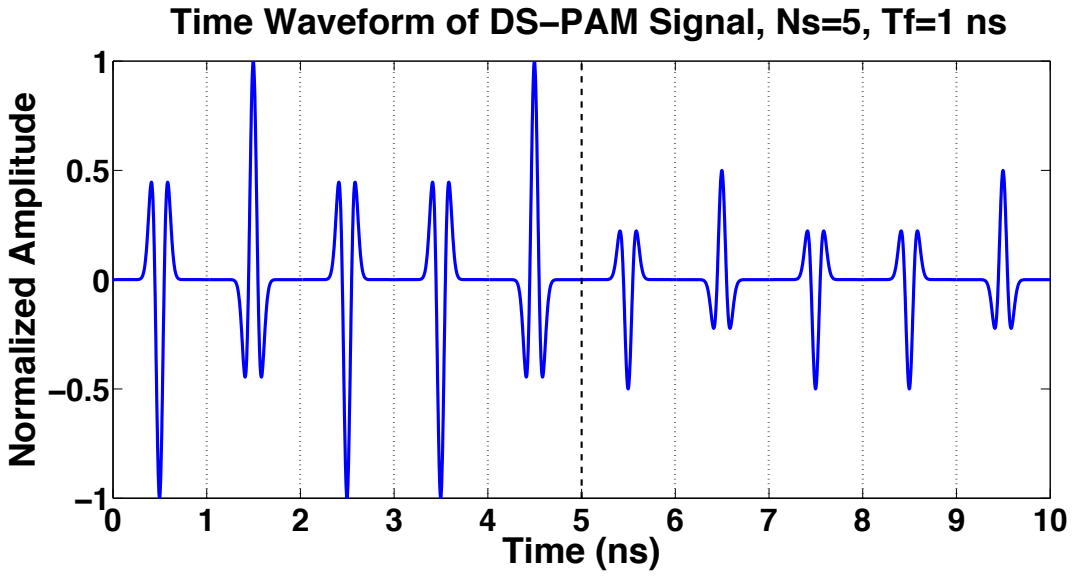

Figure 5.3: Time Representation for 2 symbols extracted from a DS-PAM signal, consisting of 5 frames/symbol, the DS code is [1 -1 1 1 -1] and T_f=1 ns, where the basic transmitted pulse is the Gaussian Doublet.

5.3.2 Direct Sequence

With this scheme, a random sequence is multiplied by the transmitted pulses instead of changing their time location inside each frame. The formula of the DS signal modulated by PAM is expressed in (5.5), where all parameters are the same as has been defined for TH. Figure 5.3 describes the time waveforms of 2 consecutive symbols with a DS code of [1 -1 1 1 -1], the first bit is 1 and the other is 0, where the utilized waveform is the Gaussian Doublet. The number of frames per symbol is $N_s = 5$, where T_f= 1 ns (which is not divided into chips). It is clear how the polarity of transmitted pulses is reversed between different frames inside each symbol. (Here the same code is used for the 2 symbols just for a better readability). This technique outperforms Time Hopping in terms of spectral lines reduction and data rate, unfortunately it requires more complexity as two power supplies are needed to generate pulses with opposite polarities. This scheme is not suitable for PPM modulation format, since the time delay is not considered in the randomization process.

$$s_{DS-PAM}(t) = \sum_{k} \sum_{j=0}^{N_s-1} d_k c_j p(t - kT_s - jT_f) \tag{5.5}$$

5.4 Proposed Multi-Waveform OOK/PPM Modulation Formats

Conventional OOK and PPM impulse radio signals correspond to a stream of modulated pulses via amplitude or position, respectively. The same pulse is systematically repeated along different transmitted frames, leading to a periodicity in time domain and hence to high spectral spikes. Our approach aims to alleviate this undesirable properties by changing the pulse shape over time while conserving the digital modulation format principle. Adjusting the pulse waveform is not new in UWB communications [9], but here it is for

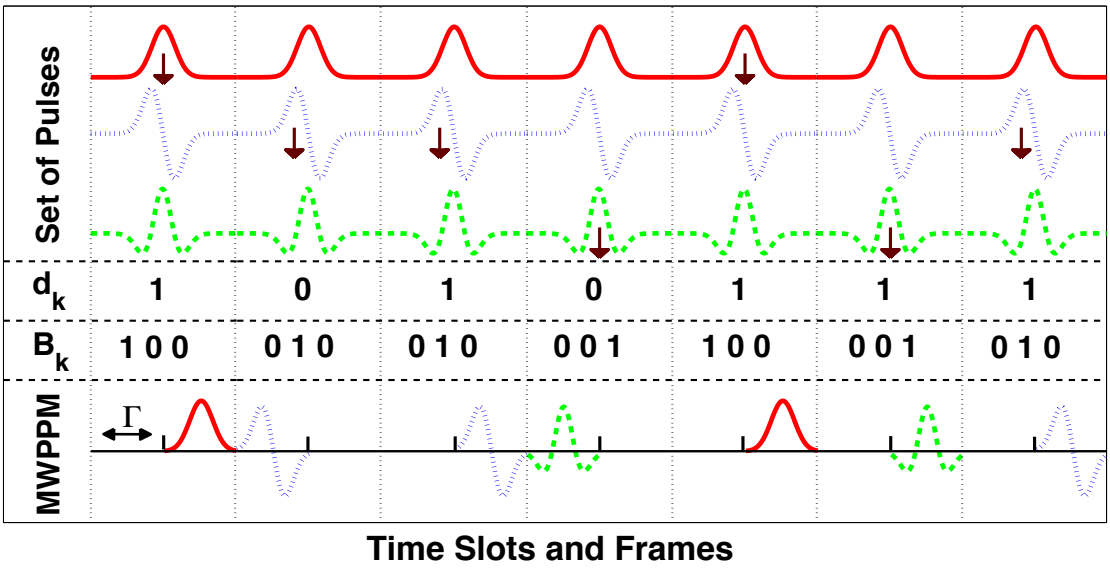

Figure 5.4: A simple description for Multi-Waveform PPM transmission, where each frame consists of 2 time slots.

randomization purpose and not for modulation. In case of an OOK-modulated signal, the proposed Multi-Waveform OOK scheme consists in transmitting different pulse shapes for the bit '1', each pulse being selected randomly from a particular set $\mathcal{P}$ containing N candidate waveforms, and no transmission is done for bit '0' as in the conventional scheme. The transmitted signal is then expressed as

$$w_{MWOOK}(t) = \sum_{k} \sum_{j=1}^{N} b_{j,k} d_k p_j(t - kT) \tag{5.6}$$

where $d_k \in \{0,1\}$ denotes the binary data to transmit, T is the frame duration, and $b_{j,k} \in \{0,1\}$ stands for the j^{th} bit of the N-bits coded number $B_k = (2^{R(k)})_2$, with $R(k)$ being a random integer from the uniform distribution on the interval $[0, N-1]$. Hence, $\sum_{j=1}^{N} b_{j,k} = 1$ which means that only one pulse p_j is triggered in the set $\mathcal{P}$.
Similarly, as illustrated in fig. 5.4, a Multi-Waveform PPM can be expressed as

$$w_{MWPPM}(t) = \sum_{k} \sum_{j=1}^{N} b_{j,k} p_j(t - kT - d_k\Gamma) \tag{5.7}$$

where Γ denotes the modulation index.

As different pulses are involved in the randomization process, no correlation must appear between any 2 waveforms from the set $\mathcal{P}$ over the pulse interval T, (notice that frame duration is considered to be equal to the pulse period in this work) :

$$\int_0^T p_m(t) p_n(t) \mathrm{d}t = 0 \quad \forall m \neq n \tag{5.8}$$

Following a similar approach than that used in [8], closed-form expressions of the power

spectral densities (PSDs) can be easily derived for the proposed MWOOK/MWPPM formats (see the Appendix in this chapter for an outline of the proof). For MWOOK, we get the following PSD expression:

$$S_{MWOOK}(f) = \left|\sum_{j=1}^{N} P_j(f)\right|^2 \left[\frac{\mu_d^2}{T}\Big(\frac{2}{N} - \frac{1}{N^2}\Big) + \frac{\mu_d^2}{N^2T^2}\sum_k \delta\big(f - \frac{k}{T}\big)\right] \tag{5.9}$$

where μ_d stands for the expectation of the binary data d_k and $P_j(f)$ is the spectrum of pulse $p_j(t)$. For the MWPPM format, the PSD takes the form

$$S_{MWPPM}(f) = \left|\sum_{j=1}^{N} P_j(f)\right|^2 \left[\frac{1}{T}\Big(\frac{1}{N} - \frac{|\mu_m|^2}{N^2}\Big) + \frac{|\mu_m|^2}{N^2T^2}\sum_k \delta\big(f - \frac{k}{T}\big)\right] \tag{5.10}$$

where $\mu_m = cos(\pi f \Gamma)$ is the expectation of the random process $m_k = e^{-j2\pi f \varepsilon_k}$ in the spectral domain, with $\varepsilon_k = d_k\Gamma$.

With the view to characterize the spectrum smoothness, we define the Discrete to Continuous Spectral Ratio ($DCSR$) as the factor multiplying the series of frequency comb lines divided by the continuous part of the spectrum. For the MWOOK scheme we obtain the following expression

$$DCSR_{MWOOK} = \frac{1}{T\big(2N-1\big)} \tag{5.11}$$

whereas for MWPPM the ratio takes the form

$$DCSR_{MWPPM} = \frac{|\mu_m|^2}{T\big(N - |\mu_m|^2\big)} \tag{5.12}$$

The DCSR criterion has been established based on theoretical PSD expressions; so, this criterion will no longer be suited to spectral estimates. In the sequel, we will adopt a complementary principle for assessing the benefits of randomization, the Peak-to-Average Spectral Ratio ($PASR$), corresponding to the mean of discrete lines intensity divided by the average of the overall power spectral density. We will also consider the important criterion of power efficiency for a modulated signal defined in chapter two. From Eqs. 5.11 and 5.12, it can be clearly seen that increasing the number N of pulses tends to decrease the DCSR, which can result in a better power efficiency as will be illustrated in the next section. Note also that for a unit processing gain transmission, the data rate is $R_b = 1/T$, so the DCSRs are linear with R_b. A critical step for taking advantage of the randomized signals is the design of the set of candidate pulses $\mathcal{P}$. One obvious constraint is to conserve energy per bit for all transmitted frames. In addition, we must ensure that the pulses are all mutually uncorrelated (Eq. 5.8). There are mainly two approaches to achieve this goal, either the transmitter relies on sine and cosine waves with use of local oscillators, or the transmitter directly operates in baseband (Impulse Radio system). The two solutions are investigated in the next section.

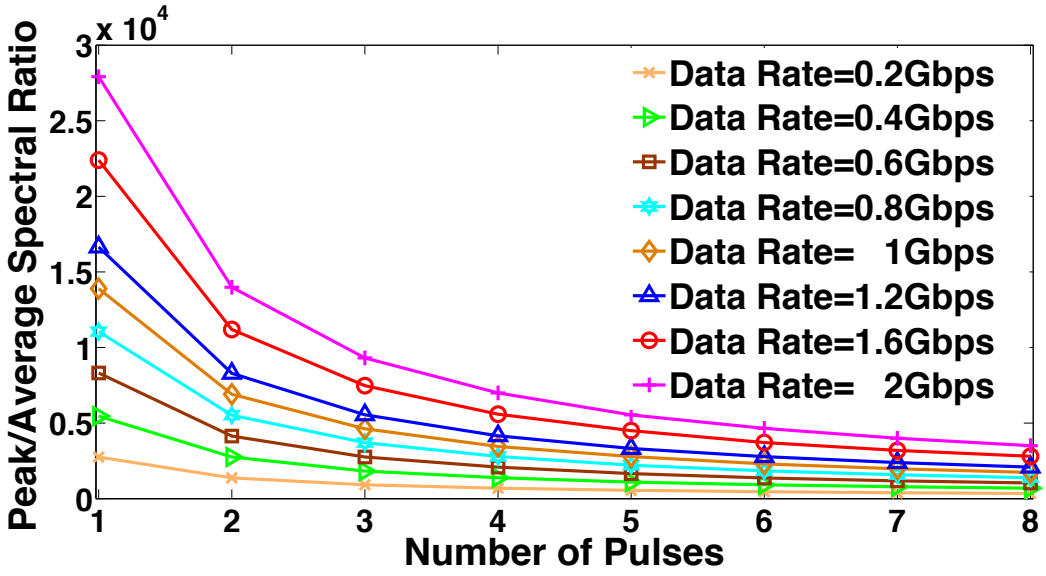

Figure 5.5: The Peak-to-Average Spectral Ratio versus number of pulses used for OOK randomization, at different data rates.

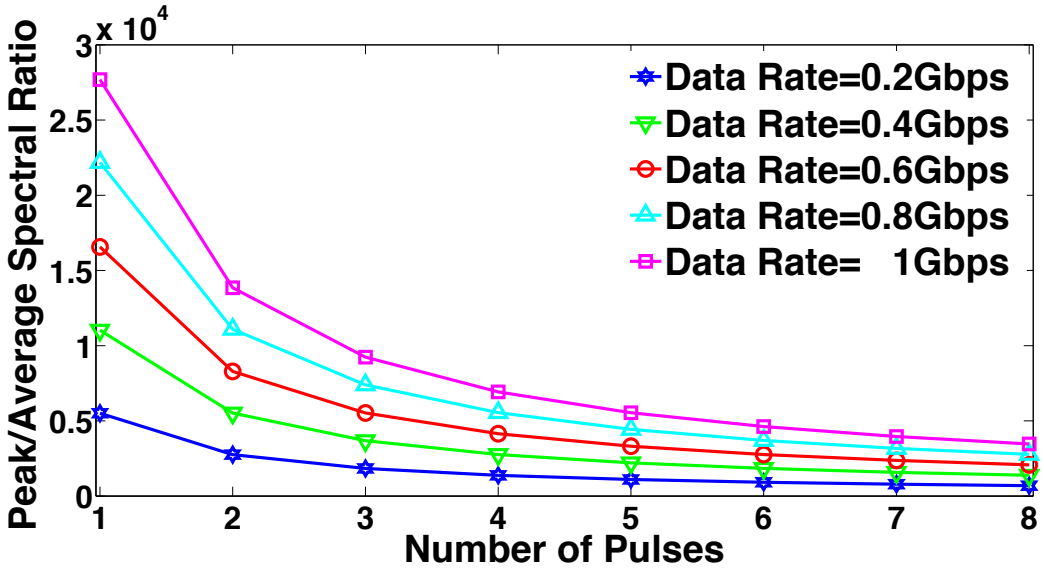

Figure 5.6: The Peak-to-Average Spectral Ratio versus number of pulses used for PPM randomization, at different data rates.

5.5 Carrier-Based versus Carrierless Shape Randomization Techniques

5.5.1 Carrier-Based Randomization

To satisfy the decorrelation constraint for a system using local oscillators with inphase and quadrature components, we can design a set $\mathcal{P}$ of rectangular pulses modulated by sine waves at frequencies f_n, $n = 1, 2, ..., N/2$; in this case, the orthogonality is ensured

provided that

$$\int_{-\frac{T}{2}}^{+\frac{T}{2}} \sin(\frac{2\pi f_i t}{T})\sin(\frac{2\pi f_j t}{T})\mathrm{d}t \ = 0, \forall i \neq j \tag{5.13}$$

This is also true in case of sine and cosine waves operating at same frequency. For the purpose of illustration, if we consider a system operating with a pulse period T of 0.5 ns, we can identify 4 frequencies satisfying the orthogonality condition over the [3.1,10.6] GHz band: $f_1 = 4$ GHz , $f_2 = 6$ GHz , $f_3 = 8$ GHz , $f_4 = 10$ GHz; thus, with 4 local oscillators and using inphase and quadrature components we can get $N = 8$ pulses. With this approach, the pulse shape randomization results from a random selection of the sinusoid. As observed in fig. 5.5 and fig. 5.6, for both modulation types (MWOOK and MWPPM, respectively), the PASR decreases when increasing the number N of pulses, which means a lower intensity of discrete spectral lines and hence a much more effective randomization. As already pointed out, the frequency comb lines grow linearly with R_b, so the benefits of using a large set $\mathcal{P}$ is more pronounced at high bit rate but at the price of an increased complexity. The power spectral density for 2 Gbps classical OOK is shown in fig. 5.7,

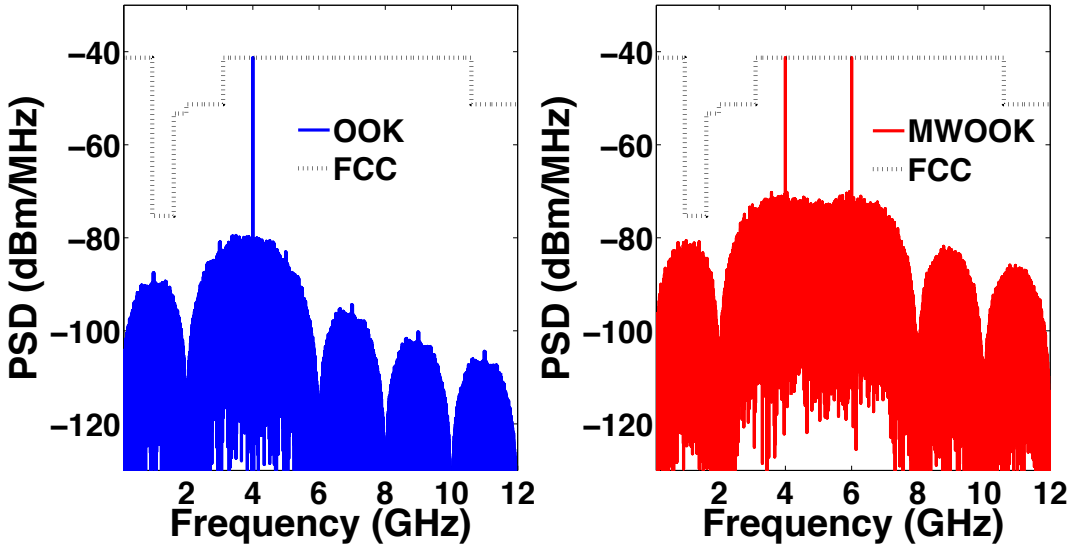

Figure 5.7: Power Spectral Densities of 2Gbps standard OOK (left) and multi-waveform OOK based on 4 pulses (right).

besides to the spectrum of multi-waveform one based on 4 pulses. In fig. 5.8, the spectrum corresponds to 1 Gbps classical and multi-waveform PPM with same N as in MWOOK (4 pulses). The absence of discrete lines at odd multiples of data rate is due to the zero-crossings of sinc spectrum resulting from the 0.5 ns rectangular pulse. PPM time shift is fixed at $\Gamma = 0.5$ ns, which is required for non-coherent energy detector receiver. The discrete spectral term is scaled by $cos^2(.)$ as described in (5.10) associated with spectral peaks located at even multiples of data rate, this is a bad spectral phenomenon as comb lines have a higher intensity for PPM than OOK. On the other hand, thanks to the zero crossings of oscillating term which eliminate spectral lines at odd multiples of bit rate, specially at 1 GHz inside GPS band ([0.96-1.61] GHz). As smoothing the power spectral density permits to step-up the spectrum level without violating FCC mask, we can see in fig. 5.9 a raise in the power efficiency as we increase the number N of randomizing pulses. Simulations were done for a 1 Gbps-MWPPM and 2 Gbps-MWOOK. The lower

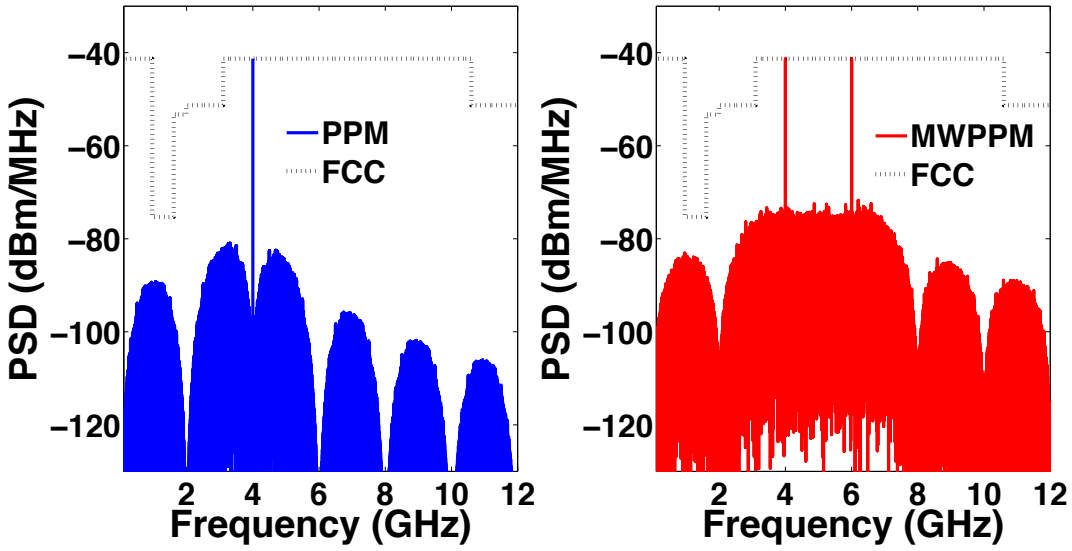

Figure 5.8: Power Spectral Densities of 1 Gbps classical PPM (left) and MWPPM based on 4 pulses (right).

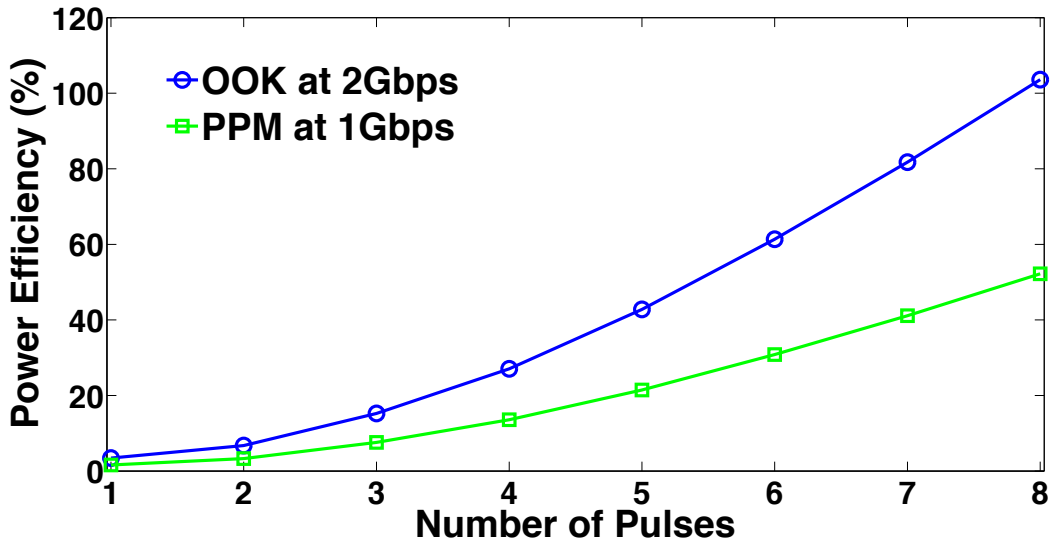

Figure 5.9: Power Efficiency versus the number of pulses used for 2 Gbps MWOOK and 1 Gbps MWPPM.

power efficiency associated with PPM is due to the strong spectral peaks described above. In terms of average power, our randomization scheme shows a consequent improvement with respect to OOK and PPM as observed in fig. 5.10. That promises with a SNR enhancement when applied in real transmission systems.

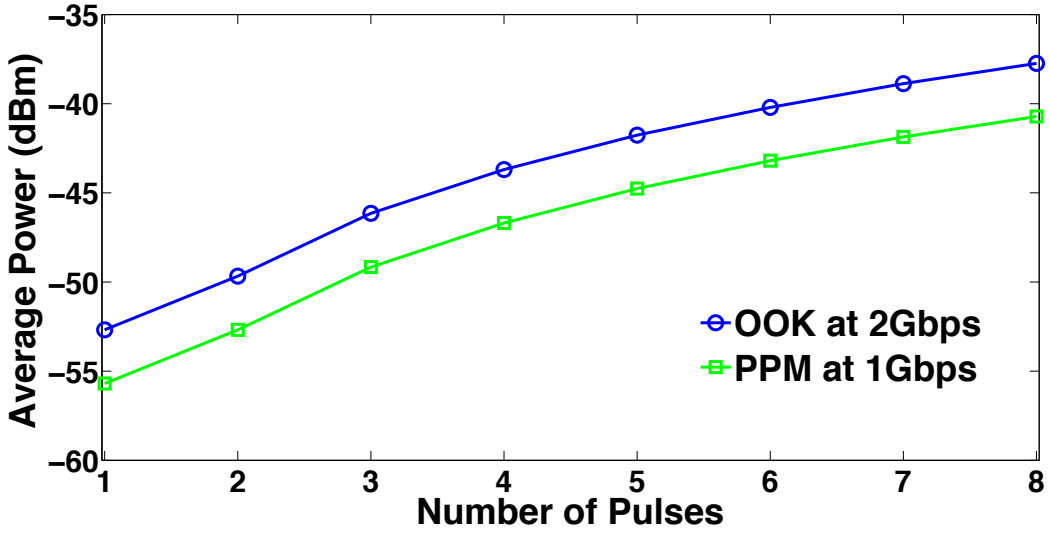

Figure 5.10: Average Power versus the number of pulses used for 2 Gbps MWOOK and 1 Gbps MWPPM.

5.5.2 Carrierless Randomization

The interest of the previous approach is that it gives us some performance bounds for MWOOK and MWPPM schemes, but evidently the use of local oscillator(s) translates into an increase of complexity with respect to a carrierless scheme, which may not be suitable for practical applications. In this section, we investigate the alternate solution of a baseband system (IR-UWB). With the aim of designing a simple low cost system, we

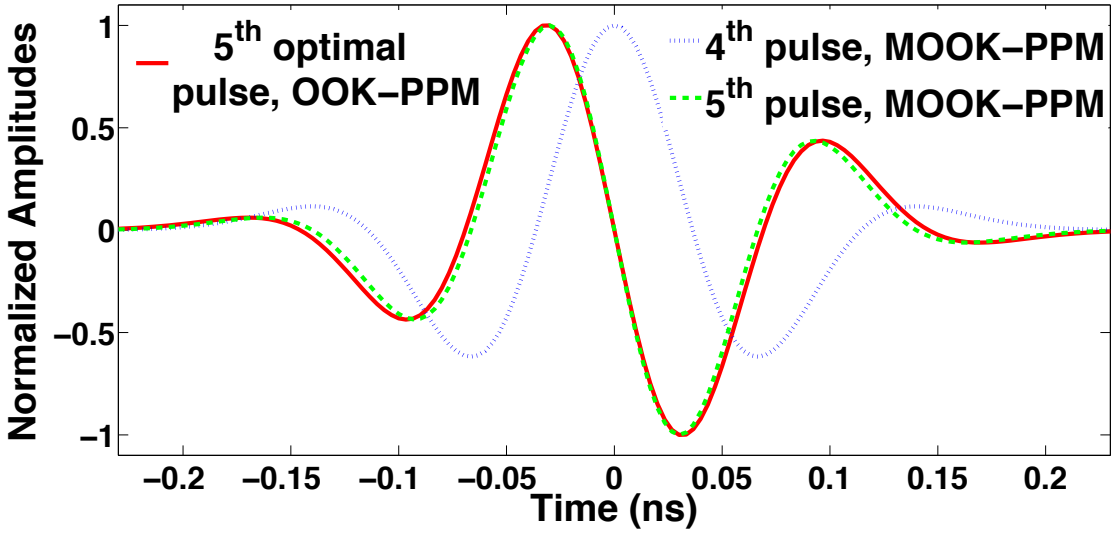

Figure 5.11: The 5-th optimal Gaussian used for OOK-PPM, besides to 4-th/5-th pulses utilized with MWOOK-MWPPM.

focus on the case where only two pulse waveforms are used for achieving the randomization. There is not a unique choice for the two elementary pulses, but we typically have to respect key constraints such as zero correlation (5.8), spectral mask compatibility, constant energy, and low complexity of generation. In this study, we considered the 4-th and

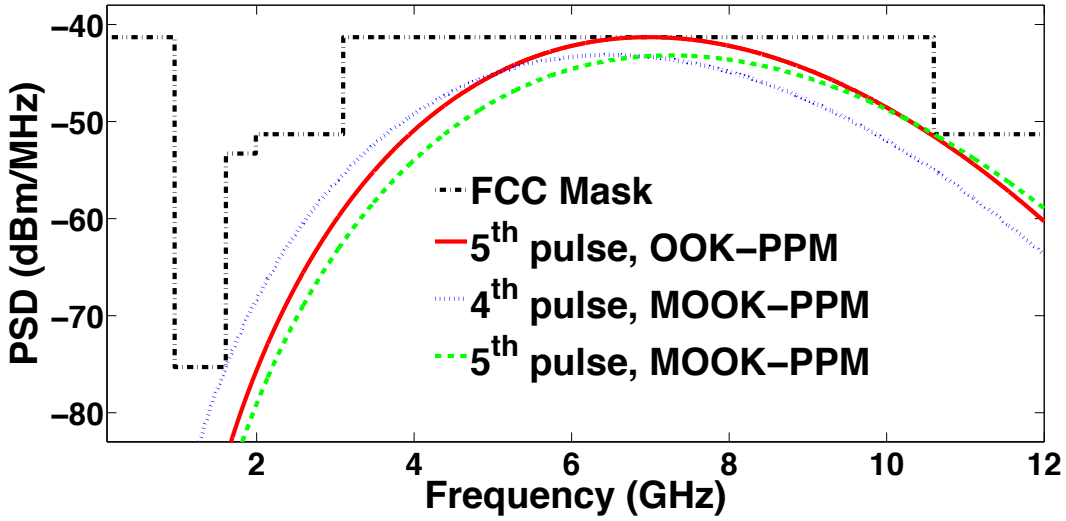

Figure 5.12: The power spectral densities of 5-th optimal Gaussian used for standard OOK-PPM, besides to that of 4-th and 5-th pulses utilized with MWOOK-MWPPM.

5-th order Gaussian monocycles $\{g_4(t), g_5(t)\}$, with same pulse shaping factor σ, as they can easily be generated via CMOS circuits while offering favorable spectral properties [10]:

$$g_4(t) = (\frac{t^4}{\sigma^8} - \frac{6t^2}{\sigma^6} + \frac{3}{\sigma^4})e^{\frac{-t^2}{2\sigma^2}} \tag{5.14}$$

$$g_5(t) = (\frac{-t^5}{\sigma^4} + \frac{10t^3}{\sigma^2} - 15t)e^{\frac{-t^2}{2\sigma^2}} \tag{5.15}$$

For the conventional modulation schemes (OOK, PPM), the 5th Gaussian pulse with $\sigma = 51$ ps is known to be the optimal choice as it provides the maximum power efficiency [11]. If MWOOK or MWPPM is adopted, a slightly different shaping factor $\sigma = 49$ ps has to be chosen so as to keep a constant energy. Thus, each pulse is no longer optimal with respect to the spectral mask but, as will be shown in the following, favorable power efficiencies will be achieved thanks to the proposed randomizing techniques. Regarding the practical aspect, we have fixed σ in order not to add more complexity to the impulse radio system adopting shape randomization, as no 2 separate pulse generators are necessitated to produce the 4th and 5th Gaussians, it is enough to reach the 4th pulse via CMOS, and apply a time derivation to obtain the 5th waveform based on simple analog components, similarly to what is demonstrated in [10], the order of derivation has been increased at limited hardware complexity . Hence, such an approach is much simpler than polarity randomization, which requires a dual pulse generator or a polarity modulator with a multiplier [6]. Time waveforms and corresponding spectra of utilized pulses are plotted in fig. 5.11 and fig. 5.12, respectively. The PASR versus data rate is studied in fig. 5.13 and fig. 5.14 for conventional and multi-waveform schemes. Due to the modulation index used for PPM ($\Gamma = 0.5$ ns), the maximum rate that can be achieved is 1 Gbps. Since the data rate R_b is multiplied by the series of frequency combs (described in Eq. 5.9 and Eq. 5.10), we can observe a linear response for both modulation types.

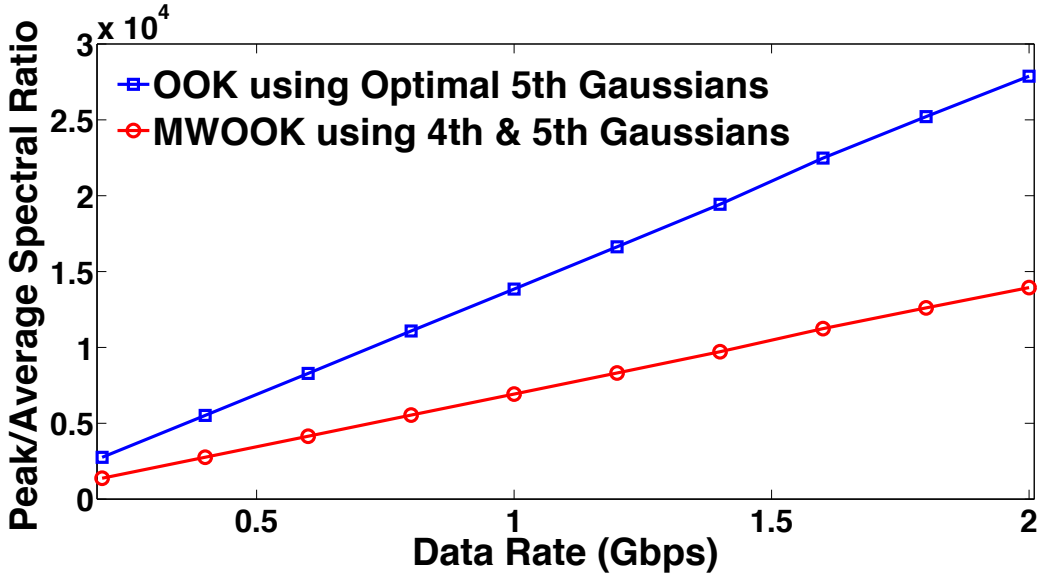

Figure 5.13: Peak-to-Average Spectral Ratio versus data rate for OOK-MWOOK based on 4^{th} and 5^{th} derivatives of Gaussian.

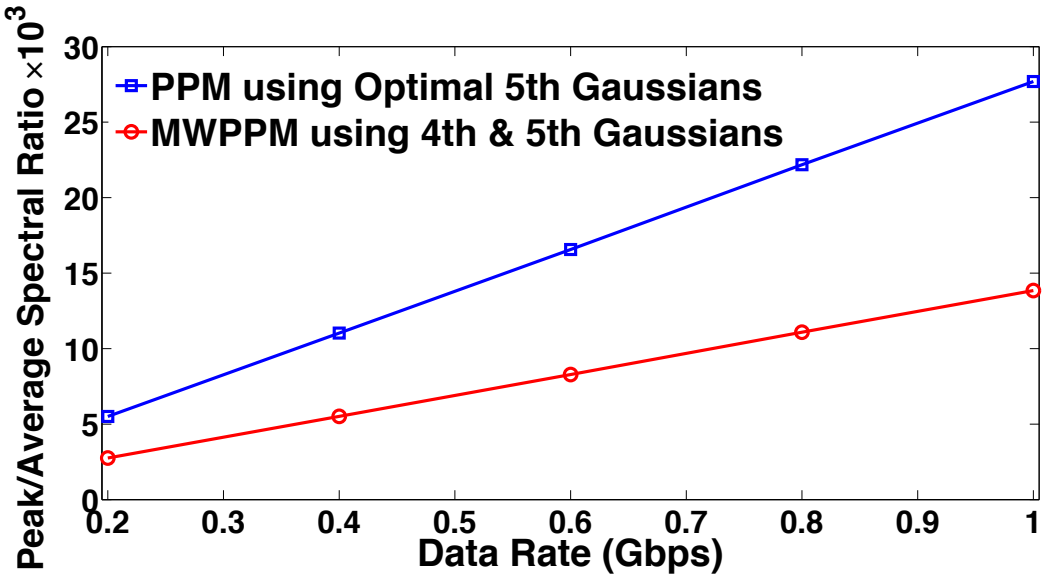

Figure 5.14: Peak-to-Average Spectral Ratio versus data rate for PPM-MWPPM based on 4^{th} and 5^{th} derivatives of Gaussian.

5.6 Applying the Randomization Scheme Considering our IR-UWB over Fiber System

Until now, the proposed modulation schemes have been analyzed only from a theoretical point of view and their benefits in the context of a realistic channel remains to be investigated. In this section, we consider an application to the Radio-over-Fiber introduced in the second chapter. For comparison purpose, we have examined first the performance gain of multi-waveform transmission in the absence of optical amplification. The Power Efficiency Gain (%) is defined as the raise in the efficiency recorded by the randomized transmission over the standard one. In fig. 5.15 and fig. 5.16 we can observe

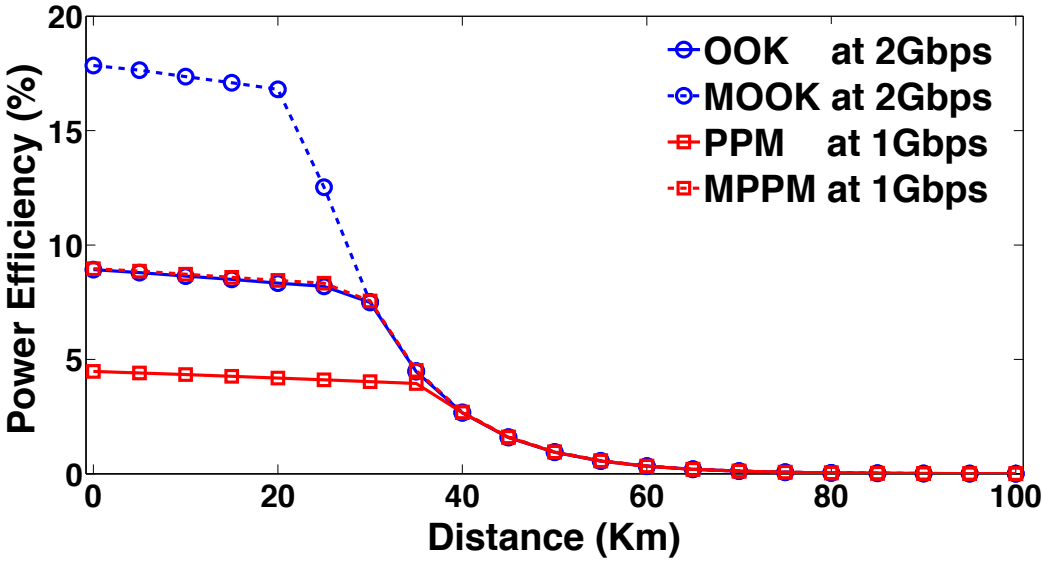

Figure 5.15: Power Efficiency versus Fiber Length, where MZM is injected by 15 dBm Laser Power.

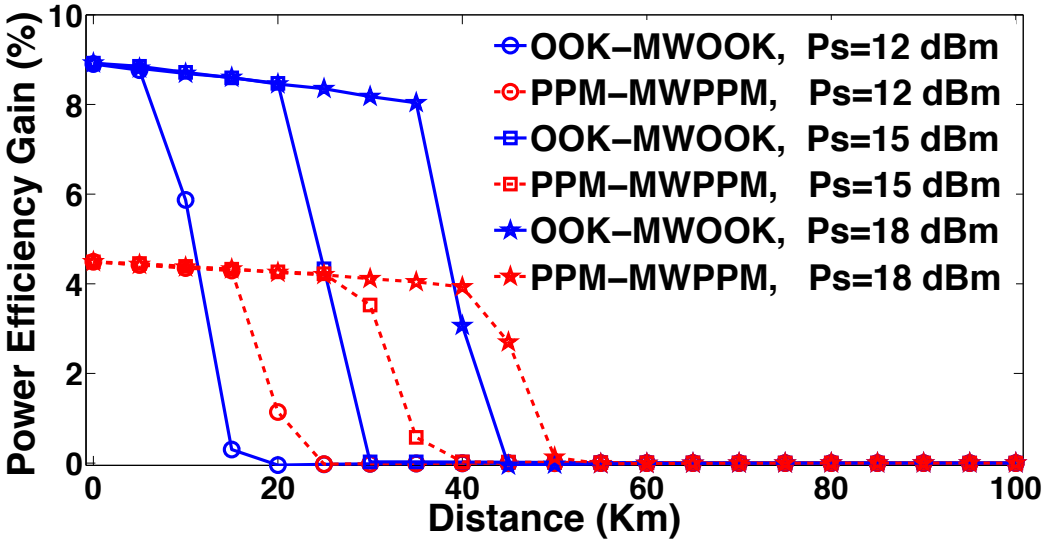

Figure 5.16: Power Efficiency Improvement (or Gain) versus Fiber Length for different input optical powers to MZM.

that the power efficiency initially exhibits an almost flat shape over several kilometers whatever the source power P_s is. This is due to FCC spectrum violation before attenuator, hence the signal is systematically scaled so as to meet FCC limit. The slight decrease of the power efficiency in this portion of the characteristics, whose width depends upon the source power, is due to the signal attenuation in optical fiber (0.2 dB/km). It can be clearly seen that MWOOK and MWPPM schemes offer a significant improvement at short reach, as a result of randomization (lower PASRs). After a certain distance related to P_s, there is a quick drop-off of the efficiency gain (fig. 5.16) which then tends towards zero because no spectral lines reduction can be achieved via randomization if the PSD at the attenuator input is already below FCC mask. The efficiency improvement at short reach is larger for MWOOK (close to 9%) than for MWPPM (slightly above 4%). For $P_s = 12$

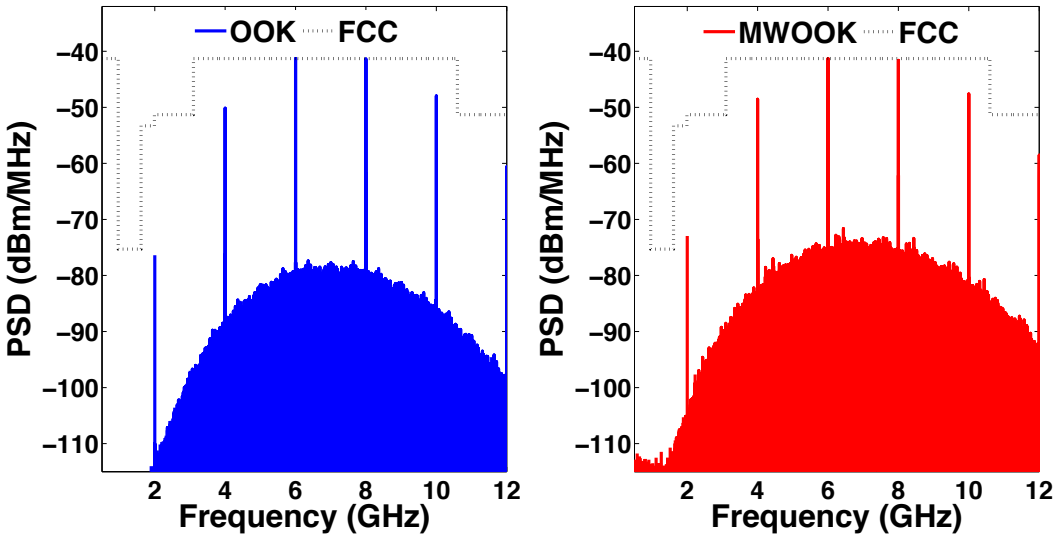

Figure 5.17: Power Spectral Densities for 2 Gbps OOK-MWOOK based on 4^{th}-5^{th} derivatives of Gaussian Pulses at SOA output, where I_{bias}=100 mA.

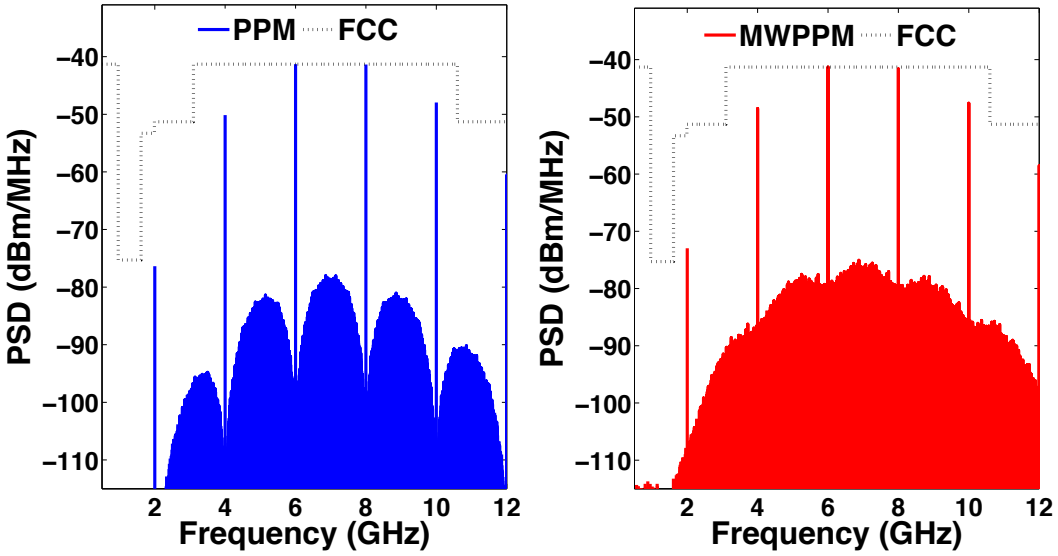

Figure 5.18: Power Spectral Densities for 1 Gbps PPM-MWPPM based on 4^{th}-5^{th} derivatives of Gaussian Pulses at SOA output, where I_{bias}=100 mA.

dBm, a performance increase with respect to standard modulation schemes is obtained up to 20 km and 25 km for OOK and PPM, respectively. The maximum distance over which the proposed schemes brings an improvement is around 40 km for a 15 dBm laser power (at this distance the spectrum at the attenuator input falls below the FCC limit). By considering the Fiber-to-the-Home (FTTH) network coverage zones mentioned in the literature [12], 40 km is not sufficiently large for evaluating the benefits of randomized transmission; thus we placed the SOA in-line amplifier at this distance, in order to get a reach extension at limited cost. A comparison of the PSDs corresponding to standard modulation schemes and MWOOK/MWPPM, for the whole stream of symbols at SOA output, is illustrated by fig. 5.17 and fig. 5.18. Lower PASRs can be clearly observed. For

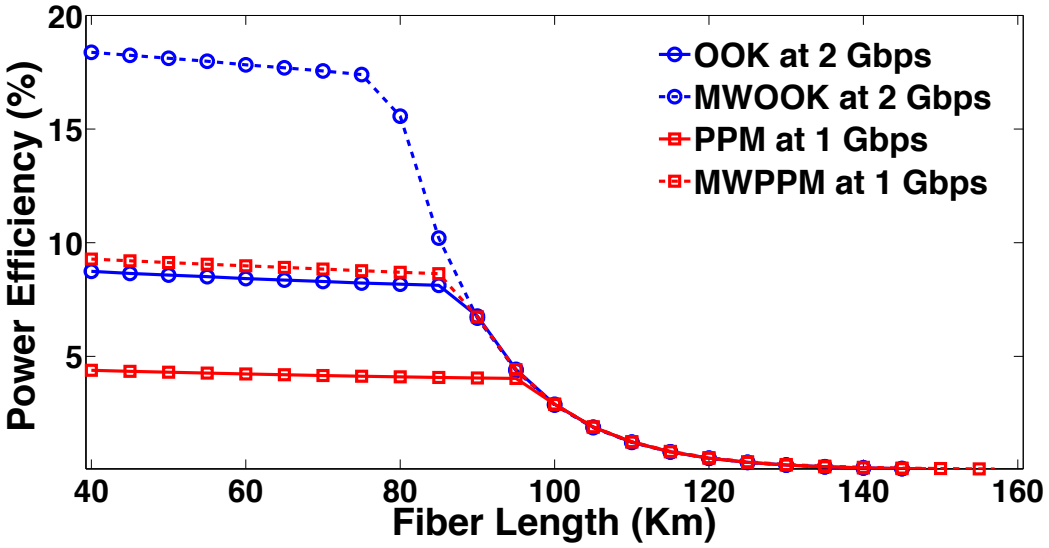

Figure 5.19: Power Efficiency versus Fiber Length, using SOA placed at 40 km, and biased with 150 mA at 15 dBm.

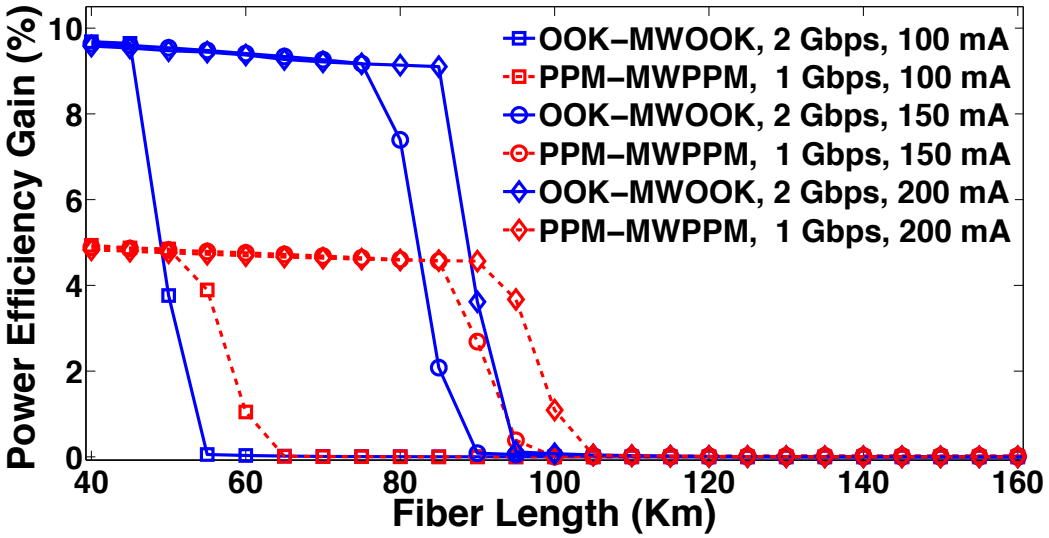

Figure 5.20: Power Efficiency Improvement (Gain) versus Fiber Length in case of utilizing SOA at 40 km for several biasing currents, with a laser power of 15 dBm.

the PPM modulations, the spectrum envelope is influenced by the oscillating term with a period of 2GHz resulting from the 0.5ns shifting in time domain. Power efficiency and corresponding performance gain are plotted in fig. 5.19 and fig. 5.20 versus fiber length, considering different values of the biasing current (I_{bias}), for a laser power of 15 dBm. An evident performance improvement can again be observed for proposed schemes until the distance matches a certain limit related to I_{bias}. Injecting high values of biasing current extends the target distance nonlinearly, a better efficiency being obtained for MWOOK and MWPPM up to 95 km and 105 km respectively, when the SOA is biased at 200 mA. The received optical power at SOA input is -1 dBm, boosted by an optical gain of 4.47 dB, 10.58 dB, or 11.75 dB ; for I_{bias} = 100 mA, 150 mA, or 200 mA, respectively. Another point to mention is that high biasing current tends to slightly lower the performance gain

at short distances due to the nonlinear effects inherent to SOA amplification. So when the spectrum at the photo-detector output is above the FCC limit, linearity of the optical amplifier has a priority over output power response, that is why the best performance gain (close to 10%) is obtained when applying I_{bias}=100 mA, provided that the receiver is located at a distance below 85 km (above this limit, MWOOK/MWPPM do not offer any advantage). Operating at larger biasing currents means slightly less power efficiency gain; we then have a trade off between reach extension and power efficiency. Shape randomization proves an advantage although the challenge of non-linearity faced in the optical system. Since the improvement against standard transmission is determined by the statistical characteristics of the modulations in electrical domain. The discrete-to-continuous spectral ratios expressed in 5.11 and 5.12 are independent of the transmitted waveforms in the case of OOK or PPM. Hence, pulse dynamics have no impact on the spectral spikes intensity, that adds a positive point for our randomization, so a kind of robustness can be observed against non-linear impairments faced in SOA.

5.7 Summary

In this chapter, a new spectrum smoothing technique is developed on the basis of OOK or PPM modulation schemes, by applying a pulse shape randomization. The benefits of the approach is first demonstrated by deriving closed-form expressions of the power spectral densities. It is shown that using a greater number of pulses leads to a better spectral behavior, and consequently higher power efficiency. The technique is compatible both with carrier-based transmitters and with impulse radio systems. With the view to propose a very simple implementation, we investigated the particular case of an IR using two pulses belonging to the Gaussian family (4-th and 5-th derivative). Not like direct sequence, which has an excellent performance but much more complicated to implement, our approach offers a good compromise between spectrum enhancement and generation complexity. We investigated an application to our UWB over optical fiber transmission system operating at 1 Gbps for PPM format and at 2 Gbps for OOK. A significant improvement at short reach of the optical link has been demonstrated if a randomized transmission is adopted. An eventual in-line optical amplification via SOA is examined for reach extension purpose at low-cost. The active distance over which the multi-waveform modulation schemes perform better is controlled by the biasing current injected into the SOA in a flexible way. In the next chapter, we show that differential chaos shift keying is an alternative scheme which is capable of improving the over fiber system performance in the presence of channel nonlinearities and time jitter.

Bibliography

[1] V. Yajnanarayana, S. Dwivedi, A. De Angelis, and P. Händel,"Spectral efficient IR-UWB communication design for low complexity transceivers," *EURASIP Journal on Wireless Communications and Networking*, 2014(1), pp. 1-13, 2014.

[2] Y. P. Nakache and A.F. Molisch, "Spectral shaping of UWB signals for time-hopping impulse radio," *IEEE J. Selected Areas in Commun.*, 24(4), pp. 738-744, 2006.

[3] G. M. Maggio, N. Rulkov, and L. Reggiani, "Pseudo-chaotic time hopping for UWB impulse radio," *IEEE Trans. Circ. and Syst. I*, 48(12), pp. 1424-1435, 2001.

[4] H. Zhang and T. A. Gulliver, "Biorthogonal pulse position modulation for time-hopping multiple access UWB communications," *IEEE Trans. Wireless Commun.*, 4(3), pp. 1154-1162, 2005.

[5] J. Romme and L. Piazzo, "On the power spectral density of time-hopping impulse radio," *Ultra Wideband Systems and Technologies-IEEE*, pp. 241-244, 2002.

[6] A. Pearce, H. Nie, and Z. Chen, "Spectral spike reduction for ultra-wideband impulse radio system," *Microwave Symposium Digest, IEEE MTT-S International*, pp. 1-3, 2012.

[7] S. Cui and F. Xiong, "UWB system based on energy detection of derivatives of the Gaussian pulse," *EURASIP J. on Wireless Commun. and Netw.*, 2011(1), pp. 1-18, 2011.

[8] J. E. Padgett, J. C. Koshy and A. A. Triolo, "Physical-layer modeling of UWB interference effects," Telcordia Technologies Report to DARPA (NETEX Program), Jan. 2003.

[9] J. A. Silva and M. L. De Campos, "Spectrally efficient UWB pulse shaping with application in orthogonal PSM," *IEEE Trans. on Communications*, 55(2), pp. 313-322, 2007.

[10] T. A. Phan, V. Krizhanovskii, S. K. Han, S. G. Lee, H. S. Oh and N. S. Kim, "4.7 pJ/pulse 7th derivative Gaussian pulse generator for impulse radio UWB," *In Circuits and Systems, 2007. ISCAS 2007. IEEE International Symposium*, pp. 3043-3046, 2007.

[11] S.T. Abraha, C. Okonkwo, P. A. Gamage, E. Tangdiongga, and T. Koonen, "Routing of power efficient IR-UWB wireless and wired services for in-building network applications," *J. Lightw. Technol.*, 30(11), pp. 1651-1663, 2012.

[12] R. Llorente, T. Alves, M. Morant, M. Beltran, J. Perez, A. Cartaxo, and J. Marti, "Ultra-wideband radio signals distribution in FTTH networks," *IEEE Photon. Technol. Lett.*, 20(11), pp. 945-947, 2008.

Chapter 6

Different Modulation Options for SOA-based UWB over Fiber Systems: An Experimental Study

Great efforts have been devoted to enhance the performance of our proposed over fiber system; thanks to shape randomization, pre-distortion, and chirping techniques, we have succeeded in increasing the power efficiency of the UWB signal from the basic transmitted pulse and modulation sides. In this chapter, we examine the pertinence of reference-based schemes in improving the quality of transmission, by adding a kind of robustness against optical system nonlinearities and time jittering, besides to smoothing the spectrum when going towards chaotic scenarios. On the other side, we make an experimental validation for the effectiveness of chirping approach in mitigating SOA nonlinearities and reducing ASE noise impact simultaneously. In terms of bit error rate performance, both chirping and chaotic schemes have proved an advantage in the practically implemented SOA-based over fiber system.

6.1 Experimental Setup of Our SOA-based UWB over Fiber System

As stated in fig. 6.1, our experimental setup consists of a transmitter, channel, and receiver. The transmitter relies on the Agilent Arbitrary Waveform Generator (AWG - 12 Gsa/s - M8190A) [1], which electrically generates the signals designed in Matlab, where the maximum produced voltage is 700 mV. A radio frequency amplifier (SHF Communication Technologies AG - 115 BP) has been placed so as to boost the driving voltage entering the single arm MZM (Photline Technologies). On the optical source side, the laser diode embedded in the Optical Modulation Analyzer (OMA - Agilent N4391A) [2] has a fixed output power of 12 dBm, which can be tuned via Attenuator (JDS Uniphase) before being injected to the MZM optical modulator. The single mode fiber presents the optical channel, with a 0.2 dB/km attenuation and dispersion coefficient of 17 ps/nm/km, so the optical field at the modulator output propagates over 40 km of the fiber link to finally reach the SOA (Inphenix-IPSAD1581) [3]. The second span of fiber considered previously has been removed from the experimental setup, so SOA here acts as a pre-amplifier, which can be considered as a part of the receiver. This configuration is not new, as there is a growing interest for designing preamplified optical integrated receivers, and the SOA is a

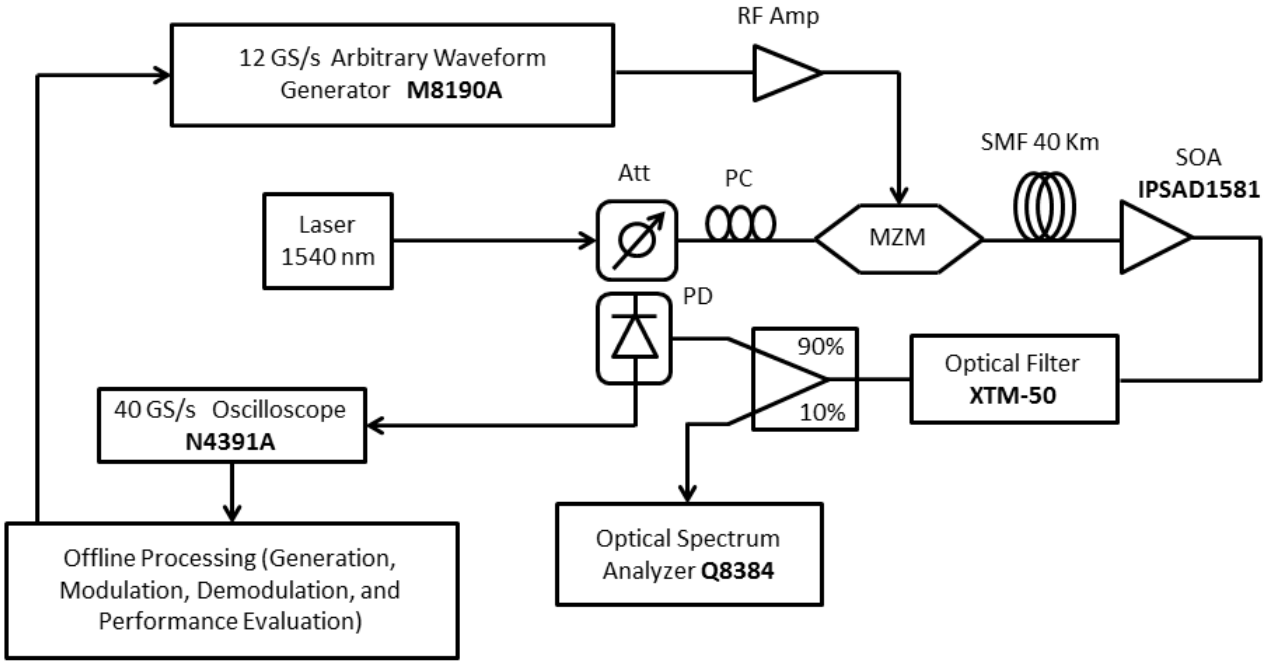

Figure 6.1: A schematic diagram for the experimental setup, (Amp: Amplifier, MZM: Mach-Zehnder Modulator, SMF: Single Mode Fiber, SOA: Semi-conductor Optical Amplifier, Att: Attenuator, PC: Polarization Controller, PD: Photo-detector).

Figure 6.2: A real photo for the experimental equipments.

pertinent solution for such applications due to its low cost and complexity [4–6]. The central wavelength of the optical filter (XTM-50) after SOA is 1540 nm, which corresponds to that at the laser output, and the 10 dB bandwidth is 30 pm. A periodic observation for the spectrum and average power is mandatory in order to re-calibrate the polarization controller after any systematical change in the fiber characteristics, as the latter are highly affected by the physical conditions of the surrounding environment; hence, an Optical Spectrum Analyzer (OSA - ADVANTEST Q8384) has been placed for that purpose. The photo-detector (HEWLETT PACKARD 11982A), with 15 GHz bandwidth, converts the optical field into an electrical voltage signal to be ready for entering the oscilloscope (which is embedded in the OMA). Finally, the received waveform is sampled at Fs=40 GHz in the oscilloscope, then saved for post processing in Matlab. Figure 6.2 shows a real photo for the operating devices, at the right we can see the OMA, the 40 km piece of fiber is placed under the table, and the computer used for off-line processing is located above the AWG at the left.

6.2 Investigation of Chaotic Transmitted Reference Schemes

6.2.1 Transmitted Reference Schemes

In chapter 3, we showed that pre-distorting the input waveforms in electrical domain is a pertinent approach to correct the SOA impact, and the chirping scheme illustrated in chapter 4 proves to be also effective in linearizing the SOA characteristics. However, pre-distortion exhibits a linearity gain at the cost of complexity, as a larger number of parameters is required for achieving a better performance, so the potential of such a technique is limited to that compromise. Also the order of nonlinearity depends on the operating conditions, hence the biasing current and input power have to be considered before optimizing the pulses parameters or choosing the slope of the phaser. Besides, the characteristics of the optical system are not always deterministic, as affected by the physical conditions of the internal and external environments which are not stable; specially the channel, which can not be assumed to be stationary in the case of UWB transmission. Hence, the performance gain for any linearization scheme may have many practical limits associated with the real time application; and establishing a feedback for channel state information is not a pertinent solution with non-coherent communication systems. An alternative to tuning the pulse dynamics for overcoming channel nonlinear effects is to exploit the modulation properties. The Transmitted Reference (TR) schemes have been investigated in literature to fit this target [7,8], where for each symbol a reference signal is transmitted to give information about the channel response, followed by the useful pulse which consists of the reference multiplied by the data level (+1 or -1). A simple cross correlation between the received reference and data waveforms is enough to capture all the available energy, in order to extract the transmitted symbol without requiring any kind of channel estimation [8,9]. The attractive feature of this pattern is that the same nonlinearities act on both reference and data pulses, hence distortions have no great influence on the final decision after cross correlation. Furthermore, such a modulation technique has a strong immunity against time jittering, since the same channel delay occurs for the reference and data signals, and no perfect synchronization is required to detect the transmitted bits [10, 11].

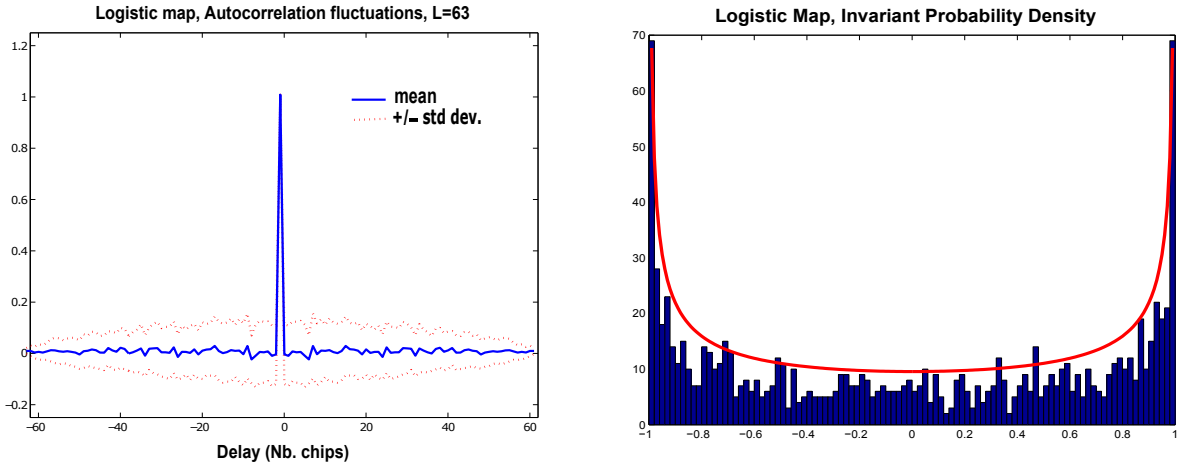

(a) (b)

Figure 6.3: The auto-correlation function of the chaotic sequence (a) with the corresponding probability density function (b).

6.2.2 Chaotic-Based Modulation Patterns

With the view to optimize the system performance at a limited order of implementation complexity, chaotic modulation schemes have been developed for adoption in wireless transmission systems, due to their interesting features including immunity against jamming and multipath fading, besides to the ease of generation and reduced probability of intercept [12, 13]. Nevertheless, the statistical characteristics of the chaotic signal broadens out the spectrum, so it is a non-periodic noise like signal hence it becomes a pertinent solution for spread spectrum communications [12–15].

In our work, the logistic map was the candidate due to its good auto-correlation properties as clearly seen in fig. 6.3 (a). The logistic function corresponds to the second-order Chebyshev polynomial [16], where the general recurrence formula is expressed in eq. (6.1), r is a parameter influencing the sequence dynamics (set at $r = 4$ here) and x_k is the chaotic outcome at index k. Figure 6.4 (a) describes the recurrence function $\left(x_{k+1} = f(x_k)\right)$; chaotic systems have nonlinear characteristics [17] and a high sensitivity to the initial condition (measured via Lyapunov exponent) as depicted in fig. 6.4 (b). The probability density function is described in eq. (6.2), thanks to the chaotic dynamics we can see a semi-flat response in the distribution as illustrated in fig. 6.3 (b), so the generated sequence has a high degree of randomness, where the expectation is zero and the variance of the normalized map equals to 1.

$$x_{k+1} = r x_k (1 - x_k) \tag{6.1}$$

$$\rho(x) = \frac{1}{\pi\sqrt{1 - x^2}}, \quad -1 \leq x \leq +1 \tag{6.2}$$

6.2.3 DCSK and I-DCSK Chaotic Schemes

Differential Chaos Shift Keying (DCSK) is an advanced type of chaotic modulation, which gains the benefits of chaotic dynamics and Transmitted Reference simultaneously [18].

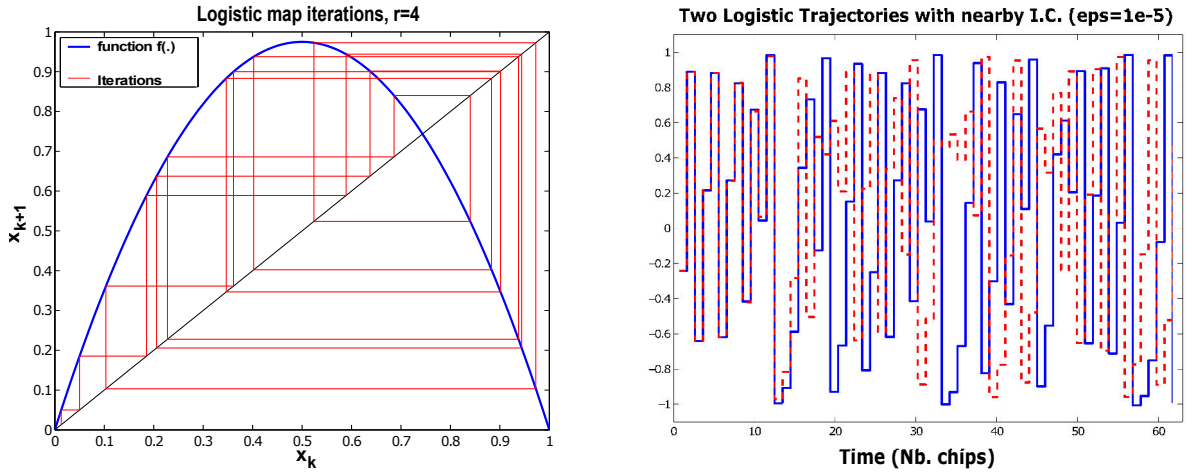

(a) (b)

Figure 6.4: The logistic map function and iterations for r=4 (a), besides to the time trajectories versus number of chips (b), where r is a parameter which influences the sequence dynamics.

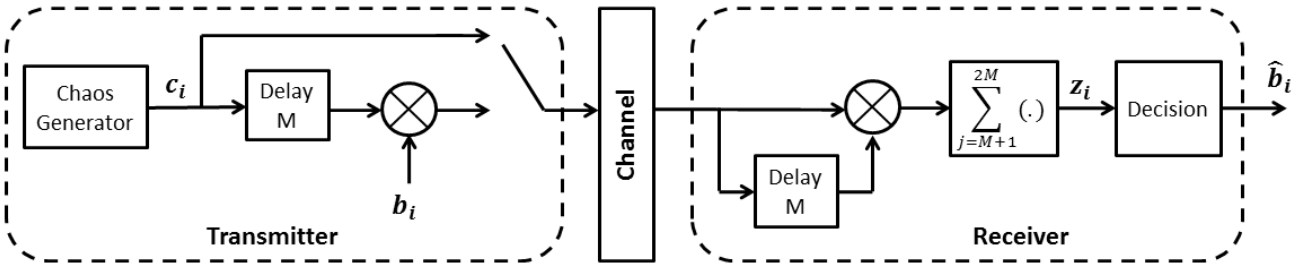

Figure 6.5: Block diagram of the DCSK transmission system

The block diagram of the DCSK transceiver is illustrated in fig. 6.5, the generated chaotic signal c_i of length M is directly sent as a reference, where a copy of c_i is transmitted after being multiplied with the original data b_i (where $b_i \in$ {-1,1}). Like the TR scheme, data detection at receiver side is based on evaluating the cross correlation between the received signal and its M samples time delayed version. The main drawback of DCSK is the degradation in the data rate associated with adding a one reference to each data bit; in order to overcome this issue, a special effort was recently made by Kaddoum who proposed an Improved DCSK (I-DCSK) scheme based on simultaneous transmission of the reference and data sequences [19]. Figure 6.6 describes the modulation and demodulation processes of I-DCSK, the reference signal is time reversed $\left(r(t) \rightarrow r(-t)\right)$ before being combined with the data one, as orthogonality has to be satisfied between the overlapped sequences just before transmission. Based on this orthogonality, it is possible to extract the transmitted bit by simply correlating the received signal with its time reversal. Another advantage for this novel scheme is the security gain over classical DCSK, as the reference is embedded in the data frame, adding thus a great challenge on irregular bodies which aim to steal information from the communication system.

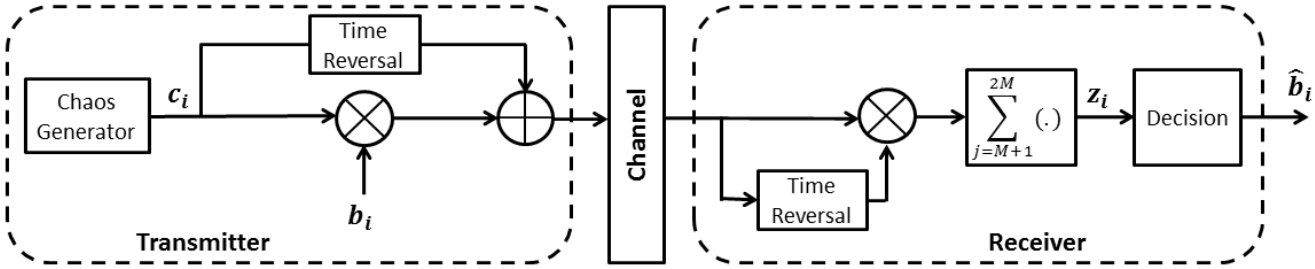

Figure 6.6: Block diagram of the I-DCSK transmission system

6.2.4 Performance Evaluation of the Chaotic Schemes in Comparison to other non-coherent modulation formats

A great deal of research effort has been allocated for adopting chaotic techniques with over fiber-to-wireless integrated transmission systems [20–22]. But what has not been investigated until now, to the knowledge of the author, is applying CSK in UWB optical access networks, which is an interesting approach for enhancing the performance with a reach extension objective. Here, we focus on using the DCSK and I-DCSK modulation options in our SOA-based over fiber system, and a performance evaluation has been done in comparison to OOK and PPM modulation formats. Establishing a synchronization

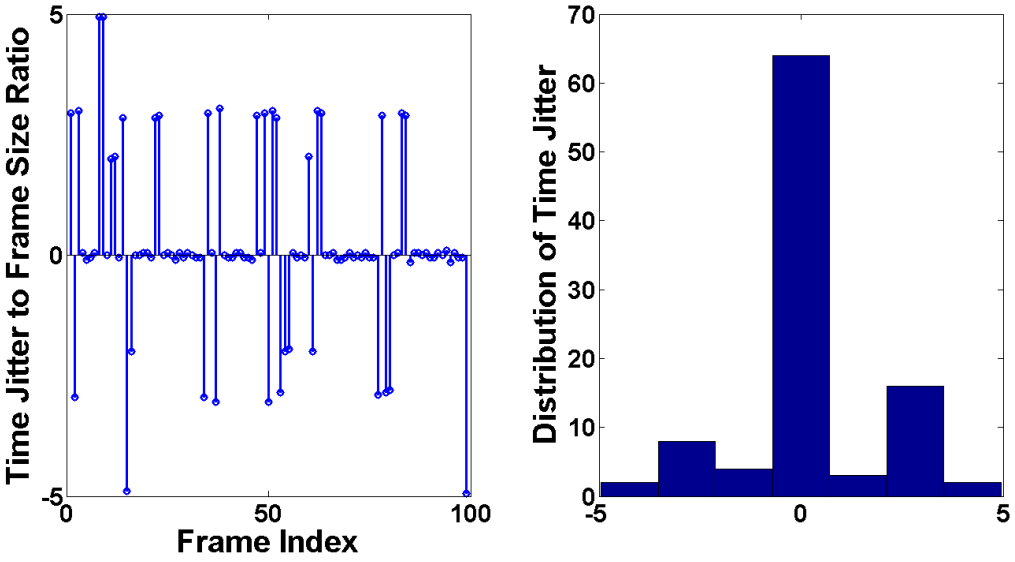

Figure 6.7: Time jittering to frame size ratio versus the frame index in the received signal, and corresponding probability distribution.

between the transmitter and receiver was a key step to extract the target signal from the stream of electrical waveforms collected by OMA. Figure 6.7 verifies that the time jitter is relatively small with respect to the frame size; hence we have used two similar preamble chaotic sequences before the modulated signal, where at receiver side the preamble is detected based on the maximum cross correlation, and the remaining part of the signal can be simply extracted prior to demodulation. Such a synchronization was enough to recover the transmitted bits without the need of further tracking, which is a positive point as the latter adds more complexity to the basic transceiver. OOK and PPM have

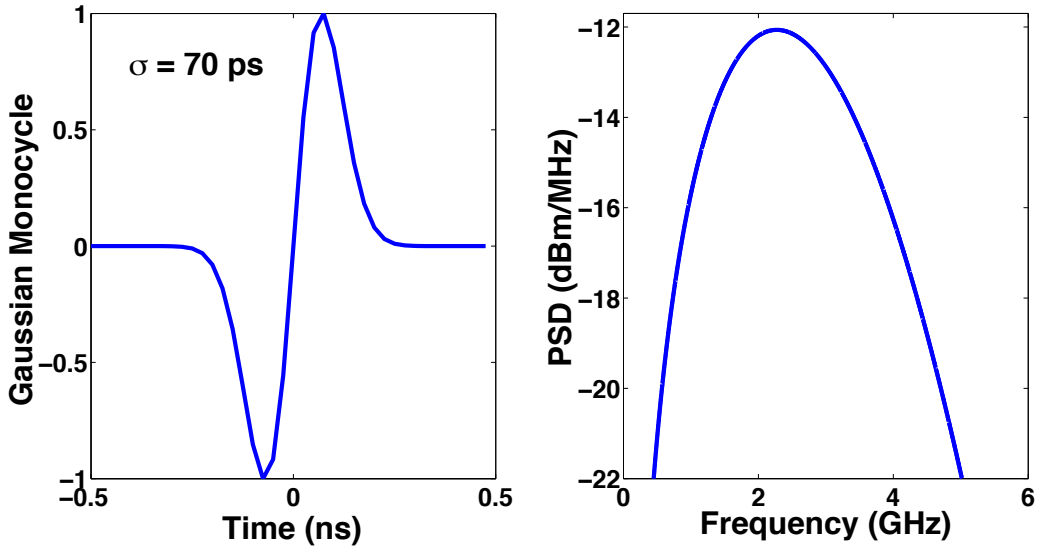

Figure 6.8: Time waveform and corresponding spectrum of the electrical Gaussian monocycle utilized with OOK and PPM, where σ = 70 ps.

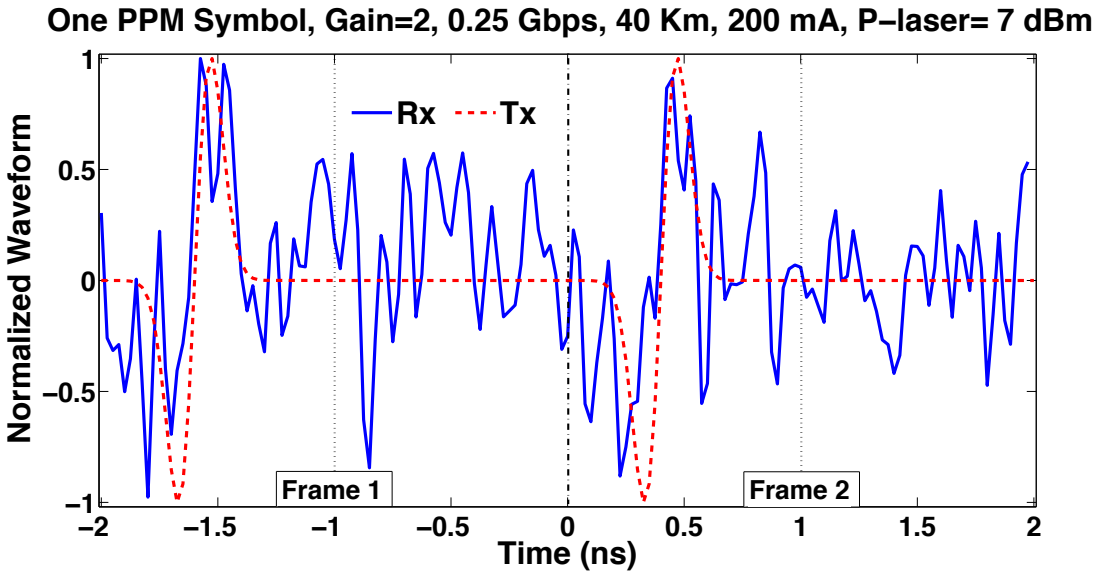

Figure 6.9: Received PPM symbol just after SOA (at 40 km), where the laser output power is 7 dBm and I_{bias}= 200 mA.

a processing gain of G=2, which means that each symbol corresponds to 2 frames, so for OOK 2 pulses are transmitted when the bit is 1 and both frames are empty when the bit is 0. However, in the case of PPM, 2 pulses are always transmitted per symbol, where the binary data is indicated by the position of the 2 waveforms inside the 2 frames (the frame duration is double to that for OOK, as a minimum limit for an orthogonal non-coherent PPM). Both modulations are based on the Gaussian first order derivative plotted in fig. 6.8, with a pulse shaping factor of σ =70 ps; fig. 6.9 shows the time waveform of one PPM symbol observed after photo-detector; as noticed, two pulses are transmitted in two consecutive frames to present one symbol. We can clearly see in fig. 6.9 the effects of chromatic dispersion in the optical link, besides to the induced noises in SOA (ASE) and photo-detector (shot and thermal noises), where is obvious the

impact of nonlinearities inherent to SOA amplification. Figure 6.10 and fig. 6.11 show the

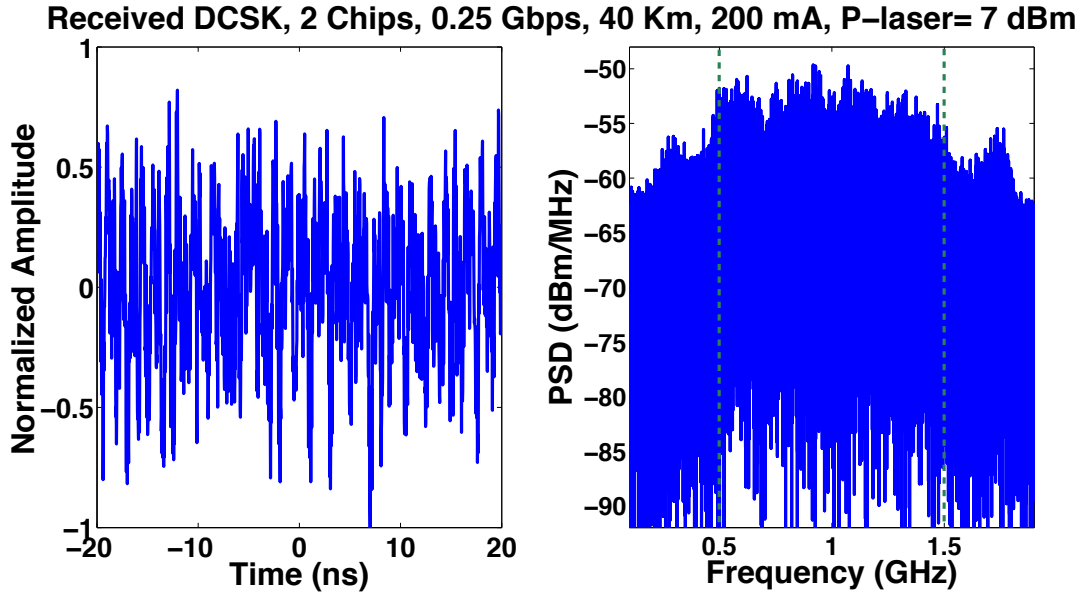

Figure 6.10: Time waveforms and corresponding power spectral density of 2-DCSK operating at 0.25 Gbps, where the laser output power is 7 dBm, I_{bias}= 200 mA, and SOA is placed at 40 km (the time waveform is a truncation of only 10 symbols).

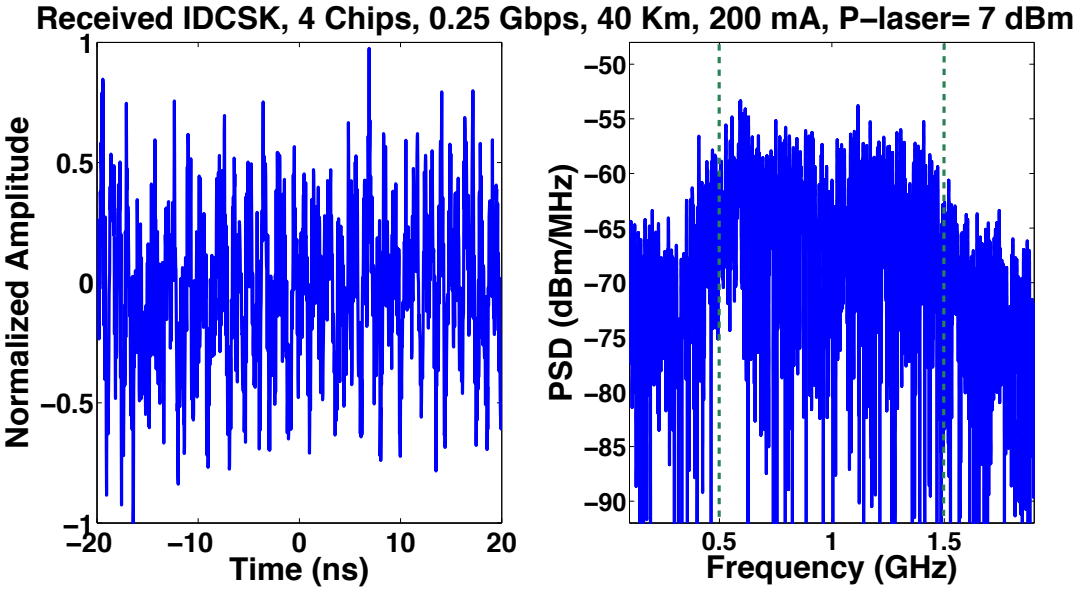

Figure 6.11: Time waveforms and corresponding power spectral density of 4-I-DCSK operating at 0.25 Gbps, where the laser output power is 7 dBm, I_{bias}= 200 mA, and SOA is placed at 40 km (the time waveform is a truncation of only 10 symbols).

received DCSK and I-DCSK signals at 40 Km respectively, where the chip frequency is 1 GHz, which exactly equals the carrier frequency. An extra beneficial property for the CSK transmission is the absence of the comb lines in the spectrum, thanks to chaotic dynamics, unlike classical impulse radio modulation patterns which results in strong spectral spikes. The left and right bounds of the 10 dB bandwidth are 0.5 GHz and 1.5 GHz respectively, which are indicated by the vertical dashed lines. Figure 6.12 and fig. 6.13 present the

time waveforms and corresponding spectra of the received OOK and PPM respectively, the envelope of the frequency discrete lines has the same shape than the basic transmitted pulse spectrum depicted in fig. 6.8, where the 10 dB band is approximately 4.6 GHz.

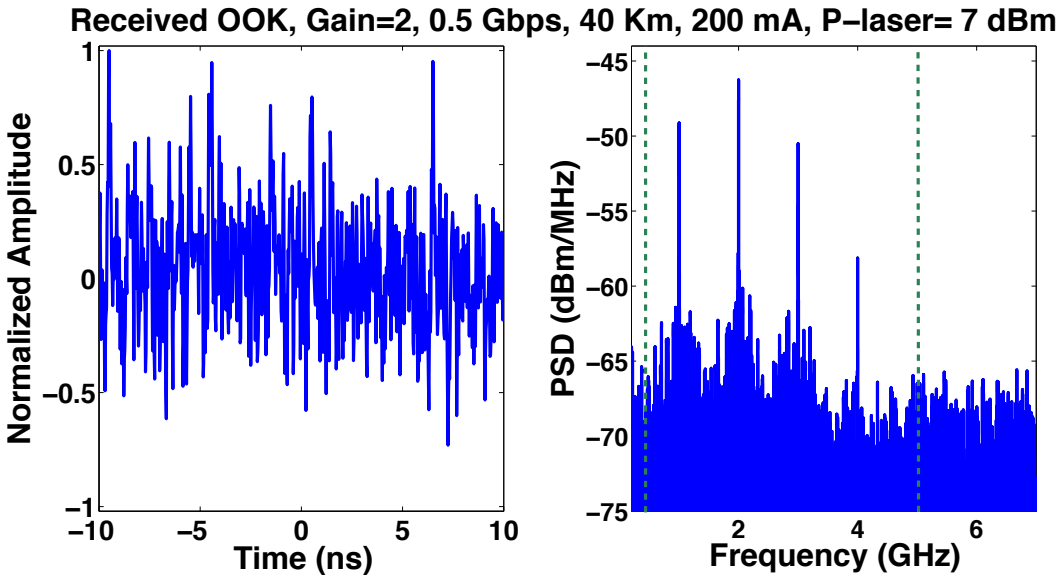

Figure 6.12: Time waveforms and corresponding power spectral density of OOK operating at 0.5 Gbps, where the laser output power is 7 dBm, I_{bias}= 200 mA, and SOA is placed at 40 km (the time waveform is a truncation of only 10 symbols).

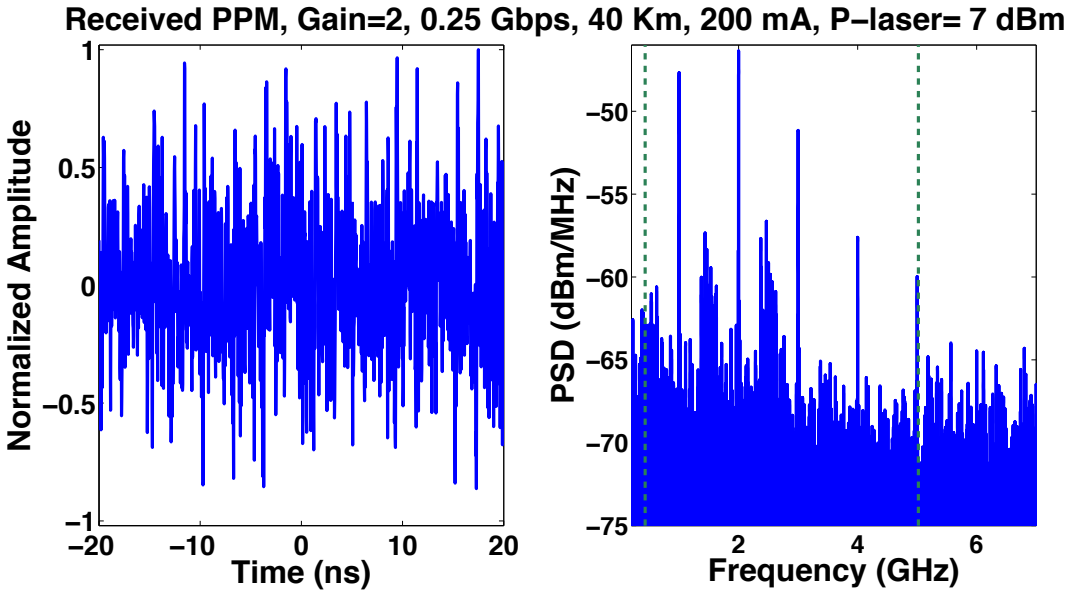

Figure 6.13: Time waveforms and corresponding power spectral density of PPM operating at 0.25 Gbps, where the laser output power is 7 dBm, I_{bias}= 200 mA, and SOA is placed at 40 km (the time waveform is a truncation of only 10 symbols).

Figure 6.14 shows the bit error rate results for the conventional DCSK based on one or two chips, for the purpose of comparison with OOK, PPM, and Improved DCSK modulation formats (where the notation N-DCSK in the legend denotes DCSK with N reference chips followed by N data chips, the same is for I-DCSK but the references and

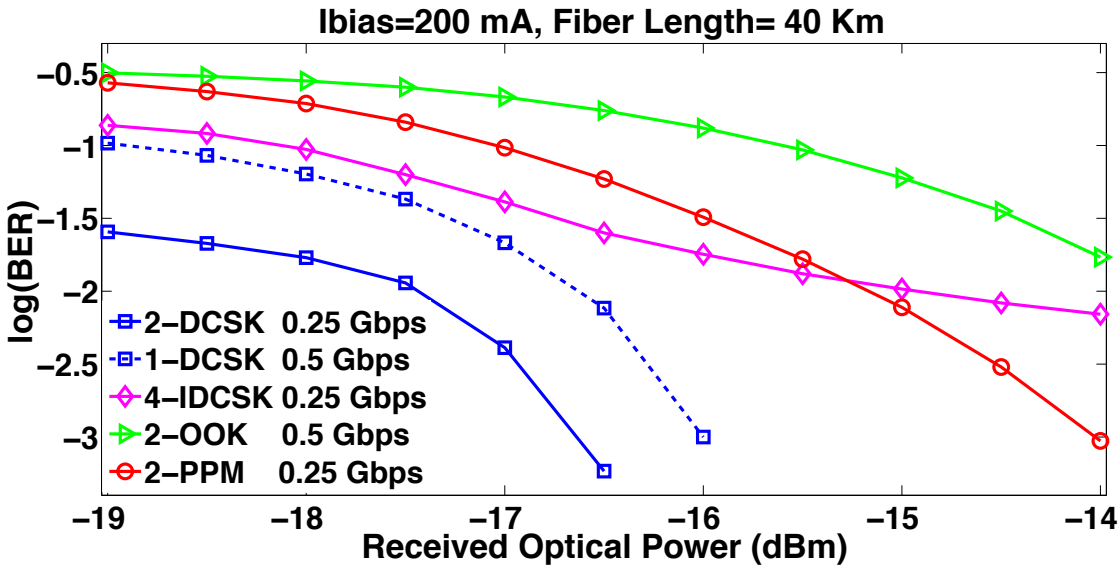

Figure 6.14: Bit error rate versus received optical power (just before SOA) for DCSK, I-DCSK, OOK, and PPM modulation schemes, where I_{bias}= 200 mA and SOA is placed at 40 km.

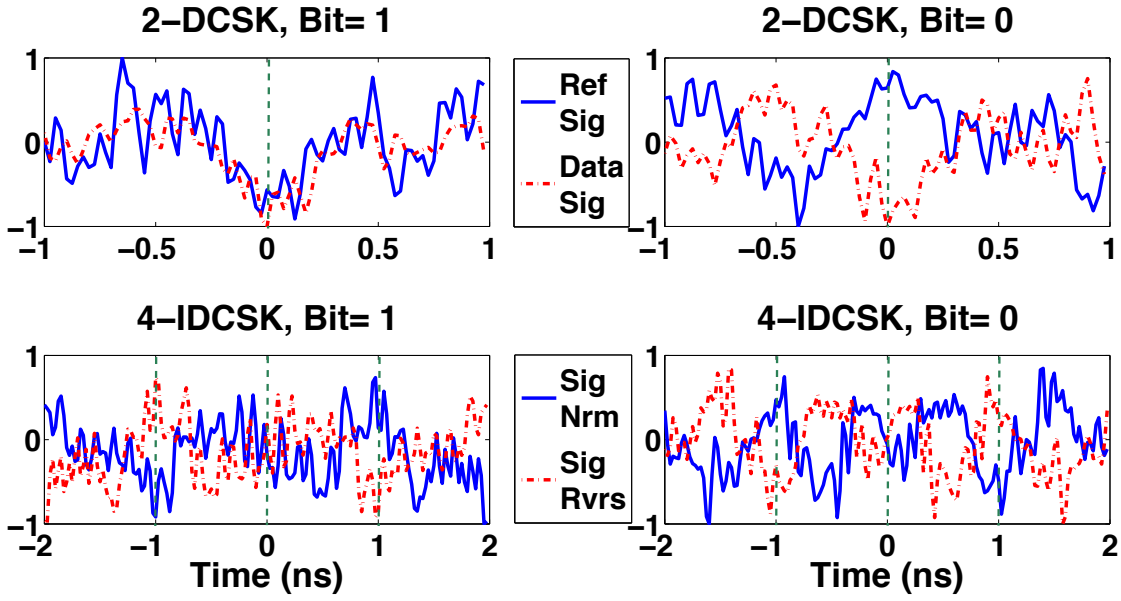

Figure 6.15: Reference and data waveforms of the received DCSK (up) and I-DCSK (down) signals corresponding to one symbol, where the laser output power is 7 dBm, I_{bias}= 200 mA, and SOA is placed at 40 km.

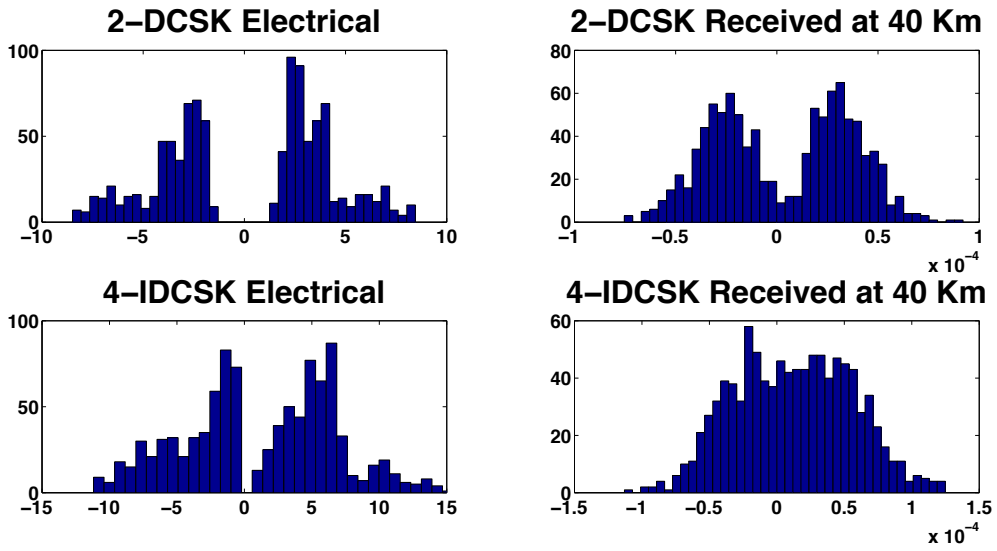

Figure 6.16: The probability density function of the 2-DCSK (up) and 4-I-DCSK (down) cross correlation measured just before decision, for electrical back-to-back (left) and after photo-detector (right), where the laser output power is 4 dBm, I_{bias}= 200 mA, and SOA is placed at 40 km.

data are totally overlapped). As the received power increases, the SOA operating point is shifted towards saturation, where a lower ASE impact is obtained and consequently higher optical signal-to-noise ratio, hence we can see an improvement in the bit error rate performance for different modulation schemes. On the side of classical DCSK, there is a strong immunity against nonlinear impairments and time jittering, thus it proves to be the best even for the case of 1-DCSK, where the achieved data rate is 0.5 Gbps, which is double that for I-DCSK. Considering 0.5 Gbps OOK, the standard DCSK operates on the same transmission rate with a lower probability of error; while in comparison with 0.25 Gbps PPM, we can see a dominance for DCSK in terms of bit error rate and data rate simultaneously. I-DCSK is highly sensitive to optical system nonlinearities, as orthogonality has to be satisfied between the reference and data overlapped signals in order to obtain a correct decision. OOK and PPM have a kind of robustness against nonlinearity, since estimating the transmitted symbol is based on non-coherent energy detection, and the received pulse dynamics have no great impact on the total collected energy over time frame. However, both modulations are not robust against time jittering, thus I-DCSK shows to be better than OOK and PPM for low input powers, associated with a lower order of SOA nonlinearity; while the poor performance of I-DCSK appears when we go towards higher values of laser power. Hence, for a limited number of chips, the improved chaotic scheme does not seem to be pertinent for application in the SOA-based optical system; except the security aspect, which is the only feature that could be added over classical DCSK schemes. That is more clarified in fig. 6.15 (down), where the I-DCSK received signal corresponding to one symbol is plotted besides to its time reversal for bit=1 (left) and bit=0 (right); the two signals have almost opposite polarity, hence the observation of their multiplication becomes close to zero (which is the threshold of decision). Unlike conventional DCSK, where it is clear from fig. 6.15 (up) how the reference and data waveforms are positively or negatively correlated based on the transmitted bit. Figure 6.16 describes the distribution of the cross correlation obtained for DCSK (up)

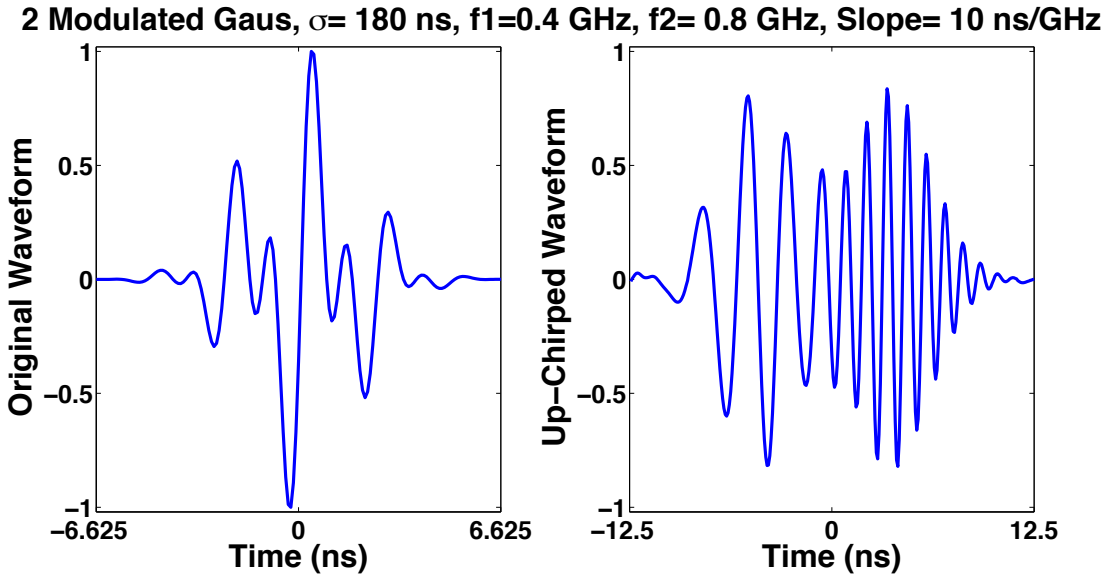

Figure 6.17: Time waveforms of the original (left) and up-chirped (right) combination of modulated Gaussians in electrical domain, where σ =180 ns, f_1= 0.4 GHz, f_2 = 0.8 GHz, and the slope is 10 ns/GHz.

and I-DCSK (down) just before decision, the nonlinear effects lead to an overlap between the distributions of the two binary symbols for the case of I-DCSK; where for DCSK, we can see a lower variance and a higher probability around the mean for the same operating conditions.

6.3 Examining the Performance of Chirping with the Proposed Transmission System

Chirping scheme has shown to be effective in previous work, here we examine the potential of this technique (which is totally different from the chaotic scenario reported in the past section) in the real SOA-based optical system so as to partially validate its effectiveness. In simulations, we have utilized the 5^{th} Gaussian pulse besides to Abraha's combination of Doublets, but due to the band limitation of AWG, it was not possible to generate such waveforms. On the other side, dealing with pulses having a frequency diversity is much easier to study the benefits of chirping and to also make a time domain observation. Therefore, we have proposed a combination of 2 modulated basic Gaussians, with different carrier frequencies, in order to see the original signal as two overlapped waveforms which could be separated via chirping. The time duration of the utilized combination is 13.25 ns, where the pulse shaping factor for both Gaussians is σ =180 ns, with f_1= 0.4 GHz and f_2 = 0.8 GHz. Figure 6.17 shows the non-chirped (a) and chirped (b) signals, the time duration of the latter is 25 ns, which is slightly less than double the original, where the chirping slope is 10 ns/GHz. As clearly noticed, the left and right portions of the chirped waveform have the same time behavior but different modulation frequencies. From fig. 6.18 we can see how a better correlation is obtained between the received and transmitted waveforms when chirping is adopted, as a lower order of SOA nonlinearity is faced against chirped waveforms. Nevertheless, a higher signal-to-noise ratio is achieved, that agrees with the result obtained in chapter 5, and promising for an improvement in the bit error rate

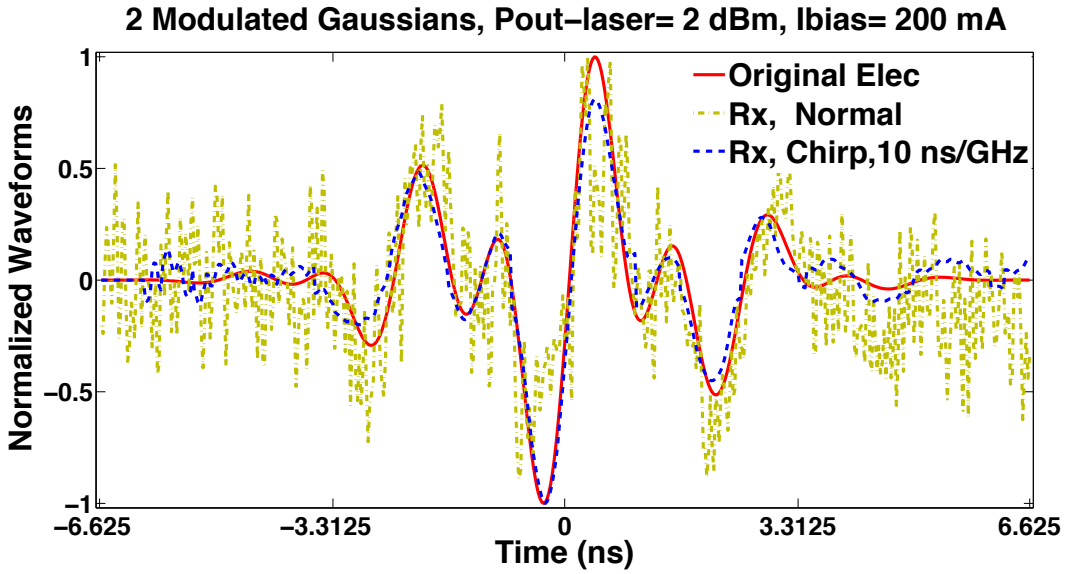

Figure 6.18: The time waveforms of the received pulse with and without chirping (at a slope of 10 ns/GHz) besides to the original pulse in electrical domain, where the laser output power is 2 dBm and I_{bias}= 200 mA.

performance associated with the chirped transmission.

$$XCTER = \frac{Max\{x_T(t) \star x_R(t)\}}{\int_{-T/2}^{+T/2} x_R^2(t)dt} \tag{6.3}$$

The cross correlation to energy ratio (XCTER) between the electrically generated pulse $x_T(t)$ and received one after the photo-detector $x_R(t)$ is expressed in eq. (6.3), this criteria is important for evaluating the potential of chirping in mitigating SOA nonlinearities. $XCTER$ has been studied versus the laser output power in fig. 6.19 considering I_{bias}= 100 mA and I_{bias}= 200 mA at 10 ns/GHz chirping slope, the increasing response for different settings is due to the raise in the optical signal-to-noise ratio (OSNR). At negative powers, we can see a crossing between the dashed curves for the non-chirped pulses, that is due to the higher degree of linearity obtained at low SOA input powers, so the linearity gain associated with decreasing the biasing current appears when the OSNR becomes extremely low, as $XCTER$ depends on both the OSNR and nonlinear effects. That's why the chirped waveforms achieve a better correlation in all conditions, since chirping mitigate the SOA nonlinearities and reduce the ASE noise impact simultaneously, where the amplifier is placed at 40 km and the maximum input power to SOA does not exceed -10 dBm. In terms of bit error rate performance, fig. 6.20 illustrates the effectiveness of chirping for OOK and PPM modulation formats; specially for the chirped PPM, it outperforms the classical transmission at the cost of data rate. Detecting the PPM symbols is based on comparing the two time slots energies in each frame; where for OOK, the threshold for data decision in each iteration is computed by estimating the average energy per bit from the total received energy (which corresponds to the overall stream of pulses). Therefore, nonlinearity has no great influence on the bit error rate of such non-coherent scenarios, as the cross gain modulation and four wave mixing are deterministic for a fixed SOA operating point. The collected errors are mainly due to ASE, in addition to the inherent noises produced by the other optical and electrical components in our system. Tens Mbps data rate is not extremely low for UWB communications as reported in litera-

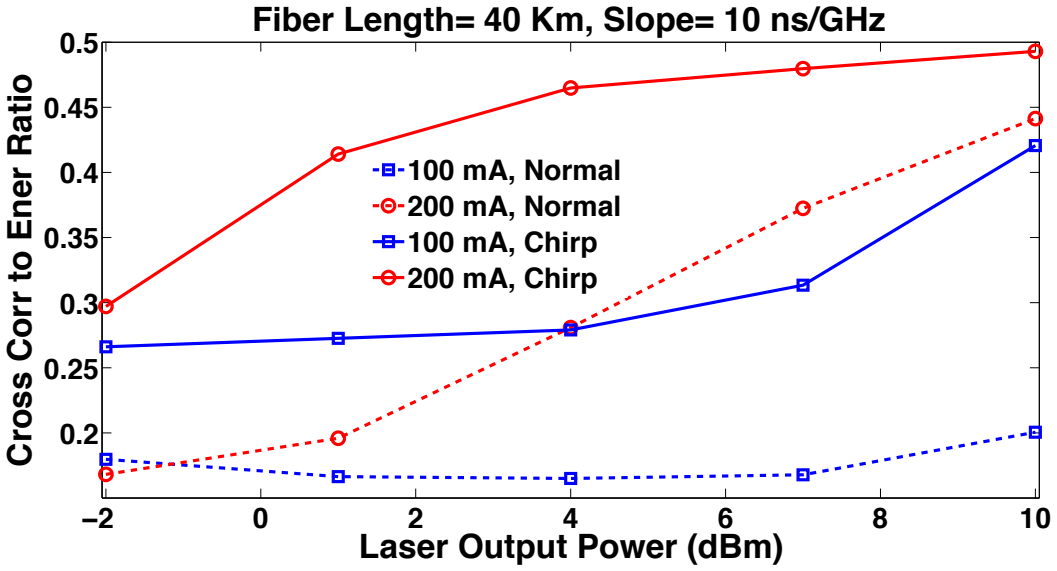

Figure 6.19: Cross correlation to energy ratio versus laser output power for I_{bias}= 100 mA and I_{bias}= 200 mA, the chirping slope is 10 ns/GHz and SOA is placed at 40 km.

ture [23], and the probability of error corresponding to the chirped transmission is within the forward error correction (FEC) limit, where SOA is placed at 40 km and injected by 200 mA biasing current. A portion of the received OOK signal is plotted in fig. 6.21 with (down) and without (up) chirping, these time waveforms justifies the enhancement in the BER performance, as the signal-to-noise ratio becomes extremely higher at receiver side, thanks to chirping.

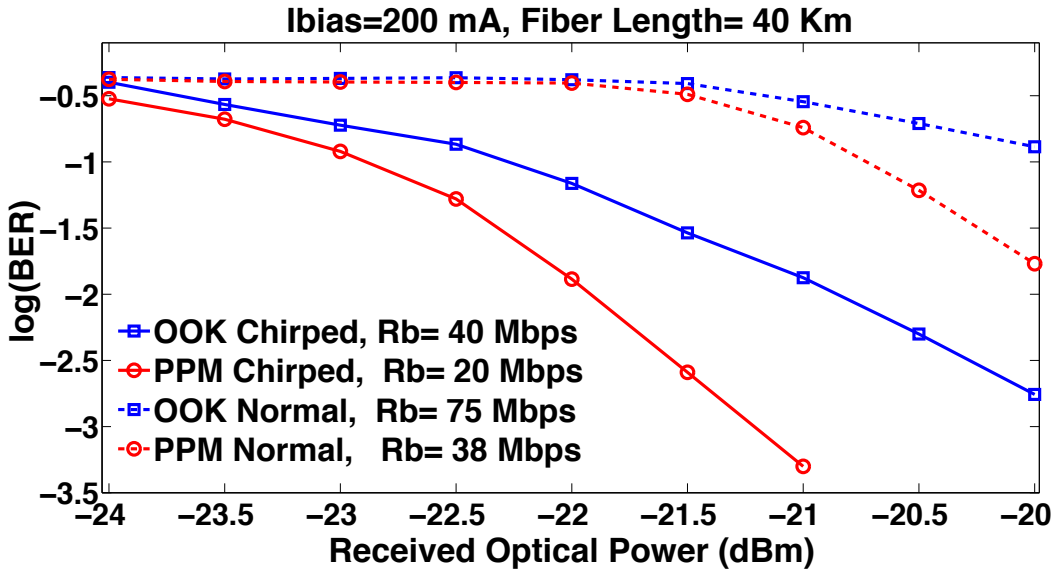

Figure 6.20: Bit error rate versus received optical power (just before SOA) for chirped and non-chirped OOK and PPM modulation schemes, where I_{bias}= 200 mA and SOA is placed at 40 km.

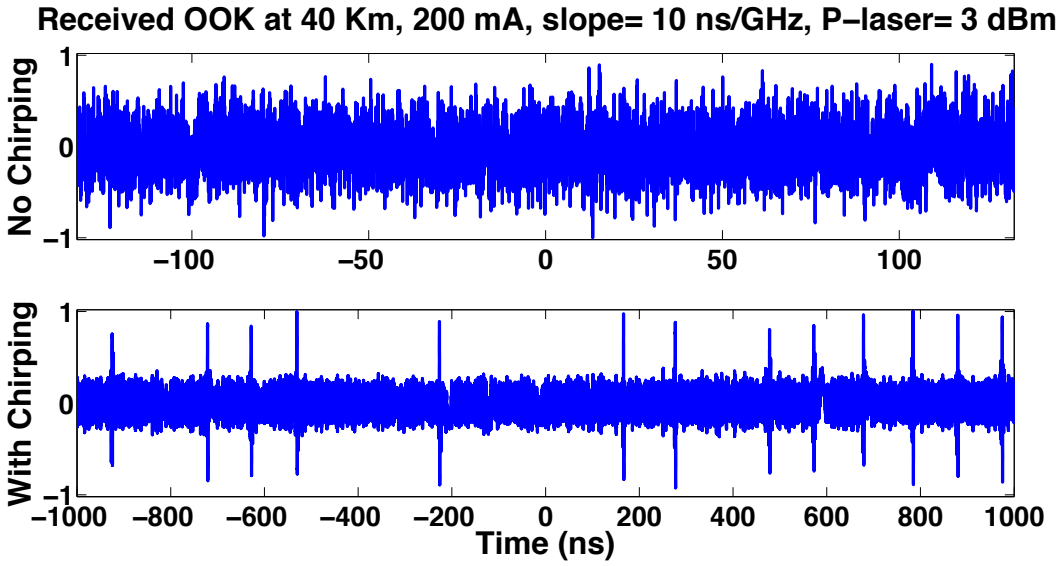

Figure 6.21: Received OOK just after SOA (at 40 km) in the case of no chirping (up) and chirping (down) with a slope of 10 ns/GHz, where the laser output power is 3 dBm and I_{bias}= 200 mA.

6.4 Summary

In this chapter, we adopt for the first time the DCSK scheme in a practically implemented SOA-based UWB over fiber system. Interesting bit error rate results have been obtained in comparison with other non-coherent modulation formats, for an extremely low number of chips and high data rate transmission. The performance of the Improved DCSK technique has been also examined, which has not shown to be pertinent in our proposed system, as it is highly sensitive to SOA nonlinearities and chromatic dispersion. As a complementary approach, we experimentally demonstrate the effectiveness of chirping technique in linearizing the SOA characteristics and reducing the ASE noise influence. Higher cross correlation between the transmitted and received pulses was achieved, and a lower probability of error has been also recorded with OOK and PPM transmissions, thanks to the chirping scheme.

Bibliography

[1] Agilent, Arbitrary Waveform Generator, M8190A, User's Guide.

[2] Agilent, N4391A, Optical Modulation Analyzer, Data Sheet.

[3] SOA-XN-OEC-1550-Non-Linear Semiconductor Optical Amplifier, Data Sheet.

[4] Caillaud, C., Chanclou, P., Blache, F., Angelini, P., Duval, B., Charbonnier, P., ... & Achouche, M. (2015). Integrated SOA-PIN detector for high-speed short reach applications. Journal of Lightwave Technology, 33(8), 1596-1601.

[5] Angelini, P., Blache, F., Caillaud, C., Chanclou, P., Goix, M., Jorge, F., ... & Achouche, M. (2015). Record 22.5-dBm Sensitivity SOA-PIN-TIA Photoreceiver Module for 40-Gb/s Applications. IEEE Photonics Technology Letters, 27(19), 2027-2030.

[6] Caillaud, C., Glastre, G., Lelarge, F., Brenot, R., Bellini, S., Paret, J. F., ... & Achouche, M. (2012). Monolithic integration of a semiconductor optical amplifier and a high-speed photodiode with low polarization dependence loss. IEEE Photonics Technology Letters, 24(11), 897-899.

[7] C. K. Rushforth, "Transmitted-reference techniques for random or unknown channels," IEEE Trans. Inform. Theory, vol. 10, no. 1, pp. 39–42, Jan. 1964.

[8] Arslan, H., Chen, Z. N., & Di Benedetto, M. G. (Eds.). (2006). Ultra wideband wireless communication. John Wiley & Sons.

[9] R. T. Hoctor and H. W. Tomlinson, "An overview of delay-hopped transmitted-reference RF communications," Technique Information Series: General Electric Company Research and Development Center, Jan. 2002.

[10] R. A. Scholtz, "The origins of spread-spectrum communications," IEEE Trans. Commun., vol. 30, no. 5, pp. 822–854, May 1982.

[11] Chao, Y. L., & Scholtz, R. A. (2005). Ultra-wideband transmitted reference systems. IEEE Transactions on Vehicular Technology, 54(5), 1556-1569.

[12] M. K. Simon, J. K. Omura, R. A. Scholtz, and B. K. Levitt, Spread Spectrum Communications. Rockville, MD, USA: Computer Science, 1985.

[13] G. Heidari-Bateni and C. McGillem, "Chaotic sequences for spread spectrum: an alternative to PN-sequences," in Proc. IEEE Int. Conf. Sel. Topics Wireless Commun., Jun. 1992, pp. 437–440.

[14] G. Heidari-Bateni and C. McGillem, "A chaotic direct-sequence spreadspectrum communication system," IEEE Trans. Commun., vol. 42, no. 234, pp. 1524–1527, Feb. 1994.

[15] Kaddoum, G. (2016). Wireless chaos-based communication systems: A comprehensive survey. IEEE Access, 4, 2621-2648.

[16] G. Kaddoum, P. Chargé, D. Roviras, and D. Fournier-Prunaret, "A methodology for bit error rate prediction in chaos-based communication systems," Circuits, Syst. Signal Process., vol. 28, no. 6, pp. 925–944, Dec. 2009.

[17] R.C. Hilborn, J.C. Sprott, "Chaos and nonlinear dynamics: an introduction for scientists and engineers", American Journal of Physics, 62 (9), pp. 861-862, 1994.

[18] Fang, Y., Han, G., Chen, P., Lau, F. C., Chen, G., & Wang, L. A Survey on DCSK-based Communication Systems and Their Application to UWB Scenarios.

[19] Kaddoum, G., Soujeri, E., Arcila, C., & Eshteiwi, K. (2015). I-DCSK: an improved noncoherent communication system architecture. IEEE Transactions on Circuits and Systems II: Express Briefs, 62(9), 901-905.

[20] Argyris, A., Syvridis, D., Larger, L., Annovazzi-Lodi, V., Colet, P., Fischer, I., ... & Shore, K. A. (2005). Chaos-based communications at high bit rates using commercial fibre-optic links. Nature, 438(7066), 343-346.

[21] Lin, F. Y., & Tsai, M. C. (2007). Chaotic communication in radio-over-fiber transmission based on optoelectronic feedback semiconductor lasers. Optics express, 15(2), 302-311.

[22] Zhang, L., Xin, X., Liu, B., & Wang, Y. (2011). Secure OFDM-PON based on chaos scrambling. IEEE Photonics technology letters, 23(13), 998.

[23] Ryckaert, J., Verhelst, M., Badaroglu, M., D'Amico, S., De Heyn, V., Desset, C., ... & Dehaene, W. (2007). A CMOS ultra-wideband receiver for low data-rate communication. IEEE Journal of Solid-State Circuits, 42(11), 2515-2527.

Chapter 7

Conclusion and Perspectives

7.1 Conclusion

The growing demand for high speed communications and error-free transmission motivates researchers to go forward in advancing existing data networks and developing new telecommunication technologies. Research efforts are oriented in two complementary paths, the first is associated with the hardware physical layer architecture, like improving the functionality of different instruments, attenuating embedded losses, increasing the gain and bandwidth of amplifiers, adding or removing some components, adopting filters, advancing the fabrication technology, exchanging a single by a multiple antenna configuration. Where the other strategy deals with pre and post processing at transmitter and receiver sides, designing efficient modulation formats, optimizing error correction codes, designing anti-fading signals, applying noise reduction methods, besides to different signal processing schemes.

The capacity of transmission strongly depends on the available bandwidth, and the channel characteristics significantly affect the quality of service, hence, Ultra WideBand over fiber has been the target system approach in our thesis. In particular, carrier-free impulse radio scenario, has been the core of our investigations due its low cost and complexity. After a broad study regarding optical generation techniques existing in literature, we have investigated a transceiver based on Mach-Zehnder Modulator, for its good compromise between complexity and system performance. The main objective of this dissertation was to achieve a reach extension while minimizing the probability of error for the UWB optical transmission.

Widening the data coverage area requires extending the optical link via in-line amplifiers, and increasing the antenna output power so as to enlarge the wireless propagation distance. The latter is challenging, due to the power constraints of regulatory bodies regarding UWB free space operation, hence a highly efficient transmission is demanded in order to maximize the electrical signal power without violating standard masks. The spectral behavior of modulated impulse radio depends on the basic pulse spectrum and modulation characteristics, both have to be considered in optimizing the corresponding spectral response. As well, enhancing the UWB power efficiency also increases the signal-to-noise ratio, which consequently reduces the number of errors collected at receiver side. Regarding the bit error rate performance, it could be also improved by applying noise reduction and pre-distortion techniques, besides to advanced modulation patterns which

have a kind of robustness against channel effects.

In this work, we take the advantage of low cost integrable Semiconductor Optical Amplifier to boost the optical signal traveling along the fiber link. The amplifier is placed at a distance from the transmitter, so as to compensate against fiber attenuation and to obtain a high electrical power after photo-detector. However, such an optical component may lead to strong nonlinearities acting on the propagated pulses, besides to the amplified spontaneous emission noise. Both degrade the power efficiency and bit error rate performance of the UWB over fiber transmission system. We have applied pre-distortion techniques to mitigate against these nonlinear effects and improve the spectral efficiency of SOA output pulses. In addition, a phaser-based configuration has been proposed, which linearizes the amplifier characteristics and reduces the noise impact simultaneously. On the modulation side, a multi-waveform impulse radio data modulation scheme has been developed, resulting in a higher degree of randomness and consequently lower intensity of discrete spectral spikes; a significant enhancement in the power efficiency was also recorded thanks to this new type of randomization. Moreover, a Differential Chaos Shift Keying modulation format has been adopted in the optical transceiver, leading to a good robustness against nonlinearities and time jitter, due to the embedded chaotic reference which holds channel state information in each symbol. Lower probability of error was obtained in comparison with other modulation options.

Regarding pre-distortion techniques, a significant raise in the power efficiency was achieved based on single Gaussian pulses and combinations. Doublets-based Abraha's proposed waveform, besides to our newly designed triple combination relying on fundamental Gaussians, both have proved to be effective in coping with SOA nonlinearities, by exploiting a higher degree of freedom in controlling time characteristics. Increasing the order of Gaussian derivation is another solution offering a lower potential but with less complexity. Over a large extension of optical link, our scheme has exhibited an enhancement in the power efficiency of 0.75 Gbps Pulse Position Modulation and 1.5 Gbps On Off Keying. Systematical up and down chirping utilizing group delay phasers is an alternative approach, which is not only capable to correct SOA impact at strong gain saturation, but also has the potential to reduce the ASE noise influence while operating in the linear region. A significant increase in the pulse efficiency of the 5th Gaussian ($>$30%) and Abraha's combination ($>$40%) waveforms has been recorded. A better bit error rate performance and higher power efficiencies have been achieved considering a 1 Gbps OOK and 0.5 Gbps PPM modulation formats, while propagating over a large extension of single mode fiber. As discussed previously, the pulse spectral response is not the only aspect to be considered, reducing the frequency comb lines resulting from time periodicity is also a key step to improve the efficiency of the UWB transmitted signal. Hence, a new spectrum smoothing technique is developed on the basis of OOK or PPM modulation schemes, by applying a pulse shape randomization. The closed-form expressions of the power spectral densities have been derived, and it is shown that using a greater number of pulses leads to a better spectral behavior, and consequently higher power efficiency. This technique is compatible with both carrier-based transmitters and impulse radio systems. For the latter, we investigated the particular case of the 4th and 5th Gaussian derivatives, considering 1 Gbps PPM and 2 Gbps OOK formats, the spectra of the randomized transmissions dominate the conventional in terms of power efficiency. The active distance over which the multi-waveform modulations perform better is controlled by the biasing current injected into

the SOA in a flexible way. Not like direct sequence, which has an excellent performance but with much more complicated implementation, our approach offers a good compromise between spectrum enhancement and generation complexity. Regarding DCSK, which has been employed for the first time in optical fiber communications, interesting bit error rate results were obtained in comparison with OOK and PPM energy detection schemes, for an extremely low number of chips and high data rate transmission.

A large piece of this work was based on simulations; due to the sampling frequency limitation of our Arbitrary Waveform Generator (12 GHz), it was not possible to occupy the full UWB standard mask. An experimental demonstration for DCSK technique was conducted, besides to a practical evaluation for chirping. In terms of bit error rate measurements, both have proved to be pertinent for adoption in the real SOA-based UWB over fiber system. In this thesis we investigate simple analog approaches based on non-coherent detection, that strongly matches the requirements of impulse radio systems in terms of cost and complexity.

7.2 Perspectives

Based on our knowledge and experience gained during this research work, we suggest several future directions that may be pertinent for improving the performance of UWB over fiber systems:

Consider Two Real Antennas and Wireless Channel

Examining the proposed schemes while considering a free-space channel is required so as to validate their effectiveness. The transmitter and receiver antennas add nonlinear effects on the propagated UWB signals, and the great challenge rises from the multipath fading which occurs even at short distances.

Study the Performance with Different Optical Components

In our setup, we have used the MZM, SOA, and single mode fiber; considering other types of intensity modulators and optical amplifiers could be pertinent; we could expect a performance gain at the expense of complexity. Adopting a multi-mode fiber may also be another question to investigate, with a study of the robustness of transmitted pulses against inter-modal dispersion.

Apply Chirping Against SOA and Fiber Effects

The phaser applies a frequency dependent time shift, so it could be useful to exploit the benefits of chirping in compensating against self phase modulation inherent to SOA, besides to the chromatic dispersion occurring in the fiber.

Phaser-based Interferometer for Pulse Shape Optimization

The power efficiency of an UWB pulse under FCC mask can be enhanced by playing with the time dynamics. Placing parallel up and down phasers with absolutely same slopes, can introduce a frequency sinusoid that modulates the spectrum of the output pulse. Such an

interferometric configuration may improve the spectral response and consequently increase the pulse efficiency.

Three Dimensional Randomization for Impulse Radio

Three randomization techniques exist for impulse radio transmission, based on the amplitude, time, or shape. Developing a new type of randomization relying on the three variables could be a good alternative, which may gain the advantages of all current schemes at the price of complexity.

Pre-distortion with Different Pulse Waveforms

Until now, pre-distortion has been applied with particular pulse shapes, mainly Gaussian derivatives and combinations. It might be interesting to see the performance with Hermites, Cubic, Laplacian, Rectangular, Sinc, and other waveforms, so as to quantify the benefits of the proposed scheme.

Consider the case of Bi-directional Transmission

In this work, we deal with downlink scenario, thus taking into account the uplink transmission is a complementary approach, so as to evaluate the performance considering a full bi-directional communication system.

Appendices

Appendix A

Interior Point Algorithm: A Brief Overview

Interior point is an iterative method for solving linear and nonlinear optimization problems, it approaches optimal solutions from the interior of the feasible domain [1–3]. This algorithm is more effective when applied with convex problems, and could be adopted with single and multi-variable functions [1–3]. As described in fig. A.1, the algorithm starts from an initial point and apply several iterations so as to reach the optimum. The latter being the minimum of the objective function $\left(Min\{f(x)\}\right)$ satisfying two criteria: $Ax = b$ and x ≥ 0, where x is the current solution, A and b are the coefficients of the linear constraint. The solution in each iteration is determined based on the previous one:

$$x^{k+1} = x^k + \alpha d_x^k \tag{A.1}$$

where $\alpha \geq 0$ is the step length and $d_x^k \in R^n$ is the moving direction, after passing by a number of points the optimal solution is obtained. As shown in fig. A.2, the interior of the feasible region is shot toward an optimal solution, and the target direction is the path which improves the objective function value at the fastest feasible rate. The current trial point x^* is translated into the center of the feasible region by a projective transformation, in order to enlarge the improvement when approaching a new direction. So by centering the trial solution in each iteration, the direction of the projected gradient is turned to reach the neighborhood of the optimal point, as the algorithm goes towards convergence. Centering is performed by changing the scale of the variable, so that the current point becomes equidistant from boundaries in the new coordinate system, $\hat{x} = D^{-1}x$, where D is the diagonal of x in the old coordinate system. The basic concept of optimality is: A current feasible solution is optimal if and only if "no feasible direction at this point is a good direction," when the optimality condition is satisfied the algorithm stops. The total complexity for the algorithm is the number of iterations multiplied by the number of operations (or function evaluations).

The interior point algorithm has a great potential for solving huge programming problems because the required linear algebra is faster. Besides, it is a practically effective algorithm which could be easily understood and implemented. In addition, it is a polynomial-time algorithm which has a low computational complexity and is efficient when high accuracy is needed.

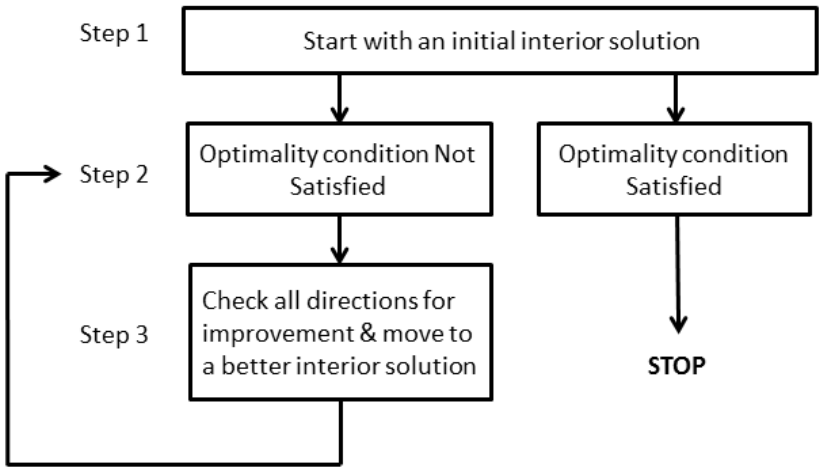

Figure A.1: General scheme of an interior point method

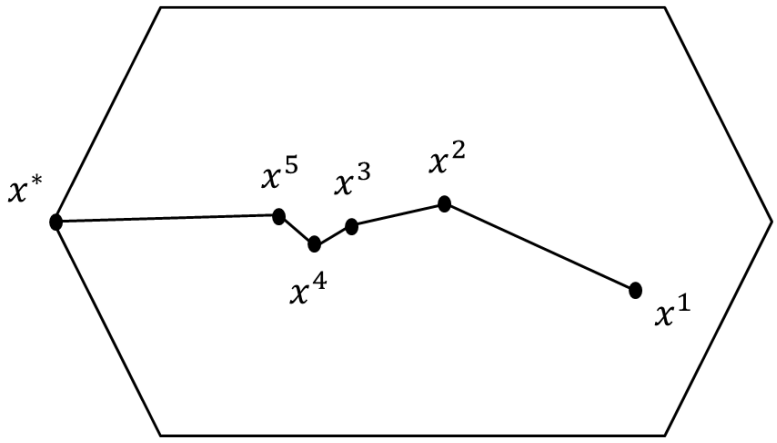

Figure A.2: Interior point optimization path.

Appendix B

SOA Model

Symbol	Parameter	Value	Unit
L	Active region length	$500\ 10^{-6}$	m
w	Active region width	$2\ 10^{-6}$	m
d	Active region thickness	$300\ 10^{-9}$	m
α_0	Active region reference losses	21692	m^{-1}
α_c	Confinement region losses	497	m^{-1}
α_s	Losses at optical defaults	395	m^{-1}
α_N	Differential active region losses with respect to carrier density	$1.139\ 10^{-21}$	m^2
α_λ	Differential active region losses with respect to wavelength	0.0	m^{-2}
Γo	Reference confinement factor	0.3	
Γ_N	Differential confinement factor with respect to carrier density	$9.914\ 10^{-28}$	m^3
Γ_λ	Differential confinement factor with respect to wavelength	10028	m^{-1}
N_0	Transparency carrier density	$6.5\ 10^{23}$	m^{-3}
a_0	Differential peak-gain coefficient with respect to carrier density	$2.617\ 10^{-20}$	m^2
a_1	Convergence parameter needed for simulations	1.2	m
λ_0	Gain peak wavelength at transparency carrier density	$1617\ 10^{-9}$	m
b_0	Differential gain peak wavelength with respect to carrier density	$-3.783\ 10^{-32}$	m^4
b_1	Second order differential gain peak wavelength with respect to carrier density	$2.017\ 10^{-57}$	m^7
λz_0	Wavelength at begin of zero-gain region at transparency carrier density	$1662\ 10^{-9}$	m
z_0	Differential begin of zero-gain region with respect to carrier density	$1.02\ 10^{-32}$	m^4
z_1	Second order differential begin of zero-gain region with respect to carrier density	$4.012\ 10^{-57}$	m^7
K_g	Spontaneous emission coefficient	2.775	
$\Delta\lambda_{se}$	Spectral shift between material gain peak and spontaneous emission peak	$-34.4\ 10^{-9}$	m
ϵ_{CH}	Compression coefficient due to carrier heating	$0.3\ 10^{-23}$	m^3
α_CH	Linear enhancement factor due to carrier heating	1	
ϵ_{SHB}	Compression coefficient due to spectral hole burning	$0.7\ 10^{-23}$	m^3
$\Delta\lambda_{SHB}$	FWHM of the spectral hole burning process	$30\ 10^{-9}$	m
R_l	Linear ohmic resistance	$6.75\ 10^{-4}$	$\Omega\ m^{-1}$
N_e	Equilibrium carrier density	$1\ 10^{17}$	m^{-3}
η	Ideality factor	2	
T	SOA's temperature	295	K
A_{st}	Linear recombination coefficient	$2.302\ 10^{8}$	s^{-1}
B_{ns}	Bimolecular recombination coefficient	$3.124\ 10^{-18}$	$m^3\ s^{-1}$
C_{au}	Auger recombination coefficient	$9.754\ 10^{-39}$	$m^6\ s^{-1}$

Figure B.1: Values of the parameters for SOA model [4].

Appendix C

Optilux Fiber Model based on Split-Step Fourier Algorithm

In our simulations we used the Optilux for modeling the single mode fiber, which is an open source collection of tools providing advanced techniques to design, simulate, and analyze optical communication systems [5]. Optilux is implemented as Matlab/Octave toolbox (so the time signal is an indexed vector) and specialized with a high computational speed [5].

As the transfer function of the optical fiber is a solution to the nonlinear Schrodinger equation, applying the split-step Fourier method is a good approach for modeling a fiber. *Fibergui* solves the nonlinear Schrödinger equation (NLSE) in absence of polarization effects using a graphical user interface (GUI). The inputs of this function are, fiber length, attenuation, effective area, nonlinear index, wavelength, chromatic dispersion coefficient, fiber slope, maximum step for the split-step algorithm, and the maximum nonlinear phase rotation in each step. NLSE in absence of polarization effects for an electric field E(z,t), z being the distance and t the time, is the following partial differential equation [6]:

$$\frac{\partial E(z,t)}{\partial z} = -\frac{\alpha}{2}E - \beta_1\frac{\partial E}{\partial t} + j\frac{\beta_2}{2}\frac{\partial^2 E}{\partial t^2} + \frac{\beta_3}{6}\frac{\partial^3 E}{\partial t^3} - j\gamma|E|^2E \tag{C.1}$$

where α is the fiber attenuation, $\beta_k = \frac{d^k\beta}{d\omega^k}\big|_{\omega=\omega_0}$, k = 1,2,..., $\beta(\omega)$ the wave propagation constant, ω_0 presents the central angular frequency of E, and γ is the nonlinear coefficient. The split-step Fourier Method (SSFM) is an efficient algorithm used in numerical analysis for solving the NLSE. It is a special application of the splitting method for solving nonlinear partial differential equations, and useful to face out the problem [7]. NLSE is solved by the SSFM with a variable step so as to have a maximum nonlinear phase rotation into each step. The solution is computed in small steps with a separation between linear and nonlinear, since linear steps are made in frequency domain and the nonlinear ones in time domain, so it is a pseudo-spectral approach.

Appendix D

Spectra of MWOOK and MWPPM: Mathematical Development

We give here an outline of the proof of equations (5.9) and (5.10), by following similar steps to those used in [8]. Let's first adopt a general expression for the multi-waveform modulation schemes:

$$w(t) = \sum_{k} \sum_{j=1}^{N} b_{j,k} a_k p_j(t - kT - \varepsilon_k) \tag{D.1}$$

where the amplitude coefficient a_k equals the binary data d_k in the MWOOK case and equals one for MWPPM; regarding the time shift, we have $\varepsilon_k = 0$ for MWOOK and $\varepsilon_k = d_k\Gamma$ for MWPPM. The transmitted signal can be alternatively expressed as a convolution product:

$$w(t) = \sum_{j=1}^{N} d_j(t) * p_j(t) \tag{D.2}$$

where the impulse train signal $d_j(t) = \sum\limits_{k} b_{j,k} a_k \delta(t - kT - \varepsilon_k)$ reflects the modulation scheme adopted (MWOOK or MWPPM).
Assuming that the set $\mathcal{P}$ is made of mutually uncorrelated pulse waveforms and that the pulse trains $d_j(t)$ have the same spectral characteristics, we get the power spectral density

$$S_w(f) = S_D(f) | \sum_{j=1}^{N} P_j(f)|^2 \tag{D.3}$$

where $S_D(f)$ stands for the PSD of the pulse train and $P_j(f)$ being the Fourier transform of $p_j(t)$. The discrete spectral lines resulting from the modulation pattern correspond to the term $S_D(f)$ only; with the view to derive its expression, it can be written as

$$S_D(f) = \left\langle \mathbb{E}\left[\frac{d|D(f,t)|^2}{dt}\right] \right\rangle \tag{D.4}$$

where $< . >$ corresponds to time averaging and the accumulated energy spectral density at time t taking the form

$$|D(f,t)|^2 = \left| \int_{-\infty}^{t} d(\tau) e^{-j2\pi f\tau} d\tau \right|^2 \tag{D.5}$$

After some algebra, it can be seen that the following equations holds:

$$|D(f,t)|^2 = \sum_k \sum_l b_k b_{k+l} a_k a_{k+l}\, e^{2\pi f T l j} e^{2\pi f j(\varepsilon_{k+l}-\varepsilon_k)} \times$$
$$u(t-kT)\, u(t-kT-lT) \tag{D.6}$$

where $u(t)$ is the unit step function. Then, it is straightforward to show that

$$\begin{aligned}\mathbb{E}\left[\frac{d|D(f,t)|^2}{dt}\right] &= \sum_k R_b(0) R_a(0)\, \mathbb{E}\left[\delta(t-kT)\right] \\ &+ \sum_{l<0}\sum_k R_b(l) R_a(l) R_m(l)\, e^{j2\pi f T l}\, \mathbb{E}\left[\delta(t-KT)\right] \\ &+ \sum_{l>0}\sum_k R_b(l) R_a(l) R_m(l)\, e^{j2\pi f T l} \mathbb{E}\left[\,\delta(t-KT-lT)\right]\end{aligned} \tag{D.7}$$

where $R_b(l)$, $R_a(l)$ and $R_m(l)$ denote the auto-correlation functions of the independent processes b_k, a_k and $m_k = e^{-j2\pi f \varepsilon_k}$, respectively.

Finally, after time averaging and applying the Poisson formula

$$\sum_l e^{j2\pi f T l} = \frac{1}{T}\sum_k \delta(f - \frac{k}{T})$$

we get the expression

$$S_D(f) = \frac{1}{T}\Big[\left(\sigma_{\hat{b}}^2\sigma_{\hat{a}}^2 + \sigma_{\hat{b}}^2\mu_a^2 + \mu_b^2\sigma_{\hat{a}}^2 + \mu_b^2\mu_a^2 - \mu_b^2\mu_a^2|\mu_m|^2\right) + \frac{\mu_b^2\mu_a^2|\mu_m|^2}{T}\sum_k \delta(f-\frac{k}{T})\Big] \tag{D.8}$$

where $\mu_\times$ corresponds to the mean of the process $\times$ and σ denoting the standard deviation of the corresponding zero mean process (e.g. $b_k = \mu_b + \hat{b_k}$ with $\mathbb{E}\left[\hat{b_k}\hat{b}_{k+l}\right] = \sigma_{\hat{b}}^2\delta[l]$).

Bibliography

[1] Byrd, R. H., Hribar, M. E., & Nocedal, J. (1999). An interior point algorithm for large-scale nonlinear programming. SIAM Journal on Optimization, 9(4), 877-900.

[2] Wachter, A., & Biegler, L. T. (2006). On the implementation of an interior-point filter line-search algorithm for large-scale nonlinear programming. Mathematical programming, 106(1), 25-57.

[3] Nesterov, Y., & Nemirovskii, A. (1994). Interior-point polynomial algorithms in convex programming. Society for industrial and applied mathematics.

[4] Morel, P., & Sharaiha, A. (2009). Wideband time-domain transfer matrix model equivalent circuit for short pulse propagation in semiconductor optical amplifiers. IEEE Journal of Quantum Electronics, 45(2), 103-116.

[5] P. Serena, Optilux Toolbox. Available from: <www.optilux.sourceforge.net>.

[6] G. Agrawal, Nonlinear Fiber Optics. Academic Press, January 2001.

[7] R. J. LeVeque and J. Oliger, "Numerical methods based on additive splittings for hyperbolic partial differential equations," Mathematics of Computation, vol. 40, no. 162, pp. 469-497, 4 1983.

[8] J. E. Padgett, J. C. Koshy and A. A. Triolo, "Physical-layer modeling of UWB interference effects," Telcordia Technologies Report to DARPA (NETEX Program), Jan. 2003.

Publications

Journal Papers

- J1- **Taki, H.**, Azou, S., Hamie, A., Al Housseini, A., Alaeddine, A., & Sharaiha, A. (2016). Improving the power efficiency of SOA-based UWB over fiber systems via pulse shape randomization. Optical Fiber Technology, 31, 161-167.
- J2- **Taki, H.**, Azou, S., Hamie, A., Al Housseini, A., Alaeddine, A., & Sharaiha, A. (2017). Simple pre-distortion schemes for improving the power efficiency of SOA-based IR-UWB over fiber systems. Optics Communications, 382, 225-231.
- J3- **Taki, H.**, Azou, S., Hamie, A., Al Housseini, A., Alaeddine, A., & Sharaiha, A. (2017). On phaser-based processing of impulse radio UWB over fiber systems employing SOA. Optical Fiber Technology, 36, 33-40.
- J4- **Taki, H.**, Azou, S., Morel, P., Hamie, A., Al Housseini, A., Alaeddine, A., & Sharaiha, A. 'Chirping Techniques for Enhancing the Performance of SOA-based UWB over Fiber Systems: An Experimental Demonstration'. Submitted to IET Electronic Letters.

Conference Papers

- C1- **Taki, H.**, Azou, S., Hamie, A., Al Housseini, A., Alaeddine, A., & Sharaiha, A. (2015, April). On optimizing the operating conditions of a Mach-Zehnder modulator for IR-UWB over fiber transmission. In Digital Information and Communication Technology and its Applications (DICTAP), 2015 Fifth International Conference on (pp. 169-172). IEEE.
- C2- **Taki, H.**, Azou, S., Hamie, A., Al Housseini, A., Alaeddine, A., & Sharaiha, A. (2016, May). Pulse shape pre-distortion for improving the power efficiency of SOA-based IR-UWB over fiber systems. In 2016 23rd International Conference on Telecommunications (ICT) (pp. 1-6). IEEE.
- C3- **Taki, H.**, Azou, S., Hamie, A., Al Housseini, A., Alaeddine, A., & Sharaiha, A., "Reach Extension of an IR-UWB over Fiber System via OOK Randomization and SOA Amplification," EuCNC 2015, IEEE, Paris-France. **(Poster)**.

Acknowledgments

This research has taken place at the École Nationale d'Ingénieurs de Brest (ENIB) in France, and the Ecole Doctorale en Sciences et Technologie (EDST) in Lebanon. I have gained solid technical skills during my fruitful period in these two laboratories, which allow me to go ahead in the world of research and specially in the field of optical communications. I would like to take the opportunity to thank Professor Stephane Azou at ENIB, who was the main supervisor, for his guidance and support. Besides to the time he spent with me in analyzing results, his advices were of great importance, so he has used to orient my research in the correct way. Thanks to his assistance I was efficient in my work, high originality and novelty was achieved due to following up my progress in all stages. Special thanks to Ammar SHARAIHA, Professor at ENIB, for sharing our research with his beneficial ideas, we have used to discus with him the optical aspects in each approach, based on his vast experience he gave us key advices for improving the quality of our work. On the Lebanese side, my gratitude is for Professor Ali HAMIE at the Lebanese University (also the Dean of Arts, Sciences, and Technology University in Lebanon (AUL)) who opened the chance for me to reach ENIB laboratory, besides to the efforts he applied to establish the collaboration between EDST and ENIB, he has supervised me during my stays in Lebanon, and participated in our scientific discussions. I would like also to thank Ali ALAEDDINE, Professor at the Lebanese University, for his support and encouragement during my research period, in addition to carrying the administrative tasks for my thesis registration in EDST. I have the pleasure to be evaluated by the reporters, Christelle AUPETIT-BERTHELEMOT, Professor at ENSIL, and Bernard UGUEN, Professor at Université de Rennes 1, and the examiners, Emanuel RADOI, Professor at UBO, and Pascal CHARGE, Professor at Polytech Nantes. I am happy to get my PhD degree approved by such a jury.

Etude de Systèmes de Transmission à Bande Ultra Large sur Fibre utilisant des Amplificateurs Optiques à Semiconducteurs

Résumé: La technologie Ultra WideBand (UWB) sur fibre est une solution prometteuse pour répondre aux enjeux des futurs réseaux de communication WLAN/WPAN. Les caractéristiques de la fibre, incluant son énorme bande passante, offrent la possibilité d'une bonne qualité de service à longue portée. La propagation sans-fil UWB doit être réalisée sous des contraintes de densité spectrale de puissance particulières, imposées par l'autorité de régulation (FCC pour les Etats-Unis). La nouveauté de notre travail provient de l'exploitation des avantages d'un amplificateur optique à semi-conducteurs (SOA) afin d'obtenir une extension de portée à un coût et une complexité limités. Cependant, les effets non linéaires et le bruit d'émission spontanée amplifiée (ASE), intrinsèques à ce type de composant, sont susceptibles de dégrader la performance du système. La réduction de ces effets indésirables a donc été d'une importance centrale dans cette étude. Les non-linéarités du SOA ont été compensées en appliquant une solution de pré-distorsion analogique des formes d'ondes électriques. Un traitement basé sur phaser a également été proposé pour réduire simultanément l'influence de l'ASE et linéariser les caractéristiques du SOA, grâce à des opérations de chirping réparties entre l'émetteur et le récepteur. Avec la transmission Impulse Radio, en raison des propriétés temporelles des formats de modulation, des raies spectrales apparaissent, ce qui peut violer la limite FCC ou réduire l'efficacité énergétique. Une nouvelle technique de randomisation de formes d'ondes a été étudiée, qui s'est révélée efficace pour supprimer ces pics spectraux. Les trois approches ont montré un grand potentiel avec les formats On Off Keying et Pulse Position Modulation, à longue portée optique. Les performances d'une modulation différentielle Chaos Shift Keying ont finalement été examinées; une probabilité d'erreur inférieure a été obtenue expérimentalement en comparaison avec d'autres modulations non cohérentes.

Mots clés: Ultra WideBand (UWB), Impulse Radio, Randomisation de formes d'ondes, Amplificateur optique à semi-conducteurs (SOA), Pré-distorsion, Chirping, Chaos Shift Keying (CSK).

On Ultra-Wideband over Fiber Transmission Systems Employing Semiconductor Optical Amplifiers

Abstract: Ultra WideBand (UWB) over fiber is a promising technology for meeting the demands of future wireless local-area networks (WLANs) and wireless personal-area networks (WPANs). Thanks to the enormous bandwidth and fiber characteristics, a high communication quality may be established at long reach. UWB wireless propagation must be achieved with special power and spectral constraints fixed by the regulatory bodies (e.g. US Federal Communication Commission). The novelty of our work originates from exploiting the benefits of a Semiconductor Optical Amplifier (SOA) so as to get a reach extension at limited cost and complexity. However, the inherent nonlinear effects and Amplified Spontaneous Emission (ASE) noise associated to such device may affect the system performance. Overcoming these impairments has been of central importance in this study. SOA nonlinearities have been mitigated by applying analog pre-distortion in electrical domain. Phaser-based processing was also proposed to simultaneously reduce ASE influence and linearize SOA characteristics, thanks to up/down chirping performed on the transmitter/receiver sides. With Impulse Radio UWB transmission, due to the time properties of modulation patterns, discrete lines arise in the corresponding spectrum, which may violate FCC limit or reduce the power efficiency. A new shape randomization technique has been investigated, which proved to be effective in suppressing these spectral spikes. The three approaches have shown a great potential with On Off Keying and Pulse Position Modulation formats at long optical reach. The performance of Differential Chaos Shift Keying was finally examined in the over fiber system, a lower error probability was experimentally achieved in comparison with other non-coherent modulations.

Keywords: Ultra WideBand (UWB), Impulse Radio, Shape Randomization, Semiconductor Optical Amplifier (SOA), Pre-distortion, Chirping, Chaos Shift Keying (CSK).